Characterization of silicon and diamond semiconductor devices in the low temperature regime

Nina Eikenberg

School of Physics

University of Melbourne

Submitted in total fulfilment of the requirements of the degree of

Doctor of Philosophy (PhD)

October 2015

Abstract

At ultra low temperatures, materials reveal interesting behaviours that become evident due to the freezing out of thermal vibrations. We report studies of two important group IV material systems using a newly-commissioned dilution refrigerator at temperatures of less than 50 mK, and under axial magnetic fields of up to 7 Tesla and 1 Tesla in the lateral plane. We realized these magnetic fields with a 3D vector magnet and calibrated the system using well-known test samples.

The first material studied in detail was nitrogen enhanced grown ultra-nano-crys-talline diamond (N-UNCD). Diamond displays a combination of many extreme physical properties such as a high thermal conductivity, the highest number density of atoms, and a wide optical band gap, and is in addition to these properties also biocompatible [1]. The ultra-nanocrystalline form of diamond is composed of small, 3-5 nm diameter grains of diamond and shares many of the desirable properties of the single crystal form, but is much easier to produce in thin form and can be used in wide variety of applications [2], especially for nanomechanics due to its strength and high Young's modulus [3]. When doped with boron, nano-crystalline diamond (B-NCD) displays superconducting properties below a critical temperature of less than a few Kelvin [4, 5]. The nitrogen doped form has found application in biomedical devices [6], but its superconducting behaviour at very low temperatures has not yet been demonstrated [7]. We fabricated N-UNCD thin films using microwave-enhanced CVD growth and used optical lithography to create Hall bar designs. We found that the conductivity of N-UNCD decreased with decreasing temperature, and between 36 mK and 4.9 K, a negative magneto-resistance was observed. Fitting the temperature

and magnetic field dependent data with the 3D weak localization model developed by Kawabata [8], we found that 3D weak localization indeed plays a main role in the conduction mechanism of N-UNCD films even at ultra low temperatures.

The second project was on the characterization of erbium doped silicon (Si:Er) semiconductor devices. Erbium has long been known to be important for use in optical fibre amplification in silica [9], and it also shows strong luminescent properties when it is added to Si as a dopant [10]. As such, Er is also of interest as optoelectronic semiconductor material [11]. Since the recent demonstration that it is possible to optically address single erbium ions in the silicon lattice [12] interest in Si:Er has increased. We studied silicon doped with erbium using ion implantation and report on our attempts to create CMOS devices with Er doped channels. The implanted material was characterized by optical spectroscopy, deep level transient spectroscopy, and measured both electrically and magnetically at low temperatures in the dilution refrigerator. Deep level transient spectroscopy performed on devices with varying anneal temperatures showed the emergence of electronically active traps with the minimum trap density occurring at annealing temperatures above 700 °C. Our results reveal that a rapid thermal anneal at 900 °C activates the luminescence from the implanted erbium ions. This effect remains, even if the sample is subjected to subsequent high temperature treatments. MOS devices co-doped with Er and P were fabricated and characterised to the extent they could be, based on the processing issues that arose.

This is to clarify that:

1. the thesis compromises only my original work towards the PhD except where indicated in the Preface,
2. due acknowledgement has been made in the text to all other material used,
3. the thesis is fewer than 100 000 words in length, exclusive of tables, maps, bibliographies and appendices OR the thesis is [number of words] as approved by the Research Higher Degrees Committee.

Signature from the PhD candidate:

Dedication

This thesis is dedicated to my little sister Bettina, the youngest of three. She took her own life on the 9th of March 2015 at the age of only 22 years. We all dearly miss her.

Acknowledgements

I would like to thank my supervisors Prof. Steven Prawer and Dr Laurens Willems van Beveren for introducing me to the topic and helping me throughout the creation of this piece of work. Furthermore, I am very grateful to Prof. Jeffrey McCallum for his extraordinary helpfulness and patience, and for sharing his wealth of knowledge and information with me. Especially when both of my supervisors left Melbourne, he was a very resourceful and helpful contact.

I am grateful to Dr Brett Johnson who shared his expertise in many areas with me. I am very thankful for everyone who helped with keeping all equipment running, especially Roland Szymansky. I'd also like to thank those who helped train me to use equipment, such as Dr Kumar Ganesan, Chris Schroen, Dr Nikolas Stravias. Moreover, I am grateful for the help of my colleagues, especially Mark Edmonds, Michael Stuiber, and many other office mates who helped me deal with the ups and downs of my research.

Lastly, I would like to thank my friends and family, particularly my wonderfully supportive husband Craig Longhurst, for helping me to keep going and overcome difficulties that occur in any research.

This work was performed in part at the Melbourne Centre for Nanofabrication (MCN) in the Victorian Node of the Australian National Fabrication Facility (ANFF).

The author acknowledges access to ion-implantation and/or ion-beam analysis facilities at the ACT node of the Heavy-Ion-Accelerator Capability funded by the Australian Government under the NCRIS program.

The author would like to acknowledge S. Rubanov, K. Fox, and M. R. Notivoli for performing the SEM and TEM imaging, XPS spectra, and AFM imaging.

Contents

List of Figures **xi**

List of Tables **xxi**

1 Literature review **1**

1.1 Diamond materials 1

1.1.1 Background 1

1.1.2 Conduction mechanism in N-UNCD 9

1.1.3 Motivation for studying N-UNCD 15

1.2 Erbium in Silicon 16

1.2.1 Silicon at low temperatures 24

1.2.2 Motivation for this study on Si:Er semiconductor devices 26

2 Experimental Techniques **29**

2.1 Deep-Level Transient Spectroscopy 29

2.1.1 Capacitance versus voltage measurement 33

2.1.2 The DLTS measurement 34

2.2 Rutherford backscattering 39

2.3 Electrical measurement techniques 45

2.3.1 Classical Hall Effect 45

2.3.2 Van der Pauw method 47

3 **Cryogen-free Dilution Refrigerator** **49**

3.1 The operation of a Dilution Refrigerator 49

3.2 The Coldfinger 56

3.3 3D Vector magnet and optical access 58

3.4 Low Temperature Measurements 59

3.4.1 Measurement Setup 60

3.5 Calibration 62

3.5.1 Silicon MOSFET 62

3.5.2 Aluminium films 70

3.5.3 Niobium SQUID 71

3.5.4 Summary 75

4 **Fabrication** **77**

4.1 Diamond Hall bar device fabrication 77

4.1.1 CVD growth 81

4.1.2 Optical Lithography 83

4.1.3 Metal deposition 84

4.1.4 Lift off 86

4.1.5 N-UNCD Etch 87

4.1.6 Chromium removal 88

4.1.7 Deposition of ohmic leads 90

4.1.8 Wire Bonding 92

4.2 Silicon device fabrication 92

4.2.1 Device designs 93

4.2.2 Process flows 97

4.2.3 Prior simulations 102

4.2.4 Oxide growth 109

4.2.5 Silicon clean 113

4.2.6 Definition of the alignment markers 114

4.2.7 Boron guard ring and phosphorus leads 118

4.2.8 Field oxide 120

4.2.9 Gate oxide 120
4.2.10 Ion implantation 122
4.2.11 Anneal 122
4.2.12 Ohmic contacts 122
4.2.13 Gate metallization 124
4.2.14 Final steps 125
4.2.15 Fabrication issues in the MU devices 125

5 Diamond devices: Experimental Results and Analysis 129
5.1 AFM and SEM imaging 129
5.2 RBS 136
5.3 Raman Spectroscopy 141
5.4 XPS 143
5.4.1 Analysis of Raman and XPS 148
5.5 Electrical measurements 149
5.5.1 Analysis of electrical measurements 158

6 Silicon devices: Experimental Results and Analysis 167
6.1 DLTS 167
6.2 Photoluminescence 176
6.3 Oxide quality and thickness 180
6.4 Electrical measurements 183

7 Summary and outlook 203
7.1 Installation of a dry dilution refrigerator 203
7.2 Nitrogen enhanced grown diamond 204
7.3 Erbium doped silicon 205
7.4 Further work 206

References 209

List of Figures

1.1 Octahedral nano-diamond model [13]. 1
1.2 Sketch of an energy band diagram of diamond with nitrogen/boron indicated donor/acceptor levels. 3
1.3 SEM image of a boron-doped polycrystalline diamond film deposited by microwave plasma-assisted CVD method [14]. . . . 5
1.4 Fan diagram according to Langer and Neal of an electron scattered via two different sequences [15] 10
1.5 a) Sketch of possible path a diffusive electron may take returning to its origin [15]
b) Probability diffusion of a diffusing electron [15]. 12
1.6 Charge carriers tunneling through localized barriers. 14
1.7 Resistivity versus temperature for varying boron concentration [16]. 15
1.8 Schematic diagram of the energy levels of a Er^{3+} ion [17]. . . . 17
1.9 EPR spectrum of a sample with 10^{19} Er/cm^3 + 10×10^{20} O/cm^3 with the magnetic field nearly parallel to [001] at low temperatures [18]. 19
1.10 PL spectrum for an Er implanted layer in Si
(a) without co-implantation
(b) after oxygen implantation [10]. 20
1.11 Sketch of various defect types in a silicon lattice. 22
1.12 DLTS spectrum of Er implanted n-type Si [19]. 23

1.13 Sketch of the band structure visualizing the principles of impact ionization [20] 24
1.14 Moore's Law shown by the example of microprocessor transistor counts from 1970 to 2005 [21] 26
1.15 Sketch of a bit versus a qubit. 27

2.1 Sketch of the band structure bending at a semiconductor/metal interface. 31
2.2 a) Sketch of the DLTS sample layout.
b) 3D image of the actual sample taken via optical interferometry profiler. 32
2.3 Measurements of an as-implanted Si:Er sample at 295 K showing (a) capacitance versus voltage and (b) inverse capacitance squared versus voltage. 33
2.4 Capacitance versus time at various temperatures and the resultant DLTS signal [22]. 35
2.5 Capacitance versus time (bottom) shown while the bias voltage is pulsed (top). 37
2.6 DLTS signal of an Er implanted Si sample taken at 4 successive time intervals in one measurement run. 38
2.7 Arrhenius plot of $ln(e_n/T^2)$ versus $1/k_BT$ of the largest peak observed in 2.6. 40
2.8 Sketch of the RBS chamber used at Melbourne University. . . 42
2.9 a) RBS spectrum in counts versus channel number of a gold on silicon sample with an incident alpha particle energy of 1 MeV.
b) Same RBS spectrum in normalized yield versus energy, including the simulation. 43
2.10 Calibration plot of energy versus channel number for the backscatter angle detector with an incident alpha particle energy of 1 MeV including the linear fit in red. 44

2.11 Hall bar in a magnetic field illustrating the Hall effect. 46
2.12 Arbitrary shaped sample with four contacts A, B, C, and D along the circumference to illustrate van der Pauw geometry. . 48

3.1 He^3/He^4 Phase-diagram [23, 24]. 50
3.2 Schematic of the ^3He flow in a dilution refrigerator (detail of Fig. 3.3). 51
3.3 Sketch of the cryogen-free dilution refrigerator illustrating the He^3/He^4 cycle, pulse tube, and heat exchangers (according to[25]). 52
3.4 Photograph of the cryogen-free dilution refrigerator. All vacuum cans and heat shields are taken off to show the interior. 54
3.5 Photograph of the assembled cryogen-free dilution refrigerator with the gas handling system (GHS) visible in the background (red). 55
3.6 Photograph of the finished coldfinger. 57
3.7 Sketch of the samples situated in the bore of the 3D vector magnet. 59
3.8 Schematics of the electrical setup during measurements. 61
3.9 Scanning electron micrograph (SEM) of the Silicon MOSFET device, Hall bar defined by photolithography [26]. 62
3.10 Experimental results of the silicon MOSFET DRD1 taken at the University of Melbourne (UM) at ca. 160 mK. Top: Resistivity versus gate voltage.
Bottom: Charge carrier density versus gate voltage. 64
3.11 Experimental results of the silicon MOSFET DRD1 taken at the University of Melbourne (UM) at ca. 160 mK. Top: Mobility versus gate voltage.
Bottom: Mobility versus Charge carrier density. 65

3.12 Si MOSFET measured at UNSW at ca. 40 mK. Top: Resistivity versus gate voltage.
Bottom: Charge carrier density versus gate voltage. 66
3.13 Si MOSFET measured at UNSW at ca. 40 mK. Top: Mobility versus gate voltage.
Bottom: Mobility versus Charge carrier density. 67
3.14 Resistivity versus magnetic field of Silicon MOSFET device DRD1 measured at 160 mK with a gate voltage of 0.7 V. . . . 69
3.15 Four terminal voltage versus source drain current of a 120 nm thick Al Hall bar at varying magnetic fields perpendicular to the plane of the sample at 0.26 K. 70
3.16 Results of Nb SQUID in the upper sample carrier with a perpendicular magnetic field at ∼5 K. Top: Voltage versus magnetic field with constant source-drain current of 2 mA.
Bottom: Critical current versus parallel magnetic field. 72
3.17 The Nb SQUID measured in the upper sample carrier in a rotating magnetic field of the x and y coils. The graph shows source-drain voltage versus field angle with a constant source-drain current of 1 mA at ∼5 K. 74

4.1 Steps involved with optical lithography. 78
4.2 Sketch of the four Hall bar designs on the available mask. . . . 80
4.3 Structure of the substrate wafer used for N-UNCD processing. 81
4.4 Simplified C-N-O diamond deposition diagram according to [28]. 82
4.5 Sketch of the electron beam evaporation chamber. 85
4.6 Isotropic (left) versus anisotropic etching (right). 87
4.7 Optical pictures of the four different Hall bar patterns before the electrical contacts were created. 89
4.8 Two optical pictures of the same sample of the second Hall bar design. a) taken with the optical profiler.
b) taken with a conventional microscope. 90

4.9 Photograph of a finished diamond device wire bonded to the sample carrier it is glued into. 91
4.10 Optical image taken with a microscope of a bonded up device. 92
4.11 Sketch of a cut through the UNSW device design showing the depth profile. 93
4.12 Optical image taken with a microscope of 10× magnification of the 4 finished designs. 94
4.13 Optical image taken with a microscope of 20× magnification of the 4 finished designs in the channel area (central parts of Fig. 4.12). 95
4.14 Graphical visualization of the process flows of both MU and UNSW devices. 98
4.15 SRIM simulations of (left) As 195 keV and (right) Er 110 keV, showing implanted ion concentration versus substrate depth, used for the MU devices. 103
4.16 SRIM simulations of Er at 85 keV into the gate oxide and silicon substrate, as used for the UNSW devices. 105
4.17 SRIM simulations of a) O 15.5 keV and b) Ab 70 keV for the UNSW devices. 106
4.18 Diffusion simulations after As implantation of an energy of 240 keV and fluence of 6.7×10^{14} cm^{-2} under varying annealing and oxidation conditions. 108
4.19 Silicon oxide thicknesses versus oxidation times of blank silicon and erbium doped silicon and their fitted curves. 111
4.20 a) Optical lithography mask for the alignment markers for the MU devices.
b) 3D optical profilometry image of an alignment marker in a silicon wafer. 115
4.21 BOSCH process used for etching silicon. 117

4.22 Optical lithography mask for the boron guard ring and the P-diffused regions. 119
4.23 Optical lithography mask for the gate oxide and the erbium implanted region. 121
4.24 Optical lithography mask for the oxide windows and gate metallization. 123
4.25 TEM image taken of a cross section through the gate of a fully fabricated Er and O implanted device. 124
4.26 Optical image taken with a microscope of a device prior to metal evaporation. 126

5.1 AFM image taken of the 20% N-UNCD sample. 130
5.2 SEM images of the surface of a 5% N-UNCD film. 131
5.3 SEM images of a 10% N-UNCD film. 132
5.4 SEM images of a 20% N-UNCD film. 133
5.5 SEM images of cuts through the 5%, 10%, and 20% N-UNCD films. 135
5.6 RBS spectrum of the 20% N-UNCD film and the C-O reference sample with an incident alpha particle energy of 1 MeV and backscatter angle of 10°. 136
5.7 Cross section of the RBS sample. 137
5.8 Normalized yield versus incident proton energy in the laboratory system. 137
5.9 RRBS spectra of the 20% N-UNCD film and reference samples. 138
5.10 a) RRBS spectrum of the 20% N-UNCD film including simulation.
b) Simulated RBS spectra of varying nitrogen concentration. 140
5.11 Raman spectrum of the 20%, 10%, and 5% N-UNCD. 142

5.12 Top: XPS spectrum of 20% N-UNCD, showing the counts per 1000 s versus the binding energy.
Bottom: XPS of the 20% N-UNCD film after the top layer was removed via Ar sputtering. 144
5.13 a), b), c) XPS spectra of the 20%, 10%, and 5% N-UNCD including fits for sp^2 and sp^3 carbon bonds.
d) XPS spectrum of the 20% N-UNCD around 400 eV. 147
5.14 The electrical setup of the hardware for Hall bar measurements. 149
5.15 4-terminal IV curves. Top: at RT of the 5%, 10%, and 20% N-UNCD films.
Bottom: at varying low temperatures of the 20%N-UNCD film showing the non-linear feature. 150
5.16 Top: Conductivity versus temperature of the 20%, 10%, and 5% N-UNCD films on a half logarithmic scale.
Bottom: Logarithm of conductivity versus 1/temperature on logarithmic scale of the 20%, 10%, and 5% N-UNCD films. . . 153
5.17 Normalized resistance as a function of magnetic field of the 20% and 10% N-UNCD films at 36 mK and 4.2/4.9 K. 154
5.18 Normalized conductivity as a function of magnetic field of the a) 10% and b) 20% N-UNCD films at varying temperatures. . 155
5.19 Top: Voltage versus time of a 10% N-UNCD film, including the sample temperature.
Bottom: LED voltage versus time. 159
5.20 Conductivity versus temperature of the 20% N-UNCD sample between 17 mK and 15 K at zero magnetic field, including the 3D WL model fit. 160
5.21 Relative conductivity versus magnetic field of a 20% N-UNCD sample at 4.2 Kelvin. The experimental data in red, including the 3D WL model fit. 162

5.22 Normalized conductivity versus magnetic field of the 10% N-UNCD sample at various temperatures, including fits. 163

6.1 Top: DLTS spectrum of all samples together.
Bottom: Defect concentration versus anneal temperature. . . . 171
6.2 DLTS spectra of the as-implanted sample at all correlator delay times. 172
6.3 Top: DLTS spectrum of the as-implanted sample and the sample annealed at 200 °C.
Bottom: DLTS spectrum of the samples annealed at 300 °C and 400 °C. 173
6.4 DLTS spectrum of the as-implanted sample and sample annealed at 700 °C. 174
6.5 Photoluminescence of silicon doped with erbium (4x10^{12} cm^{-2}) at - 195 °C for varying anneals. 178
6.6 a) Sketch of a metal-oxide-semiconductor (MOS).
b) Capacitance versus voltage through a MOS capacitor [29]. . 181
6.7 CV measurement of a silicon dioxide on a p-type silicon sample at room temperature. 182
6.8 Top: MU device layout with all mask levels superimposed.
Bottom: Voltage versus current 2-point measurement of an Er doped Si Hall bar, between two ohmic contacts and the gate and an ohmic contact including their linear fits. 184
6.9 Image taken using the optical profilometer of a finished Er doped Si Hall bar device. 185
6.10 Optical image taken with a microscope of 20× magnification of the 4 finished designs in the channel area (detail from Fig. 4.12). 187
6.11 IV curves of UNSW fabricated device from batch 4, design δ.
(a) gate and drain contact. (b) source and drain contact. . . . 188

6.12 3D graphs showing the gate dependency of a device from batch 4 at ∼4.5 K, design δ. (a) and (b) have the source and drain contacts swapped in respect to each other. 189
6.13 3D graphs showing the gate dependency of a device from batch 4 at ∼4.5 K, design δ. In (a) the y-axis is the source-drain voltage, in (b) the gate-drain leakage current through the gate oxide is shown on the y-axis. 190
6.14 Capacitance versus voltage graph of the gate oxide of a fully fabricated device at room temperature and at liquid nitrogen temperature. 192
6.15 Illumination dependency of a batch 4, design δ sample. 195
6.16 Magnetic field dependency of a batch 4, design γ device at ∼5.0 K. 198
6.17 Schematic of freed electron-hole pairs according to impact ionization under the accelerating field of an applied source-drain voltage. 199
6.18 a) Hall resistivity and source-drain resistivity versus magnetic field at ∼5.0 K with a constant source-drain current of -50 nA. b) Sample temperature versus magnetic field. 200

List of Tables

4.1 Process flow for N-UNCD Hall bar fabrication. 79
4.2 Dimensions of the four designs given in fig 4.2. 80
4.3 Recipe for microwave assisted CVD grown UNCD with 20%, 10%, and 5% nitrogen doping. 82
4.4 Optical lithography recipe with photoresist AZ1514H and developer 826MIF. 84
4.5 Parameters for N-UNCD etch recipe. 87
4.6 Chromium etchant recipe. 88
4.7 Er:Si new sample design dimensions. 96
4.8 Er:Si batches and their additional implant ions. 97
4.9 Process sheet for Er:Si Hall bar fabrication as undertaken at MU. BHF stands for buffered HF. 100
4.10 Process sheet for Er:Si Hall bar fabrication as undertaken at UNSW. 102
4.11 Parameters for SiO_2 deposition with the PECVD method. . . 112
4.12 Details of the cleaning process of silicon wafers. 114

5.1 Ratio of sp^2 and sp^3 bonds of carbon found from XPS. Errors estimated from the accuracy of the peak fitting. 146
5.2 Fitting parameter alpha for the 10% N-UNCD sample. 161

6.1 Anneal temperatures and times of the DLTS samples. 168

6.2 Correlator initial delays and time constants for the shorter time settings. 169
6.3 Observed DLTS peaks and their defect type as well as energy - calculated and literature values. 170
6.4 Hot temperature treatment of the samples characterized with photoluminescence. 176
6.5 Comparison of experimentally found photoluminescence peaks and peaks found in the literature [30]. 179
6.6 Er:Si batches and their additional implant ions (also see table 4.8 from chapter 4.2). 186

Chapter 1

Literature review

1.1 Diamond materials

1.1.1 Background

History Diamond is well known for its qualities such as its extreme hardness, high thermal conductivity, and broad optical transparency. It consists of tetrahedrally arranged carbon atoms, joined by sp^3 hybrid bonds. Diamond has a large band gap of about 5.5 eV, rendering the possibility of thermal electron excitation at room temperature negligible. This leads to diamond's electrical insulating properties; pure diamond is highly resistive.

Figure 1.1: Octahedral nanodiamond model [13].

Synthetically grown diamond was first created with the high pressure high temperature (HPHT) tech-

nique in Sweden in 1953 [31]. The HPHT approach requires extremely high pressures of about 60 kbar and temperatures of about 1400 °C [32], resulting in considerable cost and time invested during the production process. A different method to grow diamond synthetically was developed in the 1950s, via chemical vapour deposition (CVD) [33, 3]. This technique involves growing diamond on a substrate (either diamond, or often silicon containing small diamond seeds) from a carbon-rich gas mixture. The gas mixture is heated up with a hot filament or microwave beam until it forms a plasma. Without applying high pressures, the carbon atoms are deposited layer by layer on the substrate, forming diamond crystals [33].

In 1911 Bolton was the first to create polycrystalline diamond films via low-pressure CVD [34]. In the 1960s many advances were made in the CVD technology and technique [35]. This led to a more widespread production of CVD grown nano-diamond films in the 1980s using a mixture of me-thane and hydrogen gases [36, 37, 38, 39] (Fig. 1.1 shows a model of the structure of octahedral nano-diamond as present in nanodiamond thin films). These hydrogen-rich CVD grown thin films contained diamond grains ranging from 100 nm to 30 nm [3] and are called nano-crystalline diamond (NCD). Researchers tried to further reduce the crystal size by increasing the methane concentration in the hydrogen/methane gas mixture. The result is not only the decrease of the grain size, but also the creation of amorphous carbon, leading to diamond nano-crystals surrounded by amorphous carbon [40, 41]. Gruen's 1991 idea of substituting argon for the hydrogen gas in the mixture led to a breakthrough in the process of creating diamond thin-films [42], as it prevented the formation of amorphous carbon. In 1994 he grew the first diamond films via CVD using fullerene precursors in a microwave-activated argon-rich gas [43]. Even though hydrogen is necessary for the diamond thin-film growth, Gruen discovered that the hydrogen contained in the methane was all that was needed. If too much hydrogen is added, structural defects are introduced when hydrogen is incorporated into the crystal lattice. Thus,

Gruen was able to further decrease the diamond crystal size by growing the thin-films in an argon-rich atmosphere. The term ultra-nano-crystalline diamond (UNCD) films was introduced to differentiate the new material of 2-5 nm sized phase-pure diamond crystals created in an argon-rich, hydrogen-poor plasma enhanced CVD growth, from nano-crystalline diamond films of 30 - 300 nm sized crystals created by conventional CVD methods using methane and hydrogen gases. Both NCD and UNCD films generally have high Young's modulus, a high hardness, and a low surface roughness [3]. UNCD's extreme properties as well as biocompatibility [1] and its now relatively easy fabrication have made it interesting for researchers.

Addition of dopants

Diamond is a high band-gap (5.5 eV) semiconductor (see Fig. 1.2) and is highly resistive when undoped in its single- or poly-crystalline form. By adding elements other than methane and hydrogen/argon to the feedstock gas during CVD growth, one can dope the UNCD films and introduce charge carriers. Doping via ion implantation on the other hand is always paired with the problem of induced damage to the crystal lattice, leading to the need to repair the defects via subsequent annealing. Doped UNCD is of interest for a variety of biological and electrochemical applications, including sensing [13]. The former makes research on diamond doped with nitrogen particularly exciting, as both nitrogen and

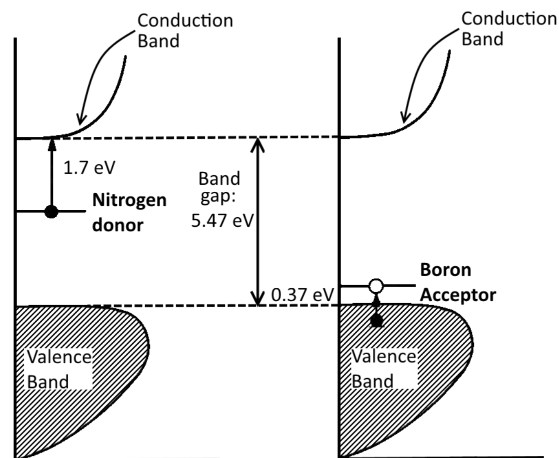

Figure 1.2: Sketch of an energy band diagram of diamond with nitrogen/boron indicated donor/acceptor levels.

carbon are biocompatible and yield broad application opportunities in the medical field [44, 6].

P-type doping has easily been realized with boron by adding it in the gas phase during CVD growth [45] (see Fig. 1.3 for an SEM image of boron-doped diamond). With its relatively small radius, boron is easily incorporated into the dense diamond lattice [46]. Finding an appropriate dopant for n-type conduction has proven to be more difficult [47]. Possible candidates for n-type dopants are nitrogen, phosphorus, sulphur and lithium, amongst others.

Phosphorus has shown n-type conduction in Hall effect measurements in Koizumi's work [48], with an activation energy of 0.6 eV and mobilities of tens of cm^2/Vs. Due to the low reported mobility and too high activation energy of phosphorus, other dopants were tested for n-type conductivity in diamond. Even though sulfur showed positive results [49], the samples later turned out to be contaminated with boron, resulting in the previous results being questionable [50]. Lithium has turned out to be rather difficult to incorporate into diamond. Some research groups reported conductivity in diamond in presence of Li [51, 52], whereas other research groups were not able to repeat these results [47]. Nitrogen on the other hand manifests itself as an interstitial dopant, giving rise to a donor level of 1.7 eV below the conduction band, and is therefore not expected to contribute to electrical conductivity at room temperature. The fact that nitrogen sits energetically very deep inside the diamond makes it surprising that nitrogen doped CVD grown diamond does indeed show room temperature conductivity [53]. Simulations by Zapol et al. [54] on CVD grown UNCD with nitrogen addition have shown that the incorporation of nitrogen into the grain boundaries is favoured as compared to the incorporation into the bulk diamond, with the nitrogen substitution energy for the grain boundaries between 2.6 eV to 5.6 eV lower than that for bulk diamond. It is concluded that nitrogen added during CVD growth will most likely not be incorporated into the diamond grains, but rather in the grain boundaries (in contrast to Boron doping).

Recent interest Since the discovery of superconductivity in boron-doped nanocrystalline diamond in 2004 [4, 14] (see SEM image of superconducting material in Fig. 1.3), not only boron-doped, but also nitrogen-doped diamond has become a more popular material to study. Superconductivity in boron-doped diamond has proven to be a robust phenomenon, making it a promising candidate for applications in the field of superconducting nano-electro-mechanical systems [5]. With nanostructured devices of about 100 nm width fabricated via electron beam lithography on CVD grown boron-doped samples, critical temperatures of 2.5 K are observed with critical magnetic fields of 500 mT [5] -comparable to the critical temperatures of 'bulk' films of 3.5 K.

Optical characterization of N-UNCD The morphology of N-UNCD films is best visualized with SEM and TEM imaging. When above about 10% nitrogen concentration in the gas mixture, a further increase of the nitrogen content during CVD growth leads to an increase of the grain size of the diamond crystals [55] and consequently the surface roughness [56]. 800 nm thick films grown using gas feed stock containing 79% Ar, 1% CH_4 and 20% N_2, with a grain size of approximately 16 nm according to TEM measurements, show sharp spike-like crystal shapes of about 200 nm length in SEM images [57].

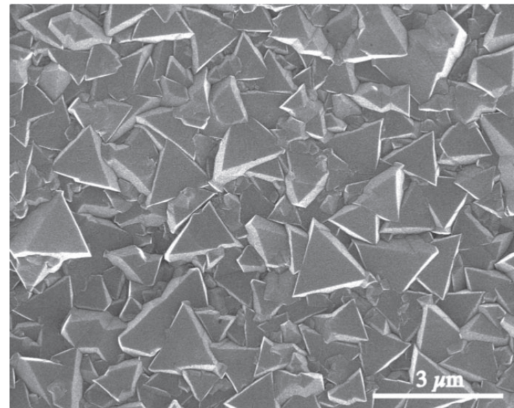

Figure 1.3: SEM image of a boron-doped polycrystalline diamond film deposited by microwave plasma-assisted CVD method [14].

The typical Raman spectrum of N-UNCD excited at a wavelength of 514.5 nm has two prominent, broad features [57]. One of these is the peak at approximately 1555 cm^{-1} which is commonly referred to as the G-mode of disordered graphite, and the other is at approximately 1350 cm^{-1}, commonly referred to as the D-mode [58]. The G-mode originates from the relative motion of all sp^2 carbon atoms and the D-mode is in fact the breathing mode of sp^2 bonds in the rings [59]. The other obvious peak at 1140 cm $^{-1}$, as well as the small peak at 1480 cm^{-1}, derive from the vibrational modes of trans-polyacetylene (PA) [58]. The PA peak can be reduced by annealing [60] or through hydrogen plasma etching of the samples [61].

With increasing nitrogen content in the studied samples, an increase of the ratio of the intensities I(D)/I(G), as well as a shift towards higher wavenumbers of the G-mode was observed [58]. According to Cancado et al. [62] the ratio of I(D)/I(G) can be taken as an indicator of the level of disorder in the grain boundaries - a higher value relating to a higher level of disorder - as the ratio is related to the size of the crystalline graphite grains. Recently it was shown that even though the value of I(D)/I(G) initially rises with increasing nitrogen doping, it then rapidly decreases in a high nitrogen percentage regime [63].

XPS analysis by Garrett et al. shows a detectable nitrogen peak of just 1% of the elemental composition, for a minimum of 20% nitrogen addition only [56]. Separating the main carbon peak into the graphitic sp^2 carbon at 284.5 eV and the diamond sp^3 carbon at 285 eV reveals an almost even distribution of sp^2 to sp^3 bonds with no real observable trend with increasing nitrogen concentration [56].

Electrical characterization of N-UNCD In 2001, nitrogen incorporated into UNCD thin films by microwave plasma-enhanced CVD was reported to show highly-conducting characteristics [55]. A thin film with nitrogen concentration of up to 20% in the gas feed stock was examined down to 4.2 K

with Hall measurements. Increasing the nitrogen content led to an increase in the electrical conductivity by five orders of magnitude to 143 Ω^{-1}cm^{-1} at room temperature for 20% N_2 in the gas feed stock. Temperature dependent Arrhenius plots show a finite conduction at low temperatures, as well as a non-linear behaviour, indicating the presence of multiple, thermally activated conduction mechanisms with different activation energies. Bhattacharyya et al. believe that conduction occurs via the grain boundaries, not via the grains themselves [55]. On the other hand, Hall effect measurements on 2 - 3 μm thick N-UNCD films (20 % N_2) by Williams et al. in 2004 [64] revealed a largely temperature insensitive charge carrier concentration, varying from 1.8 x 10^{17} cm^{-2} at 300 K to 1.3 x 10^{17} cm^{-2} at 15 K with a mobility of 1.045 cm^{2}V^{-1}s^{-1} at 50 K, indicating an extremely low thermal activation energy.

Even though increasing room temperature conductivity has been observed with increasing nitrogen content, this trend levels out at a percentage of 10% N_2 in the gas phase, not showing a further increase of conductivity with higher nitrogen content [65]. Bhattacharyya's work on 0.1 - 20 % doped N-UNCD studying the type of conductivity [66] concludes that for varying nitrogen concentrations as well as temperature, various conduction mechanisms apply. At low temperatures (from roughly 85 to 10 K) Mott's variable range hopping (VRH) [67] is thought to be the dominating factor contributing to conductivity in all N-UNCD films. In 2006, Nesladek et al. [57] examined nitrogen doped (20% in the gas mixture) UNCD films prepared by plasma-enhanced chemical-vapour deposition (PE-CVD) at even lower temperatures, down to 1.28 K. The measurements consistently show a higher resistance with lower temperature. The work of Nesladek et al. assumes that the nitrogen is mainly incorporated in the grain boundaries, where the origin of the conduction mechanism is supposedly confined to. A negative magneto resistance (NMR) was observed and points towards weak localization (WL), a characteristic feature for conduction in disordered metals. A model was derived for the critical magnetic field B_k which can be determined

geometrically from the plots of resistance ρ versus magnetic field B. At this point the electric and magnetic contributions to the phase-breaking process are equal, which can only be the case if the dimensions of the weakly localized orbit exceeds the magnetic length $\lambda = (\hbar/eB)^{1/2}$ [2]:

$$\sqrt{B_k} = \gamma(\hbar/e)^{1/2}(G - G_0), \tag{1.1}$$

with G the conductivity, and G_0 and γ empirical constants [2]. However, the same work by Nesladek et al. also examined 150 nm thick boron doped NCD films where the dopant is preferentially substitutionally incorporated into the diamond grains. Here, a positive magnetoresistance is observed, pointing towards a localisation of the wave functions on boron atoms. This indicates a completely different conduction mechanism for boron doped NCD than for nitrogen doped UNCD. Later published work by Nesladek et al. [7], in which the same materials are studied in more depth, suggests possible superconductivity at low temperatures on the basis of the coherence length being comparable to the weak localization orbits and also approximately equalling the grain size. The data reveals a sudden drop in resistivity in a 20% N-UNCD (in the gas feed stock) sample at about 0.33 K, suggesting a local superconducting transition. However the resistivity does not drop to zero, so it is assumed that the transition to superconductivity is not homogeneous in the whole sample volume.

Feliciangeli et al. [68] proposed that since the nitrogen is mainly incorporated in the grain boundaries (as shown by [54]), the effect of nitrogen incorporation in UNCD films is more related to structural changes rather than an actual doping. In their work nitrogen doped UNCD was studied using impedance spectroscopy between 115 K and 300 K. The examined diamond nano-crystals have a diameter of 3-5 nm in films with a thickness of 1.5 μm. The results show a higher resistance with lower temperatures, indicative of a non-ohmic behaviour at even at lower temperatures. The quality factor $Q = \omega C/G$ dependency of the frequency shows that the system behaves

like a resistor in the low frequency regime. Around 100 kHz a capacitive behaviour occurs, and at higher frequencies C increases because dispersive transport takes place, where charge carriers stay within their potential wells. At around 1 MHz G shows negative values because charge carriers remain localized inside the potential wells into the degenerate grain boundaries. The developed model is that of completely depleted p-type UNCD grains embedded into nitrogen n-type grain boundaries, with the charge carriers remaining localized inside the potential wells.

While it is now known that added nitrogen during CVD growth of UNCD will be incorporated into the grain boundaries, the conduction mechanism at low temperatures is not completely understood. The formation of UNCD with nitrogen addition [69] as well as its morphology [70] has been extensively studied in the past. The results of a local superconducting transition in N-UNCD thin films do not seem to be reproducible [7], but a negative magneto resistance indicating WL has been measured repeatedly [2][57][63]. The temperature range during which WL is dominant is unclear so far.

In order to elucidate the conduction mechanisms in N doped UNCD we measured N-UNCD samples of varying nitrogen content at temperatures as low as 18 mK and at high magnetic fields. Once the conduction mechanism is understood, the knowledge of the electrical structure of the material might help to understand the superconducting state.

1.1.2 Conduction mechanism in N-UNCD

Weak localization We wished to find out more about the origin of conductivity in N-UNCD at very low temperatures. So far most research groups report having observed a negative magneto-resistance and weak localization at low temperatures. It is useful to consider here the theory of WL, Bergmann offers a comprehensive review of the physical explanation of weak localization in his book "Weak localization in thin films" [15].

The first idea of weak localization (WL) was proposed by Abrahams et al. [71] as an asymptotic case of a more general theory for two-dimensional conductors. It was found that WL is caused by the quantum-interference of the conduction electrons on the defects of the system [15]. Even though Abrahams et al. developed the theory for two-dimensional systems, WL also occurs in three-dimensional conductors. The effect corresponds to a time-of-flight experiment of the conduction electrons. As such, magnetic fields perpendicular to the sample are used to examine WL, revealing characteristic times of the system [15].

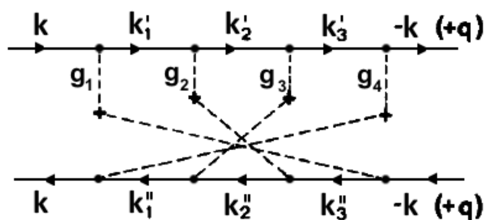

Figure 1.4: Fan diagram according to Langer and Neal of an electron scattered via two different sequences from the state k to the final state -k [15].

Negative magneto-resistance Anomalies within the resistance of thin, disordered metal films were observed in the past, but not theoretically understood until much later [15]. These anomalies consisted of the resistance changing with a magnetic field perpendicular to the sample and the magneto-resistance being strongly temperature dependent. Neither should be the case according to the classical theory. Thus the observed anomaly of i.e. Cu thin films at low temperatures in form of a negative magneto-resistance became an indicator for the new effect: weak localization.

Origin The theoretical origin of WL lies within the Langer-Neal graph (see Fig. 1.4) in the Kubo formalism [72]. The Kubo formalism is based on a perturbation to the Hamiltonian in order to calculate electronic quantum transport [73, 74]. WL corresponds to an interference experiment of conduction electrons that are split into partial waves which then self-interfere during

back-scattering [75], pictured in a "fan diagram" (also called "Langer-Neal diagram", after Langer and Neal who first studied this in 1966 [76]). Even though the fan diagram had already been studied by Langer and Neal [76], it took a more detailed analysis by Abrahams et al. [71] to reveal its meaning for weak localization and weak anti-localization. The interpretation of the fan diagram shown in Fig. 1.4 is explained in the following paragraphs.

Physical interpretation For free electrons the Drude formula for conductivity applies [77]:

$$\sigma = \frac{ne^2}{m}\tau_0, \tag{1.2}$$

with the conductivity σ, for n free electrons, the electron charge e, the electron mass m, and the elastic lifetime τ_0 between collisions. This equation does not take into account the inelastic lifetime τ_i, which can be higher than τ_0 by several orders of magnitude at temperatures below 4 K [15], as the Boltzmann theory does not account for particles scattered on impurities. Therefore it shows a temperature independent conductivity.

Now consider an electron with a diffusive path as shown in Fig. 1.5 a) (which is consistent with the physical interpretation of the afore-mentioned fan diagram) that returns to the origin 0. According to the classical theory the probability of the electron travelling clockwise is equal to the probability of the electron travelling anticlockwise along the scatter path, and these two probabilities add up to the total probability. Quantum mechanics on the other hand considers the wavelike character of the electron. In reality there are two partial waves, each going in opposite directions around the path. Upon their return to the origin their amplitudes (but not their intensities) add up to the total probability [75]. With the mechanical amplitudes $|A|^+$ and $|A|^-$ of the path the electron can take clockwise and anticlockwise, the probability of the electron returning to its starting point is given by

$$|A^+ + A^-| = |A^+|^2 + |A^-|^2 + A^+A^{-*} + A^{+*}A^-. \tag{1.3}$$

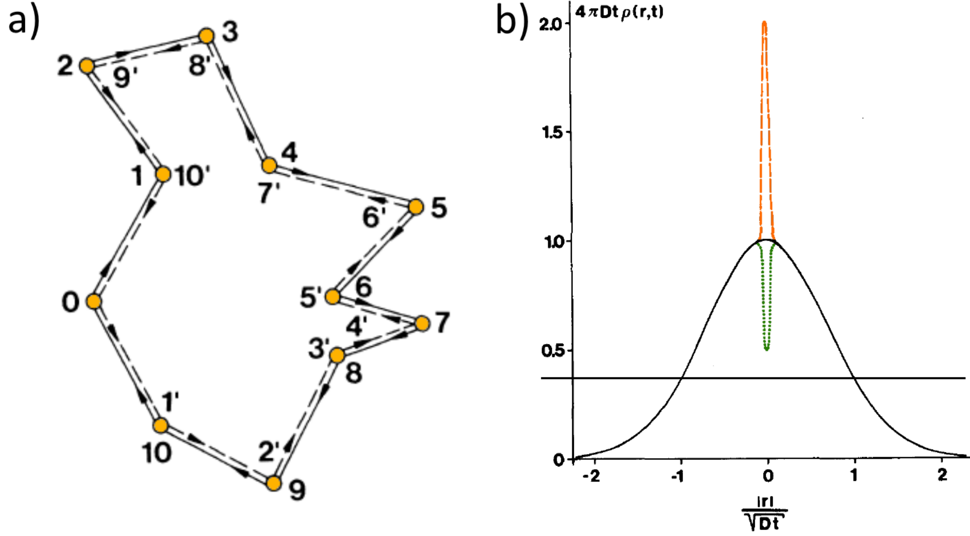

Figure 1.5: a) Sketch of possible path a diffusive electron may take returning to its origin [15]. b) Probability diffusion of a diffusing electron. Quantum diffusion shown in orange, classical case in black, weak anti-localisation in green [75].

As long as time reversal symmetry applies, the two partial waves are in phase and have the same amplitude when they both return to the origin, so $A^+ = A^-$. This simplifies equation 1.3 to $|A^+ + A^-| = 4|A|^2$. If we compare this result with the classical probability of the electron returning to its origin, we notice that the two last terms in equation 1.3 are not taken into account. Consequently there is a difference of a factor of two between the classical and quantum approach. This can be seen in Fig. 1.5 b), where the probability distribution of a diffusing electron is qualitatively graphed. The probability of quantum diffusion is shown in orange, showing a probability twice as high as the solid black line (classical calculation) of the electron returning back to its origin at 0. This tendency of the electron to remain at or return to the origin has shaped the name of the effect: weak localization. The green dotted line (dip) in Fig. 1.5 b) is the quantum diffusion in the presence of large spin-orbit coupling, showing a by a factor of 2 reduced probability to

return to the origin, also called weak anti-localization [75].

Once time is introduced into our system, $A^+ = A^-$ does not apply any more. Time reversal symmetry can be broken up by applying an external magnetic field. The introduced magnetic-field induced phase shift between the two complementary waves results in a partial destruction of the quantum interference and thus in a lower probability of the electron returning to its origin. Hence the conductivity is increased and a negative magneto-resistance is observed.

Calculations The temperature dependence of the conductivity under zero magnetic field can be calculated by using the Drude-conductivity σ_0 and the temperature dependent terms for WL σ_{WL} and Coulomb (electron-electron) interactions σ_{e-e} [78]. These terms are additive in first order:

$$\sigma(0,T) = \sigma_0 + \sigma(0,T)_{WL} + \sigma(0,T)_{e-e}, \tag{1.4}$$

with the WL term

$$\sigma_{WL} = \frac{e^2}{2\hbar\pi^2} T^{0.35} \tag{1.5}$$

and the Coulomb term

$$\sigma_{e-e} = \frac{e^2}{4\pi^2\hbar} \frac{1.3}{\sqrt{2}} \left(\frac{4}{3} - \frac{3}{2}\tilde{F}_\sigma\right) \frac{\sqrt{T}}{D}, \tag{1.6}$$

where $\tilde{F}_\sigma$ is a constant depending on the dimensions of the examined sample and D is the diffusion coefficient.

Kawabata derived a formula to calculate the conductivity σ in presence of a magnetic field B in 1980 [8], given in the following equation:

$$\Delta\sigma = \frac{e^2}{2\pi^2\hbar} \sqrt{\frac{eB}{c\hbar}} F(\delta), \tag{1.7}$$

with $\delta = \frac{l^2}{4\tau_\epsilon D}$ including the energy relaxation time of electrons τ_ϵ, $l = \frac{c\hbar}{eB}$ and the Kawabata function [8]

$$F(\delta) = \sum_{N=0}^{\infty} 2(\sqrt{N+1+\delta} - \sqrt{N+\delta}) - \frac{1}{\sqrt{N+\frac{1}{2}+\delta}}. \tag{1.8}$$

By using this formula, we can calculate the change of conductivity with an external magnetic field perpendicular to the thin film and thus derive the scattering parameters and time scales of the sample.

Possible superconducting transition According to Mares et al. [79] a superconducting transition would be possible through a pairing of similar WL orbits as this could lead to a coherent collective ground state percolating through the whole sample. Scattering of a carrier to this state would require the scattering of another carrier out of this state [79]. Since the collective state of WL orbits is dissipationless, the scattering process would be equivalent to the electric transport through a superconductor [79].

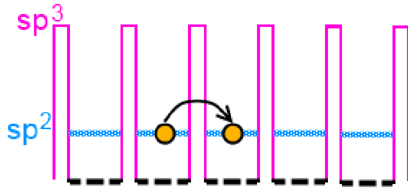

Figure 1.6: Charge carriers tunneling through localized barriers.

Thermal activated tunneling Conduction in the N-UNCD films is achieved via thermal activation of the charge carriers above a certain temperature. In this thermally activated regime the charge carriers located in the diffusive sp^2 carbon bonds are able to tunnel through the localized sp^3 barriers (see image 1.6). This is not Mott's variable range hopping (VRH) which takes place in disordered systems, but with localized charge carrier states [67]. VRH is an incoherent, phonon-assisted process with the hopping probability depending on the barrier height. Its temperature dependent conductivity is as follows in three dimensions [80]:

$$\sigma = \sigma_0 e^{-\frac{T_0}{T}^{1/4}}. \tag{1.9}$$

The observed thermal activated tunnelling on the other hand is a coherent process which does not include phonons. The tunnelling probability depends

on the area underneath the barrier. The temperature dependency of conduction is here given by

$$\sigma = \sigma_o e^{-2\sqrt{\frac{c}{T}}}. \tag{1.10}$$

1.1.3 Motivation for studying N-UNCD

With the discovery in 2004 of superconductivity in boron-doped nano-crystalline diamond [4], the material has sparked new interest. Boron-doped diamond shows an insulator-to-metal transition from a carrier density above $3\text{x}10^{20}$ cm^{-2} [16]. The higher the boron concentration, the more dominant the metallic component in the sample becomes and the higher the superconducting transition temperature rises (see Fig. 1.7).

The fundamental interest in understanding the phenomenon of superconductivity in diamond lay within the assumption that similar conclusions could be drawn for the major semiconductors silicon and germanium, due to them having the same diamond lattice structure [4]. Not surprisingly, superconductivity was found shortly after, in 2006, in boron doped silicon [81].

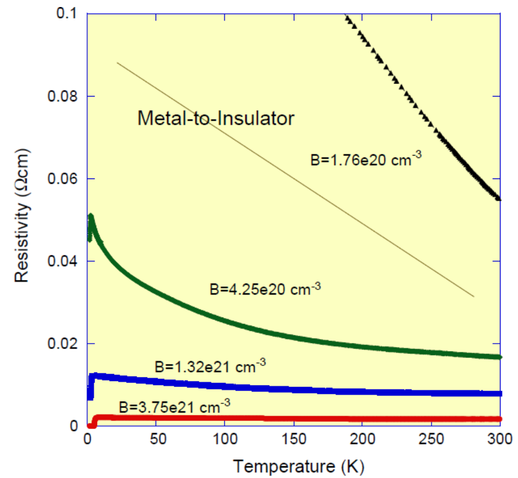

Figure 1.7: Resistivity versus temperature for varying boron concentration [16].

In boron doped diamond, a T_C of about 55 K was predicted [82] for boron concentrations between 20% and 30%, but such high concentrations are hard to achieve. Boron is an acceptor in diamond, as opposed to nitrogen which acts like a donor. With nitrogen and boron straddling carbon in the periodic table, analogous behaviour of nitrogen and boron in UNCD may be assumed. This led

to the decision to study nitrogen doped diamond. With N-UNCD recently being utilized in bionic applications [6], it is important to learn about the conduction mechanism of the material. We aimed to create highly nitrogen doped UNCD and then examine these samples at low temperatures, hoping to get past the metal-to-insulator line of Fig. 1.7. With the installation of a new dry dilution refrigerator we were able to achieve temperatures as low as 15 mK, while applying a magnetic field of up to 7 T, an environment at which nitrogen doped diamond has so far not been studied and which we hoped would reveal the origin of the conduction mechanism of the material at those temperatures. While examining the samples, we discovered that they were in fact not nitrogen doped, their changed characteristics were rather due to a nitrogen-enhanced CVD growth, as will be discussed in the following chapters.

1.2 Erbium in Silicon

Erbium is a rare earth element with the preferred bonding state of Er^{3+}. It is well known for its optical fluorescent properties, with its emission wavelength peak at 1.54 μm [10].

Er^{3+} has an incomplete 4f electronic shell, surrounded by the full 5s and 5p shells [83, 10]. This leads to it having sharp optical intra-4f transitions [17]. A schematic of the energy level diagram for Er^{3+} is shown in Fig. 1.8. This diagram includes the Stark splitting due to an electric field. With the transition from the first excited state to the ground state having an energy of 0.8 eV, or a wavelength of 1.54 μm, erbium is an ideal candidate for use as an optical amplifier in optical fibres [9]. After Er was successfully used for optical amplification in fibres, it was used as a planar optical amplifier [17], and has been used in silicon based optically pumped waveguides [84] as well as splitters [17]. With the detection of single Er^{3+} ions [12] the possibility arises for using Er in optical quantum computing. Optical emission

from excitons bound to phosphorus donors in silicon can be used to measure the state of both the electron spin and the nuclear spin [85]; however, the measurement efficiency is low, prohibiting even single-spin measurements let alone qubit state transfer. Other defects in silicon, such as erbium, result in luminescence from an inner-shell transition and may be better suited to such applications. If such a state transfer is successful, single optical photons could be routed on-chip using silica-on-silicon waveguides, which have been used to perform quantum logic operations, albeit non-deterministically [86]. Development of such a protocol will require a detailed exploration of erbium-donor interactions and Er/P co-doped EDMR devices provide one important avenue for studying this.

Er doping During this work, silicon was used as a substrate in which we introduced erbium dopants (Si:Er). Typically erbium doping is achieved via implantation. Since erbium has a high stopping cross section, its penetration depth in the target material is relatively small. Consequently high implantation energies of several MeV are required to reach ion ranges in the micro metre range (typical of optical waveguide materials) [17]. Parameters such as range and straggle of Er implantation can be simulated with the Monte Carlo program SRIM before the implantation process is commenced [87], as will be described in further detail in chapter 4.2.3. Different techniques for introducing erbium into silicon

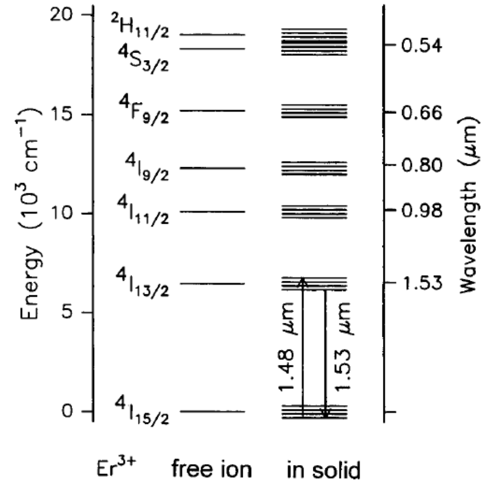

Figure 1.8: Schematic diagram of the energy levels of a Er^{3+} ion [17].

include molecular beam epitaxy (MBE), sputtering, thermal diffusion, and chemical vapour deposition [84]. The advantage of ion implantation is the high amount of control possible over the density, depth and location of the implanted ions. There is also the possibility of implanting pre-fabricated devices (as used in an example in [88]) which allows various configurations of devices to be explored relatively quickly. On the other hand, this technique creates a significant amount of damage to the silicon lattice. To avoid implantation damage, MBE is a useful method to grow erbium doped silicon thin films. It produces films of very high quality [84], making it possible to produce optically active erbium ions on a single well-defined site [17], which is needed for the fabrication of qubits. Overall, it is advantageous to first fabricate samples using ion implantation for faster examination of varying devices, and to then move on to MBE fabrication.

Co-doping with oxygen Co-doping Si:Er substrates with oxygen is very common as it has many advantages [89]. These advantages include an increased luminescence intensity by adding oxygen to Si:Er [90, 10], as well as a reduction in temperature quenching of the luminescence [91]. The higher PL intensity is partially due to an increased density of O-coordinated erbium in the oxygen implanted substrate. Thus oxygen is a popular impurity to co-implant Si:Er substrates with, especially if the luminescence properties of Er^{3+} are intended to be used. Within the silicon crystal the erbium interacts with the oxygen. The common configuration of Er in Si forms clusters with four to six O atoms in the first neighbour shell [17]. As such, Er bonds with any O within a relatively large distance [17]. Consequently an increase of oxygen content in the wafer will increase the solubility of erbium in the silicon crystal [92, 18].

Electron paramagnetic resonance In order to characterize the erbium complexes in the doped material, electron paramagnetic resonance (EPR)

measurements are useful. Depending on the type and concentration of co-dopants as well as anneal treatments, different complexes with different g-values are found [18]. Carey et al. [18] reported sharp lines in the low temperature EPR spectra of erbium samples with an oxygen concentration of $10^{20}/\mathrm{cm}^3$ at low temperatures in nearly parallel magnetic fields (see Fig. 1.9), attributed to two Er^{3+} centres with monoclinic C_{1h} and trigonal symmetry.

Electrically detected magnetic resonance (EDMR) uses microwave frequencies to excite a sample while reading it out electrically, generally by monitoring a source-drain current through the channel of the sample. Using this technique, the electron spin resonance (ESR) can be detected. This method is capable of detecting a small number of donors [93], making even single spin detection possible in Si:P devices [93, 94]. The hyperfine-split electron spin resonances of phosphorus donors in silicon MOSFETs have been observed with this method [95]. This all makes EDMR a promising technique to observe the ESR on Er doped silicon MOSFETs.

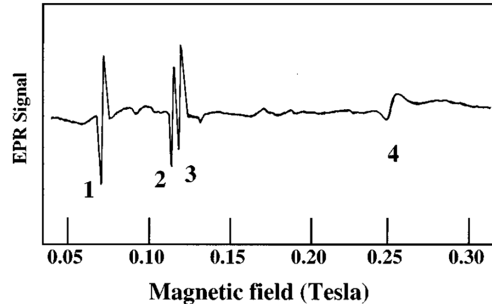

Figure 1.9: EPR spectrum of a sample with 10^{19} Er/cm^3 + 10×10^{20} O/cm^3 with the magnetic field nearly parallel to [001] at low temperatures [18].

Optical properties The photoluminescence (PL) of erbium is most commonly used to describe its optical properties. Figure 1.10 shows a PL spectrum of an Er implanted layer in a Si layer taken at liquid nitrogen temperature (77 K) with an argon laser excitation source [10]. This graph shows not only the PL spectrum of erbium at 1.54 μm, but also the possibility of increasing the PL intensity by co-implanting with oxygen. Fig. 1.10 (a)

is the PL spectrum of the sample without co-implants, showing a very low intensity. As (b) shows, the PL intensity was considerably increased after the sample was implanted with oxygen. It is possible to excite the PL of erbium at energies down to the wavelength of $\lambda = 1540$ nm, energies that are substantially lower than the silicon band gap width ($\lambda = 1060$ nm) [96]. A comparison of Er^{3+} incorporated into porous silicon via implantation and immersion has shown that the erbium sites responsible for the strong 1.5 μm luminescence are on the surface of the silicon nano-crystals [97], as opposed to inside the silicon crystals.

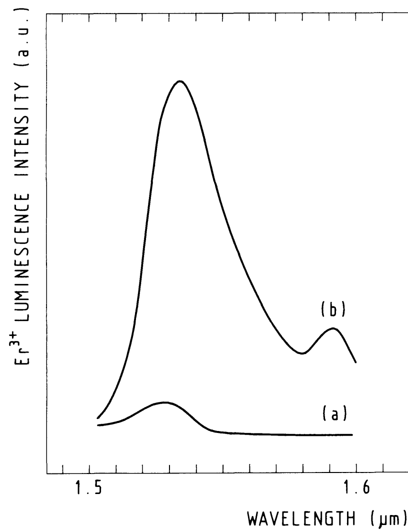

Figure 1.10: PL spectrum for an Er implanted layer in Si (a) without co-implantation, (b) after oxygen implantation [10].

Optical activation The introduction of impurities is essential in order to create optically active Er^{3+} centres in crystalline silicon [90, 10, 18, 98, 92]. These impurities can be for example oxygen, carbon or phosphorus, and are the main reason why room temperature luminescence has been observed from Er related centres [90]. The impurities can be intentionally introduced (by co-implanting the substrate) or they can already be inside the Si:Er material through contamination. Subsequent exposure of erbium doped silicon to high temperatures after the implantation process will also increase the PL intensity [17]. It has been shown that annealing at 1000 °C results in the optimum PL intensity [17].

Electroluminescence Electroluminescence (EL) measurements of erbium doped p-n silicon diodes can be performed by biasing the devices with a pulsed signal and varying the current through the diode. This can be done in either forward or reverse bias. The optical signal is then collected via lenses. It is even possible to observe the EL signal at 1.54 μm at room temperature in both forward and reverse bias operation [89]. In reverse bias direction, a 2-10 times higher EL yield is observed [89]. Under reverse bias the erbium is excited through impact excitation of hot carriers accelerated across the junction [89, 17], whereas in forward bias the EL signal is caused by an excitation of the Er^{3+} due to electron-hole recombination [89, 17].

Electrical characteristics Co-implanting Er with O or C can enhance the electrical activation of Er by at least two orders of magnitude [98]. Erbium is found to have donor character in n-type as well as p-type silicon, with higher activity present in n-type silicon [19]. The mobile carrier concentration depends not only on the erbium concentration, but also on the annealing treatment following the implantation [99].

Erbium related defects A study by Sobolev et al. [100] using transmission electron microscopy (TEM) on erbium implanted silicon to find structural defects has shown that annealing the samples in an oxidising ambient (i.e. chlorine) at 1100 °C leads to the formation of interstitial dislocation loops due to a supersaturation with self-interstitials. These defects become larger with a longer annealing time. On the other hand, if the samples are annealed in an inert ambient (i.e. argon), the formation of dislocation defects is prevented, resulting in the dominance of Er-related lines in the PL spectrum [100].

Deep level transient spectroscopy (DLTS) is most commonly used to study electrically active defects due to its high sensitivity (see more about the DLTS technique in chapter 2.1). There have been many studies on n-type silicon, and a short summary is given here. Not all electrically active

defects have yet been labelled confidently. The main defects are *VO*, where in the silicon lattice there is a vacancy situated next to a substitutional oxygen atom (see Fig. 1.11 a)), *VOH*, a vacancy-oxygen that has captured a hydrogen atom (Fig. 1.11 b)), *VP*, a vacancy neighboured by a phosphorus atom (Fig. 1.11 b)), and finally V_2^-, a single negatively charged divacancy, and V_2^{2-}, a double negatively charged divacancy (Fig. 1.11 d)).

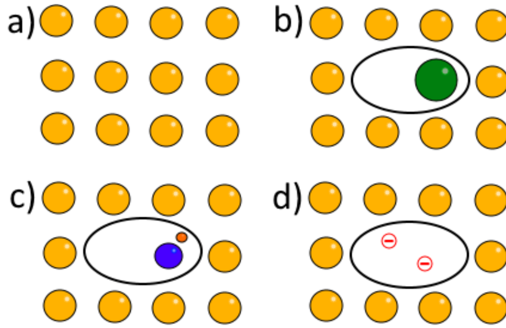

Figure 1.11: a) Sketch of a defect-free flattened silicon lattice. b) Vacancy with neighbouring substitutional atom (green). c) Vacancy-oxygen-hydrogen defect (H in orange, O in blue). d) Double negative charged divacancy.

Figure 1.12 shows erbium related defects that are characteristic for ion-implanted Er in n-type silicon at $\sim$ 0.5 MeV followed by an anneal at 900 °C for 30 minutes (data is taken from a sample with an erbium concentration of 4 x 10^{15} cm^{-3}) [19]. The numbers in the graph are the activation energies for carrier emissions from each discrete defect level to the conduction band observed between 50 and 275 K. The erbium related defects found are of donor character [19]. Benton et al. [19] believe that in PL spectra the optical excitation creates electron-pair holes and that the same electronic mechanism is also responsible for the production of light in EL. They believe that a deep centre is acting as a recombination site for energy transfer and that the DLTS observed donor states are necessary for the erbium to be optically active.

On the other hand, in 1995 Libertino et al. [101] found five erbium in silicon related defects in n-type silicon. They discovered the defect at

0.20 eV (at ca. 130 K) was characteristic in pure crystalline silicon and the defect at 0.15 eV (at ca. 90 K) was characteristic in oxygen rich crystalline silicon. An implantation angle dependent study by Lay et al. [102], on n-type silicon implanted with P, revealed three dominant peaks in the DLTS spectrum. The peaks are independent of the implantation angle and due to VO (at 0.17 eV), V_2^{2-} (at 0.22 eV) and the superposition of VP and V_2^- (at 0.42 eV). Studies on hydrogen interactions on silicon samples doped with silicon by Evans-Freeman et al. [103] reveal that the hydrogenation led to the passivation of many deep levels and thus removed their electrical activity. Also, VOH (vacancy-oxygen-hydrogen) and VO (vacancy-oxygen) levels were found not to be created with the hydrogenation of the samples.

Johnson et al. [104] studied FETs, n-type (P doped) Si substrates with a SiO_2 layer on top and P diffused leads for source and drain contacts as well as arsenic implanted channels. The samples were annealed to recover the damage (RTA at 1000 °C for 5 s in nitrogen ambient, or furnace anneal at 950 °C for 30 minutes in forming gas, or a combination of both anneal types). The DLTS signal showed a continuous background level with one large peak near RT due to minority carrier generation-recombination processes. No peaks were associated with bulk traps due to the implantation with either anneal technique.

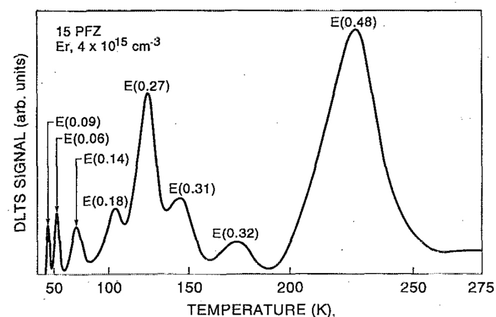

Figure 1.12: DLTS spectrum of Er implanted n-type Si [19].

P-type silicon substrates were examined by Binetti et al. [105]. They created epitaxial layers of indium melts containing silicon and erbium on a substrate of B doped silicon and examined these with DLTS. The study

Figure 1.13: Sketch of the band structure visualizing the principles of impact ionization [20]. A charge carrier gains energy in the electric field (a) and creates an electron-hole pair by colliding with a lattice atom (b). During shallow impact ionization an energetic electron (c) frees another electron from a donor atom upon collision (d).

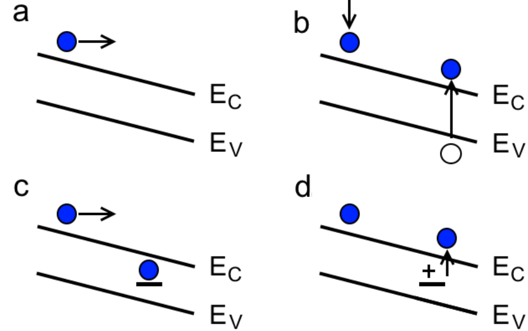

showed several Er related traps. These were the majority carrier trap at an energy of E_v + 0.45 eV, as well as minority carrier traps at E_c - 0.20 eV and E_c - 0.40 eV.

The project within this thesis studies n-type erbium doped silicon and the development of electrically active defects with annealing temperature. The observed defects confirm the defect types already seen in previously mentioned literature. These are VO, V_2^{2-}, VOH, VP, and V_2^-. The DLTS results are discussed in chapter 2.1.

1.2.1 Silicon at low temperatures

During the course of this project, most electric measurements on Si:Er were done at liquid helium (4.2 K) temperatures. At these temperatures electrical characteristics change due to suppression of the lattice vibrations, and other effects start to dominate. This section describes some of these effects, which have been observed and made use of during this work.

Impact ionization Impact ionization is a form of charge carrier multiplication induced by a high electrical field (see [20] for more information). Once the electric field is above a critical value, the charge carriers have enough energy (so-called *hot charge carriers*) to create an electron-hole pair (see Fig.

1.13 (a) and (b)), thus multiplying the available charge carriers. In small dimension devices, this charge multiplication can create a significant current at relatively low drain voltages. In an n-type silicon device the multiplied electrons are drawn toward the drain region (a fraction can be swept through the gate oxide), and the remaining holes become the substrate current. We differentiated between band-to-band ionization and shallow-level impact ionization [20]. Band-to-band ionization occurs when the charge carrier has enough energy to transfer some of its energy to ionize a silicon atom and thus create a free electron in the conduction band and leave a free hole in the valence band. Shallow-level ionization (more typical for cryogenic temperatures, below the freeze-out temperature of the dopant atoms) occurs when an inelastic collision of a high energetic charge carrier with an occupied dopant atom takes place. The excess energy is used to liberate the electron into the conduction band, leaving a fixed charge (the ionized dopant) behind (see Fig. 1.13 (c) and (d)).

Optical addressing of an individual erbium ion in silicon [12] In 1997 it was suggested that the combination of the electrical and optical functions of Er^{3+} can be realized on a single silicon chip, provided that efficient light emission from the PL centre can be achieved [17]. A major breakthrough for quantum computing was made in May 2013 when Yin et al. were able to optically address a single erbium ion in silicon [12], proving the possibility of electrically reading out the spin of a single optically excited erbium ion. The nuclear spin states (hyperfine coupled) of this PL centre can hopefully be used as long-lived quantum states for a quantum bit (qubit) used in the proposed quantum computer. The $^4I_{15/2}$ - $^4I_{13/2}$ transition, referring to the transition between states within the inner 4f electron shell of Er^{3+}, has a narrow spectral line width and a specific resonant photon energy for each individual erbium ion [12]. This transition was studied by Yin et al. on Er^{3+} implanted single electron transistors (SET) of polycrystalline silicon on

silicon dioxide by exciting the $^4I_{15/2}$ - $^4I_{13/2}$ transition optically and detecting the resulting tunnelling current through the SET electrically.

1.2.2 Motivation for this study on Si:Er semiconductor devices

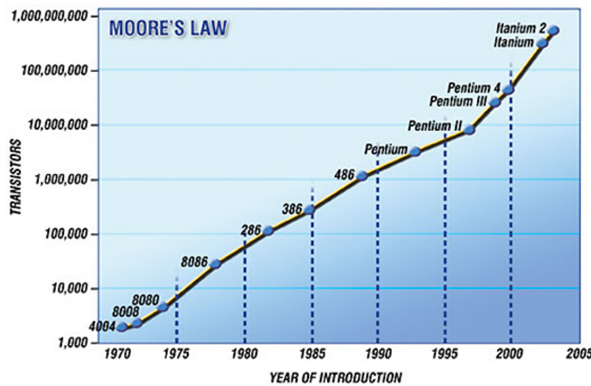

Figure 1.14: Moore's Law shown by the example of microprocessor transistor counts from 1970 to 2005 [21]

According to Moore's Law [106] the past trend shows that the overall processing power for computers doubles every two years, specifically the number of transistors on an affordable CPU. IBM expects to start commercially manufacturing at the 7 nm node in 2017-2018 [107]. With a typical atom size of 0.5 nm, this gives us a channel width of only 14 atoms. Consequently, we're starting to run out of scope to make ever smaller functional transistor structures. Hence something disruptive is likely to happen for Moore's law in the near future. Figure 1.14 shows the past development of processors since 1970, visualizing Moore's law. A roadmap for the semiconductor industry [108] implies the number of electrons needed to switch a transistor should fall to one single electron before 2020 [109]. The question arises as to how one can realize devices that would keep up with this fast development.

The answer might lie within quantum computers. Unlike classical computers they don't encode data with binary digits (bits), but rather use quantum bits (qubits) for data processing. Qubits are a superposition of both states of a two state system, unlike the bit which has to be either one or the

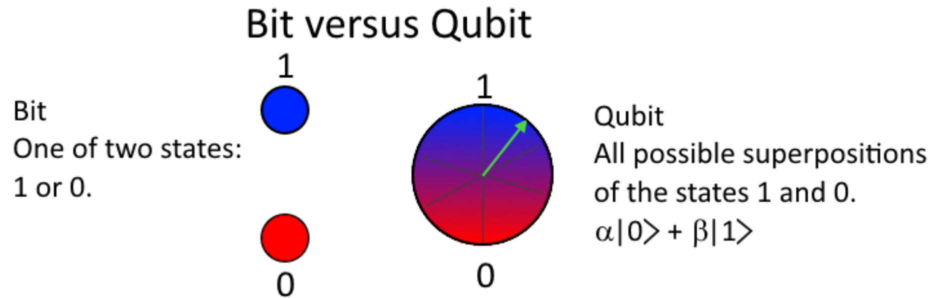

Figure 1.15: Left: A bit is always either 1 or 0. Right: A qubit can be any possible superposition of 1 and 0.

other state (see illustration in Fig. 1.15). By making use of quantum mechanical properties such as entanglement and superposition, quantum computers will be able to achieve a faster process speed than classical computers for solving complex problems [110]. This should enable quantum computers to have an advantage over classical computers regarding processing speed when doing calculations such as factoring [111], as well as in their ability to simulate quantum systems [112].

However, being still in its early stages, quantum computing faces many difficulties. One of these is decoherence of the qubits. Decoherence has to be slow enough so that quantum states can be manipulated and read out. Unfortunately fast processing needs strong interactions, which will lead to decoherence [113]. Another big issue is scalability. A large enough number of qubits need to be entangled to make a powerful enough quantum computer. In 2011 Austrian scientists broke the worlds record by achieving controlled entanglement of 14 qubits [114]. Early in 2012, D-Wave claimed to have built a 512-qubit processor based on superconducting logic which needs to be run at cryogenic temperatures [115].

Electron spins and their detection can also play an important role in the exchange of quantum information. Important milestones have been reached, such as using nitrogen-vacancy (NV^-) centres in diamond to transfer quantum information through a spin system [116, 117, 118]. Recently

Erbium has become very interesting for quantum information [12]. It has been considered important for applications in opto-electronics due to Er^{3+} showing luminescence at 1.54 μm, a wavelength that falls in the minimum of the absorption of light in silica based optical fibres [84]. This transition can be optically and electrically excited [18]. With Yin et al. having been able to electrically read out the spin of a single optically excited erbium ion [12], the combination of electrical detection and optical addressing became a real possibility. Until then the detection of electron spins in centres in crystalline solids had only been possible for phosphorus in silicon (electrical readout) [94] and the nitrogen-vacancy centre in diamond (optical readout) [119].

In this study, we hope to build on the foundation of the work of Yin et al. by deterministically studying erbium doped silicon semiconductors at low temperatures and high magnetic fields. If we are able to observe how the erbium reacts to electrical as well as optical stimulation and its electronic energy levels, Si:Er will become a more useful a tool for future projects.

Chapter 2

Experimental Techniques

Several different techniques were used for the fabrication and characterization of the samples, many of which are standard nowadays and are therefore not explained in detail here. These include fabrication techniques such as optical lithography, as well as characterization techniques such as photo luminescence and Raman spectroscopy. Instead, the following paragraphs concentrate on describing less well known characterization techniques, such as deep-level-transient-spectroscopy and Rutherford backscattering, as well as the methods used for electrical characterization of the examined samples.

2.1 Deep-Level Transient Spectroscopy

Deep-level transient spectroscopy (DLTS) is used for the identification and quantification of the energy levels associated with defects in semiconductors. It is a very sensitive technique, capable of measuring trap concentrations as low as 10^{-5} times the doping concentration of the material [22]. In addition to the concentration, the DLTS technique can also be used to determine the energy levels in the band gap that are associated with these impurities as well as gaining a measure of the carrier capture cross section [22]. In 1974 D. V. Lang developed this method which uses the capacitance across a depletion

region (of a Schottky barrier or p-n junction) to observe changes in the charge state of the impurity centres [120]. A pulsed bias is applied to the sample to modulate the depletion width, which causes the charge traps to fill and drain. When applying the bias V_{pulse} to the diode, the traps begin to fill (carrier trapping). Applying a lower offset bias V_{offset}, causes the trapped charge carriers in the increased depletion region ω to be released (carrier emission), resulting in a capacitance transient. The measurement is performed over a temperature range to modulate the Fermi level and address different defect levels within the band gap.

Schottky barrier diode In this work, DLTS is performed on Schottky barrier devices defined by a metal-semiconductor interface. The Schottky barrier can be seen as a parallel plate capacitor; the separation of the two plates d is analogue to the depletion width ω. The depletion width is the area close to the metal-semiconductor junction that is depleted of mobile carriers (see Fig. 2.1). The capacitance, C, is then given by

$$C = \epsilon \frac{A}{d} = \epsilon_r \epsilon_0 \frac{A}{\omega}, \tag{2.1}$$

with the permittivity $\epsilon = \epsilon_r \epsilon_0$ (ϵ_r is the dielectric constant of silicon, ϵ_0 is the permittivity of free space), and the area of the diode, A.

The bending of the band structure at the metal-semiconductor (Au-Si) interface is shown in Fig. 2.1, representing the region of the junction where the bands of the metal (yellow, left side) and semiconductor (grey, right side) join together. In thermal equilibrium (at zero bias voltage), there is a constant Fermi energy E_F throughout the junction (left part of diagram 2.1, for V_{pulse}=0 V), which causes the traps to fill. Thus even with no external voltage applied, the depletion region still exists. It can be increased/decreased by applying a voltage in reverse/forward bias. In the right half of Fig. 2.1 an offset voltage V_{offset} is applied so that the Schottky is in reverse bias. This raises the Fermi level of the metal with respect to the Fermi level of the

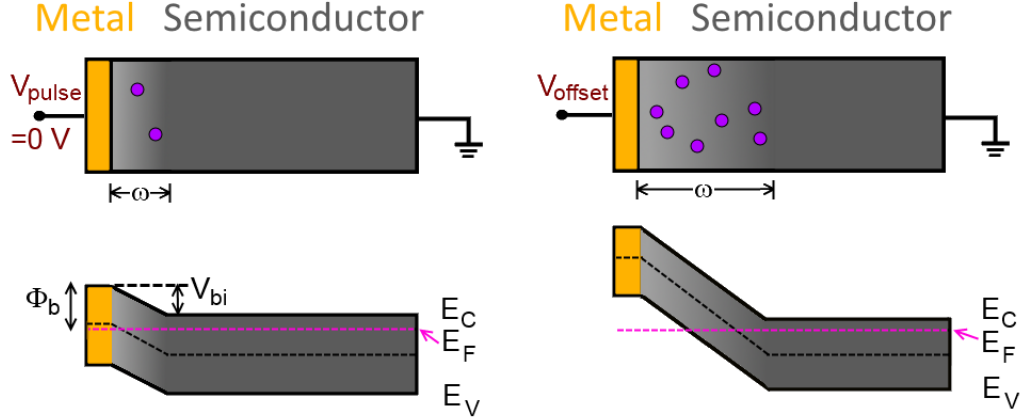

Figure 2.1: Sketch of the bending of the band structure at a semiconductor/metal interface with the applied voltage pulse (left) and the applied voltage offset (right) showing the traps (purple) in the depletion region ω.

semiconductor and causes the traps to empty. The barrier height Φ_b is given by the difference of the valence band and the Fermi energy of the metal. The built-in voltage $V_{\rm bi}$ is the difference between the conduction band of the metal and that of the semiconductor at equilibrium. The metal work function Φ_m and the semiconductor work function Φ_s are given by the difference of the vacuum level and the Fermi level of the metal or semiconductor. The depletion region ω is defined by $V_{\rm pulse}$ and $V_{\rm offset}$ which define the measurement window. Therefore it is important to select appropriate bias values in order to include all the deep level traps in the depth region of interest in the Schottky barrier during the measurement.

The depletion width in the depletion approximation neglects minority carriers and assumes total depletion of majority carriers throughout the depletion width as well as perfect charge neutrality beyond the depletion width. It is given by [121]

$$\omega = \sqrt{\frac{2\epsilon}{qn}(V_{\rm bi} - \frac{k_B T}{q} - V)}, \tag{2.2}$$

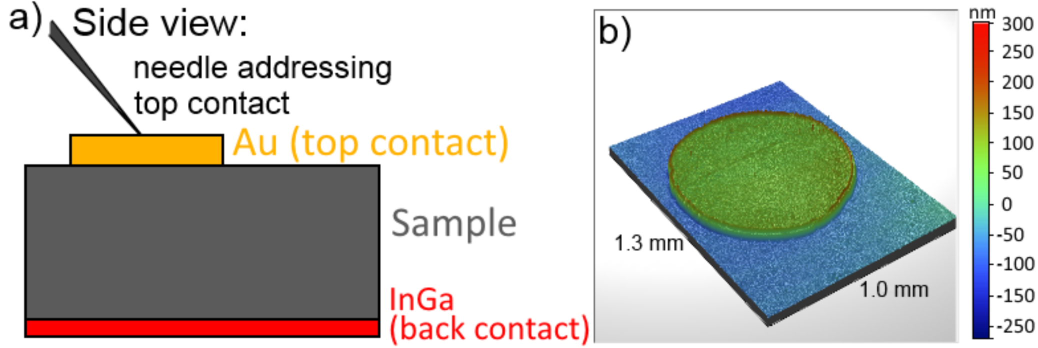

Figure 2.2: a) Sketch of the DLTS sample layout. The metal contact (yellow) is the top contact of the semiconductor (grey) and the indium-gallium eutectic (red) is the back contact. b) 3D image of the actual sample taken via optical interferometry profiler.

where q is the carrier charge, n is the active dopant concentration in the semiconductor, and V the applied bias voltage. The sample configuration that was used for our DLTS system is shown in Fig. 2.2 a). The sample itself is shown in grey and consists of an erbium implanted n-type silicon wafer (phosphorus doped with a bulk resistivity of (0.8 - 0.9) Ω cm) in which we intended to look for traps. The implantation was done at ANU with an energy of 2 MeV and a fluence of $1\text{x}10^9$ cm^{-2}. Following the implantation, some samples were annealed in nitrogen atmosphere for 15 minutes at temperatures varying between 200 °C and 700 °C. Next, the native oxide layer was removed via wet etch in HF, immediately followed by an evaporation of 150 nm gold through a shadow mask (via electron beam enhanced metal deposition), and a 240 °C 15 minute anneal to improve Au-Si adhesion. The circular gold contact is shown in yellow in Fig. 2.2. The Au-Si interface forms the Schottky barrier. We use indium-gallium (InGa) eutectic (which forms an ohmic contact with silicon) for the back contact (red) so that we are able to measure through the sample. Fig. 2.2 b) is a false colour image of an optical interferometry profiler trace of an actual sample. The silicon is in blue and the deposited gold is the circular area of approximately 800 μm

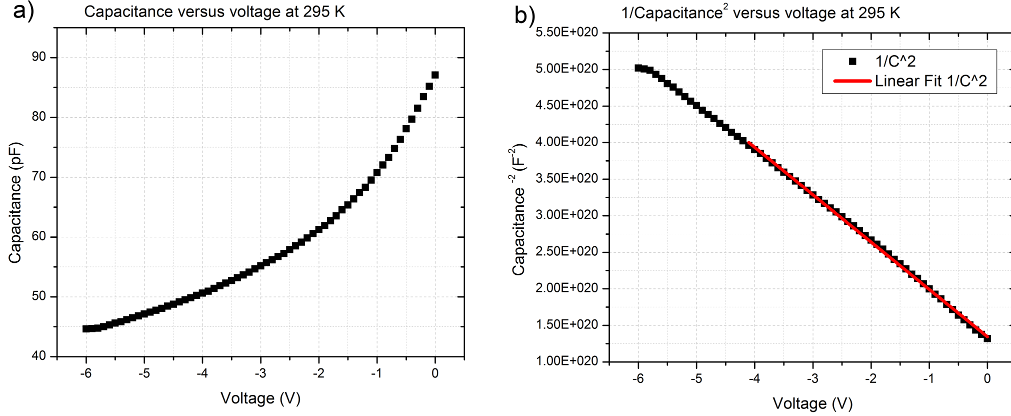

Figure 2.3: Measurements of an as-implanted Si:Er sample at 295 K showing (a) capacitance versus voltage and (b) inverse capacitance squared versus voltage including linear fits close to zero volts.

in diameter and about 100 nm thickness.

2.1.1 Capacitance versus voltage measurement

Capacitance versus voltage (CV) measurements provide important information about the characteristics of a Schottky-barrier junction including the built-in voltage and the active carrier concentration as a function of depth and will quickly reveal any potential problems with excessive leakage. It is customary to perform CV measurements at room temperature and at LN2 temperature prior to performing more time consuming DLTS measurements. The CV measurement quickly reveals any problems and allows suitable biasing ranges for the DLTS studies to be identified. By substituting equation 2.2 into equation 2.1 we obtain the relationship between capacitance C and applied voltage V. After solving for $1/C^2$ we have

$$\frac{1}{C^2} = -\frac{2}{qn\epsilon A^2} \cdot V + \frac{2}{\epsilon A^2 qn}(V_{\text{bi}} - \frac{k_B T}{q}). \tag{2.3}$$

To extract the active dopant concentration n and the built-in voltage V_{bi}, a CV measurement at a constant temperature is undertaken. Figure 2.3 a) shows such a measurement of capacitance versus applied voltage of an as-implanted sample at 295 K. The applied voltage was swept from -6 V to 0 V while the capacitance through the sample was recorded. From the graph of $1/C^2$ versus V (Fig. 2.3 c)) we can then use the slope, $-\frac{2}{qn\epsilon A^2}$, to obtain n, and the x-intercept, $\frac{2}{\epsilon A^2 qn}(V_{\mathrm{bi}} - \frac{k_B T}{q})$, to obtain V_{bi} with the calculated n. A slight temperature dependence of these values was observed. The calculated active dopant concentration n is 7.39 x 10^{17} cm^{-2} and the built-in voltage V_{bi} is 2.10 V at room temperature.

2.1.2 The DLTS measurement

The pulsed bias voltage versus time is shown in Fig. 2.5 a) which initially biases the device (with $\mathrm{V_{offset}}$) into depletion as discussed with Fig. 2.1. The filling pulse $\mathrm{V_{pulse}}$ is applied to sweep carriers into the depletion region and fill the charge traps. The concentration of the majority carrier trapped charges n_T in an n-type semiconductor decreases exponentially

$$n_T(t) = n_T(t=0)e^{-e_n t} \tag{2.4}$$

and depends on the emission rate e_n of each individual trap given by [122]:

$$e_n(T) = \frac{g_0}{g_1} \cdot \exp(\frac{\Delta S}{k_B}) \cdot N_C \cdot v_{th} \cdot \sigma_c \cdot \exp(\frac{-\Delta H}{k_B T}), \tag{2.5}$$

where $\frac{g_0}{g_1}$ is the degeneracy factor [123], ΔS the change in entropy, N_C the effective density of states in the conduction band, v_{th} the average thermal velocity of electrons, σ_c the capture cross section of the defect, and ΔH the activation enthalpy needed to promote an electron to the conduction band. If σ_c doesn't depend on the temperature, the activation energy E_a is equal to ΔH and equation 2.5 can be rewritten as

$$e_n = \gamma_n \sigma_c T^2 e^{-(\frac{E_c - E_T}{k_B T})}, \tag{2.6}$$

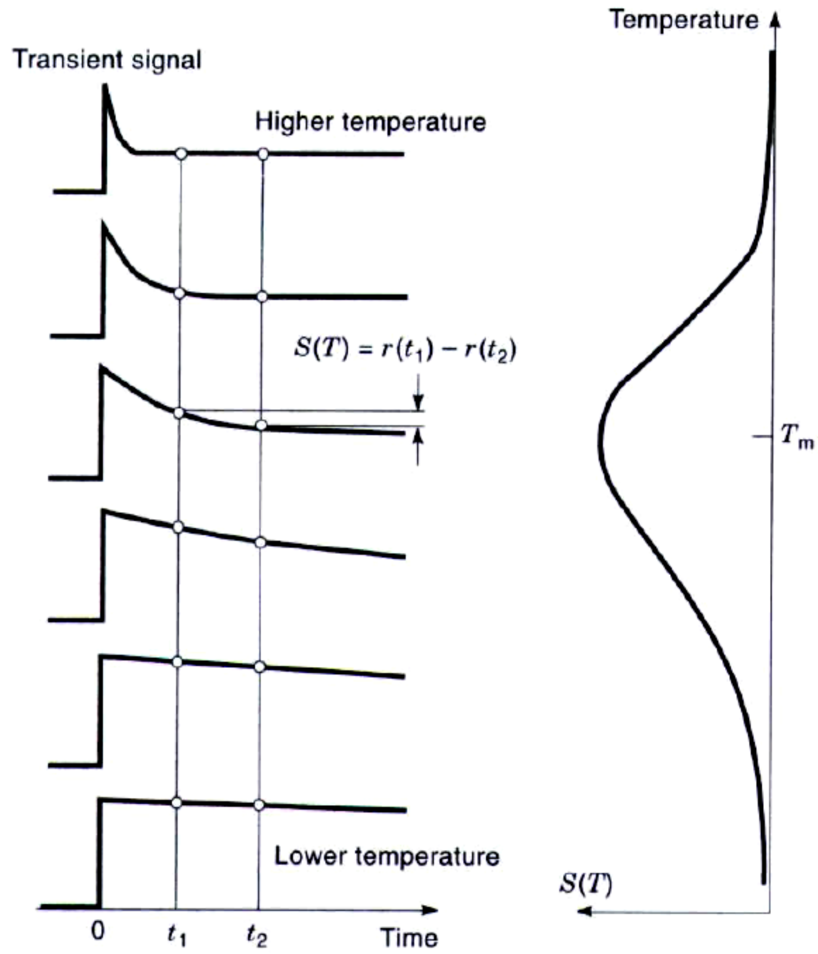

Figure 2.4: Capacitance versus time (left) at various temperatures and the resultant DLTS signal (right) [22].

with the constant γ_n

$$\gamma_n = 2\sqrt{3}M_c(2\pi)^{3/2}k_B^2 m^* h^{-3}, \tag{2.7}$$

where M_c is the number of minima in the conduction band (6 for silicon) and m^* is the effective electron mass in the conduction band. The charge carriers are emitted from traps in the measurement window, affecting the depletion width and consequently also the capacitance. Figure 2.5 b) shows the corresponding capacitance signal through the sample. At the applied offset voltage we measure a constant capacitance of C_0. When the bias voltage is applied, the capacitance changes to C_{pulse}. After the voltage offset is reapplied, the capacitance drops until it levels out at its original value of C_0 again. The capacitance transient is given by

$$C = C_0\sqrt{1 - \frac{n_T(t)}{n}} \tag{2.8}$$

for majority carriers, as shown in Fig. 2.5. For minority carriers the transient will decay in the opposite direction following $\sqrt{\frac{n_T(t)}{n}}$. To extract the time constant associated with the capacitance transient, the boxcar method (see [124]) is employed and so the difference in capacitance ΔC between t_1 and t_2, as shown in the Fig. 2.5, is determined.

For each temperature the capacitance is taken at two successive delay times after the applied voltage pulse. The difference between the two values versus the temperature constitutes the DLTS spectrum. Each peak in the spectrum indicates the presence of at least one trap. The sign of the peak defines whether we observe majority or minority carriers. The peak height corresponds to the defect concentration n and the peak position corresponds to the trap energy E_T and the cross section of the defects σ_c [22], as can be shown from equations 2.6 and 2.8.

The graph of capacitance versus time changes for different temperatures, as the emission from defects is temperature dependent. The emission rate e_n of a trap depends exponentially on the inverse temperature T, but

also on the trap energy level E_T. Consequently the emission rate is different for each specific defect. The temperature dependence of the transient signal associated with traps is illustrated in Fig. 2.4. This graph shows on the left hand side the signal of capacitance versus time for different temperature values. From the two consecutive capacitance values at t_1 and t_2 we calculate the difference $C(t_1) - C(t_2) = \Delta C$. The signal on the right hand side of the Fig. is obtained by plotting ΔC values versus each temperature value T. In addition to this spectrum, a capacitance versus temperature measurement is acquired, without pulsing the voltage, C_0.

The change of capacitance ΔC is calculated by substituting equation 2.4 in equation 2.8. After differentiating with respect to T we obtain the emission rate for the temperature values where the DLTS signal shows a peak T_{peak}:

$$e_n(T_{\text{peak}}) = \frac{ln(\frac{t_2}{t_1})}{t_2 - t_1} \tag{2.9}$$

for measuring at the time intervals t_1 and t_2.

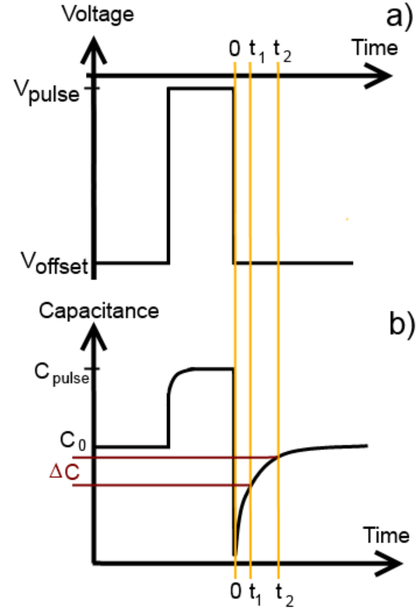

Figure 2.5: Capacitance versus time (bottom) shown while the bias voltage is pulsed (top).

To analyse the DLTS spectrum $(\Delta C - \Delta C_{\text{offset}})/C_0$ versus T is graphed. The values for ΔC_{offset} are obtained by applying zero volts to the sample and only measuring the offset of the equipment. An example DLTS spectrum is shown in Fig. 2.6. This spectrum was taken at four different delay times of 50, 20, 10, and 5 ms during one scan. The peaks in this plot are of Gaussian nature

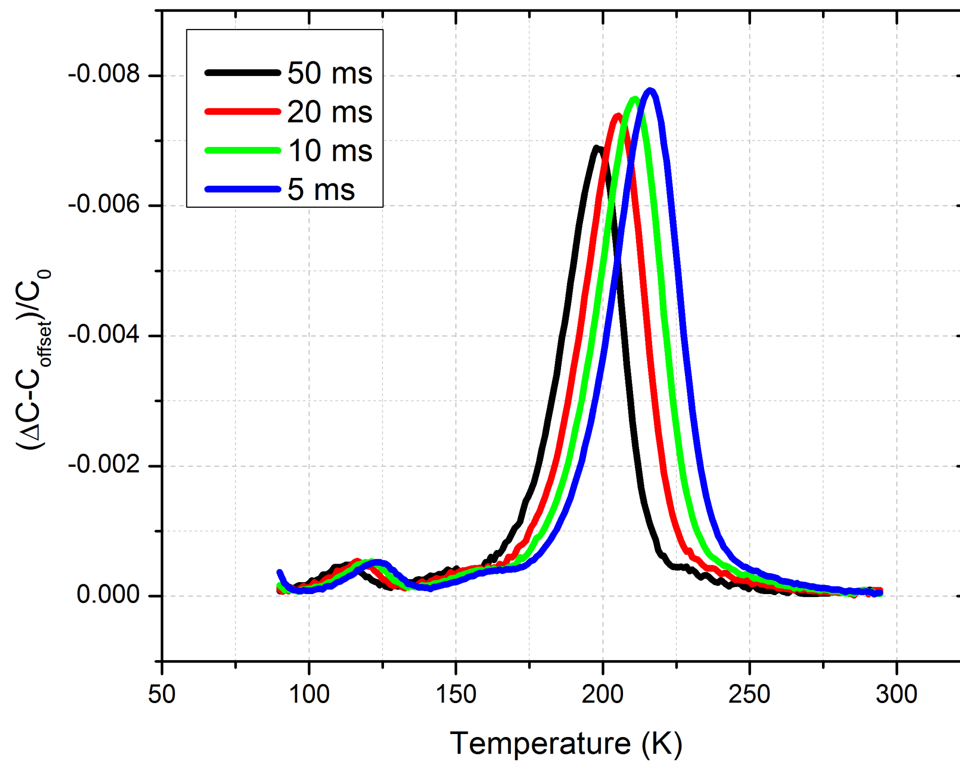

Figure 2.6: DLTS signal of an as-implanted sample (erbium in silicon at 2 MeV, 1 x 10^9 cm^{-2}) taken at 4 successive time intervals in one measurement run (50, 20, 10, and 5 ms).

and can be fitted to gain the peak height and corresponding temperatures T. Rearranging equation 2.6 gives us

$$ln\frac{e_n}{T^2} = ln(\gamma_n \sigma_c) - \frac{E_c - E_T}{k_B T}. \tag{2.10}$$

Following that, the Arrhenius plot of $ln(e_n/T^2)$ versus $1/k_BT$ is linear and enables us to extract the cross section of the defects σ_c from the x-intercept, as well as the trap energy $E_c - E_T$ from the slope. The Arrhenius plot of the largest peak around 200 K in Fig. 2.6 is shown in Fig. 2.7. The calculated capture cross section is 3.98 x 10 $^{-23}$ cm^{-2} and trap energy is 0.44 eV. With this information it is possible to identify the defects we discovered in the Er doped samples.

Equipment The DLTS setup is by Sula Technologies and consists of a voltage source that applies a pulsed voltage with a defined offset voltage (maximum voltage output of 10 V), and four correlators that measure at the delay times t_1, t_2, t_3, and t_4 (variable between 100 ms and 0.001 ms) during one temperature scan. The temperature is controlled via a Lakeshore 331 Temperature Controller by heating the copper stage on which the sample is situated. The sample chamber is cooled throughout the measurement with liquid nitrogen. The heater enables the temperature control between liquid nitrogen temperature and over room temperature. During the DLTS we generally sweep from 80 K to 295 K. The sample chamber is evacuated to ensure moisture will not interfere with the capacitance measurements. The hardware is connected to the BNC-2090 interface of National Instruments which in turn is connected to the computer that is used to collect the data.

2.2 Rutherford backscattering

Rutherford backscattering (RBS) is a process during which a high energy particle beam (typically 0.4 - 4 MeV) is directed at a target, resulting in

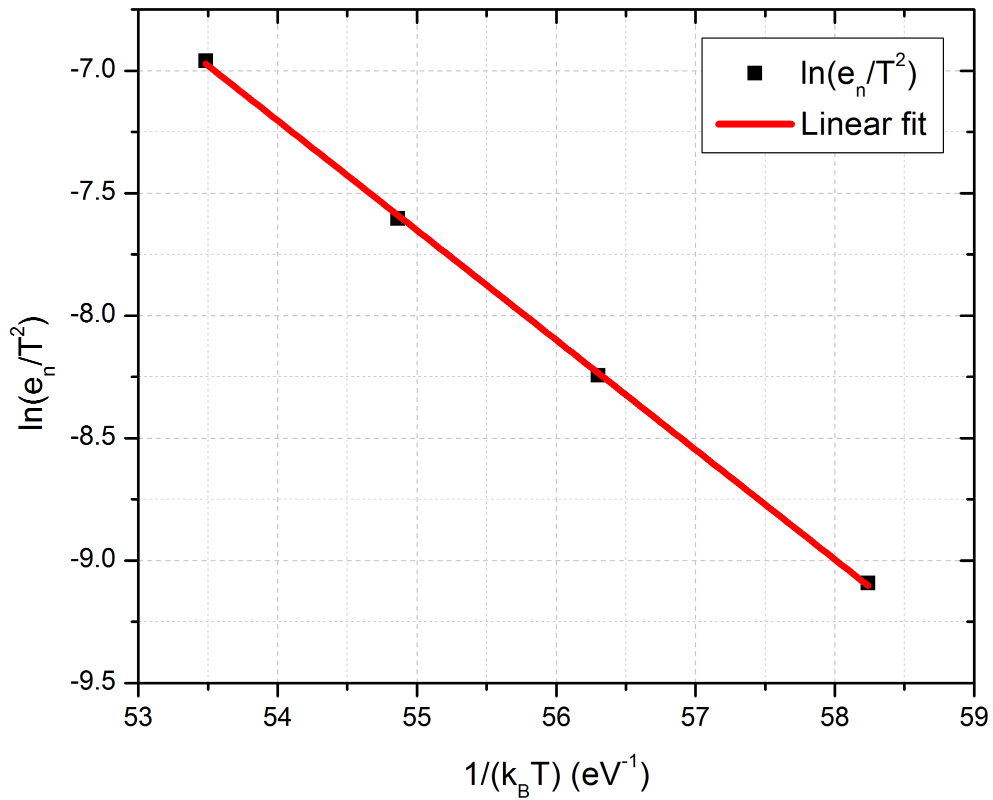

Figure 2.7: Arrhenius plot of $ln(e_n/T^2)$ versus $1/k_BT$ of the largest peak observed in 2.6, including the linear fit used to extract the capture cross section and trap energy.

elastic collisions between the ion beam and the target atoms. It is used to determine the composition and structure of the target by measuring the energy of the backscattered particles with an energy sensitive detector. RBS is very sensitive for heavy elements, especially when using light ions in the ion beam. The energy of the scattered particle E_1 is reduced from the initial energy E_0 by the kinematic factor k:

$$E_1 = k \cdot E_0, \tag{2.11}$$

where the kinematic factor is given by [125]

$$k = \left(\frac{\sqrt{1-(m_1/m_2)^2 \sin^2\Theta} + (m_1/m_2)\cos\Theta}{1 + m_1/m_2}\right)^2, \tag{2.12}$$

m_1 and m_2 are the masses of the incident ion and target atom, and Θ is the scattering angle. Equations 2.11 and 2.12 show that the energy loss for any scattering angle depends on the masses only, resulting in a higher resolution for higher mass ratios. Energy is lost by scattering with the sample nuclei and by scattering with the sample electrons. The first process depends on the scattering cross-section of the nucleus and therefore the mass of the target atoms, creating distinct peaks for each element. The latter process results in a gradual energy loss depending on the distance travelled within the sample, shifting peak positions towards lower energies of elements appearing within some depth inside the sample. The analysed depth depends on the energy of the incident particles as well as the target composition, but is typically about 20 μm for protons. Without reference samples, RBS is qualitative only. Reference samples are needed to calibrate the detector and achieve quantitative results. More about nuclear micro-probe techniques can be found in [125], [126].

The RBS target chamber at the University of Melbourne houses two silicon surface barrier detectors (see [127] for more information on silicon surface barrier detectors). One detector is fixed at 10° from the incident ion beam path. This back-angle detector gives good elemental resolution. A

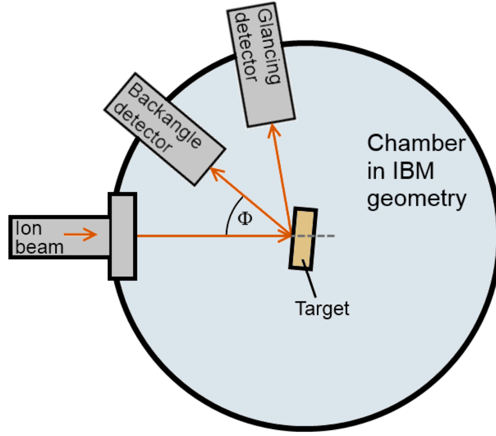

Figure 2.8: Sketch of the RBS chamber used at Melbourne University.

glancing detector is fitted to a stage which can be rotated about the sample axis and can be made to have greater depth resolution (see Fig. 2.8). In order to reduce contamination a copper shield cooled with liquid nitrogen surrounds the target. The scattering geometry is IBM geometry: incident beam, exit beam, and surface normal to the sample are in the same plane. On the Melbourne Pelletron, H^+ and He^{2+} particles with energies between 0.4 and 4 MeV can be used. The charge read by the detector is proportional to the ion energy. A multi channel analyser (MCA) converts this analogue signal into a digital signal by sorting the data into channels. The output of the MCA consists of a yield versus channel number with the channel number proportional to the particle energy. Since the ion source changes over time, this relationship changes over time, so the system needs to be calibrated every day. The used ion source emits alpha particles, the incident energy of which can be varied, but is typically between 1 to 2 MeV. We used an incident energy of 1 MeV with a glancing angle set at 70° and back scattering angle of 10°. The energy calibration was performed by examining 4 reference samples: gold (Au) on silicon (sample 1), germanium (Ge) (sample 2), carbon (C) and oxygen (O) (sample 3), and blank silicon (Si) (sample 4). By creating a plot of the channel number at which the front edges of these five elements occur and the expected energy, we were able to determine the relationship between channel number and energy. Fig. 2.9 shows the RBS spectrum of sample (1), gold on silicon. The

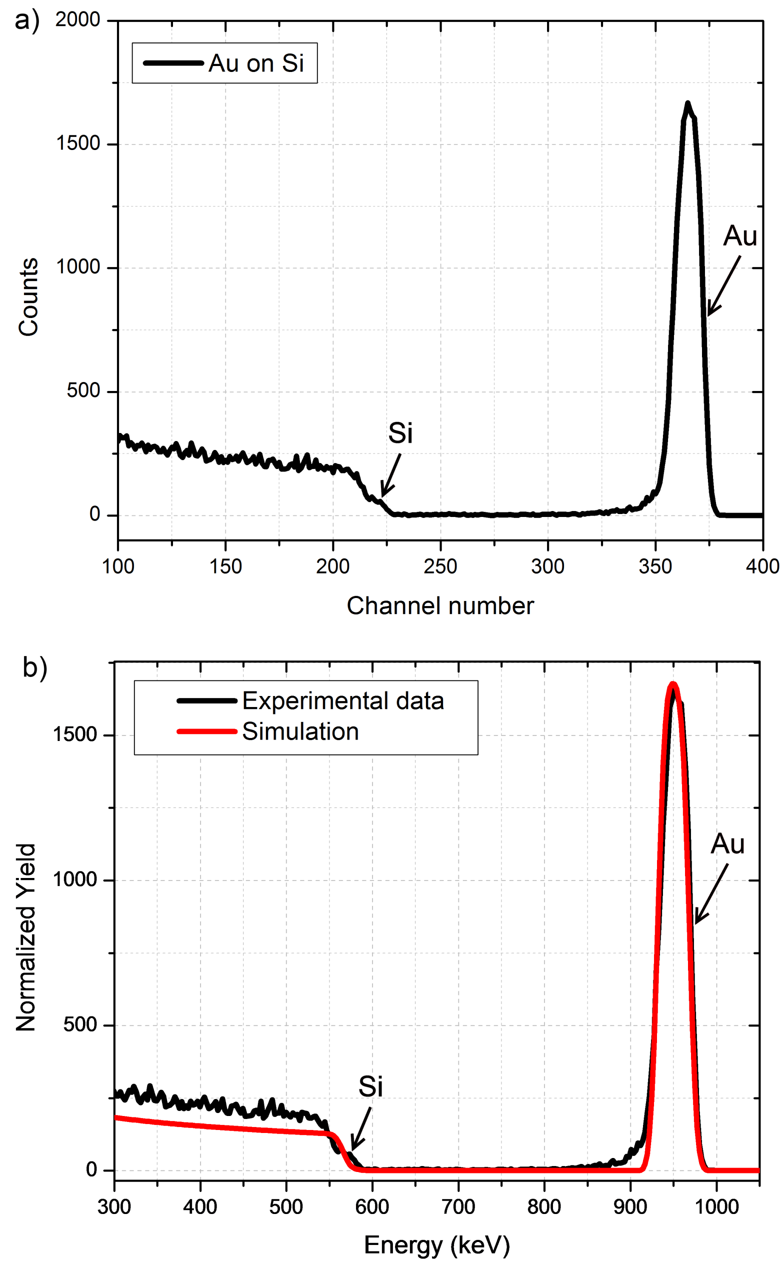

Figure 2.9: a) RBS spectrum in counts versus channel number of a gold on silicon sample with an incident alpha particle energy of 1 MeV. b) Same RBS spectrum in normalized yield versus energy, including the simulation in red.

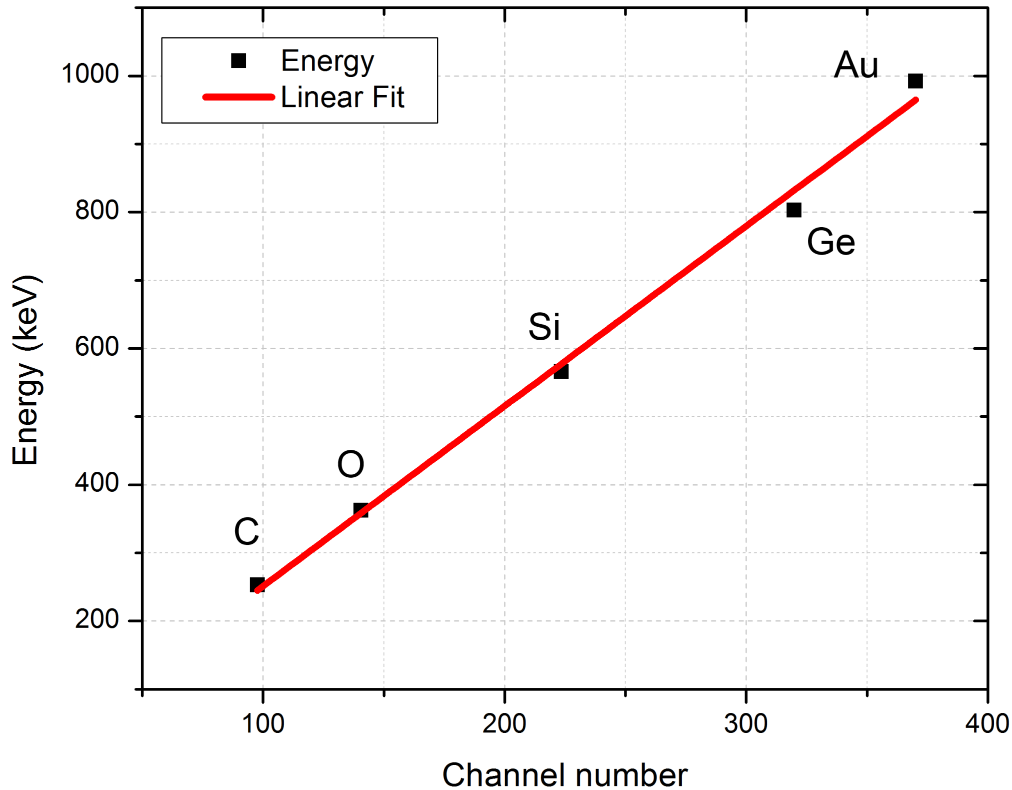

Figure 2.10: Calibration plot of energy versus channel number for the backscatter angle detector with an incident alpha particle energy of 1 MeV including the linear fit in red.

heavier element, gold, is visible as a peak at a higher channel number than the lighter element, silicon. From this plot we could read off the channel number of the Au front edge. This was repeated for the remaining 4 elements in the other samples, but their RBS spectra are not shown here. The theoretical energy value of each element can be found in dependency of the incident alpha particle energy. The experimental determined channel number and the calculated value for the energy is given in Fig. 2.10 for each of the five examined elements. Figure 2.10 shows the calibration plot of the energy versus channel number of the five reference elements. The fit has an

R^2 value of 0.994 and the following relationship between yield and energy is found:

$$\text{Energy} = 2.64(\frac{keV}{channelnumber}) * \text{channel number} - 12.59(keV).$$

Following the 4 reference samples, the actual target of interest is examined. The obtained data can be fitted with a simulation program called "RUMP" (based on the plotting package "GENPLOT") and provides analysis and simulation of RBS spectra [128]. It loads data of the atomic stopping power and isotope information, which can be used in "SIM" (a sub-processor included in RUMP) to simulate the RBS spectrum. The best fit with the experimental spectrum gives the parameters of the run. This makes it possible to extract layer composition and thickness of examined samples with RBS. If a qualitative analysis is sufficient, the simulation is not necessary. Such a simulation is shown in Fig. 2.9 b) in red, overlapping the experimental data in black. Both the Au and Si edges were in agreement with the simulation. Note that the particle beam loses energy through the gold layer before reaching the silicon, introducing an energy shift. This is accounted for in the simulated data.

2.3 Electrical measurement techniques

In this project we used a variety of methods for measuring effects such as the Hall effect and Quantum Hall effect. These techniques were used at room temperature, as well as at low temperatures. Through our electrical measurements, information was gained regarding the electrical properties of the studied materials.

2.3.1 Classical Hall Effect

In 1879 Edwin Hall discovered the effect named after him [129]. The Hall effect is used to obtain the carrier type and concentration of a conducting

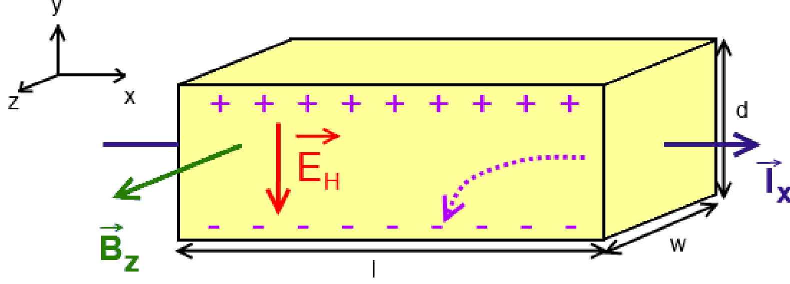

Figure 2.11: Hall bar in a magnetic field illustrating the Hall effect.

sample. If a magnetic field $\vec{B}$ is applied in the z-direction of a sample and a current $\vec{I}$ is passed through the sample in the x-direction, there will be a resulting Lorentz force $\vec{F}$ [130]

$$\vec{F} = e\,(\vec{E} + \vec{v} \times \vec{B}), \tag{2.13}$$

causing the charge carriers to move in the y-direction (as in Fig. 2.11) with the velocity $\vec{v}$. This accumulation of charges induces an electric field, the Hall field $\vec{E_H}$. At equilibrium it is

$$e\,(\vec{v} \times \vec{B}) = -e\,\vec{E_H}. \tag{2.14}$$

According to the illustration in Fig. 2.11 equation 2.14 can be simplified to

$$E_H = Bv_x. \tag{2.15}$$

The Hall coefficient is defined as the ratio of the Hall field E_H to the current density along x, j_x, times the magnetic field, B [131]:

$$R_H = \frac{E_H}{j_x B}. \tag{2.16}$$

Using $j = nve$ [130] and equations 2.15 and 2.16, the Hall coefficient can be written as

$$R_H = \frac{1}{ne}. \tag{2.17}$$

From this equation the charge carrier concentration n can be determined. The sign of the Hall coefficient reveals the type of dominant charge carriers (positive for holes and negative for electrons). Generally speaking the charge carriers contributing to conduction will be mixed [132]:

$$R_H = \frac{1}{|e|} \frac{n_p - b^2 n_e}{(n_p + b n_e)^2} \tag{2.18}$$

with $b = |\mu_n/\mu_p|$ as the ratio of the mobilities of electrons and holes, n_p the concentration of holes, and n_e the electron concentration. The mobility is determined via the Hall effect using

$$j_x = ne\mu E_x. \tag{2.19}$$

2.3.2 Van der Pauw method

In 1958 Leo J. van der Pauw proposed that if a sample is approximately two dimensional, a sample of any shape can be examined and its resistivity, charge carrier density and mobility can be calculated [133, 134]. The conditions for using this technique are that (i) the sample is free from pinholes, (ii) the contacts are sufficiently small compared to the entire sample surface and are located on the perimeter of the sample, and (iii) the sample thickness is homogeneous.

Such a sample is shown schematically in Fig. 2.12 a). The contacts (blue) are exaggerated in size for visibility, but should ideally be much smaller in size. The "clover" shaped sample in b) is preferred to minimize the effects of the contacts. In order to calculate the resistivity ρ of the sample we need to measure the resistance $R_{AB,CD}$, derived from the potential difference between contacts C (V_C) and D (V_D) per current through the contacts A and B I_{AB}, as well as the resistance $R_{BC,DA}$, derived from the potential difference between contacts D (V_D) and A (V_A) per current flowing through the contacts B and C. The resistivity is then given by the following relationship derived

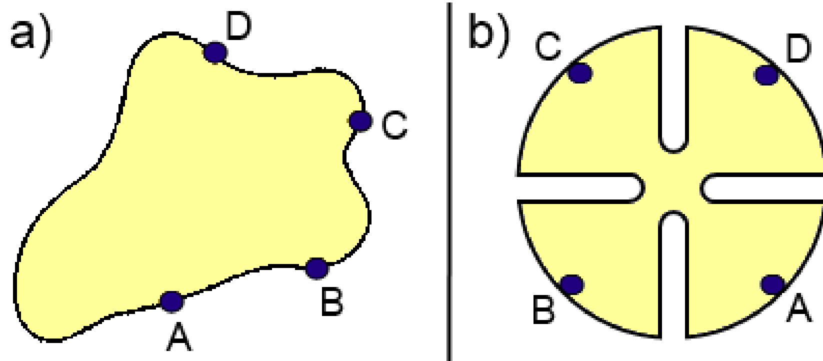

Figure 2.12: Arbitrary shaped sample with four contacts A, B, C, and D along the circumference to illustrate van der Pauw geometry.

by van der Pauw [133]:

$$\rho = \frac{\pi d}{\ln 2} \frac{R_{AB,CD} + R_{BC,DA}}{2} f \frac{R_{AB,CD}}{R_{BC,DA}}, \tag{2.20}$$

with the sample thickness d and f being a function of the ratio $R_{AB,CD}/R_{BC,DA}$,

$$\frac{R_{AB,CD} - R_{BC,DA}}{R_{AB,CD} + R_{BC,DA}} = f \,\mathrm{arcCosh}\, \frac{\exp[\ln 2/f]}{2}.$$

When adding a magnetic field B perpendicular to the sample, the change of resistance $\Delta R_{BD,AC}$ will give the mobility μ:

$$\mu = \frac{d}{B} \frac{\Delta R_{BD,AC}}{\rho}. \tag{2.21}$$

The method for measuring at low temperatures including the electronics is described in chapter 3.4. Not only the hardware setup, but also further useful equations are explained in detail there.

Chapter 3

Cryogen-free Dilution Refrigerator

This chapter explains the operation of a dilution refrigerator and the theory that lies behind the cooling process, and details the particular features of the dilution refrigerator installed during this research. The coldfinger, which holds the samples, as well as the 3D vector-magnet and the optical access, are highlighted, and the measurement setup is outlined.

3.1 The operation of a Dilution Refrigerator

The dilution refrigerator used for this project is a cryogen-free model made by Leiden Cryogenics. Cryogen-free, or dry, means that it does not consume any cryogenic liquids (i.e. helium) during operation. Key components are shown in Fig. 3.3. Liquid nitrogen may be used to accelerate the cooling processes starting at room temperature, but this is not a requirement. One can also reach low temperatures using the pulse tube alone, though this will extend the cool-down process by a few days. A conventional dilution refrigerator has a bath of liquid helium to pre-cool a mixture of the isotopes helium 3 and helium 4 that runs through the cycle. A cryogen-free refrigerator on the

other hand uses a pulse tube for this purpose. The pulse tube pre-cools the dilution refrigerator by rhythmically compressing and adiabatically expanding a helium gas (99.999% purity) contained in itself with heat exchangers transferring the heat outside the system. The pulse tube unit itself is water cooled. It is able to reach a temperature of about 4 Kelvin.

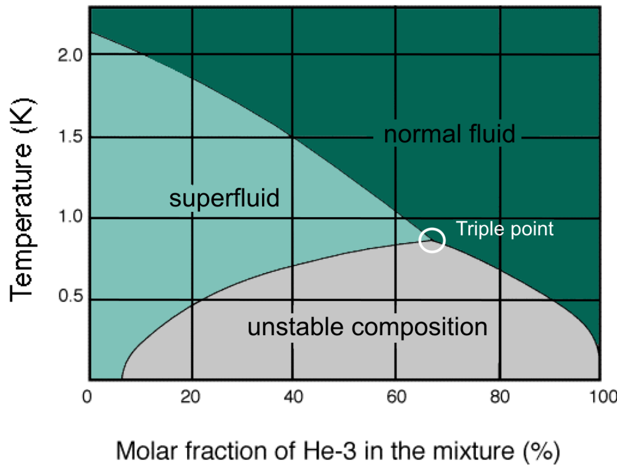

Figure 3.1: He^3/He^4 Phase-diagram [23, 24].

Dilution refrigerators use a mixture of two isotopes of helium, the rare ^{3}He and the more common ^{4}He. By using a mixture of these isotopes it is possible to cool the sample far below liquid helium temperature, into the milli-Kelvin regime. This works due to a phase separation that the mixture undergoes below the triple point at 0.86 Kelvin (see Fig. 3.1). The heavier ^{3}He diluted phase consists mainly of ^{4}He and has superfluid properties, meaning it is devoid of viscosity [135, 136, 137]. The ^{3}He atoms in this phase move freely, as they are effectively a gas [138]. The lighter ^{3}He concentrated phase consists almost exclusively of ^{3}He and is a normal liquid. This phase separation occurs in the mixing chamber. The transfer of a ^{3}He atom from the ^{3}He rich phase into the diluted phase equates to a transition from a liquid to a gaseous phase (see 1 in Fig. 3.2). This quasi-evaporation requires energy, analogous to evaporation cooling. This energy is taken from the surroundings in form of thermal energy, resulting in a temperature drop. Hence the mixing chamber is the coldest part in the whole dilution refrigerator.

Extracting ^{3}He atoms from the diluted phase by pumping requires a sufficiently high vapour pressure. The lower the temperature is, the lower the vapour pressure becomes [139]. To provide a high enough vapour pressure, the diluted phase is connected to the still (see Fig. 3.3). Here the diluted phase is heated up to just under 1 Kelvin in order to extract ^{3}He. Due to the slightly different vapour pressures of the two isotopes, pumping on the still will evaporate mainly ^{3}He (see 2 in Fig. 3.2). According to Fig. 3.1 there can never be less than 6% of ^{3}He in the diluted phase at equilibrium, even at zero Kelvin [140]. This is the reason why it is possible to reach a few milli Kelvin with this technique [24]. Consequently, the diluted phase needs to constantly restock itself with ^{3}He from the concentrated phase as it is continuously pumped away through the still.

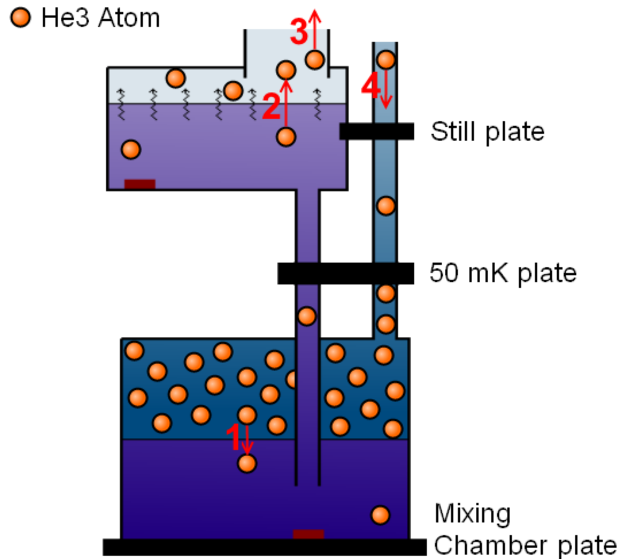

Figure 3.2: Schematic of the ^{3}He flow in a dilution refrigerator (detail of Fig. 3.3).

Once the ^{3}He gas leaves the still (see 3 in Fig. 3.2), it is heated up to room temperature outside of the fridge. The ^{3}He is then purified in liquid nitrogen cooled cold traps before it is cooled down to about 3 Kelvin by the pulse tube, followed by further cooling via the next heat exchanger coupled to the still, cooling the incoming ^{3}He atoms down to about 600 mK. The last cooling stage before reaching the mixing chamber is the 50 mK plate located between the still and the mixing chamber. Finally the ^{3}He extracted from

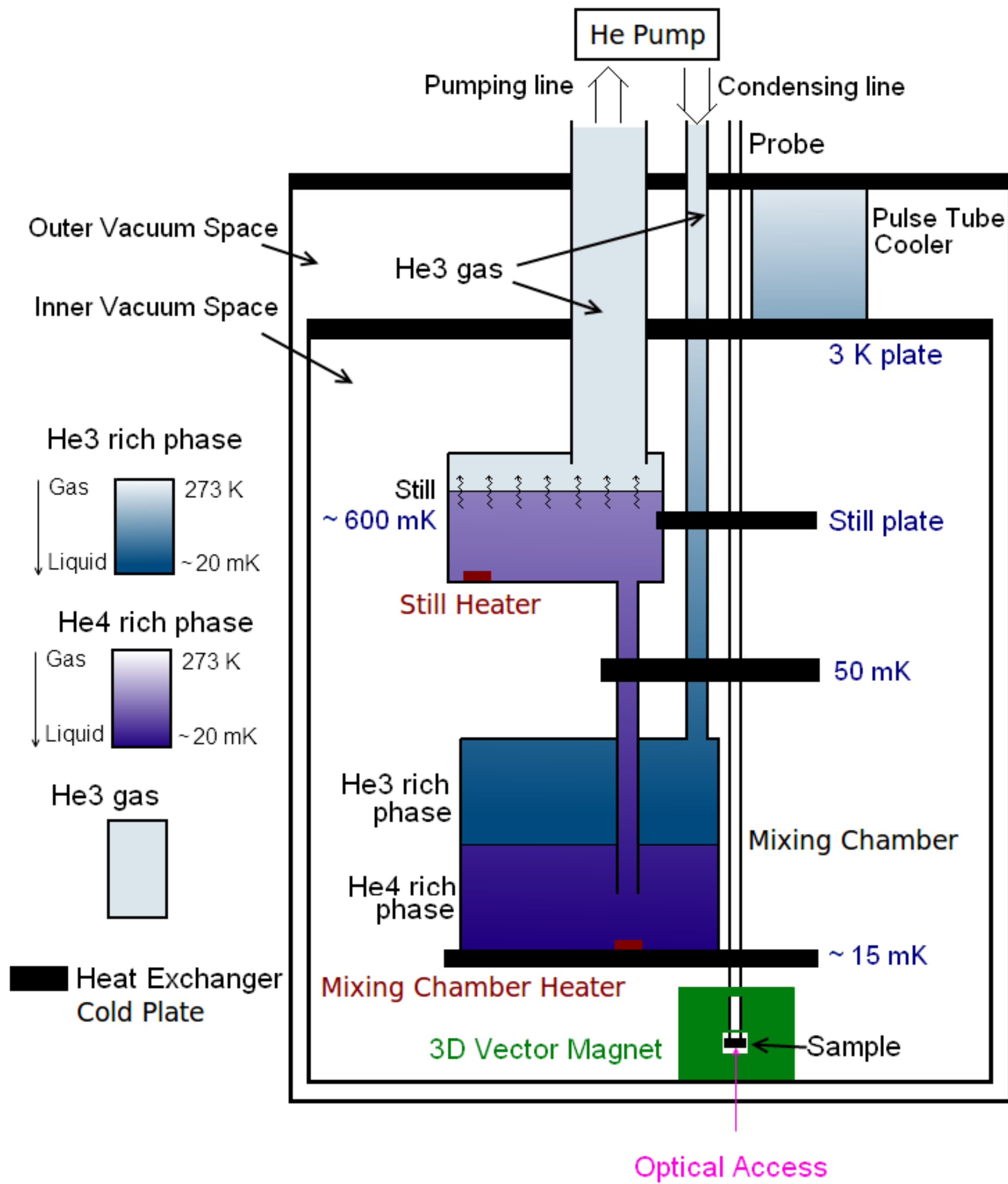

Figure 3.3: Sketch of the cryogen-free dilution refrigerator illustrating the He^3/He^4 cycle, pulse tube, and heat exchangers (according to[25]).

the still reaches the ^{3}He rich phase in the mixing chamber (see 4 in Fig. 3.2). From here, the ^{3}He replenishes the previously extracted ^{3}He in the diluted phase. This then completes the cycle of ^{3}He within the system. The sketch in 3.3 shows the full cycle that the mixture undergoes. The cooling power can be regulated by a heater that sits on the still plate. Higher temperatures favour helium evaporation [139], which increases the cooling power and makes it possible to reach very low temperatures of less than 20 mK [24]. Nevertheless, the still heater needs to be used with caution, as too much heating will work against the cooling process.

A photograph of the dilution refrigerator that was installed during this project is shown in Fig. 3.5 and 3.4. All vacuum cans and heat shields are removed in Fig. 3.4, which reveals the interior of the fridge. This picture can be directly compared to the sketch in Fig. 3.3. All plates (in gold) can be identified. The outside of the fridge is painted blue, including the outer plate at the very top. The two manual valves attached to the top right hand side of the fridge can be used to pre-cool the system with liquid nitrogen when cooling from room temperature down to base temperature. Figure 3.5 is a photograph of the assembled dilution refrigerator. Located in the background in red/silver is the gas handling system (GHS). The GHS is responsible for controlling the valves and pumps for the inner circuit (He^3/He^4 cycle) as well as the outer circuit (evacuating the OVC, IVC and still).

The Probe A probe is used to swap samples while the system remains at its base temperature of 4 - 5 K. The probe reaches from the top of the fridge down to the lowest part where the sample is positioned in the centre of the magnetic field lines. Mechanical arms that press against the cold plates are responsible for the thermal connection of the probe to the fridge. These arms pull themselves within the probe when they are released in order to extract/insert the probe. The magnetic field is produced by a superconducting magnet which is centred with respect to quartz windows providing optical

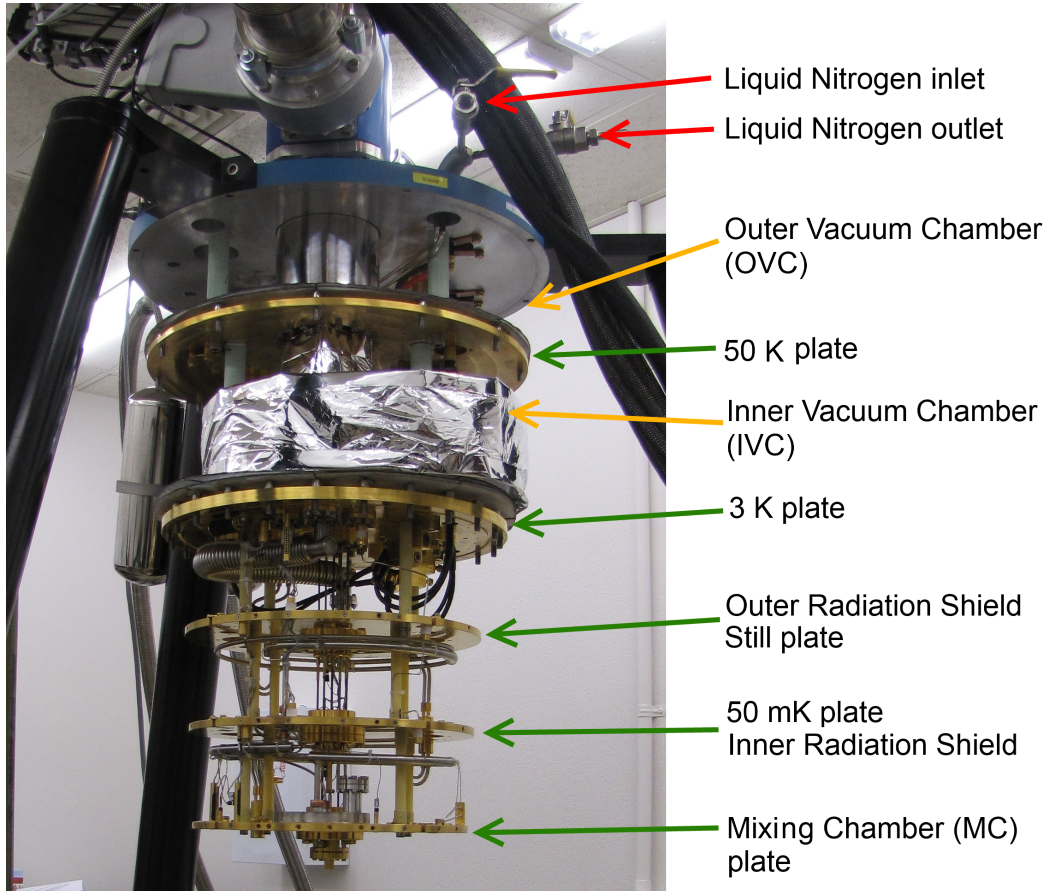

Figure 3.4: Photograph of the cryogen-free dilution refrigerator. All vacuum cans and heat shields are taken off to show the interior.

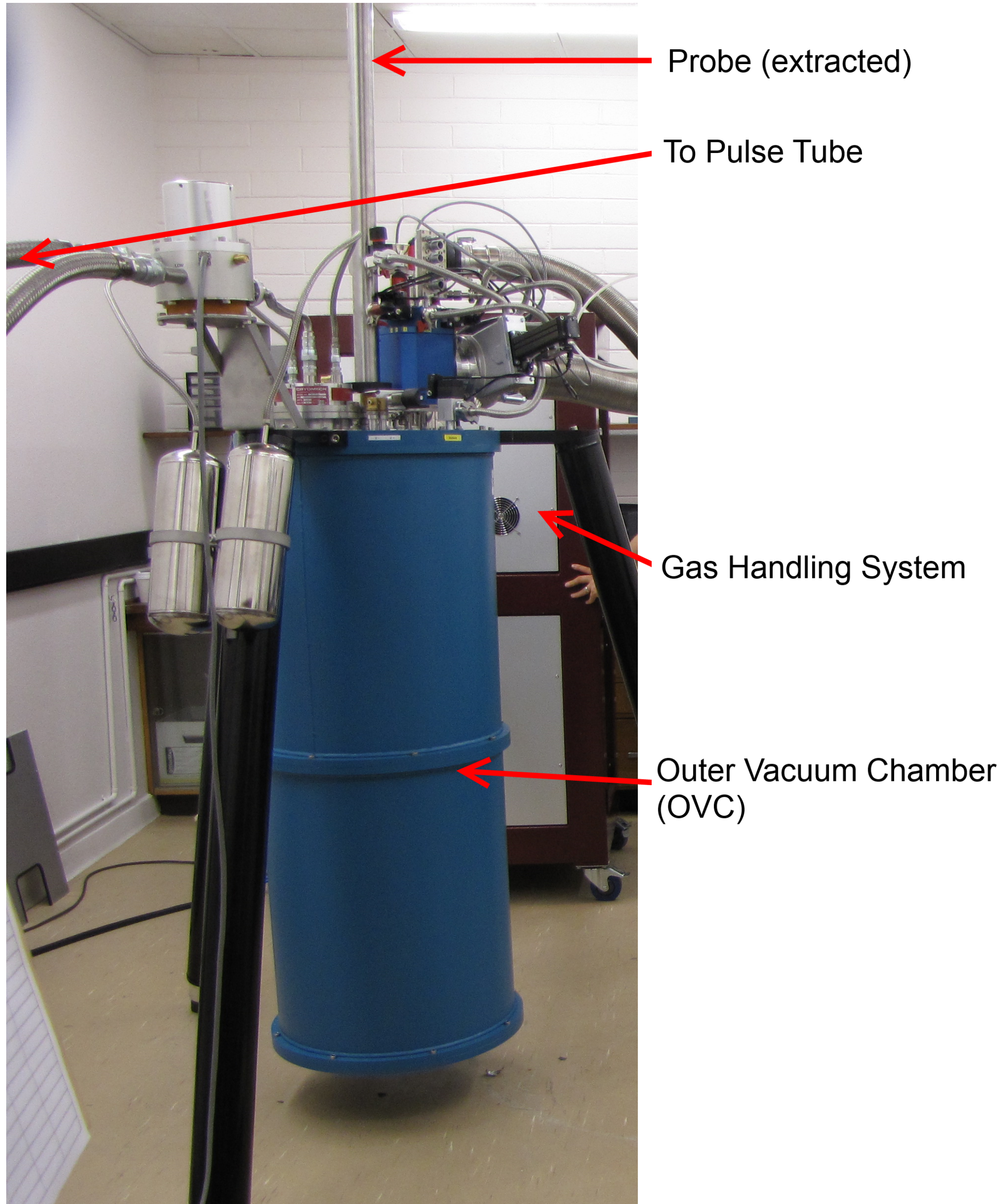

Figure 3.5: Photograph of the assembled cryogen-free dilution refrigerator with the gas handling system (GHS) visible in the background (red).

access via the bottom. However, during this project the quartz windows were not in use. The magnet is located on the 3 Kelvin plate and consists of 3 pairs of split coils that can produce fields of up to 9 Tesla in the main field, the z-direction, and up to 1 Tesla in x- and y-direction. There are 36 DC lines connected to two separate sample holders, and 10 flexible coax lines with a bandwidth of 0.5 GHz on the probe which are used to connect the samples under examination. In addition to inserting samples via the probe, devices can also be attached directly to the mixing chamber plate itself. Placed here, they can only be exchanged by completely opening up the system, which includes heating up to room temperature. There are 48 DC wires here that may be used for those samples. Each DC line has a (13-30) Ω resistance and 10 μF inductance. The sample temperature can be regulated via a heater located on the mixing chamber plate which directly heats up the samples (see Fig. 3.3). This heater is to be used with caution, as when this part of the fridge is too hot, the helium mixture will not be able to exist in a condensed state in the mixing chamber. This leads to a rapid expansion of the circulation mixture into its gaseous state and prevents the continuation of the cooling cycle.

3.2 The Coldfinger

In order to place the samples in thermal contact with the mixing chamber and in the area of homogeneous magnetic field lines that the 3D vector magnet produces, a so-called coldfinger was constructed. This is attached to the probe and holds the samples in place. Being attached to the probe, it can be inserted and extracted without the need for the dilution refrigerator to be disassembled. This is an important feature, as warming up the refrigerator to room temperature is time consuming and the procedure includes unnecessary risks, such as introducing leaks.

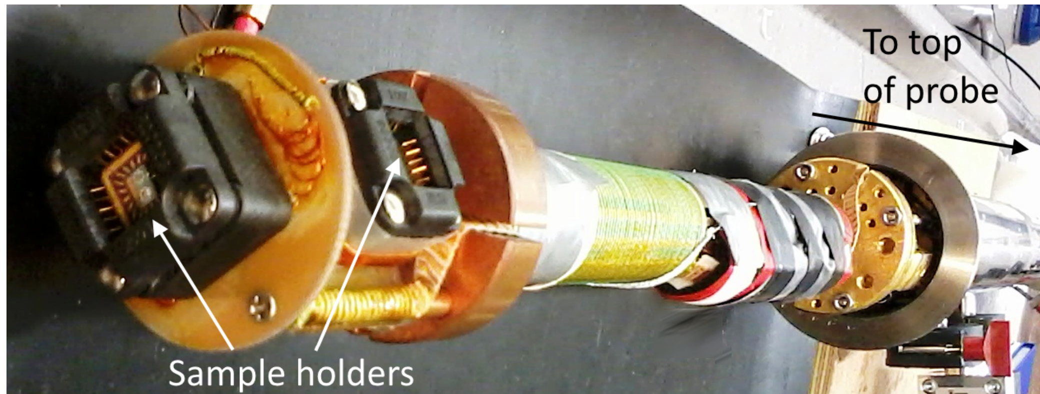

Figure 3.6: Photograph of the finished coldfinger.

A photograph of the completed current coldfinger is seen in Fig. 3.6. The coldfinger is capable of holding two samples at the same time. One sample holder is located in the centre of the magnetic field lines and faces the optical windows. The other is turned by 90 degrees and has no window access when inserted into the refrigerator. The pins of the sample holder are wired up and connected to the top part of the probe with a Fischer socket, which is accessible from the outside for measurements while the probe is inserted. Having good thermal conductivity between the sample and the mixing chamber ensures that they are the same temperature. The material used for the coldfinger is oxygen free solid copper, Alloy 101. Copper was chosen due to its high heat conductivity and its non-magnetic properties. The solid copper rod of the coldfinger has slits cut in it to avoid eddy currents (also called Foucault currents [141]). Eddy currents are created when a conductor (the copper rod) is subject to a changing magnetic field i.e. whenever the field in the 3D vector magnet is changed. This leads to the formation of circular current loops perpendicular to the penetrating, time varying magnetic flux, called eddy currents [141]. Eddy currents will induce Joule heating, causing the temperature to rise. Since the cooling power of the dilution refrigerator is minimal at base temperature such heating results in higher base temperatures. We wish to eliminate this effect as much as

possible. Reducing the area of the conductor will reduce the size of the current loops, therefore decreasing the additional I^2R heat load on the system. This is achieved by creating slits in the copper rod. The wires coming from the sample lead to the top part of the probe and are connected to a so called breakout box. This box allocates each individual pin of the sample to its own switch, making it possible to toggle between ground and BNC connectors. The BNC connectors are connected to the electrical equipment which is used for applying or measuring voltages/currents. Finally RC filters can be used in order to filter out noise.

3.3 3D Vector magnet and optical access

frigerator is equipped with a three dimensional (3D) superconducting vector magnet. This electro magnet consists of three coils, arranged in such a way that it is possible to create a magnetic field in either x, y, or z direction (see Fig. 3.7 for the directions), or any superposition of these. The sample to be measured is inserted via the coldfinger into the magnet's bore where the field lines are homogeneous. In the z-direction it is possible to create a magnetic field of up to 9 Tesla. In x- and y-direction the maximum field is 1 Tesla. It is possible to ramp from negative fields through to positive fields and vice versa. The dilution re

Optical access Direct optical access to the sample sitting on the lower carrier of the coldfinger is facilitated by quartz windows throughout the radiation shields and vacuum chambers of the fridge. If direct optical access is not required, these can be blanked off to ensure that the lowest possible base temperature can be reached. The quartz windows need to be able to withstand the pressure difference that is given by the vacuum on the inside of the vacuum can and the atmospheric pressure on the outside of the vacuum can. As direct optical access to our samples was not required, we have not had

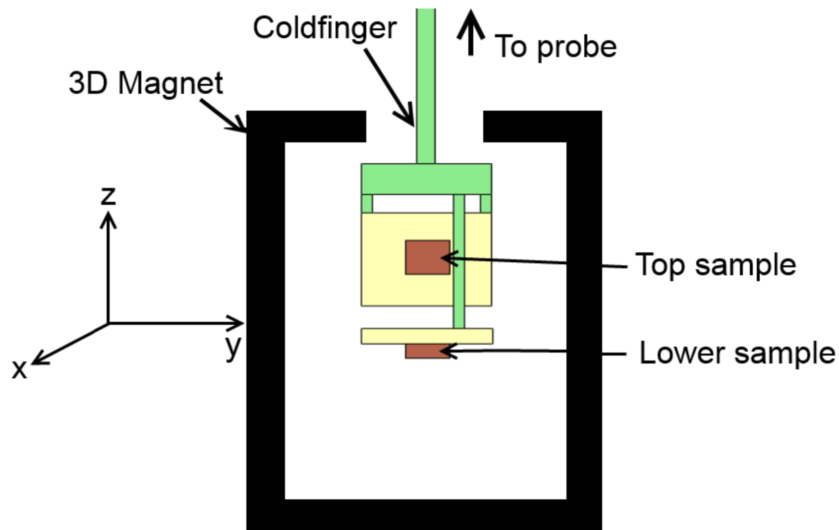

Figure 3.7: Sketch of the samples situated in the bore of the 3D vector magnet.

the quartz windows in place. The use of the windows leads to a reduction of the minimum temperature achieved by the fridge, as the cooling power is not sufficient to operate at temperatures as low as 50 mK with the quartz windows in use. Therefore their use is best avoided, unless optical access is needed.

3.4 Low Temperature Measurements

Depending on the sample setup, the techniques previously described in chapter 2.3 were used to derive characteristic parameters of the samples. Primarily Hall bar shaped samples of known dimensions - width, length, and thickness - were examined.

Resistivity In the interest of determining a sample's resistivity, a current I_{SD} needs to be sent through the length of the sample while recording the voltage along the length of the sample V_{xx}. The resistivity ρ of a sample can

only be calculated if the dimensions are known. With the sample thickness t, width w and length l, as well as $R_{\mathrm{xx}} = V_{\mathrm{xx}}/I_{\mathrm{SD}}$, the resistivity is calculated as follows:

$$\rho = \frac{R_{\mathrm{xx}}}{I_{\mathrm{SD}}} \cdot \frac{t \cdot w}{l}. \tag{3.1}$$

Conductivity The conductivity σ of the sample is given by the reciprocal of the resistivity

$$\sigma = \frac{1}{\rho} = \frac{I_{\mathrm{SD}}}{R_{\mathrm{xx}}} \cdot \frac{l}{t \cdot w}. \tag{3.2}$$

Charge Carrier Mobility The mobility of the charge carriers μ can only be calculated by varying the magnetic field while recording the Hall voltage V_{xy} as well as resistivity ρ. Using the following equation the mobility is obtained [132]:

$$\mu = \frac{1}{B} \cdot \frac{V_{\mathrm{xy}}(B)}{I_{\mathrm{SD}}(B)} \cdot \frac{1}{\rho}, \tag{3.3}$$

or

$$\mu = \frac{1}{B\rho} \cdot R_{\mathrm{xy}}. \tag{3.4}$$

Charge Carrier Density The charge carrier density n is now easily extracted with [130]:

$$n = \frac{B}{R_{\mathrm{xy}} q}, \tag{3.5}$$

with q being the charge of the charge carriers, e for electrons as the charge carriers.

3.4.1 Measurement Setup

In order to be able to perform these measurements, various pieces of equipment were used.

For the DC measurements reported herein we employed voltage sources by Stanford Research System in the SIM900 Mainframe. The advantage of the mainframe is that the voltage sources are separate from each other, as

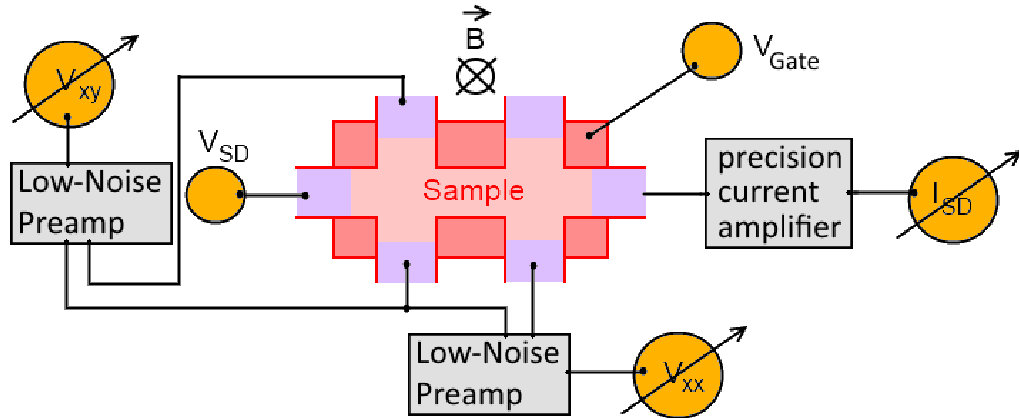

Figure 3.8: Schematics of the electrical setup during measurements.

each is independently floating. Each source is powered by two batteries, one powering the output circuitry while the second battery is being charged or in stand-by. This allows the voltage sources to be free of power-supply ripples. It is important not to introduce ground loops in the measurement setup, as they will introduce noise. Thus it is optimal to introduce only one ground point in the hardware, which is made easy by the individual floating voltage sources. For some measurements, a Keithley 6487 model was used as a voltage source; this can also be used as a picoammeter. A Keithley 238 source measure unit (SMU) was used as either a current source, measuring the voltage at the same time, or as a voltage source, measuring the current. It has a resolution of 100 fA, or 100 μV.

Generally there are several voltages that are in need of being read out simultaneously (see Fig. 3.8). Three 6.5 digit multimeters Agilent 34410A make this possible. They can be combined with two low-noise pre-amplifiers (Stanford research systems model SR560) and one low-noise current amplifier (Stanford research systems model SR570).

3.5 Calibration

Firstly the functionality of the dilution refrigerator, electrical equipment and software needs to verified. It is therefore vital to measure well-known samples before examining new unknown samples, to ensure that previously obtained results with a different system can be reproduced with the newly installed dilution refrigerator. It is important to consider temperature as well as magnetic field dependency in these electrical measurements.

3.5.1 Silicon MOSFET

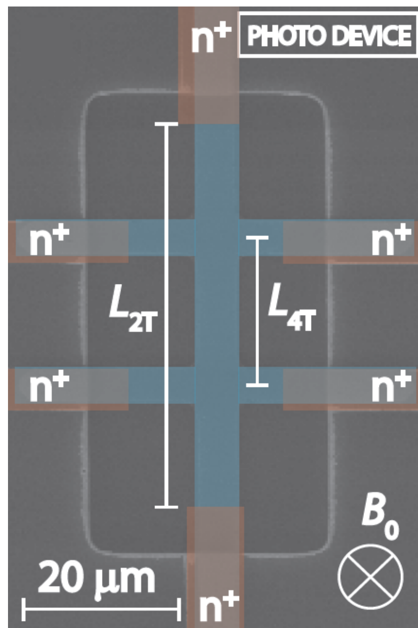

Figure 3.9: Scanning electron micrograph (SEM) of the Silicon MOSFET device, Hall bar defined by photolithography [26].

The first examined device was a Silicon Hall bar MOSFET inserted in the lower sample carrier. The device structure is as shown in Fig. 3.9. It consists of a standard Hall bar design defined by photolithography and a single gate above with a 5 nm thick gate oxide in between. The length to width ratio of the device is $L/W = 19.9\,\mu\text{m}/4.9\,\mu\text{m}$. These measurements were undertaken without additional filters in the probe. The electrical setup was as shown in Fig. 3.8. The gate was controlled via the voltage source V_{Gate} using a separate voltage source of the Stanford Research Systems SIM900 Mainframe. The source drain voltage was controlled via the voltage source V_{SD} provided by another separate voltage source of Stanford Research Systems in the same SIM900 Mainframe. V_{xx} and V_{xy} were the

measured voltages along the source drain current as well as across the channel (with 6 1/2 Digit Multimeters by Agilent 34410A). Both required a low-noise voltage pre-amplifier (Model SR560 by Stanford Research Systems) for better signal to noise ratio. The source drain current I_{SD} was measured with a precision femto-current amplifier. The amplifier gains were all set before each measurement such that the voltmeters showed best resolution without reaching overload. The data was taken and recorded with Matlab which was programmed to control and read out the data from the instruments.

Measurements were taken by stepping a magnetic field B perpendicular to the plane of the sample in the range of $\pm$ 6 T in 0.2 T steps. At each field value the Gate voltage was stepped from 0 V to 1.0 V in 50 mV steps and the source drain voltage swept from -20 mV to +20 mV in 1 mV steps at each Gate voltage step. The dilution refrigerator was kept at base temperature, resulting in a measurement temperature of 169 mK to 155 mK for the duration of this experiment. The results are shown in Fig. 3.10 and 3.11.

This MOSFET structure was chosen for the first measurement because we already had data that was taken at the University of New South Wales (UNSW) of the exact same device. The experiments at UNSW were undertaken in a dilution refrigerator at a reported temperature of 40 mK. (Please note that the temperatures quoted here are those measured by the thermometers at the base of each of the fridges and do not represent the true sample temperature. Nevertheless, the electrical measurements compare well between the two systems.) LockIns were used with an excitation voltage between 100 and 200 μV. The results of the measurements at UNSW are given in Fig. 3.13 and 3.13 and are compared with the data acquired at MU for validation purposes. Comparing the resistivity $\rho_{\text{xx}} = R_{\text{xx}}/(L/W)$ in the top graph of Fig. 3.10 with Fig. 3.12 one notices that the measurements at the University of Melbourne (UM) show slightly higher resistivities. At $V_{\text{Gate}} = 1.0$ V we measured 1860 Ω at UM, while 440 Ω was recorded at

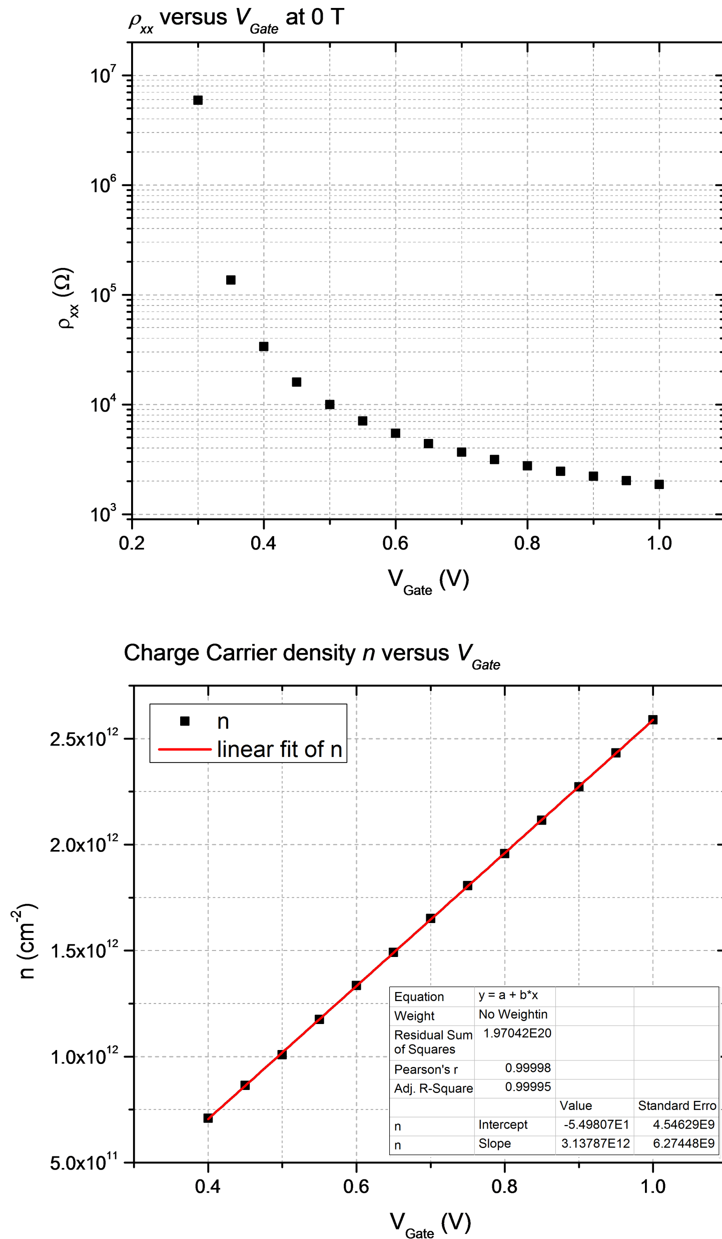

Figure 3.10: Experimental results of the silicon MOSFET DRD1 taken at the University of Melbourne (UM) at ca. 160 mK. Top: Resistivity ρ_{xx} versus gate voltage V_{Gate}. Bottom: Charge carrier density n versus gate voltage V_{Gate} including the linear fit in red.

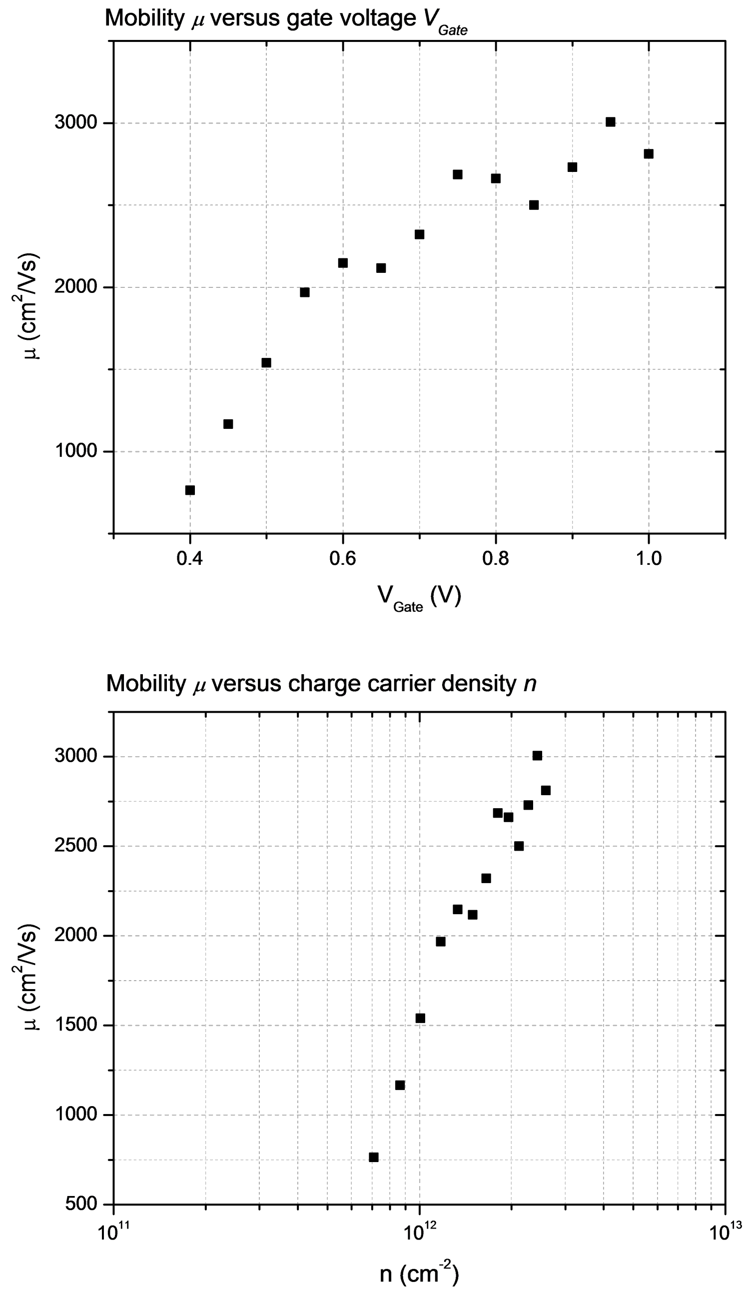

Figure 3.11: Experimental results of the silicon MOSFET DRD1 taken at the University of Melbourne (UM) at ca. 160 mK. Top: Mobility μ versus gate voltage V_{Gate}. Bottom: Mobility μ versus Charge carrier density n.

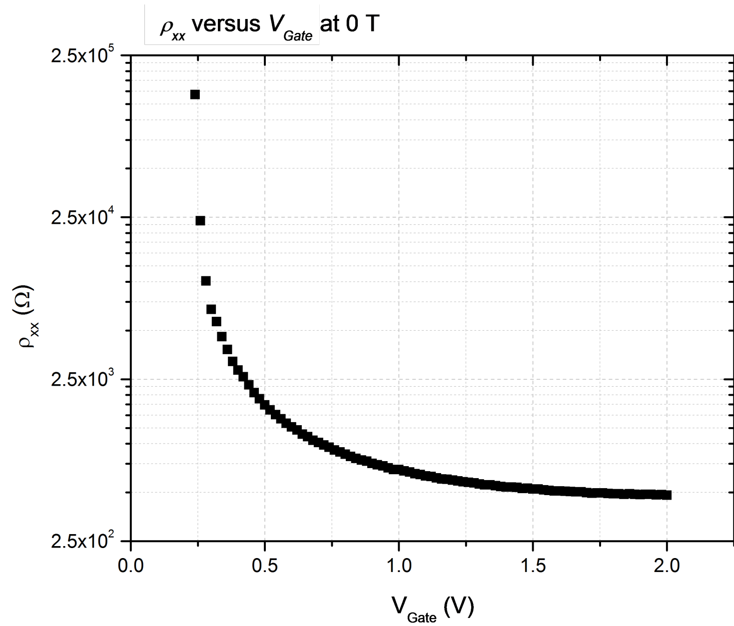

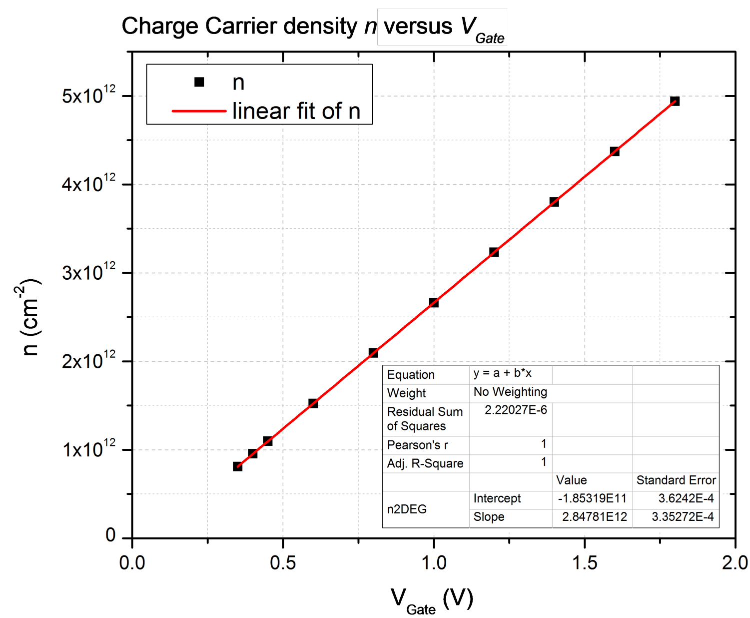

Figure 3.12: Si MOSFET measured at UNSW at ca. 40 mK. Top: Resistivity ρ_{xx} versus gate voltage V_{Gate}. Bottom: Charge carrier density n versus gate voltage V_{Gate} including the linear fit in red.

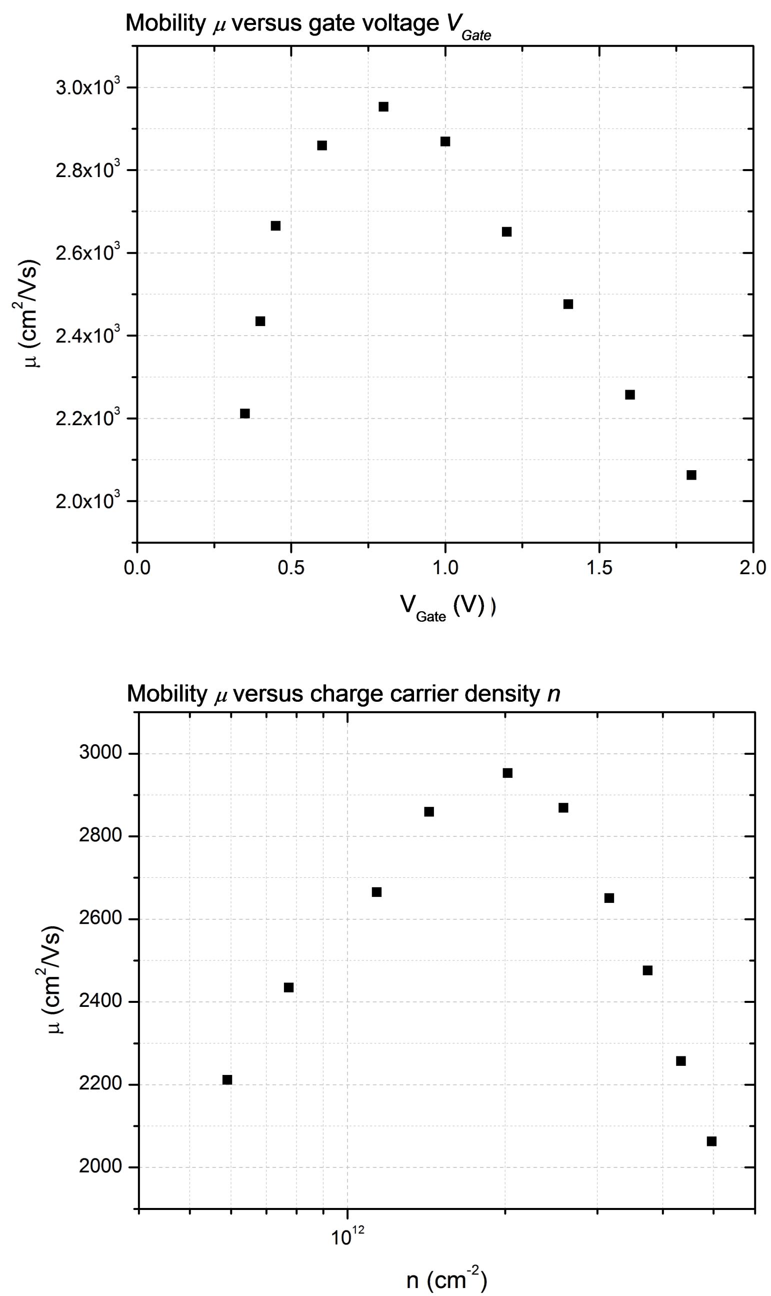

Figure 3.13: Si MOSFET measured at UNSW at ca. 40 mK. Top: Mobility μ versus gate voltage V_{Gate}. Bottom: Mobility μ versus Charge carrier density n.

UNSW. The gate voltage characteristics for the two data sets follow the same trend. The dependen The lower graphs of Fig. 3.10 and Fig. 3.12 display the charge carrier density n versus the gate voltage V_{Gate}. The fitted slopes of $3.14 \cdot 10^{12}\text{cm}^{-2}$ at UM versus $2.85 \cdot 10^{12}\text{cm}^{-2}$ match very well. From these values the oxide thickness can be derived. The mobility μ versus V_{Gate} is displayed in the top of Fig. 3.11 and Fig. 3.13. The graphs are very similar to each other regarding values and trends. The bottom graphs show the mobility versus the charge carrier density in a half logarithmic plot. Again, the data is very similar with only minor discrepancies in the values, confirming the reliability of the setup at UM.

In addition, we performed magnetic field dependent measurements. The voltage along the source drain channel is expected to show Shubnikov de Haas oscillations at higher magnetic fields. At the same time the voltage obtained across the source drain channel is expected to show Hall plateaus when plotted versus the magnetic field (see [132, 142] for the quantum Hall effect (QHE)). The data in Fig. 3.14 was taken from the same device DRD1. The black data refers to the left axis and shows the resistivity of the sample across the source drain channel, whereas the red curve refers to the right axis and shows the resistivity of the sample along the source drain channel. As expected oscillations are observed from ± 3 Tesla onwards in the red curve. The plateaus in the R_{xy} curve are not very prominent though. In order to prevent eddy current heating, this measurement was not performed as one continuous sweep. Instead, it consisted of first measuring from -6 T to 0 T, then from + 6 T to 0 T.

In summary the data taken from the Silicon MOSFET devices at the system at UM is comparable to the data taken at UNSW. Both systems produced very similar data. The values are not exactly the same due to some conditions being slightly different and differing equipment being used (as in DC measurements at UM versus AC measurements at UNSW), but

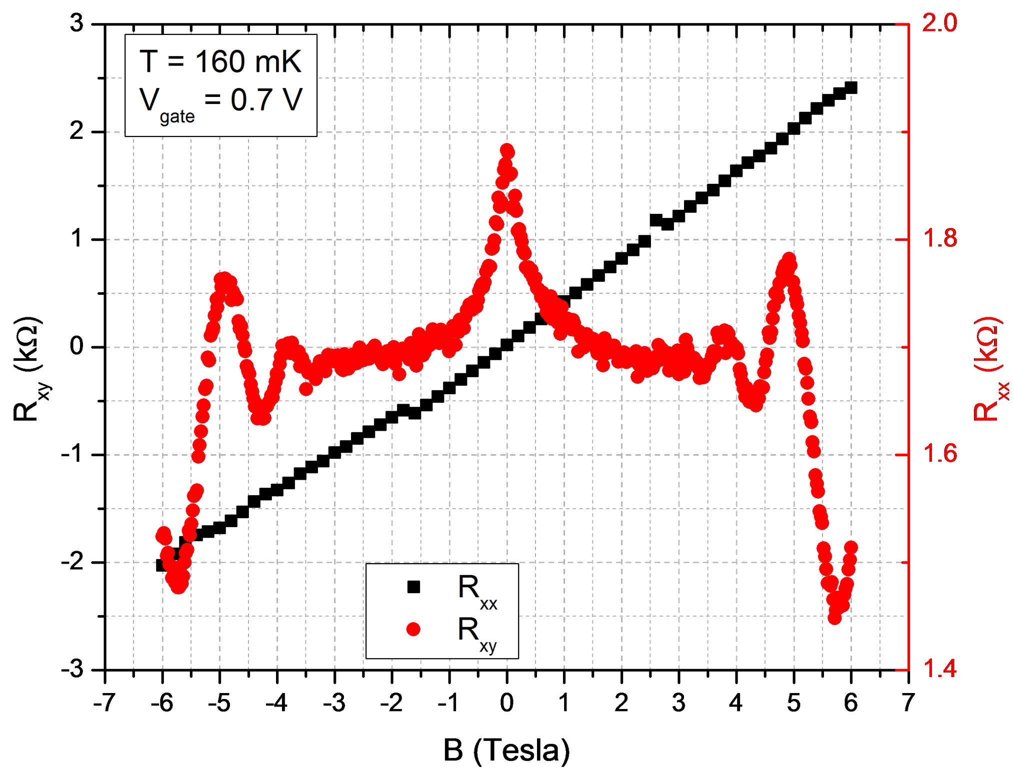

Figure 3.14: Resistivity versus magnetic field of Silicon MOSFET device DRD1 measured at 160 mK with a gate voltage of 0.7 V. The left axis, black, is the resistivity across the device channel. The right axis, red, is the resistivity along the channel.

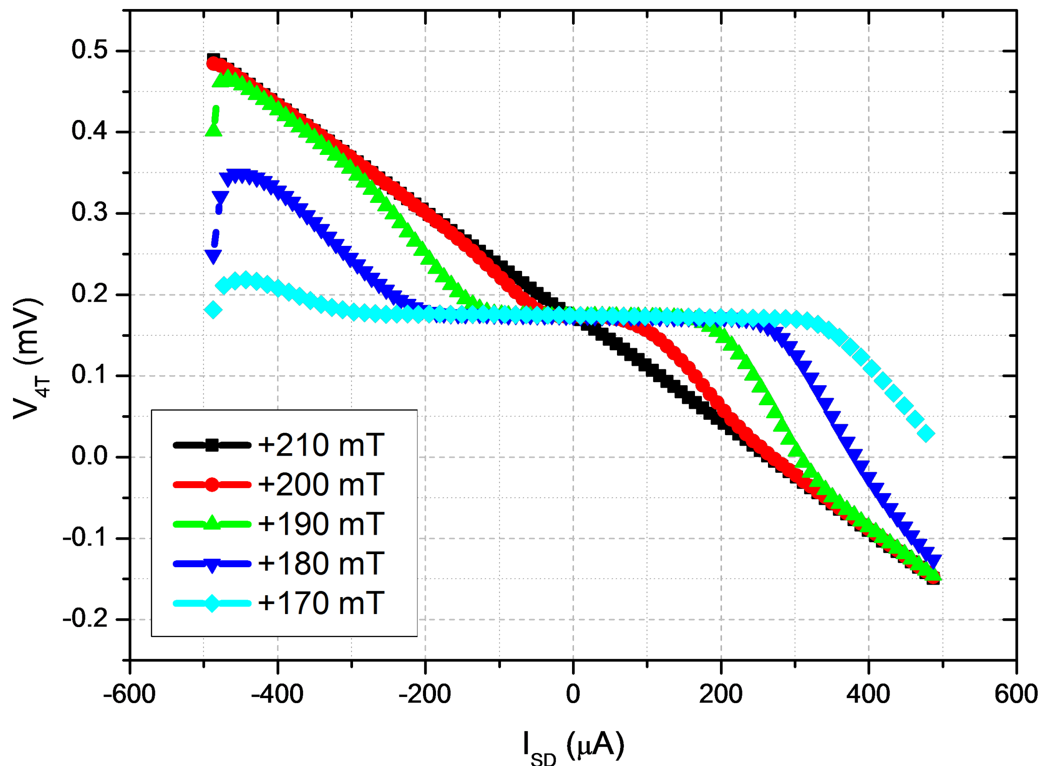

Figure 3.15: Four terminal voltage versus source drain current of a 120 nm thick Al Hall bar at varying magnetic fields perpendicular to the plane of the sample at 0.26 K.

they are definitely close enough to say that the system in UM shows reliable results.

3.5.2 Aluminium films

The dilution refrigerator was tested with a current source for superconducting experiments. Aluminium, a type I superconductor, was the material used for this purpose. It is a well known material with the critical superconducting temperature of bulk Al at 1.2 K [143]. The used substrate for these samples was an non-conducting silicon oxide on silicon wafer. Hall bars of varying

sizes were fabricated using photolithography. A 120 nm thick layer of Al was deposited on the substrate.

Thin films have different properties from bulk metals. This reduces the critical temperature and raises the critical magnetic field for observing superconductivity [144]. Fig. 3.15 shows the four terminal voltage versus source drain current of one Al Hall bar at varying magnetic fields perpendicular to the sample at temperatures from 170 mT to 210 mT. The flat area around zero source drain current corresponds to a zero Ohm resistivity for a fixed magnetic field; the sample is superconducting. Once the critical current is reached, the sample starts to behave metallic again. The critical current of a superconductor is the current that will produce the critical magnetic field at the surface of the same [145]. So the higher the surrounding magnetic field, the lower the critical current. From this graph one can extract the critical current dependency on the magnetic field. In summary, the aluminium sample behaves just as expected.

3.5.3 Niobium SQUID

In order to continue the verification and to build more confidence in the functionality of the electrical setup, a niobium superconducting quantum interference device (SQUID) was examined. With this device we can search for possible offsets of the 3D vector magnet in either of the 3 dimensions and thus calibrate the magnet for offsets. The Nb SQUID should show superconductivity at low temperatures which is broken by either a small current I_C or a small magnetic field B. As already mentioned, Nb has a relatively high critical temperature making it unnecessary to go to the base temperature of the dilution refrigerator. The measurements were therefore taken without the ^{3}He/^{4}He mixture in circulation, using only the He compressor to cool down the system, achieving a sample temperature of around 5 Kelvin. The temperature depends slightly on the amplitude of the applied current and

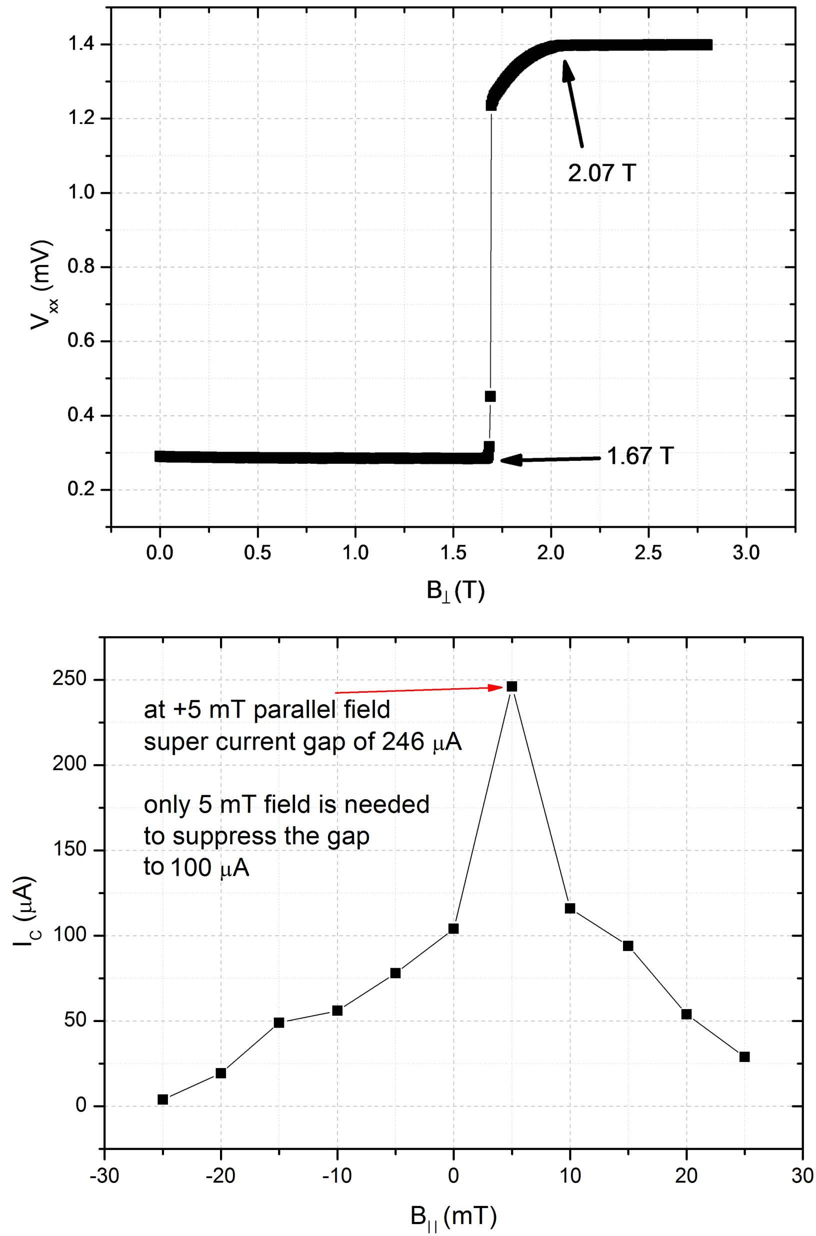

Figure 3.16: Results of Nb SQUID in the upper sample carrier with a perpendicular magnetic field at ∼5 K. Top: Voltage versus magnetic field with constant source-drain current of 2 mA. Bottom: Critical current versus parallel magnetic field.

magnetic field, as the system's temperature is affected by Joule heating by I^2R.

The results are presented in Fig. 3.16. In the top graph, the voltage is plotted versus the perpendicular magnetic field while a constant source-drain current of 2 mA is applied at a temperature of about 5 K. There is an obvious jump at 1.67 T from ~0.3 mV to ~1.2 mV. This is due to the magnetic field being high enough at the given source-drain current to break up the superconducting state of the sample. This is the so-called critical magnetic field. It depends on the temperature as well as the source-drain current of the sample. This clear jump in a definite indicator for the observation of superconductivity. By taking measurements of voltage versus current at varying magnetic fields, we can extract the critical current I_C for each field value at which the superconductivity is broken up. This was also undertaken for the magnetic field parallel to the plane of the sample. The lower graph of Fig. 3.16 shows this critical current versus the parallel magnetic field. Here it is clear that the critical current is at its maximum at a field value of +5 mT, dropping down rapidly for higher as well as lower magnetic fields. From this we conclude that an offset of +5 mT within the z-coil of the magnet was observed during this measurement. This offset is most likely caused by flux trapping [146, 147] and thus is not a fixed value. The amplitude of the offset within the superconducting coil depends on the history of previous applied currents.

In order to test the vector magnet by superimposing all three coils, we rotated the field in the x- and y-coils while applying a constant field of 1.6 T in the z-direction and measuring the sample in the upper carrier (z-direction is in plane with the sample). During this test the temperature is ~5 K and a constant source-drain current of 1 mA is applied. The overall magnetic field value in the x-y plane has a constant amplitude of 0.1 T, calculated by adding the vectors of B_x and B_y. At zero degree rotation B_x is 0.1 T while B_y is 0 T. The resulting source-drain voltage is shown versus the field angle in Fig.

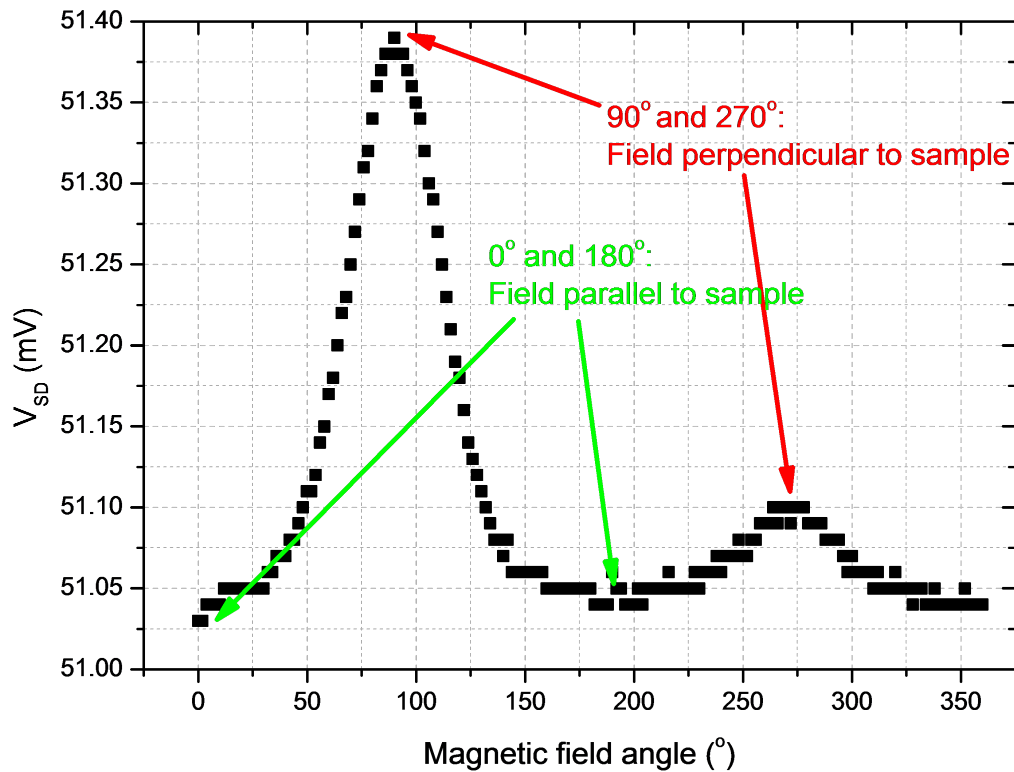

Figure 3.17: The Nb SQUID measured in the upper sample carrier in a rotating magnetic field of the x and y coils. The graph shows source-drain voltage versus field angle with a constant source-drain current of 1 mA at ∼5 K. At all times is the vector sum of B_x and B_y 0.1 T, while a constant B_z of 1.6 T is applied.

3.17. We can see how the voltage is at its minimum at 0° as well as 180°, which corresponds to the magnetic field being parallel to the sample plane. The maxima are at 90° and 270°, respectively. These are the rotation angles where the magnetic field is perpendicular to the sample. We note that the two maxima have very different amplitudes. The cause is uncertain but may be due to flux trapping in the Nb SQUID itself as we did not use magnetic shielding during the measurement. This measurement makes it clear that we are capable of applying a magnetic field in any wanted direction using the inbuilt 3D vector magnet. We are able to program the magnetic field to do rotations in any wanted direction.

3.5.4 Summary

The dilution refrigerator unit was successfully installed. Currently direct optical access is not available, as not all vacuum cans have a quartz window in place, but are instead blanked off with metal. However, we can conclude from the experiments described above that the equipment as well as the attached electronics are functioning properly. The various examined samples had differing properties, and the results of their characterizations agree with the expected values and tendencies. A slight offset in the z-direction of the magnet by 5 mT was observed. Since the cause of this field offset is most likely flux trapping, the value will vary for every experiment run.

Chapter 4

Fabrication

In this chapter the fabrication of nitrogen enhanced CVD grown diamond as well as erbium doped silicon devices is described. Details include the various methods and techniques used, such as chemical vapour deposition, photo lithography, etching techniques, and various high temperature treatments. First the creation of diamond devices is outlined, some methods overlap with the silicon device fabrication explained later.

4.1 Diamond Hall bar device fabrication

The process sheet for the creation of nitrogen enhanced grown UNCD Hall bars is given in Table 4.1 and Fig. 4.1 illustrates some of the steps involved. The first step was to grow the N-UNCD layer (Table 4.3) on the substrate (step 0). Then this layer was shaped into a Hall bar (step 1) via optical lithography (Table 4.4), followed by dry etching (Table 4.5). After the photolithography and development, a chromium (Cr) layer that acts as a hardmask for the etching process by protecting the grown N-UNCD film in the Hall bar area only, was deposited. Following this the now disposable Cr was removed with a wet etch (Table 4.6). The next step was to define the ohmic contacts of the Hall bar (step 2) via another optical lithography step.

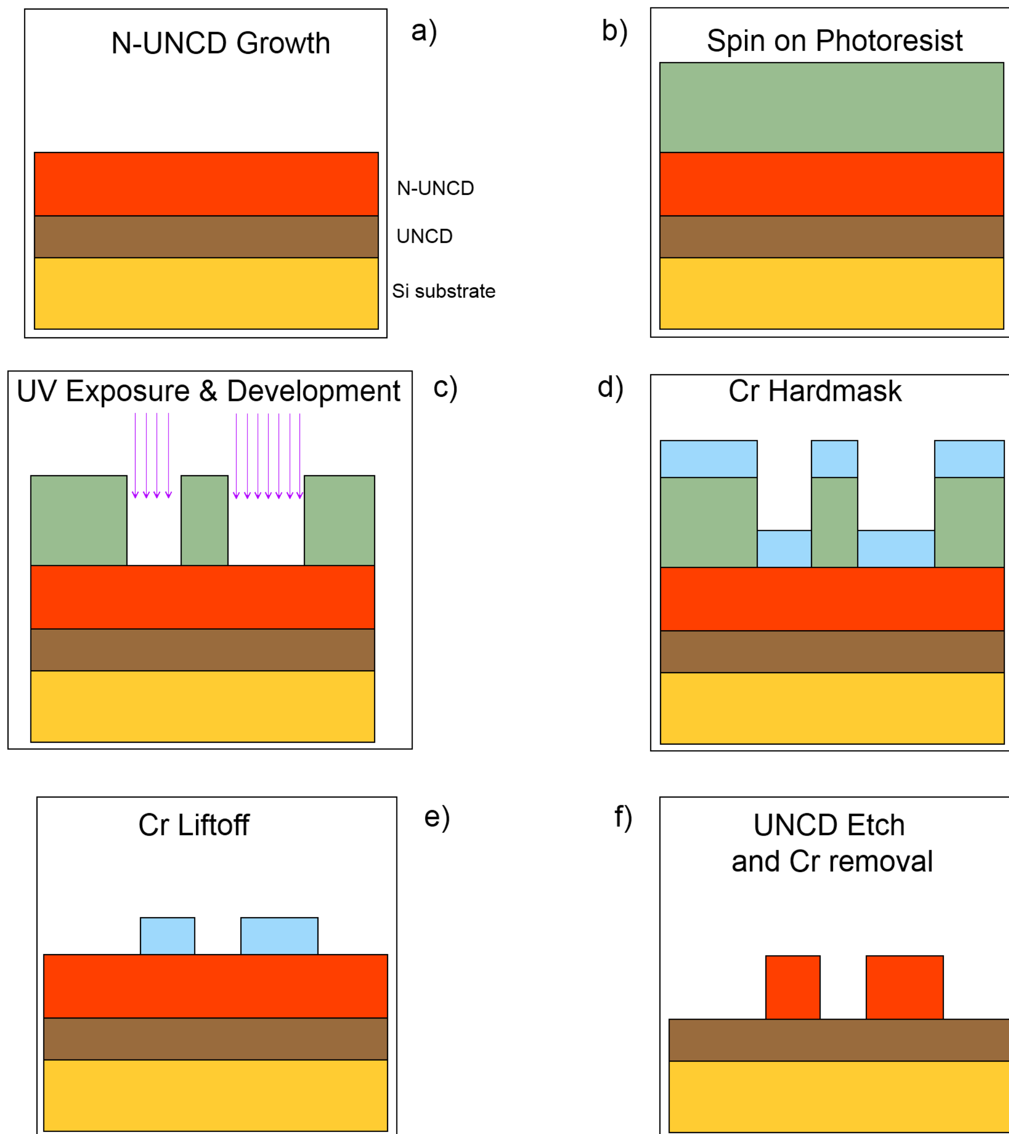

Figure 4.1: Steps involved with optical lithography. In this case positive photoresist (green) is used as well as a Cr hard mask (blue) to protect the sample surface (red).

	Step	Details
0	N-UNCD growth	Grow N-UNCD using CVD (Table 4.3).
1	Define Hall bar	With photo lithography (Table 4.4): - Deposit 250 nm thick Cr. - Lift-off in acetone to remove PR and create Cr hard mask. - Etch structure into UNCD (Table 4.5). - Remove remaining Cr (Table 4.6).
2	Define ohmic contacts	Photo lithography (contacts mask): - Deposit Ti/Au 20/100 nm thick. - Lift off with acetone to remove PR and metal in unwanted areas.
3	Prepare for measurements	- Cut chip into (5x5) mm squares. - Glue device into sample carrier. - Wire bond contacts.

Table 4.1: Process flow for N-UNCD Hall bar fabrication.

The ohmic contacts consist of a titanium/gold (Ti/Au) layer of 20 nm/100 nm thickness. Lastly, the Hall bars were made to fit into the chip carriers in which they will be examined (step 3) by cutting them into a maximum size of 5 mm $\times$ 5 mm squares and glueing them into the chip carriers. All contacts were connected to the carrier via aluminium wire bonding.

For the purpose of structuring these devices, a mask was designed to be used with the mask aligner for optical lithography. The mask makes it possible to create 5 different designs. The sizes of the four largest are shown in Fig. 4.2. Red represents UNCD, yellow the gold contacts, and green is the overlapping area of UNCD and gold. The dimensions of these four designs are given in Table 4.2. All designs had roughly the same sized contact pad of 110 μm $\times$ 110 μm to which the wire would be bonded. This size was chosen to be big enough to ensure bonding onto it was possible. The

Design	Width (μm)	Length (μm)	Width/Length
a)	754	772	0.98
b)	400	400	1
c)	80	400	0.2
d)	40	400	0.1

Table 4.2: Dimensions of the four designs given in fig 4.2.

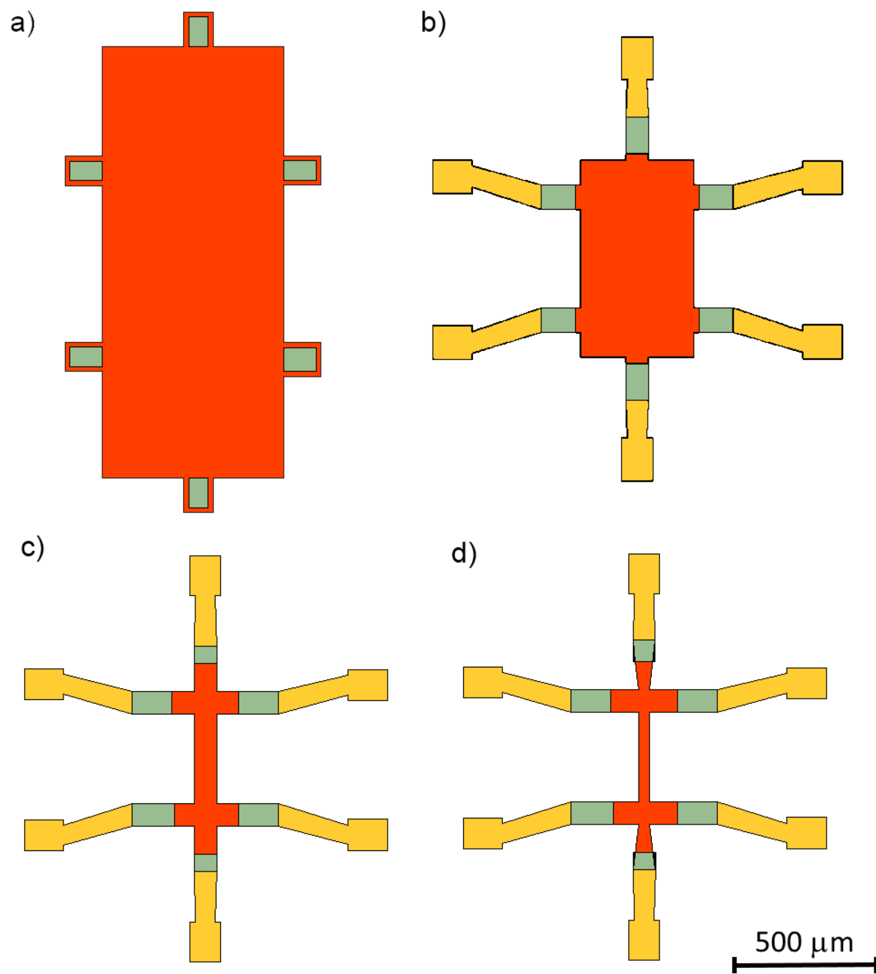

Figure 4.2: Sketch of the four Hall bar designs on the available mask.

designs have 6 contacts each. Two form the source and drain and were used to send a current through the length of the sample (the top and bottom as shown in Fig. 4.2). The other four contacts allowed us to measure across the width of the sample, as well as parallel to the source and drain contacts along the length of the sample. This four-terminal sensing method allowed us to measure with almost no voltage drop occurring in the voltage leads, as the current leads - where according to Ohm's law a voltage drop is experienced - were kept separate. This results in a more accurate voltage measurement than when a two-terminal technique is used (combining voltage and current leads) as the contact resistance is there included in the output, but this was eliminated by performing four-terminal measurements.

4.1.1 CVD growth

The N-UNCD layer was grown in the microwave assisted plasma chemical vapour deposition (CVD) reactor at Melbourne University. Since we intended to electrically characterize these samples, we chose to deposit the N-UNCD layer to be examined on an electrically insulating layer of undoped UNCD with a thickness of 1 μm. This insulator was situated on a 1 μm thick silica layer on top of a boron doped silicon wafer of 0.01 - 0.02 Ωcm resistivity (see Fig. 4.3). The substrate wafer (aqua-25 series) was purchased from www.thindiamond.com (UA25-100-1-1). It had a smoothness of < 10 nm rms and a small grain size of (3-5) nm. This substrate did not require any seeding prior to the growth of N-UNCD and ensured a smooth and even growth of N-UNCD.

Figure 4.3: Structure of the substrate wafer used for N-UNCD processing.

Growth conditions for	20% N-UNCD	10% N-UNCD	5% N-UNCD
Argon flow	79 sccm	99 sccm	38.9 sccm
Methane flow	1 sccm	1.1 sccm	0.4 sccm
Nitrogen flow	20 sccm	11 sccm	2.1 sccm
Net gas flow rate	100 sccm	111.1 sccm	41.4 sccm
Microwave power	1250 Watt	1250 Watt	1250 Watt
Chamber pressure	80 Torr	80 Torr	80 Torr
Temperature	800 °C	800 °C	850 °C
Growth time	3 hours	3 hours	5 hours

Table 4.3: Recipe for microwave assisted CVD grown UNCD with 20%, 10%, and 5% nitrogen doping.

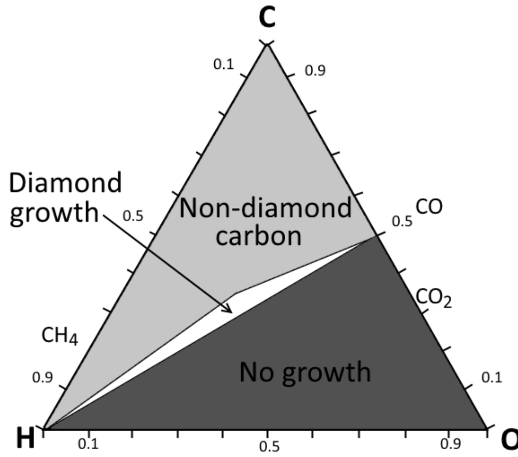

Figure 4.4: Simplified C-N-O diamond deposition diagram according to [28]. The light grey area shows the region of non-diamond growth, the dark grey area marks the region of no growth and the white area represents the region of successful diamond growth.

With the growth method we chose to use, the energy required to initiate CVD reactions is provided by a plasma discharge. It is necessary for CVD to have a gaseous precursor that will decompose on the heated substrate surface. The gas pressure and microwave power determine the rate, purity, crystallinity, uniformity and other properties of the grown films [149]. The composition of the gas determines the resulting film. The C-H-O phase diagram by Bachmann et al. [28] defines the region of successful diamond growth [149] with the ratios

of the elements C, H, and O. A schematic of the phase diagram is shown in Fig. 4.4.

For step a) in Fig. 4.1 we used the recipe outlined in Table 4.3. The gas composition was 79% argon, 1% methane, and 20% nitrogen for the 20% nitrogen enhanced grown N-UNCD films. For 10% and 5% nitrogen enhanced grown N-UNCD films we changed the argon, nitrogen and methane flow rates to achieve an overall nitrogen content of 10% and 5% in the gas feed stock. During the growth the sample stage was heated to a minimum of 800 °C, the microwave power was 1250 Watt and the pressure was kept at a constant 80 Torr for all three growths. The growth time of three hours resulted in an approximately (1 - 1.5) μm thick N-UNCD layer with an overall gas flow rate of about 100 sccm. The 5% N-UNCD was grown for a longer period due to a lower overall gas flow rate - the gas flow was restricted by the set-up of the valves via which the gases were connected to the system.

4.1.2 Optical Lithography

The as N-UNCD obtained detailed above was shaped into Hall bars using optical lithography. The steps involved were similar to the steps shown in Fig. 4.1. In this process a layer of photoresist is deposited on a sample, using the spin-on technique. Depending on the photoresist used and the recipe used for spinning it on (spin speed and time), the thickness will be around 4 μm thick. Following this, the sample is exposed through a mask to ultra violet light from a mercury lamp, to which the photoresist reacts. The next step is to develop the sample. Positive photoresist was chosen, so the exposed parts of the photoresist could be removed later. Now it could be used as a mask to etch into the exposed material, or to deposit material onto the exposed parts of the sample, as illustrated in Fig. 4.1 d). Finally the photoresist was removed with an acetone lift-off. The exact parameters of the photo lithography are given in Table 4.4. Prior to the procedure the sample was cleaned in an acetone bath and with an oxygen plasma cleaner

Photoresist AZ1514H	5000 RPM	60 s
Prebake	95 °C	60 s
Exposure	through mask	15 s
Development	826 MIF	15 s

Table 4.4: Optical lithography recipe with photoresist AZ1514H and developer 826MIF.

at 35 sccm, 25 Watt for 2 minutes. A clean sample surface ensures an even layer of photoresist which enables a clean transfer of the mask pattern. After the sample was cleaned, the photoresist AZ1514H was spun on with a spin coater (step b) in Fig. 4.1). The top speed of 5000 RPM was held for 60 seconds. Following this the photoresist was pre-baked at 95 °C for 60 seconds on a hot plate. Then the mask aligner was used to align the mask onto the sample and expose the photoresist to UV light for 15 seconds. After this the resist was developed for 15 seconds using the developer 826MIF (step c) in Fig. 4.1). A thorough rinsing with deionised water (DI) is vital to ensure that the developer is completely removed from the sample. After rinsing, the sample was dried and exposed to an oxygen plasma for 2 minutes with a power of 30 W and gas flow rate of 30 sccm, to remove any photo resist left over prior to the next step.

4.1.3 Metal deposition

The deposition of metals onto a substrate was done via a thermionics electron beam (E-beam) evaporator as shown in Fig. 4.5. In this process, the material in which the sample is to be coated is placed in a crucible of appropriate material (mostly graphite or inter-metallic (boron nitride)). A current is then applied to a hot filament which produces an electron beam that is directed at the evaporation material through a permanent magnet. The chamber has to be at pressures of less than 5×10^{-5} mbar to increase the mean free

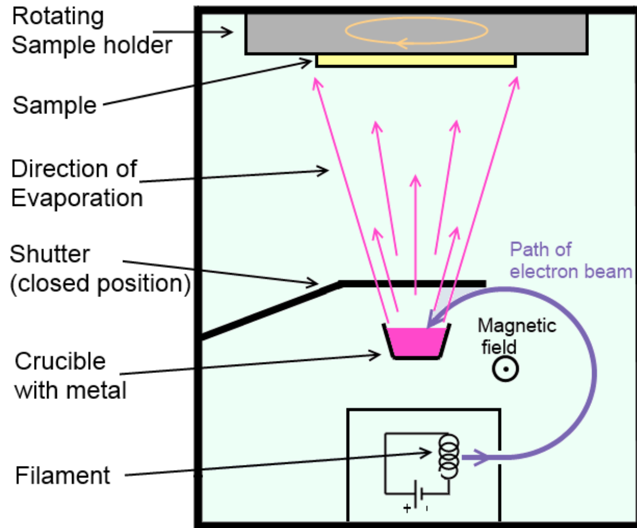

Figure 4.5: Electron beam evaporation chamber showing the hot filament (bottom), the path of the emitted electron beam as directed by a magnetic field, the crucible, and the direction of the evaporation. The shutter is shown in the closed position. The sample holder (top) is able to rotate horizontally.

path and thereby ensure that the electrons don't scatter but are allowed to reach the target. When the electrons strike the evaporation material they lose their energy. Most of their kinetic energy is transformed into thermal energy, causing the evaporation material to heat up. This electron beam intensity needs to be high enough to bring the temperature of the evaporation material up to deposition temperature, resulting in a vapour. Now the metal is deposited on the sample until the desired thickness is reached. To ensure an even coating the sample is slowly rotated on the sample holder during the process. Between the crucible and the sample is a manual shutter. Before opening it, the evaporation material is held at the deposition temperature for a couple of minutes to ensure any oxide compositions evaporate first and do not deposit on the sample. Only after this can the shutter be opened and the sample exposed to the vapour.

The deposition rate is monitored in situ with a quartz crystal. It oscillates at a resonance frequency which is dependent on its thickness as well as its mass, which will change with material being evaporated on it. If certain

frequencies of voltages are applied, a very sharp electro-mechanical resonance is observed. This technique enables us to measure a deposited thickness of less than an atomic layer.

The electron acceleration is controlled by the voltage between filament and target, on which the deposition rate depends. The current through the filament controls its temperature, which also controls the emission current. The faster the deposition rate, the rougher the deposited layer will be due to the tendency for particles to be ejected at higher temperatures. As soon as the desired thickness is reached, the shutter is closed and the electron beam turned off.

A 300 nm thick chromium layer was deposited on top of the sample using this technique (step d) in 4.1). This layer was to be used as a hard mask for the following diamond etch. A good choice of material for the hard mask needs to have a low etch rate compared to UNCD, be easily deposited on the sample and adhere well enough to ensure a clean lift off, plus be easily removable after it is no longer needed. If the chromium layer is too thin, it will be etched through in the UNCD etch step. If it is too thick, it will be hard to lift it off cleanly. We found that 300 nm provided a good balance between these extremes.

4.1.4 Lift off

The chromium deposited onto the photoresist is 'lifted off' by placing the sample in an acetone bath, step e) in Fig. 4.1. The acetone dissolves the photoresist and subsequently removes the metal layer on top of the photoresist. If needed, an ultrasonic bath can aid in the lift off process. The photoresist is harder to remove if the sample has previously been post baked after developing the photoresist. This is the reason why we refrained from post baking, even though generally that step is practised as it hardens the photoresist and makes it unresponsive to UV light and consequently easier to handle the sample.

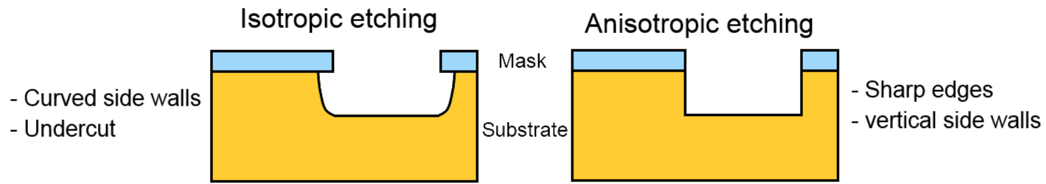

Figure 4.6: Isotropic (left) versus anisotropic etching (right).

4.1.5 N-UNCD Etch

There are various etching techniques that can be applied. When etching with a mask, isotropic etching can occur. This means that the side walls are curved and undercut the masking layer. Anisotropic etching on the other hand results in sharp, vertical side walls (see Fig. 4.6) [150]. Dry etching uses a plasma phase as etchant. The etch is controlled by changing the parameters such as the gas composition, pressure, power, and temperature. This is an isotropic etch since it is done by free radicals of the plasma attacking the surface where they react.

Parameter	Value
O_2	50 sccm
SF_6	5 sccm
RIE power	200 W
ICP power	2500 W
Pressure	9 mTorr
Temperature	16 °C

Table 4.5: Parameters for N-UNCD etch recipe.

Deep reactive ion etching (DRIE) has a smaller lateral than downward etch rate because the gas is accelerated downwards onto the sample. Some RIE systems use a combination of parallel plate and inductively coupled plasma (ICP). Here, the ICP creates a high density plasma with a magnetic field powered by radio frequency, which is utilized as the ion source. A higher ICP power will result in a higher etch rate. The parallel plate on the other hand creates electrical fields near the substrate, leading to more anisotropic etch profiles. Such a system was used in this project to etch diamond: the Plasmalab System 100 ICP 380 by Oxford Instruments.

Quantity	Chemical	Formula
8.29 g	Ceric ammonium nitrate	$(NH_4)_2[Ce(NO_3)_6]$
2.2 mL	Perchloric Acid	$HClO_4$
50 mL	DI Water	H_2O

Table 4.6: Chromium etchant recipe.

As diamond is such a hard material, it is not easy to etch. *Advanced Diamond Technologies* has published a recipe on their website *www.thindiamond.com* designed for etching UNCD. Using this as a guide and the DRIE etch at MC^N the recipe in Table 4.5 was established. A flow of oxygen and SF_6 was used to create carbon oxides with the UNCD substrate, thus destroying the diamond structure. The flow rates, RIE power, the ICP (inductively coupled plasma) power, and chamber pressure are listed in Table 4.5. Etch tests showed this recipe to etch through the 1 μm of UNCD plus 1 μm of N-UNCD in about 3 minutes and 40 seconds if the machine had been warmed up by previous etch processes. If the DRIE etch machine had not previously been used, the etch rate was slightly slower. In the 3 minutes and 40 seconds the 300 nm thick chromium layer was not yet fully etched through: a small layer was still protecting the N-UNCD in the masked off regions (step f) in Fig. 4.1).

4.1.6 Chromium removal

The remaining chromium was removed with a chemical wet etch (step f) in Fig. 4.1) which does not affect the UNCD. The recipe for the chromium etchant is given in Table 4.6 and can be found at *www.microchemicals.eu*. The etch rate is approximately 60 nm per minute at room temperature. More information regarding chromium etching can be found in [151]. After the chromium removal the samples were thoroughly rinsed in deionized water

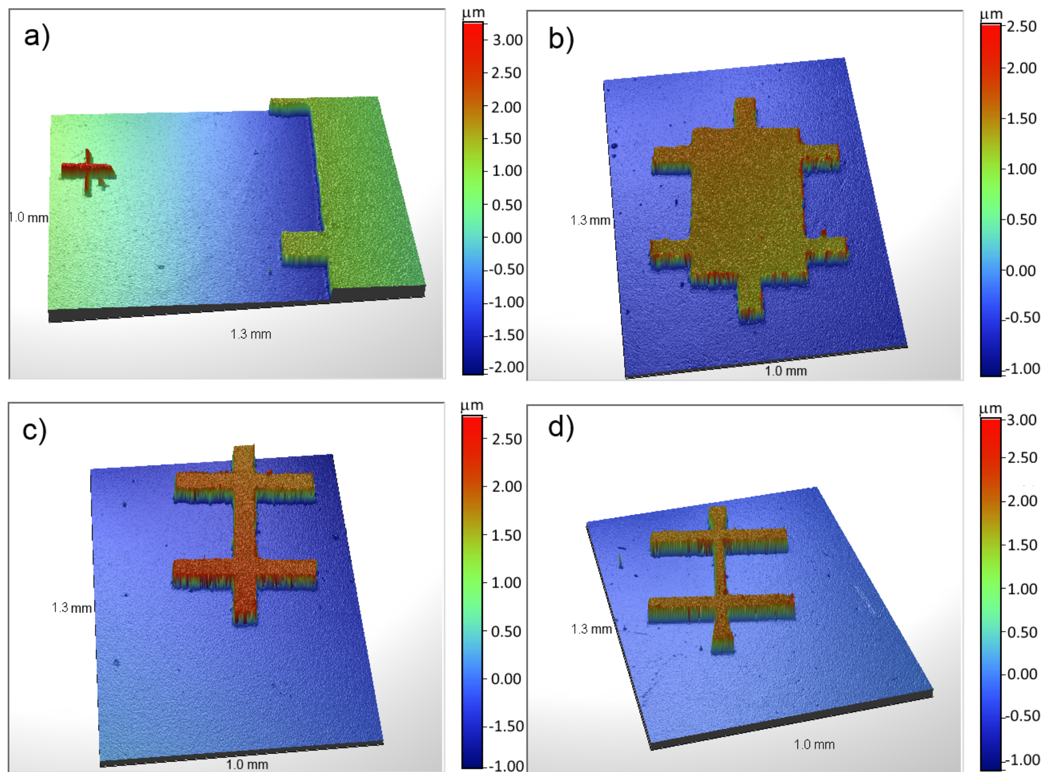

Figure 4.7: Optical pictures of the four different Hall bar patterns before the electrical contacts were created. a) Shows the largest Hall bar structure with alignment markers on the left (only partially shown due to the limited size of the field of view of the optical profiler); b), c), and d) are the other three devices according to Fig. 4.2.

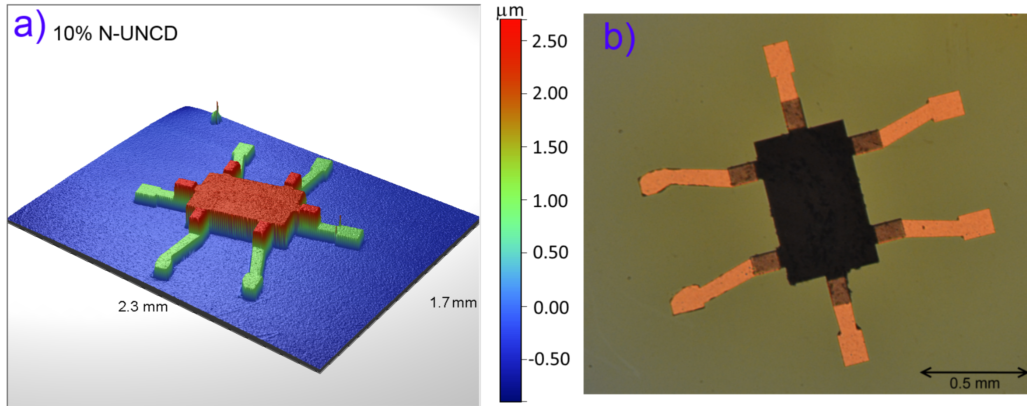

Figure 4.8: Two optical pictures of the same sample of the second Hall bar design. a) is taken with the optical profiler. b) is taken with a conventional microscope using an objective with 5x magnification. The gold contacts are visible on top of the N-UNCD material on the Si substrate.

before proceeding. The current N-UNCD Hall bars looked as shown in Fig. 4.7 for the structures a) to d) from the mask in 4.2.

4.1.7 Deposition of ohmic leads

Now that a Hall bar structure had been successfully created out of the N-UNCD material, the contacts of the Hall bar needed to be made accessible (step 2 in Table 4.1). This was done with another step of optical lithography similar to the first. Because some of the structures were so small that it was not possible to directly bond to the 'arms' of the Hall bar, the second mask fanned out to contact pads which were big enough to allow wire bonding. The mask is shown as the combination of yellow and green areas in Fig. 4.2. Using the same recipe as previously described in section 4.1.2, the photoresist was spun on the samples, exposed, and developed. Following this the samples were directly transferred into the electron beam evaporator in order to cover them in a 20 nm thick layer of titanium, immediately followed by 100 nm of gold. It is vital that the metal used for the contacts forms an

ohmic connection (linear I-V characteristic) to the N-UNCD film, so a metal with appropriate work function must be used. The chosen metals titanium and gold had been used by Jeedigunta et al. [152] and found to create ohmic contacts. Titanium is electrically conducting and it has good adhesion properties to UNCD as well as silicon. Unfortunately titanium oxidises at air, so it was sealed with a layer of gold. Gold is also electrically conducting, adheres well to titanium, does not react to air and therefore keeps its conducting properties. It can easily be wire bonded provided it has a minimum thickness of approximately 40 nm. Figure 4.8 shows optical pictures of a completely fabricated sample. Fig. 4.8 a) was taken with the optical profiler and shows the depth profile as well as the lateral dimensions. Fig. 4.8 b) was taken with a conventional microscope and a 5x magnification objective. The sample pictured in these images has the second Hall bar design.

After the two metal layers are deposited the sample is transferred to an acetone bath to lift off the metal in the unwanted areas. Once this is completed, the samples are finished and only need to be made compatible for measurements in the dilution refrigerator by placing them in the appropriate sample carriers and creating the electric connections between the sample and the sample carrier.

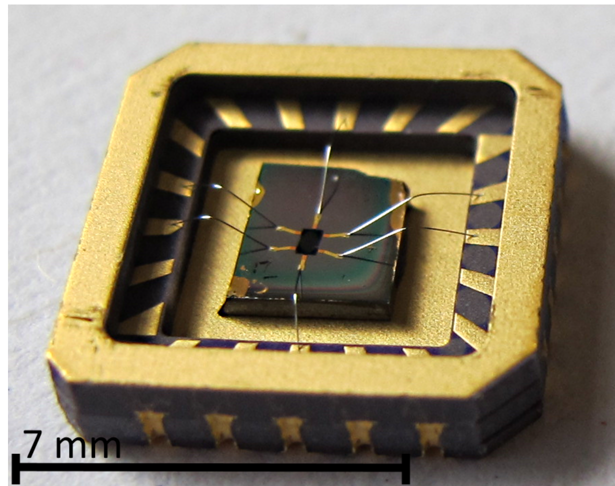

Figure 4.9: Photograph of a finished diamond device wire bonded to the sample carrier it is glued into.

4.1.8 Wire Bonding

The sample needs to be less than 5 × 5 mm^2 in order to fit into the sample carrier. It is held in place by Japanese Cemedine brand epoxy. A photograph of a fabricated diamond device sitting in its sample carrier is shown in Fig. 4.9. The electric connections between the Hall bar contacts and the sample carrier are made via wire bonding. An aluminium wire of 25 μm diameter is used with a semi-automatic wire bonder. As the wire must be lightly pushed down for it to stick to the contacts, the wire is slightly flattened and widened. This determines the size of the ohmic contacts, which need to be a minimum of 50 μm^2 or larger. Once all 6 ohmic connections are made the sample is ready to be measured in the dilution refrigerator.

4.2 Silicon device fabrication

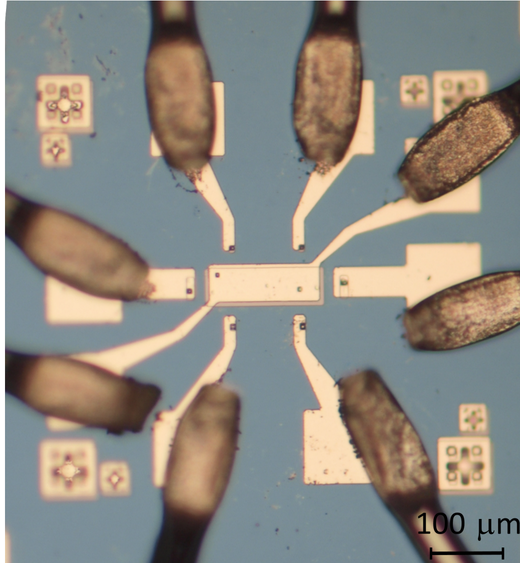

Figure 4.10: Optical image taken with a microscope of a bonded up device.

Similar to the N-UNCD devices, the silicon devices needed to be created and shaped into samples that could be electrically characterized in the dilution refrigerator. The process flow first developed used equipment at Melbourne University (MU) only, plus ANU for implantations (MU devices). Later, due to issues with contamination by foreign matter in the gate oxide introduced during fabrication using equipment at MU, the process flow was further developed and adapted for equipment available at the University of

New South Wales (UNSW). The following paragraphs detail the MU and UNSW devices separately. They briefly list the process flow of both MU and UNSW devices, describe the purpose of the chosen device designs, and explain in detail the steps involved in sample fabrication. More emphasis is placed on the UNSW devices, as their fabrication was more successful.

4.2.1 Device designs

MU devices Analogous to the N-UNCD devices, we chose Hall bar designs for ease of electrical and magnetic field characterization. The Hall bars had a width to length ratio between the contacts of width/length = 20 μm/48 μm. For these devices we implanted erbium ions with an energy of 110 keV and a fluence of 6.6×10^{10} cm^{-2} in the channel area, resulting in a peak concentration of 2×10^{16} ions per cm^3 at a depth of 20 nm beneath the surface. Arsenic was implanted to form metallic n+ type leads between the channel and the contact pads with an energy of 195 keV and a fluence of 6.6×10^{14} cm^{-2}, leading to a peak concentration of 4.7×10^{19} cm^{-3} at a depth of 100 nm. An optical image of a fully fabricated and bonded up device is shown in Fig. 4.10.

UNSW devices Figure 4.11 shows a sketch of a cut through a device fabricated at UNSW. Indicated are the silicon substrate (yellow) and the silicon dioxide (orange). The thinner gate oxide is directly underneath the metal gate; the field oxide is thicker and surrounds the whole

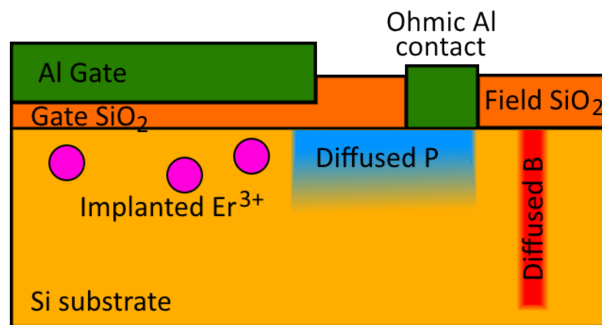

Figure 4.11: Sketch of a cut through the UNSW device design showing the depth profile.

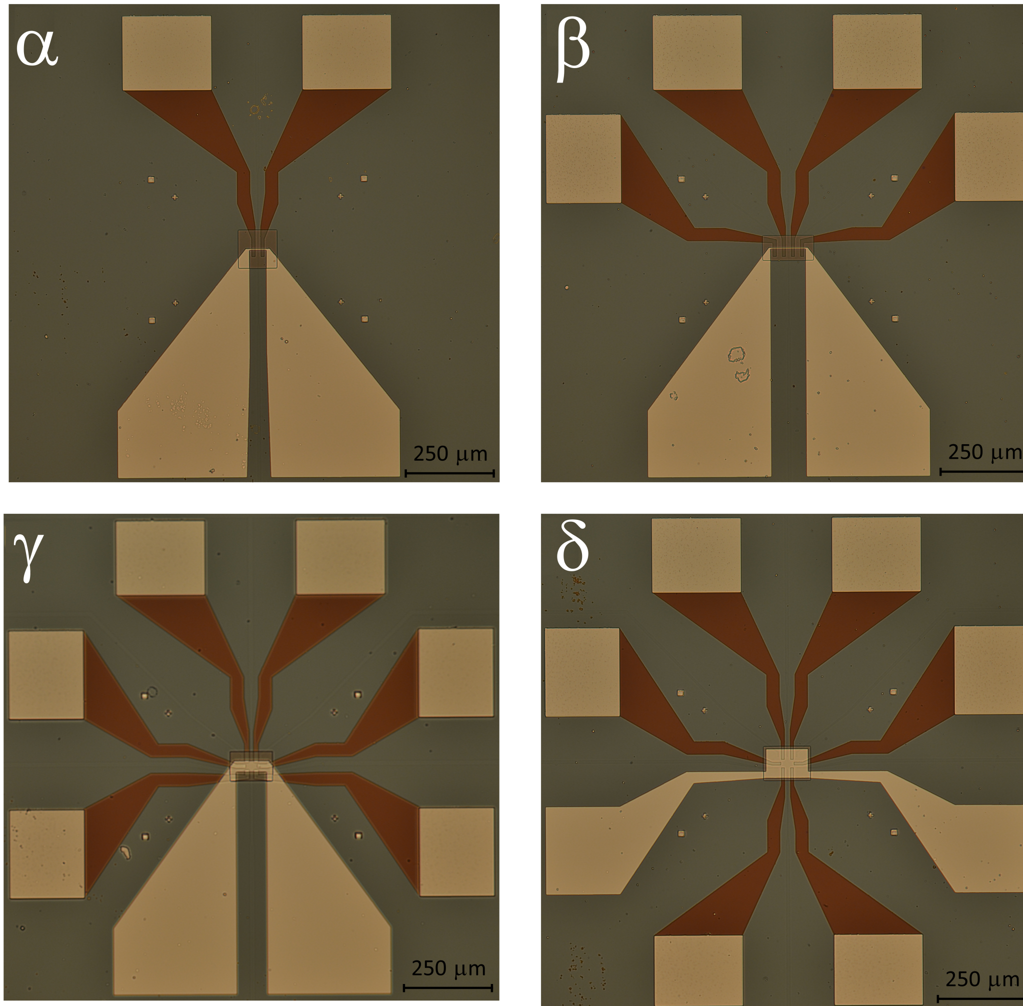

Figure 4.12: Optical image taken with a microscope of 10× magnification of the 4 finished designs, showing aluminium (yellow) and phosphorus diffused areas (brown), surrounded by the field oxide (grey).

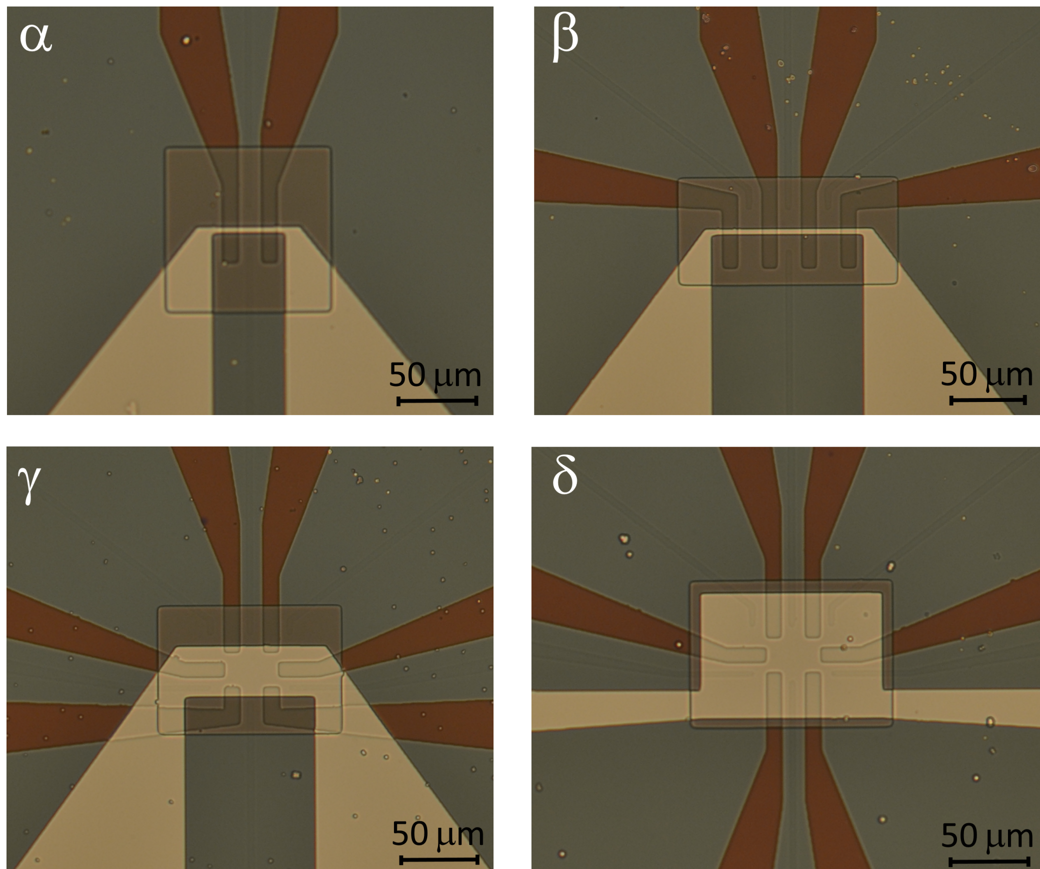

Figure 4.13: Optical image taken with a microscope of 20× magnification of the 4 finished designs in the channel area (central parts of Fig. 4.12). The squares in the centre are the thinner gate oxides, the aluminium gates are in yellow, the phosphorus diffused leads in brown, and the thick field oxide in grey.

Design	Number of ohmic contacts	Channel length (μm)	Channel width (μm)
α	2	26	5
β	4	78	5
γ	6	36	22
δ	6	36	22

Table 4.7: Er:Si new sample design dimensions.

device. Also shown are the aluminium metal (green) which forms the top gate as well as ohmic contacts to the substrate. The n-type leads consist of diffused phosphorus (blue), and the implanted erbium is shown in the channel area (pink). The device is separated from the outside via diffused boron (red). The silicon substrate of the samples fabricated at UNSW was n-type doped with phosphorus of a concentration of 1-2 $\times$ 10^{16} cm^{-3} and a resulting resistivity of 0.3-0.5 Ωcm.

For the UNSW devices we developed four different designs. An optical image of the finished devices is shown in Fig. 4.12, with a more magnified image of the channel area shown in Fig. 4.13. The dimensions of these devices are given in Table 4.7. All designs have in the centre a channel which is to be examined via contacts that form ohmic connections to it. Over this channel all designs have a top gate, which can be accessed via two points. The simplest design α has only two ohmic contacts. Its purpose is to perform EDMR (electrically detected magnetic resonance) measurements on the implanted erbium. The configuration of β is essentially the same as α, but with two more added contacts. This elongates the channel to twice its previous length. Having 4 contacts allows experiments in 4-terminal configurations, similar to the van der Pauw method which allows the extraction of sample resistivity, charge carrier density and mobility (see chapter 2.3.2). Designs γ and δ are both Hall bar designs. Both have 6 ohmic contacts in addition to the double-connected overlying gate. The channel area of width/length is

Batch	Implant ions	Implant energy and fluence
1	Sb	70 keV, 2×10^{11} cm^{-2}
2	Er	85 keV, 2×10^{11} cm^{-2}
3	none	–
4	Er	85 keV, 2×10^{11} cm^{-2}
	O	15.5 keV, 1.2×10^{12} cm^{-2}

Table 4.8: Er:Si batches and their additional implant ions.

22 μm/36 μm in both, γ and δ. The difference between these two devices is the layout of the n-type leads that access the channel as well as the size of the top gate. While δ consists of the standard Hall bar design with a big top gate, γ has a much narrower gate imitating the layout found in the first two structures. Thus, γ is thought to be a hybrid between the standard Hall bar δ and the four-contact EDMR device β.

In order to characterize the influence of erbium on the devices, four batches with varying implanted ions as outlined in Table 4.8 were fabricated. Ultimately, the motivation was to characterize erbium in these samples (batch number 2). As we know, erbium's activity is enhanced by oxygen, thus we also wanted to have a batch (number 4) that contained both of these elements. For comparison, it is important to also have one set of devices without any implanted ions (batch number 3). In addition, we also had one batch (number 1) in which we implanted antimony - it is a known dopant, relatively heavy, and thus is comparable to erbium. Details regarding the choice of the implant parameters are given in chapter 4.2.3.

4.2.2 Process flows

The process flow for the fabrication of the MU devices is given in Table 4.9 and for the UNSW devices in Table 4.10. A graphical visualization of both is sketched in Fig. 4.14. Both process flows were very similar, with

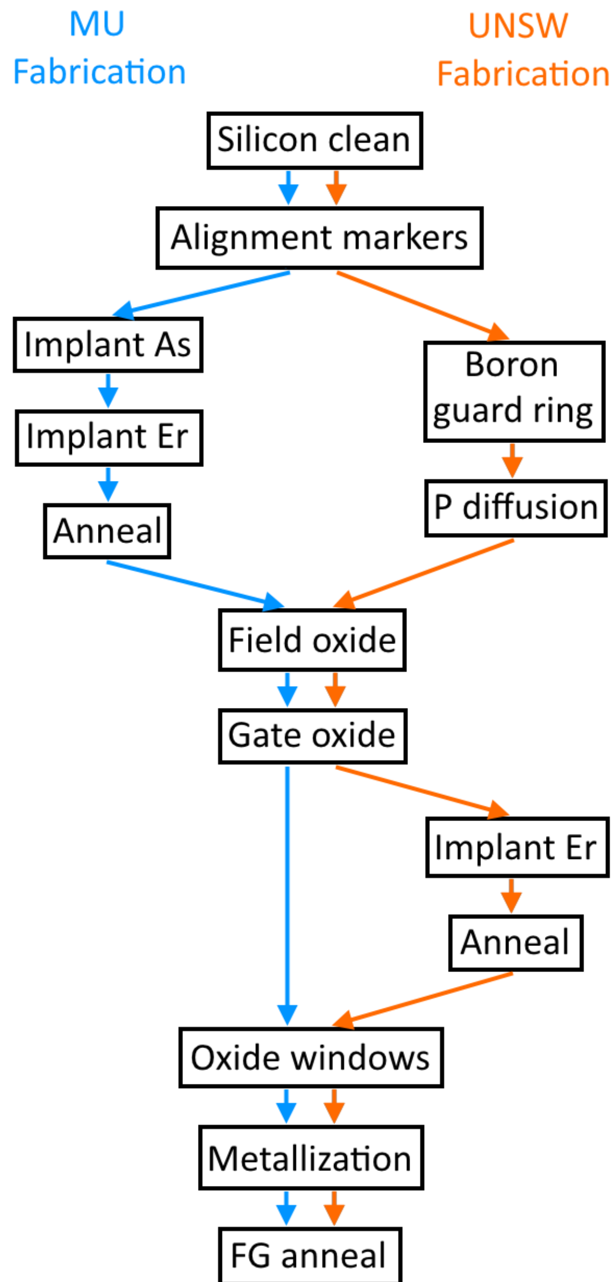

Figure 4.14: Graphical visualization of the process flows of both MU (blue) and UNSW (orange) devices.

the main differences being the choice of ion for the leads, the addition of a boron guard-ring in the UNSW devices, and the already described design differences. The most important difference was that the oxidation was post implantation with the MU devices, whereas the order of the UNSW process flow led to the devices first being oxidised and then the ions subsequently being implanted through the silicon dioxide. This section concentrates on the fabrication of the UNSW devices. The steps taken to produce the MU devices were similar and are therefore not described in as much detail to avoid repetition.

	Step	**Details**
0	Clean	Follow table 4.12 for cleaning process.
1	Define alignment markers	Grow ~160 nm thick SiO_2 layer Optical Lithography (Mask 0) including postbake: 125 °C, 30 min Etch markers into SiO_2 with BHF Etch markers into Si (BOSCH process, see Fig. 4.21) Clean Sample (remove SiO_2 with HF)
2	Create As implant mask	Grow ~160 nm thick SiO_2 layer Optical lithography (Mask 1) including postbake: 125 °C, 30 min Etch pattern into SiO_2 with BHF
3	Implant As	Energy: 195 keV; fluence: 5.5×10^{14} cm^{-2} Clean Sample (remove SiO_2 with HF)
4	Create Er implant mask	Grow ~160 nm thick SiO_2 layer Optical lithography (Mask 2) Including postbake: 125 °C, 30 min Etch pattern into SiO_2 with BHF

5	Implant Er	Energy: 110 keV; fluence: 6.6×10^{10} cm^{-2} Clean Sample (remove SiO_2 with HF)
6	Anneal samples	RTA in Ar, 900 °C, 30 sec
7	Create field oxide	Grow SiO_2 layer Furnace: 1000 °C, 10 min O_2 ($\sim$30 nm) PECVD: 4 min deposition, 250 °C.
8	Remove Oxide in gate area	Optical Lithography (Mask 3) including postbake: 125 °C, 30 min Etch gate into SiO_2 with BHF
9	Create gate oxide	Grow SiO_2 layer Furnace: 1000 °C, 10 min O_2 ($\sim$30 nm)
10	Create oxide windows	Optical lithography (Mask 4) including postbake: 125 °C, 30 min Etch windows into SiO_2 with BHF
11	Create ohmic contacts	Optical lithography (Mask 5) Evaporate 100 nm Al Lift off photoresist with Acetone
12	Anneal samples	Forming gas (FG), 425 °C, 45 min.
13	Prepare for measurements	Split chip into individual devices. Glue devices into sample carriers. Wire bond contacts to sample carrier.

Table 4.9: Process sheet for Er:Si Hall bar fabrication as undertaken at MU. BHF stands for buffered HF.

	Step	**Details**
0	Initial clean	Follow Table 4.12 for cleaning process.

1	Define alignment markers	Grow ∼100 nm thick SiO_2 layer
		Optical Lithography (Mask 0)
		Etch markers into SiO_2 with BHF
		Etch markers into Si
		Clean sample
2	Create Boron guard ring	Optical lithography (mask 1)
		Etch pattern into SiO_2 with BHF
		Boron diffusion + drive in
3	n-type leads	Clean sample
		Optical lithography (mask 2)
		Etch pattern into SiO_2 with BHF
		Phosphorus diffusion + drive in
4	Field oxide	Grow SiO_2 (min. 120 nm)
		Clean sample
5	Gate oxide	Optical lithography (mask 3)
		Etch pattern into SiO_2 with BHF
		Grow SiO_2 layer (40 nm)
6	Ion implantation	Optical lithography (mask 4)
		Etch pattern into PR with BHF
	Implant Er	Energy: 85 keV; fluence: 2.1×10^{11} cm^{-2}
7	Anneal Er	Clean sample
		RTA: 900 °C, 30 s (Ar)
8	Create ohmic contacts	Optical lithography (mask 5)
		Etch pattern into SiO_2 with BHF
		Evaporate aluminium (ca. 200 nm)
		Lift off
9	Non-ohmic contacts	Optical lithography (mask 6)
		Evaporate aluminium (ca. 200 nm)

		Lift off
10	Anneal	Hot furnace 400 °C, 15 min, FG
11	Final preparations	Split chip into individual devices. Glue devices into sample carriers. Wire bond electrical contacts.

Table 4.10: Process sheet for Er:Si Hall bar fabrication as undertaken at UNSW.

Before we began the fabrication, some prior calibrations and simulations had to be run to confirm certain parameters. The equipment used for the oxide growths had to be calibrated, the exact values for ion implantation had to be determined, the technique for defining alignment markers needed to be tested, the parameters for optical lithography needed to be finalized, and finally the optimum temperature and time for the sample anneal had to be determined.

4.2.3 Prior simulations

Before any fabrication was commenced, simulations were run regarding implantation parameters, ion diffusion, and anneal conditions. The results of these simulations were then used as a guideline for parameters used during the fabrication process.

Stopping and Range of Ions in Matter(SRIM) Around 1983 James Ziegler and Jochen Biersack developed the software package SRIM (Stopping and Range of Ions in Matter) and since this time it has been continuously upgraded [153]. The core of SRIM is a program called Transport of Ions in Matter (TRIM). Using the input parameters of the target material, the ion

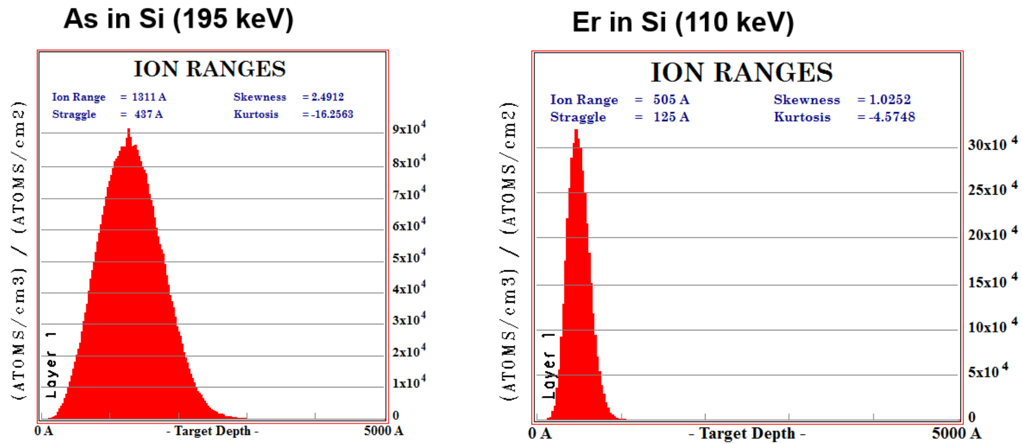

Figure 4.15: SRIM simulations of (left) As 195 keV and (right) Er 110 keV, showing implanted ion concentration versus substrate depth, used for the MU devices.

type as well as energy, TRIM gives information about the three-dimensional distribution of the ions in the target material. The penetration depth as well as the straggle of the ions is calculated along with several other parameters, amongst them vacancy concentration and ionization. The Monte Carlo simulation method is used for these calculations. Several approximations during the calculation process in SRIM limit its applicability. In particular, the program does not take into account the recombination of interstitials with vacancies, and it neglects the influence of neighbouring atoms, and thus overestimates the degree of ion induced damage. Despite these deficiencies, SRIM is very accurate in mapping the penetration depth of ions. More details regarding the stopping of ions in SIMS can be found in [154]. Our purpose was to estimate how deeply the implanted ions would penetrate the target material as well as to estimate the ion concentration versus depth profile, and the SRIM simulations helped to determine implantation parameters such as ion energy as well as fluence. We used SRIM specifically to simulate erbium and arsenic implantations for the MU devices, and to simulate erbium, oxygen and antimony concentrations for the UNSW devices.

The aim for the MU devices was to implant erbium ions so that the finished device had erbium with a concentration of 2×10^{16} cm^{-3} at a depth of 20 nm beneath the surface and arsenic of a concentration of 4.7×10^{19} cm^{-3} at a depth of 100 nm. This concentration was at that point believed to be deleterious to oxide performance, so we planned to create the gate oxide after the implantation (unlike in the later developed UNSW devices). We had to take into consideration that we would be growing silicon dioxide in a hot furnace (which uses up existing silicon) after the implantations; chapter 4.2.3 discusses dopant diffusion that occurs during the oxide growth. The oxide growths in the furnace post implantation were planned to be a combined 60 nm thick - 30 nm for the first part of the field oxide and 30 nm for the gate oxide. We expected that for each nm of SiO_2, roughly half a nm of Si would be consumed during planar oxidation. We needed to allow for these 30 nm that the silicon substrate would be reduced by, and aim for implanting the Er and As ions 30 nm deeper into the material. For a desired erbium concentration of 2×10^{16} cm^{-3} at a depth of about (20 + 30) nm beneath the Si surface we simulated an ideal ion energy of 110 keV with a fluence of 6.6×10^{10} cm^{-2} (see right graph in Fig. 4.15). For arsenic, the desired concentration of 4.7×10^{19} cm^{-3} at a depth of (100 + 30) nm would be achieved according to the simulation (left graph in Fig. 4.15) with an energy of 195 keV and fluence of 6.6×10^{14} cm^{-2}. The penetration during implantation of both implant ions, arsenic and erbium, was comparable in either target material, silicon or silicon dioxide.

At the time of planning the UNSW devices, we realized that the Er concentration of the MU devices was indeed not high enough to render the gate oxide useless. As a result, our new plan was to implant the Er ions through the silicon dioxide, which would be recovered with an anneal. Also, since not all of the erbium ions were active, the required fluences to prevent freeze-out at lower temperatures was larger than that used for the MU devices. So we chose to use P-doped silicon substrates and implant Er in order to be able to

study both P and Er EDMR as well as interactions of Er and P. The desired erbium concentration of the UNSW devices was around 8×10^{16} cm^{-3} at about 10-20 nm depth underneath the surface. In order to electrically access these erbium implanted areas, we introduced free charge carriers for leads by diffusing phosphorus into the material. We made the change from the previous arsenic implantation to phosphorus diffusion in order to avoid one implantation step by substituting diffusion for it, as unlike UM, UNSW has a phosphorus diffusion capability. For ohmic conductivity we needed a concentration above the metal-insulator transition, which has a critical concentration of 3.5×10^{18} cm^{-3} [155, 156]. We chose a slightly higher concentration of around 4.7×10^{19} cm^{-3} at a depth of 100 nm underneath the surface. For the simulations, we had to take into account that the erbium was to be implanted through the gate oxide into the silicon substrate, unlike the process used during the fabrication of the MU devices, where the gate oxide was created post implantation. For a desired erbium concentration of 8×10^{16} cm^{-3} at a depth of about 10 nm beneath the SiO_2/Si interface, we simulated an ideal ion energy of 85 keV with a fluence of 2×10^{11} cm^{-2} (see Fig. 4.16). In the simulation we created two layers, a 30 nm thick SiO_2 layer that represented our gate

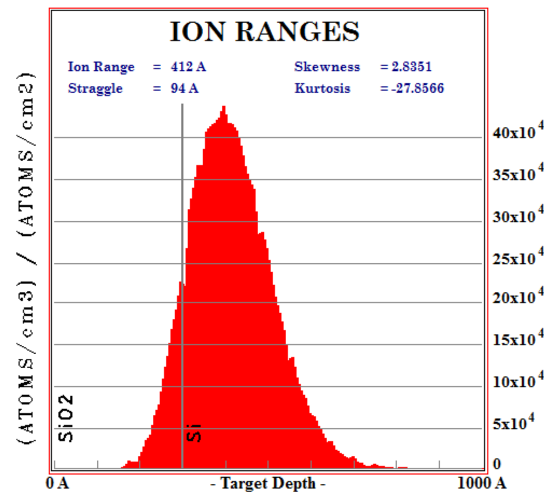

Figure 4.16: SRIM simulations of Er at 85 keV into the gate oxide and silicon substrate, as used for the UNSW devices. Plotted is the implanted ion concentration versus substrate depth.

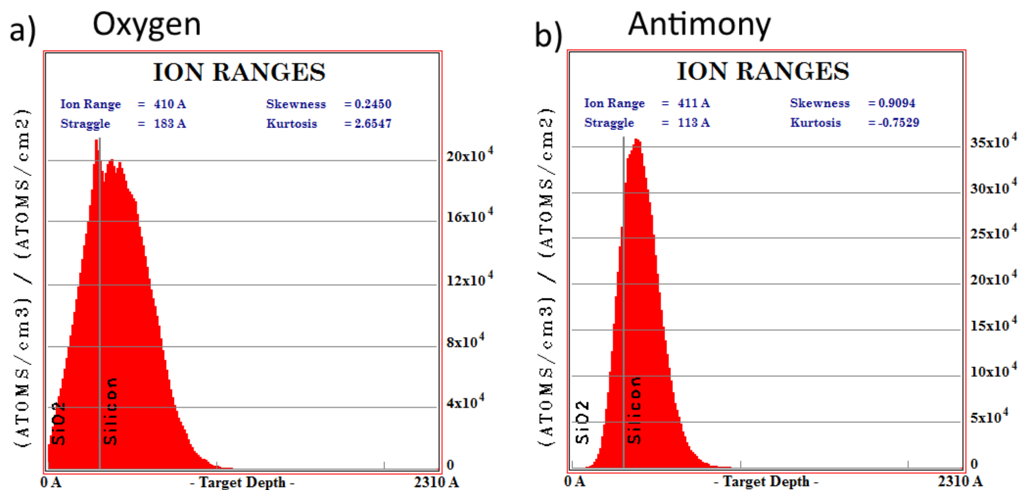

Figure 4.17: SRIM simulations of a) O 15.5 keV and b) Ab 70 keV for the UNSW devices, showing implanted ion concentration versus substrate depth.

oxide (which was measured to be 30 nm thick) and a Si substrate. The result showed a very similar penetration of Er in silicon as well as silicon dioxide.

In batch one, implanted with antimony as comparison, we wished to achieve the same concentration at the same depth as we had for the erbium, in order to keep as many variables as possible the same. Figure 4.17 b) shows that a Sb concentration of 7x10^{16} cm^{-3} at a depth of about 40 nm beneath the surface was achieved with an implantation energy of 70 keV and a fluence of 2×10^{11} cm^{-2}. In batch four, which had erbium as well as oxygen incorporated in it, we used the simulation in Fig. 4.17 a) to calculate an oxygen ion concentration of 2.4×10^{17} cm^{-3} (higher by a factor of almost 10 than the Er concentration) at around 40 nm depth, with an implantation energy of 15.5 keV and a fluence of 1.2×10^{12} cm^{-2}.

Florida Object Oriented Process Simulator (FLOOPS) Technology computer aided design (TCAD) models semiconductor fabrication and device operation, thus creating a simplified picture of devices. Semiconductor pro-

cess simulation - the modelling of the fabrication of semiconductor devices - is part of TCAD, aiming for an accurate prediction of dopant distribution throughout the device. The first version of FLOOPS was completed in 1994 [157]. It is designed for semiconductor process modelling and semiconductor device modelling. Its scripting language is C^{++} with command-line control language [158]. The main limiting factor with any TCAD is the computing limitations. Only a few devices can be simulated at the same time on a conventional computer using FLOOPS, so the number of points of the mesh size to use for simulations is limited. Since this mesh represents a continuous system, it gives the limitations of the accuracy of the approximations provided by the simulation. Poisson's equation is used for simulating the electrostatic potential, and the electron and hole continuity equations for the electron and hole concentration throughout the simulated device.

In this project FLOOPS was used to simulate ion diffusion in material during thermal oxide growth and high temperature annealing. It is important to learn about the diffusion of implanted ions during high temperature anneals, as too long/high temperature anneals may cause the implanted ions to diffuse so much that the resulting concentration at a certain depth is too low for the purpose of the experiment. On the other hand, the anneal time/temperature still needs to be long/hot enough in order to repair any damage in the sample. Unfortunately FLOOPS cannot be used for simulations of erbium implants, as erbium is not one of the species with available parametrisations in the program. Instead, we ran all FLOOPS simulations for arsenic (which was initially supposed to be implanted for the ohmic leads before we later chose to diffuse phosphorus for this purpose). We know that erbium is more than twice the mass of arsenic and consequently diffuses less. From this we drew educated guesses regarding the erbium distribution after high temperature treatment. Tests regarding activating the erbium by annealing (described in section 6.2) showed that the best results are obtained by a rapid thermal anneal (RTA) at 900 °C for 30 seconds. Such an RTA takes

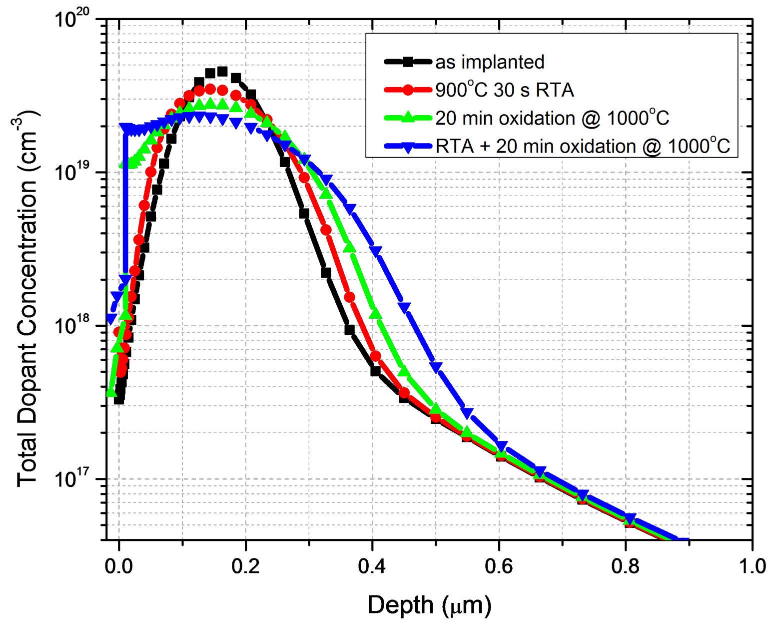

Figure 4.18: Diffusion simulations after As implantation of an energy of 240 keV and fluence of 6.7×10^{14} cm^{-2} under varying annealing and oxidation conditions.

place in a rapid thermal processing furnace in an argon atmosphere. The ambient temperature is raised rapidly (within seconds) up to temperatures in excess of 1000 °C by several halogen lamps and monitored with a thermocouple. The sample is kept for less than a minute at this temperature. Once the desired time is reached, the halogen lamp is turned off and the substrate cooled down with a constant argon gas flow. These high temperatures not only activate the erbium, but also repair formed defects and dissociations that can lead to undesired diffusion during this and later processes. Figure 4.18 shows a simulation of the arsenic concentration versus sample depth without subsequent anneals in black, compared to a subsequent RTA at 900 °C for 30 s (red), an oxidation for 20 minutes at 1000 °C (green), and an RTA with following oxidation at 1000 °C for 20 minutes (blue). The as-implanted arsenic concentration has a much sharper as well as slightly higher peak compared to the other curves (see Fig. 4.18). This is due to the ions diffusing

during the exposure at high temperatures. Comparing the plots of the oxidised arsenic with and without the preceding RTA, we could see that the RTA was necessary to prevent arsenic diffusion during the subsequent oxidation. Simulations have also shown that the arsenic will diffuse less when the silicon dioxide is grown at higher temperatures for a shorter time, rather than at slightly lower temperatures for a longer time - the time needs to be adjusted to result in the same oxide thickness. The furnace to be used has a maximum temperature of 1000 °C, consequently 1000 °C was the temperature chosen during oxide growths.

4.2.4 Oxide growth

As the process sheets in Tables 4.9 and 4.10 show, silicon dioxide needs to be created on the silicon samples in several steps. Two methods for growing this oxide were used during this project: first thermal growth and secondly deposition (PECVD). Both methods need to be calibrated before commencing the device fabrication. It is especially important to have accurate control over the thickness of the oxide growth. The devices need two different oxide thicknesses: the thinner gate oxide which separates the metal gate from the silicon substrate, serving as a dielectric, and the thicker field oxide which separates the individual devices from each other. Both of these oxides are created via the thermal oxidation technique. Consequently this technique needs oxide thickness as a function of oxidation time for the used temperature to be calibrated as accurately as possible. The calibration and oxide quality tests are shown in chapter 6.3.

Thermal oxidation On a blank silicon wafer a 'native oxide' will naturally form in air within a very short time frame. This layer will only be few nano metres thick and protects the underlying clean silicon from further oxidation. If this wafer is heated, the oxidation process will continue. An oxygen atmosphere will speed this up. Growing an oxide this way, by placing

the wafer in a hot furnace without water vapour with molecular oxygen as the oxidant, is called 'dry thermal oxidation'. The reaction that takes place is the following:

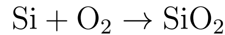

$$Si + O_2 \rightarrow SiO_2$$

The growth rate will depend on the temperature and the exposure time as well as the flow rate of the oxygen. It will also depend on the composition of the sample. An implanted silicon wafer will have a damaged structure as a result of the ion implantation which will lead to a faster oxidation process due to the oxygen being able to penetrate a damaged substrate faster than a perfect crystalline structure. The substrate doping will also influence the oxidation rate, as well as any other impurities. Thus the oxidation rate will be higher for a substrate with dopants diffused in it than for a pristine substrate. The more damaged the sample is, the higher the difference in growth rate is compared to an unimplanted silicon sample. It is important that the furnace temperature can be monitored accurately, as a change in temperature will have a significant influence on the growth rate. The oxygen flow rate also has a high influence on the growth rate. The higher the fluence and temperature, the faster the oxidation. As silicon is being consumed from the substrate and oxygen supplied by the ambient, the growth of silicon oxide grows both into the substrate as well as on top of it. For each grown nm of SiO_2 0.44 nm of Si is consumed [159].

A calibration curve (Fig. 4.19) for the oxidation process in the MU furnace was created using two sets of silicon samples. The first set contained unimplanted silicon. The second set contains Er implanted Si (400 keV energy, 1×10^{12} cm^{-2} fluence). These were oxidised in the furnace with varying times with a constant O_2 flow rate at fixed temperature of 1000 °C. The oxide thickness was measured using the Rutherford backscattering technique as described in section 2.2, and the simulation with the best fit was used to determine the thickness. The growth rate was described using the Deal-Grove model [160], which assumes that the oxidant diffuses through

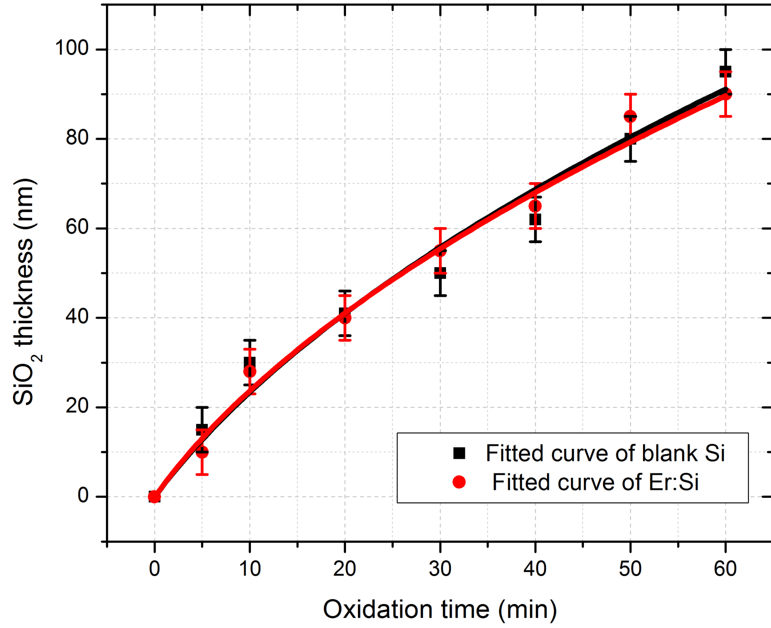

Figure 4.19: Silicon oxide thicknesses versus oxidation times of blank silicon (black) and erbium doped silicon (red) and their fitted curves.

an existing oxide layer to the substrate surface where it reacts. It can be simplified with the following equation:

$$y = \frac{a}{2}(\sqrt{(1 + \frac{4b}{a^2}x)} - 1), \tag{4.1}$$

where y is the thickness of the silicon oxide, x is the anneal time, and a and b are the parameters to be fitted, assuming there is no oxide present at the beginning of the process. The parameters for the fitting of the growth rate of the used furnace at 1000 °C (Fig. 4.19) are as follows:

	blank Silicon	Erbium doped Silicon
a (m)	889	1020
b ($\frac{m^2}{s}$)	26679	29326

The two curves are surprisingly close to each other. They are hardly distinguishable within the error bars. This indicates that the damage introduced

Pressure	1000 mTorr
RF/RIE Power	20/0 Watt
N_2O	710 sccm
5% SiH_4/95% N_2	170 sccm
Temperature	250 °C
Time	4 min

Table 4.11: Parameters for SiO_2 deposition with the PECVD method.

by the erbium ions at those energy and fluence settings has little effect on the growth rate.

The quality of a silicon oxide grown via thermal oxidation can generally be very good and is optimally dense. They can be strongly insulating [161]. The quality of the grown silicon dixode was tested by performing a capacitance versus voltage (C-V) measurement through a cross section of the sample. This is further explained in section 6.3.

Plasma-enhanced chemical vapour deposition (PECVD) The other method used to create a silicon dioxide layer on top of a silicon layer is plasma-enhanced chemical vapour deposition (PECVD). This method deposits a layer of silicon dioxide on top of the existing silicon substrate. It works very similarly to the previously explained CVD method of deposition. The substrate is placed in a chamber in which a gas is directed. A plasma is created by radio frequency (RF) on the top electrode. For this project the PECVD system of the Melbourne Centre for Nanofabrication (MC^N) is used. The parameters used for the silicon dioxide growth are given in Table 4.11. The advantages of this method over the dry thermal oxidation method are the much lower deposition temperatures. This however leads to a much lower quality oxide due to silanol and water impurities as well as the structure being less dense/more porous [161]. The impurities are regulated by

changing the growth parameters. This so-called 'dirty' oxide means that a current will leak earlier through the interface compared to a thermally grown oxide. Thus we chose to use only thermally grown oxides as a gate oxide. However, the PECVD method was chosen for field oxides that are used as masks. These masks are not used as an electrical insulator and will be removed after they serve their purpose as a mask. The PECVD method was chosen here because it would not use up the substrate and is done at low temperatures which avoid the dopant diffusion that occurs at higher temperatures. Using up the substrate Si during furnace oxide growth would result in implanted dopants being closer to the surface after stripping off the silicon dioxide, which would be difficult to account for.

4.2.5 Silicon clean

Prior to any processing, the silicon wafers were chemically cleaned in order to remove all contaminations. The details of the cleaning process are outlined in Table 4.12. It included a piranha etch, RCA I, HF, RCA II, and another HF etch. Caution had to be exercised as the chemicals are highly corrosive.

Name	Composition	Etch details	Removal details
Piranha	H_2SO_4+H_2O_2 30% + 30%	5 min, 80 °C	Removes organic matter
DI Water	H_2O	rinse	Removes Piranha
RCA I	NH_4OH+H_2O_2 28% + 30%	5 min, 80 °C	Removes particles + organic residues; creates SiO_2 layer + metallic contamination
DI Water	H_2O	rinse	Removes RCA I
HF	H_2O+HF 6:1	RT, 30 sec	Removes SiO_2

DI Water	H_2O	rinse, dry	Removes HF
RCA II	$HCl+H_2O_2 + H_2O$	5 min, 80 °C	Removes metals + creates passivating layer
DI Water	H_2O	rinse	Removes RCA II
HF	H_2O+HF 6:1	30 sec, RT	Removes SiO_2
DI Water	H_2O	rinse, dry	Removes HF

Table 4.12: Details of the cleaning process of silicon wafers.

The piranha etch removes all organic matter from the surface. The following RCA I etch extracts particles and organic matter, while creating a thin silicon dioxide layer, which would be dissolved with an HF etch. Metal contaminations are removed with an RCA II etch and lastly HF is used to etch native silicon dioxide before starting to process the wafers.

4.2.6 Definition of the alignment markers

After a wafer is cleaned, the alignment markers need to be defined. A silicon dioxide grown onto the silicon substrate was used as the mask for the first process steps. This can either be done via PECVD or dry oxidation in the hot furnace (see section 4.2.4 for details). As the oxide is only used as a mask and will be removed later on, its quality isn't as important. But as it will be used as a mask for the first implantation it therefore requires a minimum thickness, which is defined by the implanted ions and their energy. We grew at least 200 nm of silicon dioxide for this purpose. The photo lithography to define the alignment markers followed the recipe outlined in Table 4.4 and the mask is shown in Fig. 4.20 a), including a post bake. The desirability of using a post bake - or hard bake - on a hot plate depends on the next

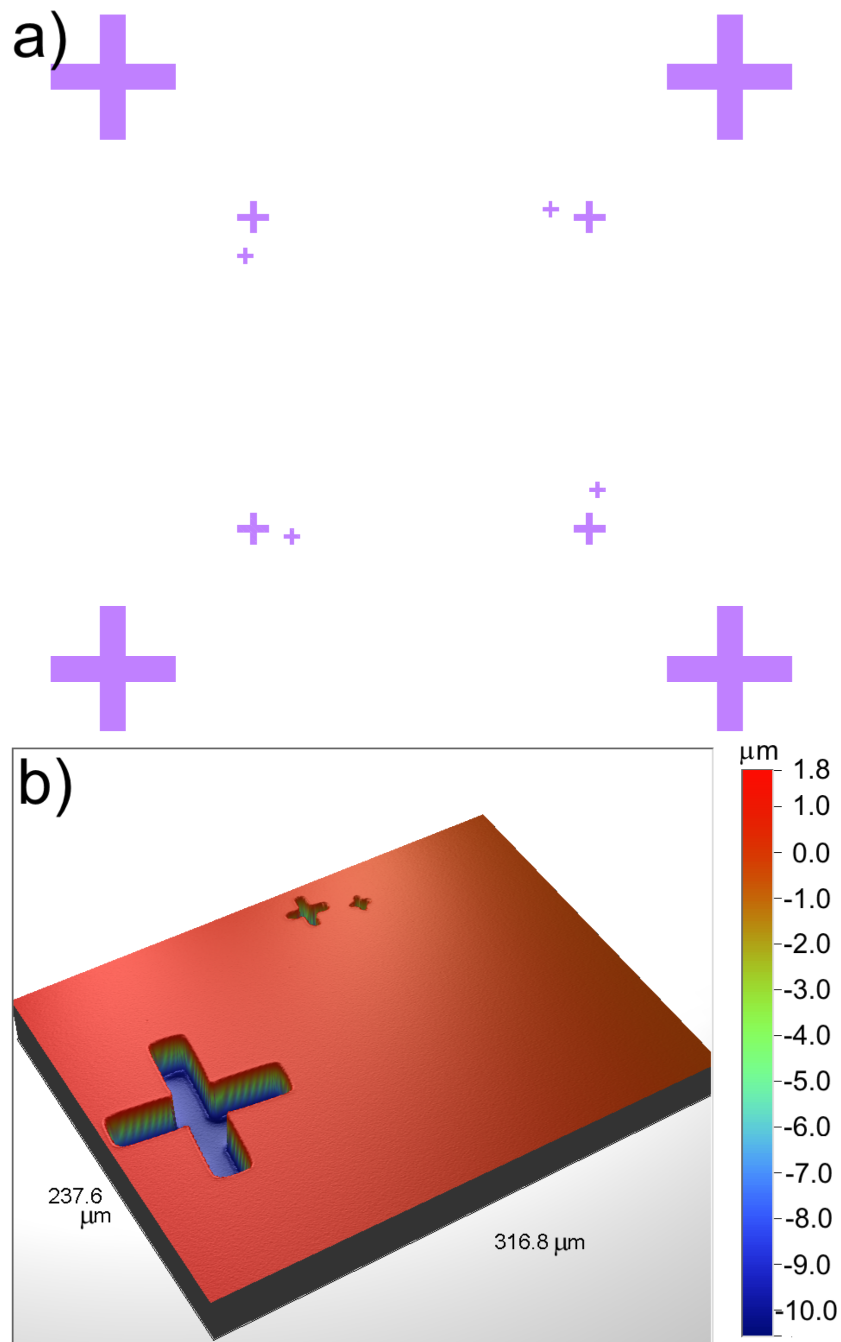

Figure 4.20: a) Optical lithography mask for the alignment markers for the MU devices. b) 3D optical profilometry image of an alignment marker in a silicon wafer.

processing step. A post bake hardens the photo resist (PR) and makes it insensitive to UV light. It also makes it harder to chemically remove the photo resist. If the sample is immediately coated with a metal, no post bake is necessary as the sample will not be exposed to light and therefore the resist does not need to be hardened. Here, the photo resist is the mask used for etching the markers into the silicon dioxide via buffered hydrofluoric acid (BHF) and therefore needs to be hardened to be able to endure the wet etch. Buffered HF consists of a buffering agent (ammonium fluoride) mixed with HF and is commonly used as an etchant if photo resist is used as the mask as it has a slower etch-rate compared to pure HF, making the etching process more controllable. An increased temperature will raise the etch-rate. This is an isotropic etching process and includes soaking the sample for several minutes in BHF before thoroughly rinsing and subsequent soaking in deionised water (DI). With a 200 nm thickness of the silicon dioxide, an etch-time of 2 minutes was sufficient to etch through the SiO_2.

BOSCH process Now the alignment markers had to be etched into the silicon so that they would be visible for all subsequent process steps. Sharp and deep etch-walls ensure accurate alignment. We achieved this with the BOSCH process [162]. This is a dry etch and as such uses a plasma phase as etchant. The etch is controlled by changing the parameters such as the gas composition, pressure, power, and temperature. This is an isotropic etch since it is done by free radicals of the plasma attacking the surface where they react. Deep reactive ion etching (DRIE) has a smaller lateral than downward etch rate because the gas is accelerated downwards onto the sample. The BOSCH process is divided into cycles, each of which contains one step of etching and one step of passivation of the side walls (see Fig. 4.21). SF_6 is the gas commonly used for etching the silicon during the etch step. During the passivation step a gas like CHF_3 is sent into the chamber. It bonds to the silicon surface and thus creates a protective layer. Due to the

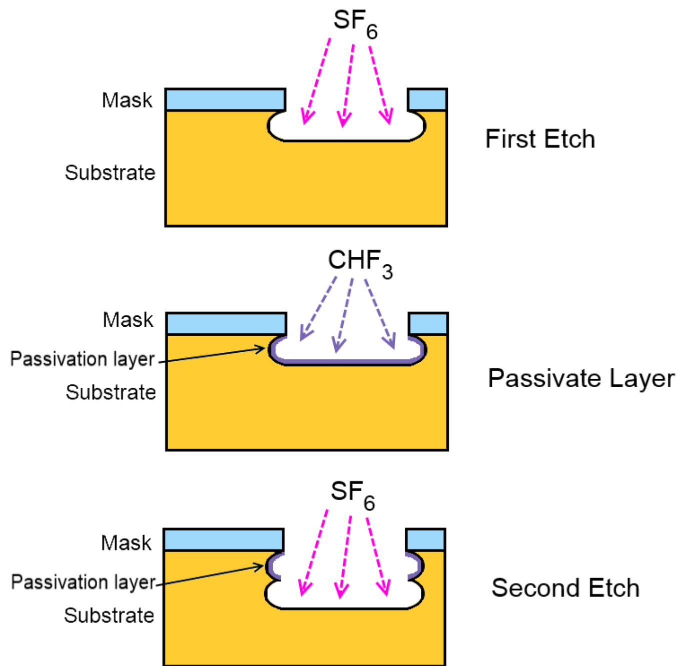

Figure 4.21: BOSCH process used for etching silicon.

downward acceleration of the etchant gas, the lateral etch rate is much lower than the downward etch rate, and the side walls do not lose their protective film as fast. Thus the isotropy is reduced and deep side walls are possible. They will not be straight vertical, but have a wave like shape, as can be seen in Fig. 4.21. The number of cycles determines the depth of the etch. The shorter the cycle time, the smoother (and straighter) are the side walls. A 3D optical profilometer image of an alignment marker of a MU device is shown in Fig. 4.20 b). The large cross has the dimensions of 100 μm $\times$ 100 μm, the smaller cross of 25 μm $\times$ 25 μm, and the smallest cross of 12.5 μm $\times$ 12.5 μm.The side walls are very sharp with a depth of about 11 μm. This ensured that the marker would be seen throughout the whole fabrication process even though multiple thermal oxide growths were planned. Smaller alignment markers are not ideal as they show rounded corners, but they still aid with fine adjustment during mask alignment.

4.2.7 Boron guard ring and phosphorus leads

In order to avoid electrical connections between separate devices, as well as between the contacts of one single device via a possible fixed oxide charge beneath the field oxide or even via diffusion of the dopants that would be later introduced to the substrate, we created a so-called guard-ring around the single devices and also between the n-type phosphorus leads. This guard-ring consisted of diffused boron, a p-type dopant in silicon, as opposed to phosphorus which constitutes n-type doping and as such 'neutralizes' any diffusing n-type charges. This avoided the possibility of n-type charge carriers causing electrical connections and thus shorting the ohmic contacts. As this process was available in UNSW, we used it in the fabrication of the UNSW devices.

Figure 4.22 shows in red the mask for the boron guard-rings. The image shows all four different device designs, fabricated at the same time on the same chip. Each device is surrounded by a 10 μm wide closed ring consisting of diffused B. In addition, there are 'arms' with a minimum width of 4 μm leading towards the centre of each device, in between the P diffused leads, shown in blue in the same picture. The n-type doping is designed to create a metallic connection between the small centre of each device - where the implanted channel and its gate will lie - and the larger scaled outer area. This is necessary so that connecting the electrical contacts with a wire bond is possible (a minimum area of 50 μm $\times$ 50 μm is needed).

The diffusion of B/P consists of two stages: firstly the deposition phase, during which a layer of high B/P concentration is deposited on the surface (boron-/phosphorus glass), and secondly the drive-in phase which requires slightly higher temperatures (ca. 1000 °C) to drive the B/P dopants into the substrate. In between these two steps the sample needs to be 'deglassed'. This means that the boron-/phosphorus-glass is removed with HF and thoroughly rinsed before the boron/phosphorus drive-in is commenced.

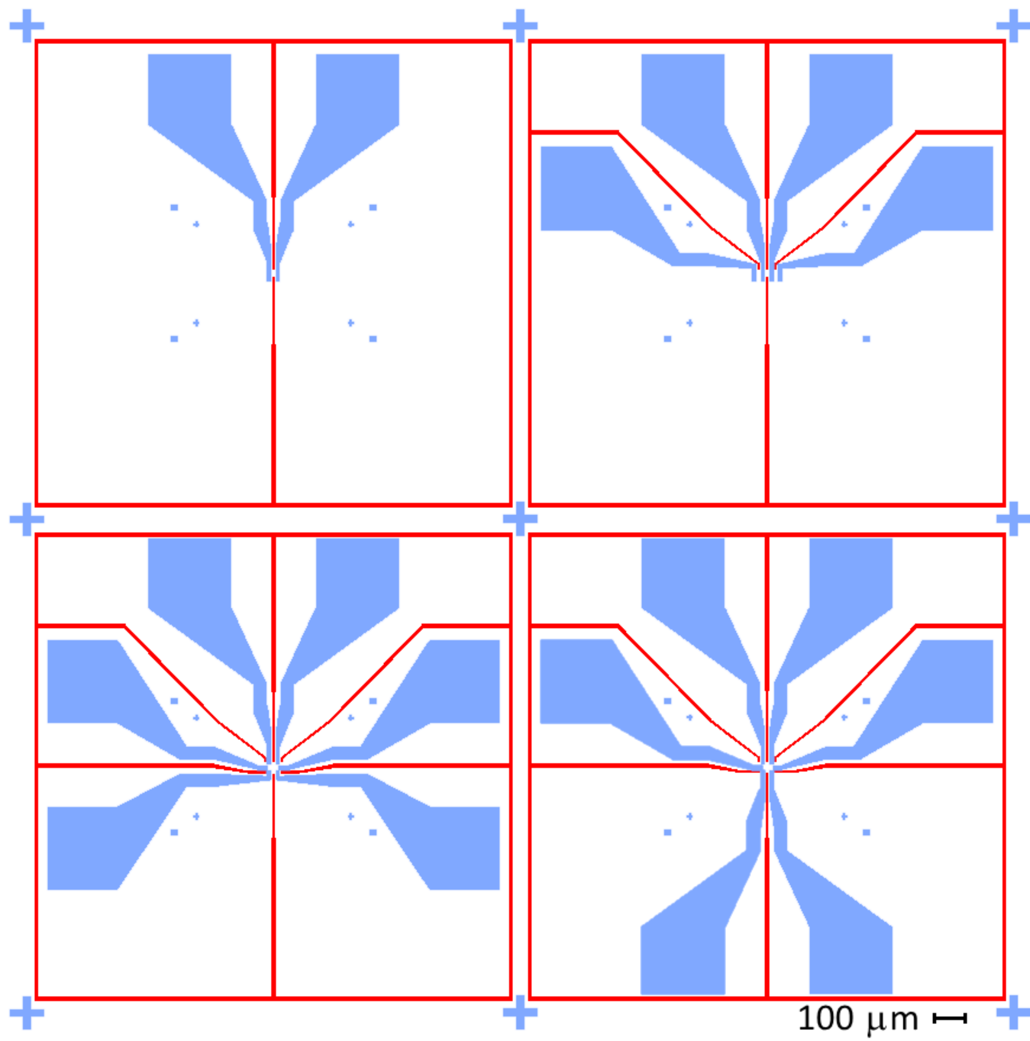

Figure 4.22: Optical lithography mask for the boron guard ring (red) and the P-diffused regions (blue).

4.2.8 Field oxide

A silicon dioxide layer about 120 nm thick is grown on top of the whole substrate in a dry furnace. This constitutes the field oxide. The purpose of this is to separate the individual devices from each other as there are 30 devices of each design on every chip and electrical insulation needs to be guaranteed. This field oxide needs to be a rather thick oxide of high quality as the aim is to create a perfectly insulating layer. We tested fabricated chips by applying electrical charges of up to 10.0 V between two devices. They remained successfully isolated from each other with no electrical connection apparent.

4.2.9 Gate oxide

In some areas, a thinner (or even no) oxide is required. Unlike the field oxide, the gate oxide serves as a dielectric layer separating the top gate from the conductive implanted area underneath. The conductivity of this channel can be modulated by applying a bias voltage to the top gate. Over-stressing the gate oxide or a poor quality gate oxide will lead to induced leakage current between the top gate and the channel. Consequently a high quality oxide is needed. The thicker the SiO_2 layer beneath the gate is, the higher is the required applied voltage in order to be able to influence the underlying charge carriers, and the higher the applied voltage needs to be before the silicon dioxide 'breaks down' and becomes conducting. The 120 nm of SiO_2 that covered the whole substrate after the field oxide has been grown was too thick and would require unacceptably high voltages applied to the top gate. In addition, the field oxide is generally of not as high quality as the gate oxide needs to be and hence can have, for example, larger than observed threshold voltage shift. Therefore we reduced the oxide thickness in the gate area by using the mask as shown in Fig. 4.23 in red. As it is very hard to etch SiO_2 down to a certain thickness, even when using a buffered HF (BHF)

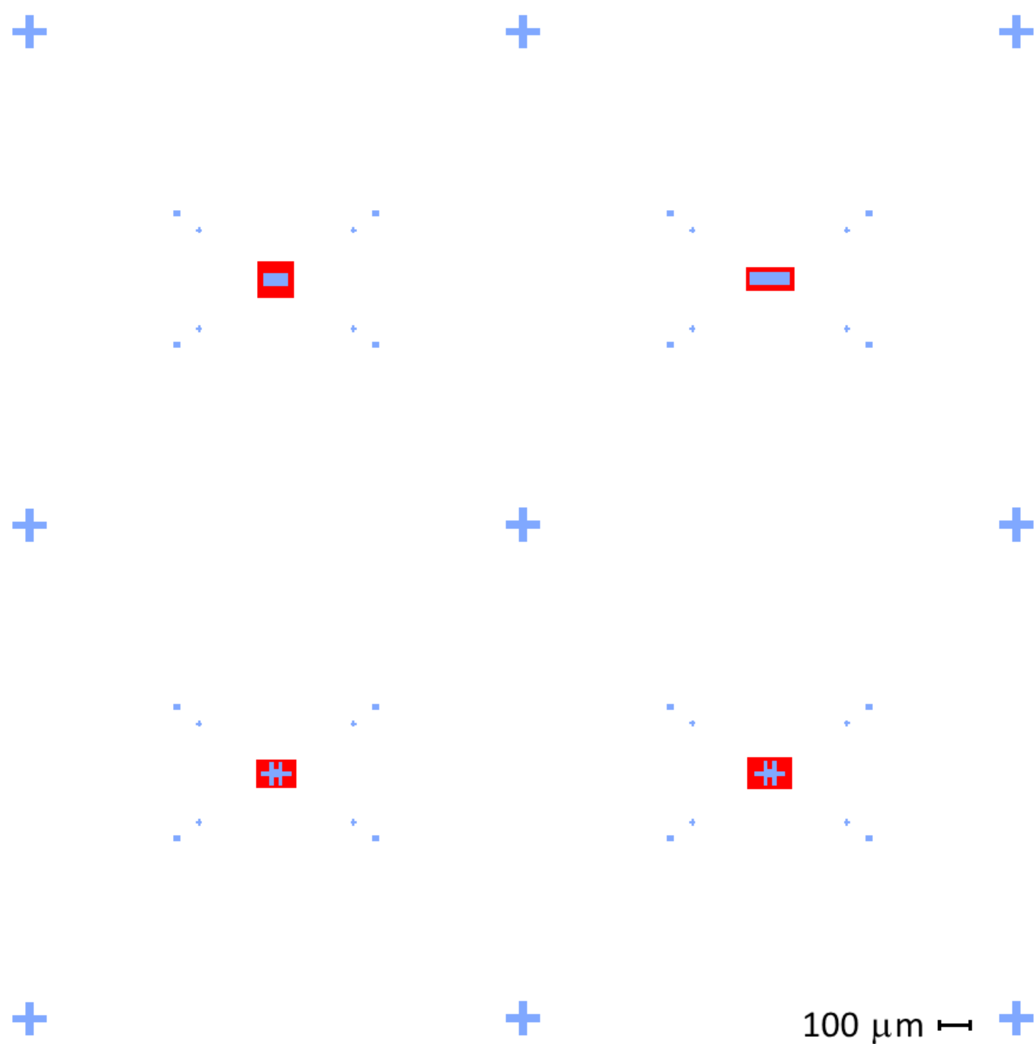

Figure 4.23: Optical lithography mask for the gate oxide (red) and the erbium implanted region (blue).

solution (due to a very fast etch rate), we removed all the silicon dioxide in the gate area by using the red mask given in Fig. 4.23 with BHF. Then a thinner, ca. 30 nm thick gate oxide was grown in a hot furnace dedicated for ultra-dry oxidation using dichloro-ethylene. This new SiO_2 layer covered the whole substrate, so it slightly thickened the field oxide as well.

4.2.10 Ion implantation

Following the oxidation steps, the ion implantation was commenced. As already described and summarized in Table 4.8, there were four different batches of devices that differed in the details of the implantation conditions. The area of the implantation is shown in Fig. 4.23 in blue. The ions are wanted only in a small channel area centred in the devices. They slightly overlap with the phosphorus leads (Fig. 4.22) to ensure electrical contact to the implanted channel. The implantation parameters were as per the simulations in chapter 4.2.3. All implantations were conducted at ANU.

4.2.11 Anneal

The samples underwent a rapid thermal anneal (RTA) after the ion implantation. This high temperature treatment is necessary to reduce further diffusion during subsequent hot temperature treatments by allowing the dopants to diffuse to vacant lattice sites and allowing vacancies and interstitials to recombine to reduce residual implantation damage. In addition, this treatment helps to activate the erbium optically (see chapter 6.2). During the RTA the sample was held at 900 °C for 30 seconds in an argon ambient.

4.2.12 Ohmic contacts

The ohmic contacts of the devices needed to be created via metal evaporation. In order to achieve an electrical contact, the silicon dioxide needed to be removed in the contact regions. This was done by photo lithography and a

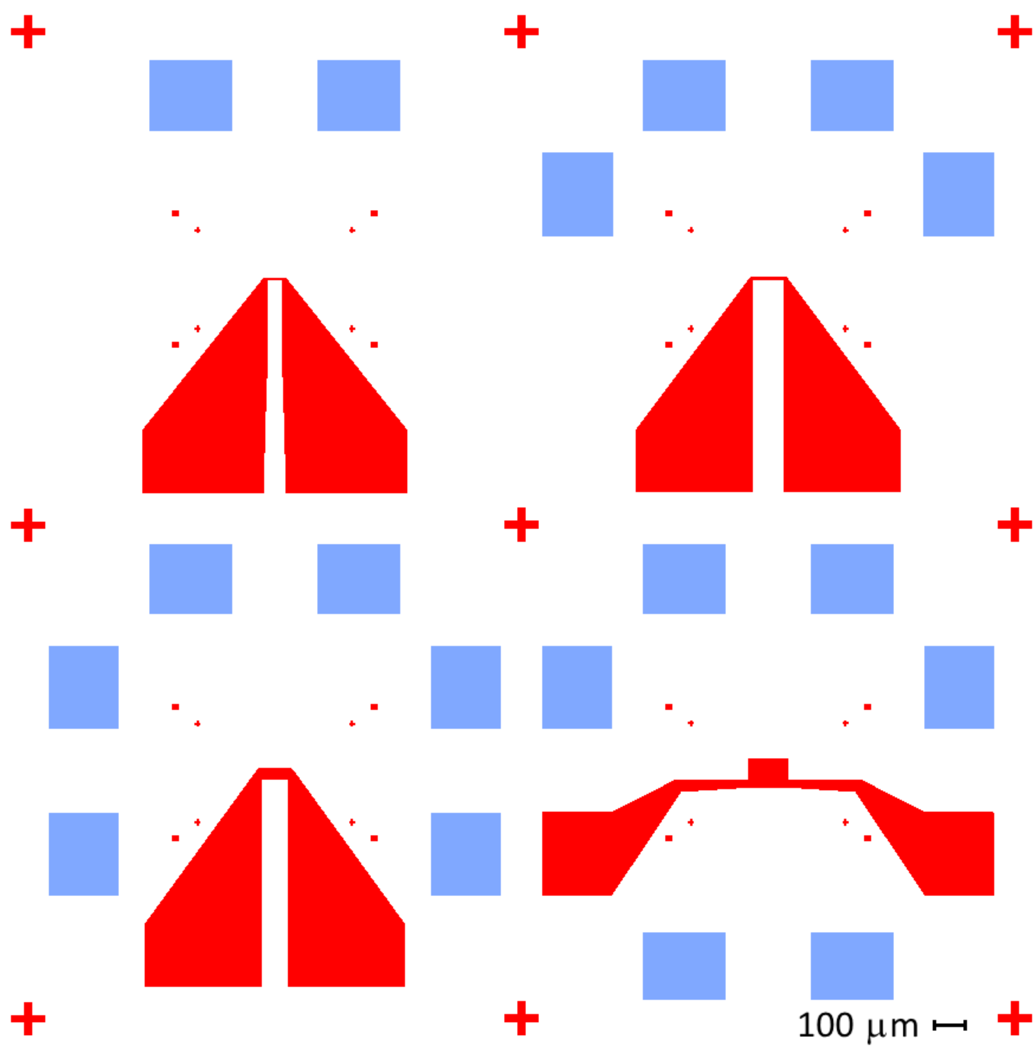

Figure 4.24: Optical lithography mask for the oxide windows (blue) and gate metallization (red).

subsequently HF etch that removed the unwanted silicon dioxide:Fig. 4.24 shows the mask used in blue. Immediately following this step we evaporated 100 nm aluminium (as explained in 4.1.3) onto the sample surface. After the lift off in an acetone bath, the unwanted Al was removed and the samples now all had their ohmic contacts. These contacts had a size that made it possible to wire bond directly onto them. They were all a minimum of 200 μm $\times$ 200 μm.

4.2.13 Gate metallization

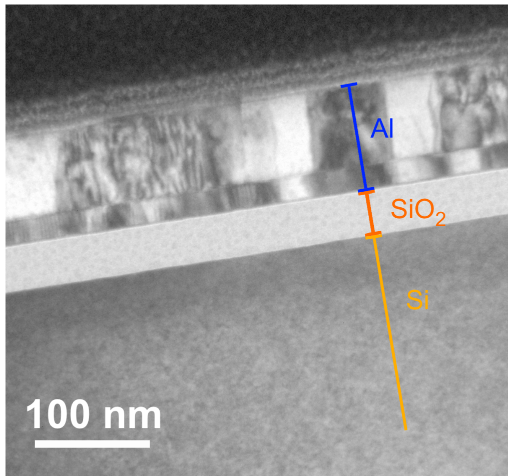

Figure 4.25: TEM image taken of a cross section through the gate of a fully fabricated Er and O implanted device. The gate oxide (orange) is shown to be 40 nm. The Al gate at ca. 120 nm thick has clearly been deposited in two steps.

The top gates were metallized in the same way as the ohmic contacts. Photo lithography defined the desired areas, as per Fig. 4.24 in red, followed by the evaporation of about 100 nm aluminium. The subsequent lift off in an acetone bath removed all unwanted Al. Each device had one gate, each of which had two big areas for wire bonding. This enabled every gate to be contacted from two sides. The advantage of this so-called double-bonding is that continuity through the gate could be tested by using the two contacts. This test was designed to show whether there were issues with the contacting of the gate, or whether one contact might be causing problems. If continuity was not confirmed, further testing could reveal which contact to the gate was causing the issue and

it would therefore not be used for the measurements. Fig. 4.25 is a TEM image of the channel area of a UNSW device, showing the aluminium gate (blue), the gate oxide (orange), and the silicon substrate (yellow). The grown SiO_2 layer looks very smooth and has a thickness of 40 nm. The top aluminium gate has a clear line going through it, indicating that the metal was not grown continuously, but rather in two steps. This does not influence its function as a gate, as TEM shows that there are no other elements present in the metal layers.

4.2.14 Final steps

Now the devices were finalized. In order to make them accessible for measurements, the chips were split into the single devices. These were then glued to chip carriers with Cemedine brand epoxy, which has been shown to be able to work at temperatures down to a few milli-Kelvin. Finally the devices were wire bonded to the sample carriers with aluminium wire. This step is shown in the optical image of one of the MU devices (Fig. 4.10), where the broadening of the aluminium wire where it touches down to the sample is clearly visible. It is obvious that if the contact pads had been smaller in size, bonding would have proved rather difficult.

4.2.15 Fabrication issues in the MU devices

Most steps of silicon fabrication are well-known and should not cause issues, such as the recipe for photo lithography. Other not-well-known steps were first tested, such as the calibration of the oxide thickness versus oxidation time of the furnace at MU. However, a small proportion of steps in the process flow proved to be the source of later problems with the finished devices. Some of these issues were noticed (and addressed) during fabrication, but others unfortunately showed only when the finished devices were examined during electrical measurements.

One major problem encountered with the fabrication of the silicon devices was the misalignment of the masks during photo lithography. Misalignment occurred due to the accuracy of the mask aligner used not being high enough and to the designed masks not having sufficient tolerances to overcome slight misalignments. Since there were so many masks involved, even a small misalignment could lead to the structures not overlapping when they should, or structures overlapping when they should not be touching. For example, Fig. 4.26 shows the outlines of the arsenic implantation area, the gate oxide area, and the area of the oxide windows, of a faulty device. In regards to the gate oxide, the arsenic is too far left as well as up in the image (indicated in orange in Fig. 4.26). The oxide windows are also too far left (indicated in green). This resulted in the oxide window at the far right touching the gate oxide, as shown in red in Fig. 4.26. The misalignment is such that the two lower oxide windows only barely overlap with the arsenic implanted area. The designed masks allow for a misalignment of only 2 - 5 μm. The accuracy of the mask aligner (Quintel Mask Aligner Q4000-6) is given as 1-2 μm, adding up to a maximum error of 4 μm. Even with great care at each photo lithography step, the error of misalignment can be as large as the tolerance of the design.

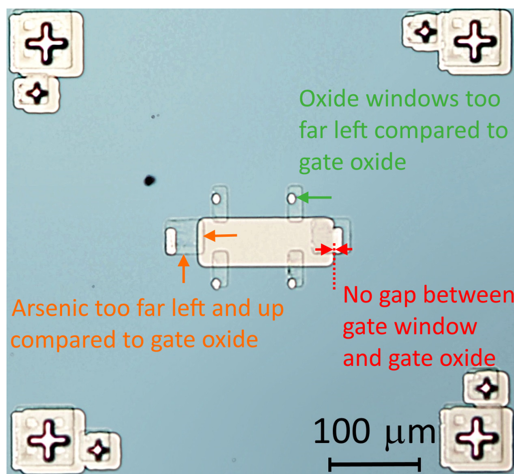

Figure 4.26: Optical image taken with a microscope of a device prior to metal evaporation.

Another issue turned out to be the etching of the silicon dioxide using HF. This is a wet etch. The etch rate depends on the sample remaining

undisturbed after its transferral into the HF solution until it is taken out after the etch time is up. If the solution is stirred during the etch, the movement of the HF will cause the etch rate to be higher due to 'fresh' HF coming in contact with the etched areas, and will also result in a more isotropic etch (see Fig. 4.6).

The oxide quality was an issue with the available MU furnace. Contamination can cause the oxide to lose its electrical insulating properties. Contaminants can also migrate during subsequent processing steps and cause further problems. Testing the oxide quality of the particular furnace used is important to achieve functioning, non-leaking devices.

Due to the known issues with the fabrication flow available at UM, the UNSW devices were developed. The equipment at UNSW was cleaner because of stricter protocols, and thus more reliable in producing good results. However, during the gate oxide growth of the UNSW samples there was an unfortunate error in the process flow used during the high quality gate oxide growth. The di-chloro ethylene used to clean the furnace prior to oxidation was left flowing throughout the growth process, which caused the gate oxide to be slightly thicker than originally planned (30 nm instead of 20 nm). This could be accommodated by an adjustment of the Er^{3+} implantation energy. However, measurements on the fabricated devices also suggest that this processing error had other deleterious affects on device performance, was detailed later.

Chapter 5

Diamond devices: Experimental Results and Analysis

This chapter presents N-UNCD films of three different nitrogen concentrations and includes results of atomic force and scanning electron microscopy, in addition to conventional microscope and 3D optical profilometry, as well as Raman and x-ray photoelectron spectroscopy. Rutherford backscattering spectroscopy (RBS) is demonstrated and electrical measurements using the previously described dilution refrigerator, including temperature and magnetic field dependency, are detailed. The results presented here give a detailed characterization of the examined materials, and can confidently be used to determine the origin of electrical conductivity at low temperatures.

5.1 AFM and SEM imaging

The samples appear smooth and featureless under a conventional optical microscope (Fig. 4.8). The optical profilometer shows an even surface with sharp side walls (Fig. 4.7). In order to visualize the structure of the grown

diamond, we used atomic force microscopy (AFM) as well as scanning electron microscopy (SEM). Figure 5.1 shows an AFM image taken of a 20% nitrogen enhanced grown N-UNCD film. The scale is rather large, with 1 μm x 1 μm being the dimensions of the figure. Unfortunately it was not possible to get images of higher resolution due to the smoothness of the sample and the limits of the sharpness of the AFM tip. The picture shows a wool-like structure. It was not possible to zoom in far enough to see the grains themselves; consequently we do not know the grain size.

SEM on the other hand enabled us to zoom in further onto the N-UNCD films. The FEI Nova dual beam - focussed ion beam (FIB) system situated at the Bio21 institute was used for all recorded SEM images. Figures 5.2, 5.3, and 5.4 show SEM scans taken of the 5%, 10%, and 20% nitrogen enhanced grown N-UNCD samples. Figures c) and d) in 5.2 and 5.4 show the films at an angle of 45° tilt. The 5% N-UNCD film looks as if there are flakes sticking out of the surface. Unfortunately it was not possible to identify individual grains. The 10% and 20% films have much sharper surface details compared to the 5%. They look as if they consist of individual spikes. Images c) and d) of Fig. 5.3 show a cross section milled with the FIB (Focused Ion Beam). The surface was first protected with platinum (smooth white layer on top) and then

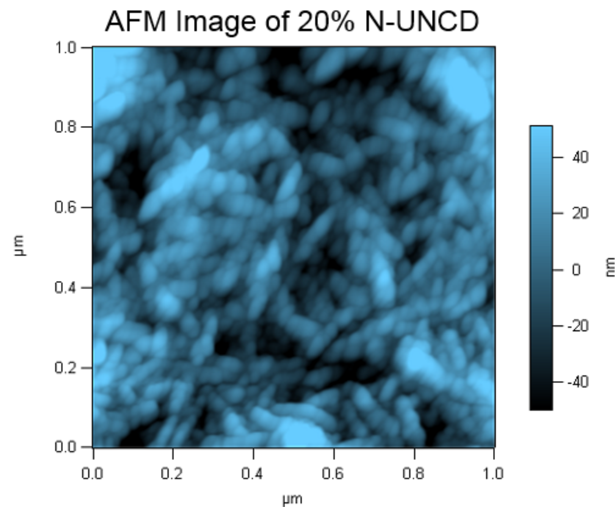

Figure 5.1: AFM image taken of the 20% N-UNCD sample.

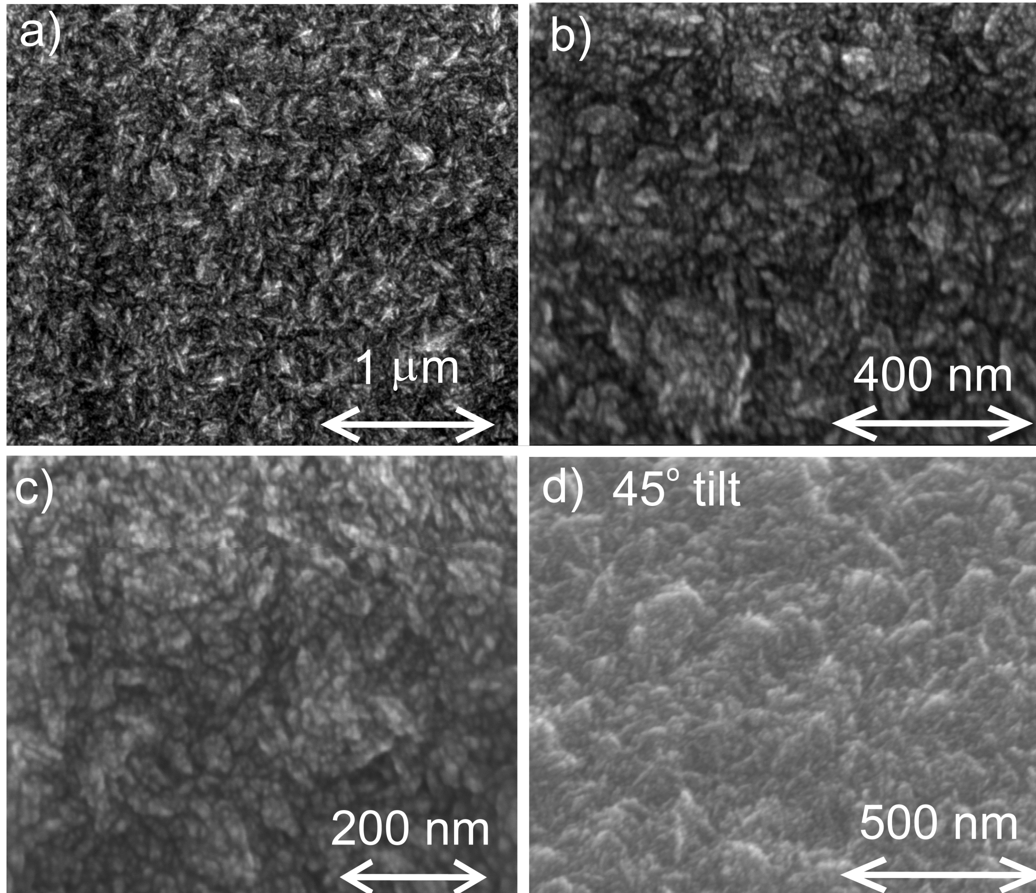

Figure 5.2: SEM images of the surface of a 5% N-UNCD film. a), b), c) normal to the surface, and d) with a 45° tilt in regards to the surface plane.

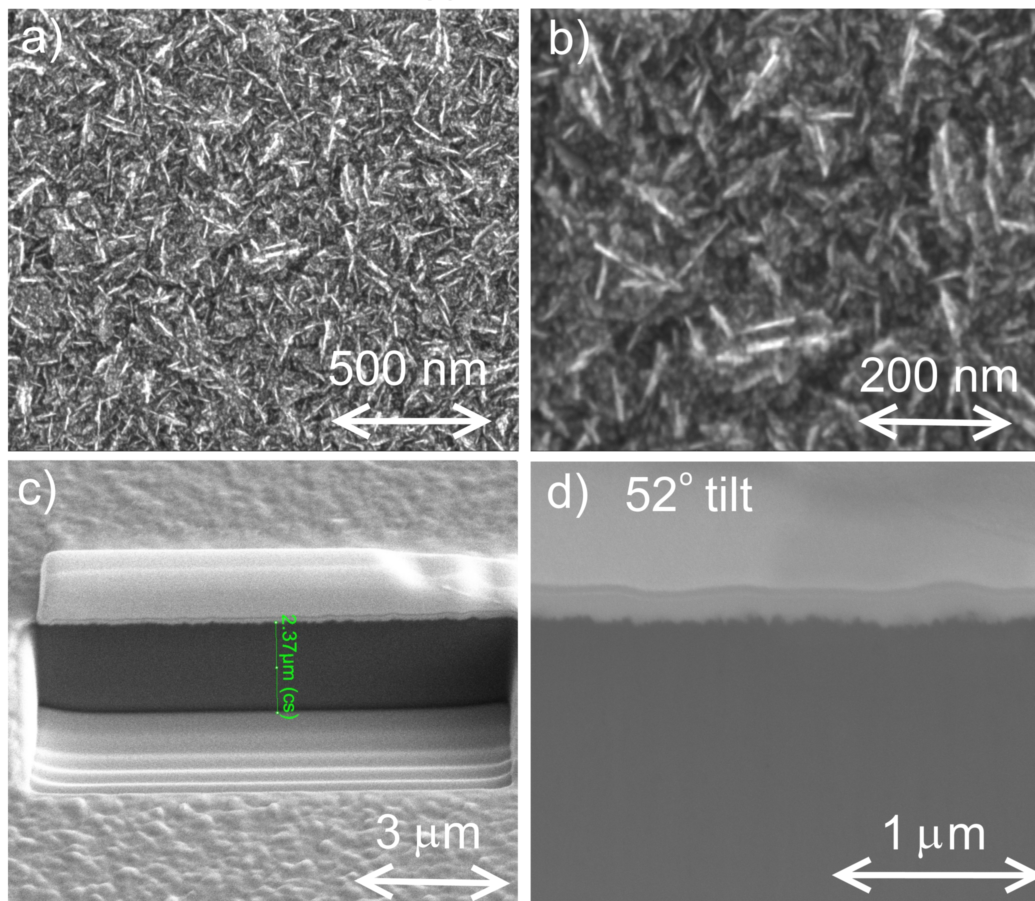

Figure 5.3: SEM images of a 10% N-UNCD film. a), b) top view of the surface, c) top view of the cross section milled via FIB, and d) view at a 52° of the cross section created by via FIB milling.

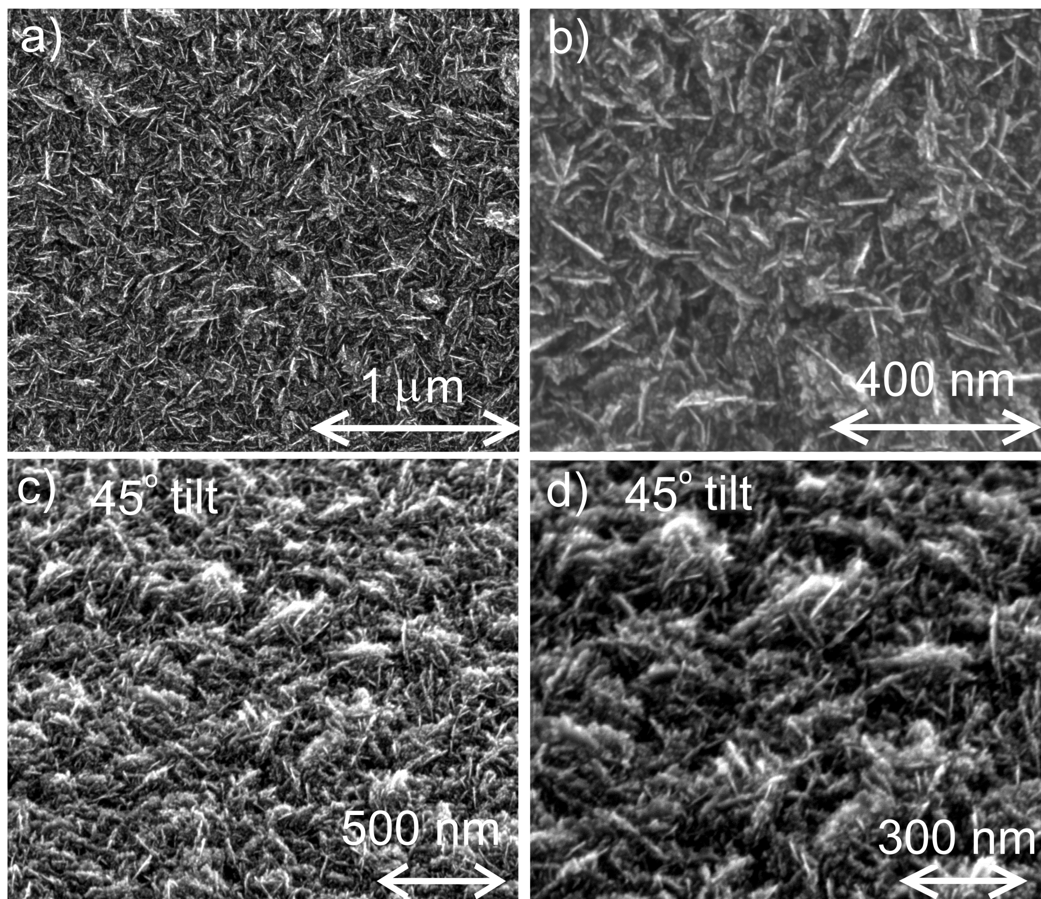

Figure 5.4: SEM images of a 20% N-UNCD film. a), b) normal to the surface, and c), d) with a 45° tilt in regards to the surface plane.

etched with a gallium ion beam. The dark part is the N-UNCD film. One can see the rough line which forms the interface between the sample surface and the protective platinum. The bulk of the N-UNCD is very homogeneous; there is no structure visible. This means either that the little structure that we see is only on the surface while the bulk is very smooth, or this impression of homogeneity created by the smoothness in the taken images could be due to the etching with the FIB influencing the structure. Transmission electron microscopy (TEM) would possibly have helped answer the question as to the structure of the bulk, but we chose to cut with a diamond scribe through the length of the sample and then mount it into the SEM and view it from the side. This was a much faster method of getting an image of the N-UNCD bulk.

The SEM images of the cut are shown in Fig. 5.5 a) through f). On the images we can see the individual layers, as indicated. In all three films we can see that the previously seen structure of the N-UNCD surface goes throughout the whole layer (blue, Fig. 5.5 e)), ∼940 nm. It has larger features than the undoped UNCD layer beneath it which is much smoother (green) with a thickness of ∼780 nm. It seems to have a flake-like appearance. The silica (amorphous; orange, ∼700 nm thick) as well as the silicon substrate (single crystal; yellow, Fig. 5.5 e)) are smoother and less textured, as expected. They are distinguished by a fine line that makes up the Si/SiO_2 interface. The thickness of the individual layers varies slightly over the whole area of the sample. These variations are very small. They do not play an important role for data analysis, as they hardly affect the Hall resistivity and as such are acceptable.

Conclusion We can conclude from the AFM and SEM imaging that the graininess observed on the surface of the N-UNCD films of all nitrogen concentrations is also characteristic of the bulk material. The observations show

5% N-UNCD

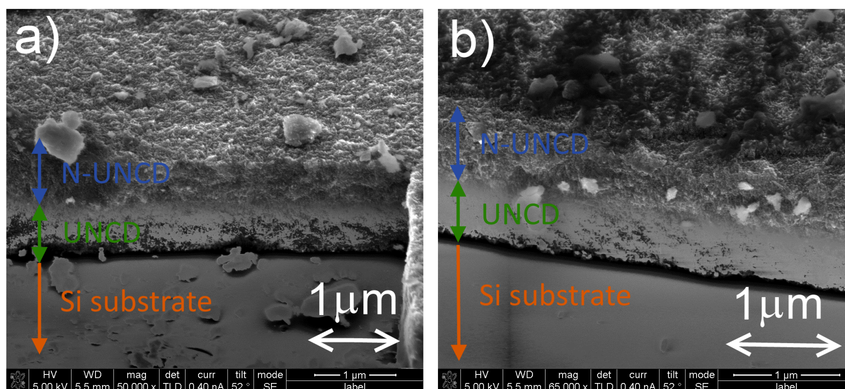

10% N-UNCD

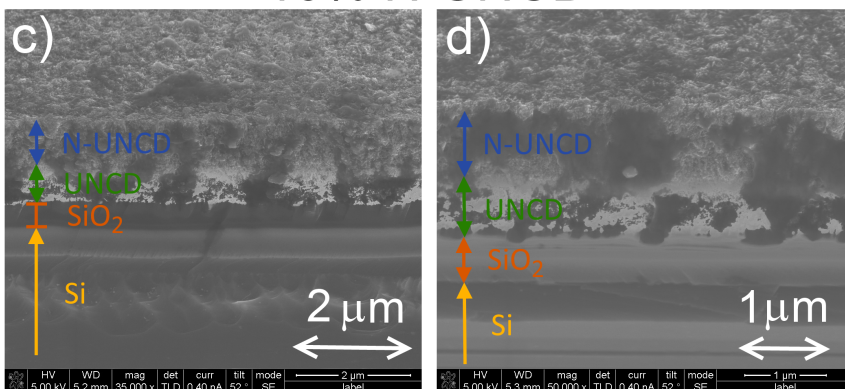

20% N-UNCD

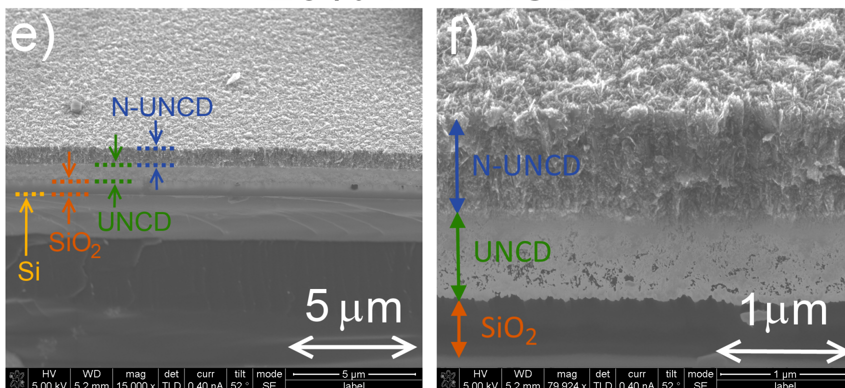

Figure 5.5: SEM images of cuts through the 5%, 10%, and 20% N-UNCD films.

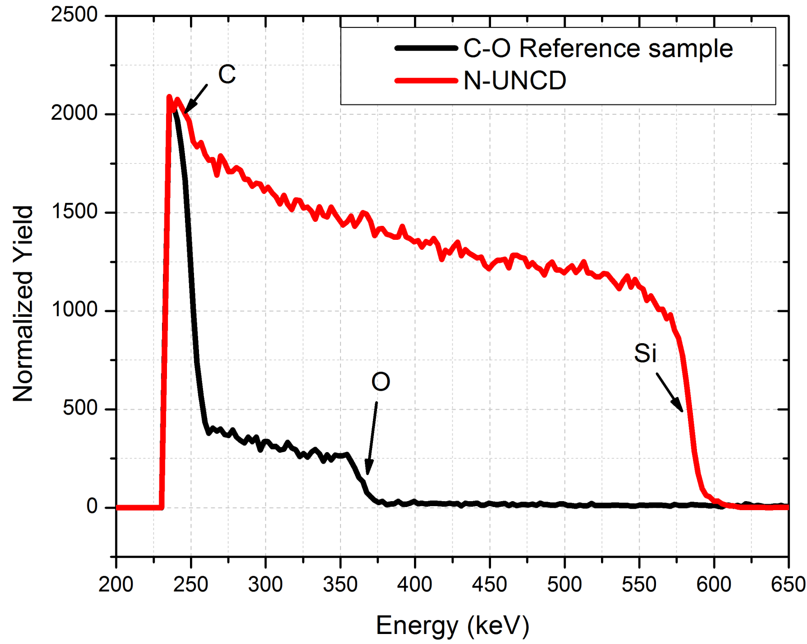

Figure 5.6: RBS spectrum of the 20% N-UNCD film (red) and the C-O reference sample (black) with an incident alpha particle energy of 1 MeV and backscatter angle of 10°.

that the grown films are homogeneous in all three dimensions, and the material is a granular thin film. Thus, measurements on the material will be characteristic of the bulk properties, not just the surface layer. Hence the planned Hall measurements are an ideal tool to identify the origin of electrical conductivity in these thin films.

5.2 RBS

RBS measurements were undertaken in an attempt to determine the total amount of nitrogen incorporated into the films, as explained in chapter 2.2. Fig. 5.7 shows a cross section of the examined N-UNCD sample. It proved difficult to extract information regarding the nitrogen content due to carbon and nitrogen having so similar (and relatively light) masses (of

12 u and 14 u, respectively) and therefore also similar scattering properties. With an incident alpha particle energy of 1 MeV, and a backscatter angle of 10°, we calibrated the detector with 4 reference samples as described in chapter 2.2. Then we acquired the RBS spectrum of the 20 % N-UNCD film as shown in Fig. 5.6. We observed a silicon peak (at ∼581 keV), originating in the silicon substrate, as well as a small carbon peak (at ∼ 245 keV) from the top UNCD layer. We did not observe nitrogen. This is due to the energy of nitrogen (311.5 keV) and carbon (252.9 keV) (source of energy values: XRUMP) being so close to each other. We also expected only a small amount of nitrogen to be incorporated into the N-UNCD film, so the intensity of the nitrogen peak would be very low, rendering it hard to observe.

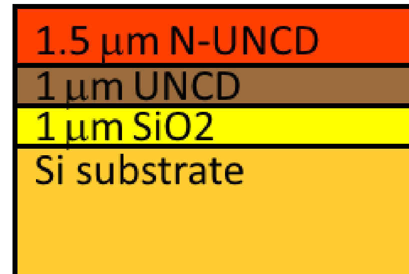

Figure 5.7: Cross section of the RBS sample.

Resonant RBS (RRBS) As a new approach, we changed the incident particles to protons with an energy at which nitrogen shows a resonance (RRBS = resonant RBS). In resonance, the yield of this particular element is multiplied. Thus we tried to 'boost' the nitrogen peak, while not changing the peak heights of other elements. We chose an incident particle energy of 2.338 MeV according to [163] Fig. 5.8. At this

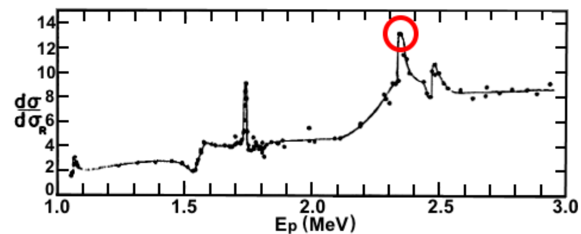

Figure 5.8: Normalized yield versus incident proton energy in the laboratory system E_p [163]. The red circle indicates the energy used for RRBS.

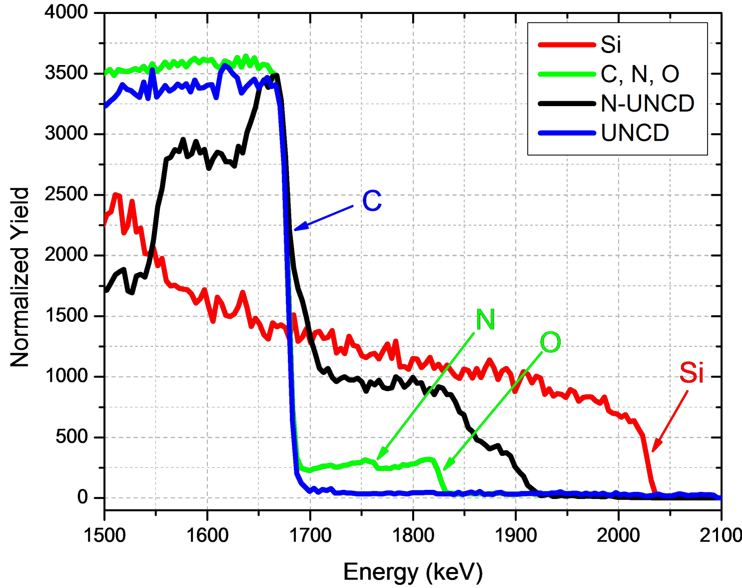

Figure 5.9: RRBS spectrum of the 20% N-UNCD film (black), Si reference sample (red), Kapton reference sample (green), and UNCD reference sample (blue) with an incident proton energy of 2.338 MeV and 10° backscatter angle.

energy, carbon and silicon also show some broad range resonance [164]. As we were looking at relatively low energies of the backscattered particles, we used a higher gain in the experimental setup, rendering the calibration samples with heavier elements useless. Consequently, we could only use organic samples for calibration purpose. We used a pure Si sample and a Kapton sample ($C_{22}H_{10}N_2O_5$). As N was now in resonance, we expect to be able to detect the nitrogen making up 5.13% of the composition in the Kapton sample. In addition, a sample consisting of a bulk of undoped UNCD was used as further reference for carbon.

In Fig. 5.9 the calibrated RBS spectrum of the N-UNCD sample (black) is shown together with the silicon reference sample (red), the Kapton reference sample (green) and the undoped UNCD (blue). It is obvious that the carbon front edge of the UNCD matches the carbon front edge of the Kapton sample very well. This also overlaps with an edge in the N-UNCD spectrum,

so we conclude that this is the carbon front edge. We ran a simulation to match up all the features of the spectrum. Fig. 5.10 a) contains this simulation (red) as well as interpretations of the N-UNCD spectrum of the information we gathered from the simulation.

Fig. 5.10 a) shows the RBS data for the N-UNCD (20%) sample (black line) and a simulation of the layered structure in Fig. 5.7 (1.5 μm N-UNCD (0% N) + 1 μm UNCD + 1 μm SiO_2 + Si substrate) using XRUMP (red line). The XRUMP simulation does not take into account the enhanced (non-Rutherford) scattering cross-sections for 2.338 MeV protons backscattering from N and from C. The scattering cross-section from C is enhanced by about a factor of 3 in the RBS data. The fact that the edges (Si, Si in SiO_2, O in SiO_2, C) agree between the RBS data and the simulation indicates that the sample does have the layered structure and thicknesses as per the schematic in Fig. 5.7. Figure 5.10 b) shows details of the RBS data and the region where N should appear in the spectrum compared to simulations with 0% (red), 10% (blue), and 20% (green) N in the N-UNCD layer. As noted, the XRUMP simulations do not take into account the non-Rutherford scattering cross-section for N which is enhanced in this energy regime. Nevertheless, the XRUMP simulation for 20% N in the N-UNCD layer clearly shows a plateau in the simulation despite the enhanced cross-section not being taken into account. The lack of evidence of such a plateau in the measured data indicates that the retained N in the film must be much less than 20%. In fact, the data in Fig. 5.8 shows that at the measurement energy the cross-section for scattering from N is enhanced by a factor of 12 over the Rutherford cross-section (which is used in XRUMP). Hence the N related plateau in the 20% simulation (green) corresponds to (20/12)=1.6% N actual. The measured data is at most equivalent to the 10% N simulation which corresponds to 0.8% N actual. Hence the RBS data and simulations show that the retained N in the films is less than 1%.

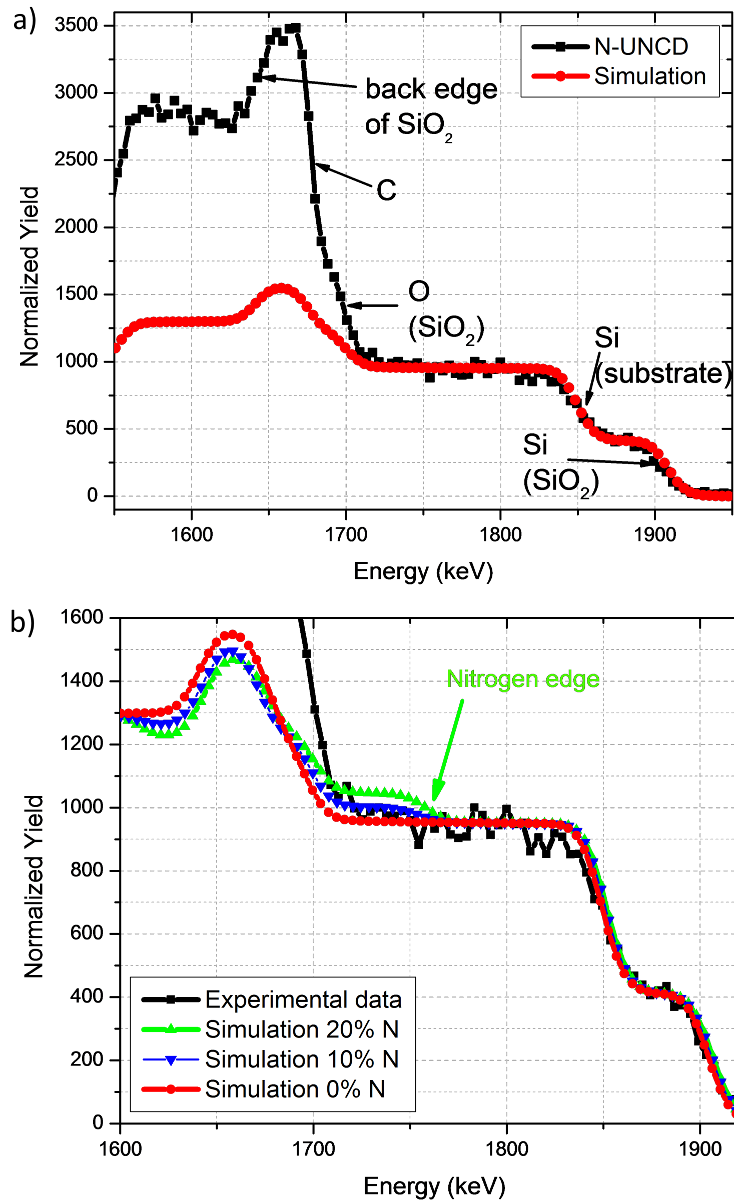

Figure 5.10: a) RRBS spectrum of the 20% N-UNCD film (black) including a simulation (red) and interpretation of the spectrum. b) Same RRBS spectrum of N-UNCD (black) with the simulation of UNCD containing 20% N (green), 10% N (blue), and 0% N (red) with an incident proton energy of 2.338 MeV and 10° backscatter angle.

We were not able to detect a nitrogen induced edge in this sample, even though this material had the highest percentage of nitrogen addition during CVD growth. We concluded that RRBS was not a technique sensitive enough to detect nitrogen in the N-UNCD films. Further investigations using other methods were required to measure how much nitrogen is incorporated during CVD growth.

5.3 Raman Spectroscopy

The inconclusive results of the RBS data made us believe that there was much less nitrogen incorporated into the N-UNCD films than first suspected. Raman spectra were taken of the samples as a well known method of characterizing the carbon bond types in the films. The Raman spectra were all collected with a Renishaw inVia Raman system at a laser excitation wavelength of 532 nm, a laser power of about 60 W, and a 20X magnification. All measurements were performed at room temperature.

The Raman spectra of the as-grown N-UNCD films with N_2 concentrations of 5% (black), 10% (red), and 20% (green) are shown in Fig. 5.11. There is no silicon peak (at 520 cm^{-1}) associated with the substrate visible due to the laser light not penetrating through the diamond layer into the silicon. The optical absorption of UNCD films is expected to increase with increasing nitrogen content due to the higher absorption of nitrogen [58]. According to our RRBS results on the other hand, only a small amount of nitrogen could possibly have been incorporated into the films. Thus we would not expect to see a correlation between Raman intensity and percentage of nitrogen in the gas feed stock because the Raman intensity is not reliable enough and we were not able to calibrate it sufficiently accurately to show such a small dependence. In Fig. 5.11 we can see that while the 5% nitrogen enhanced grown film shows the highest Raman intensity, the 10% N_2 film shows a lower Raman signal than the 20% N_2 film. As such, we can see that

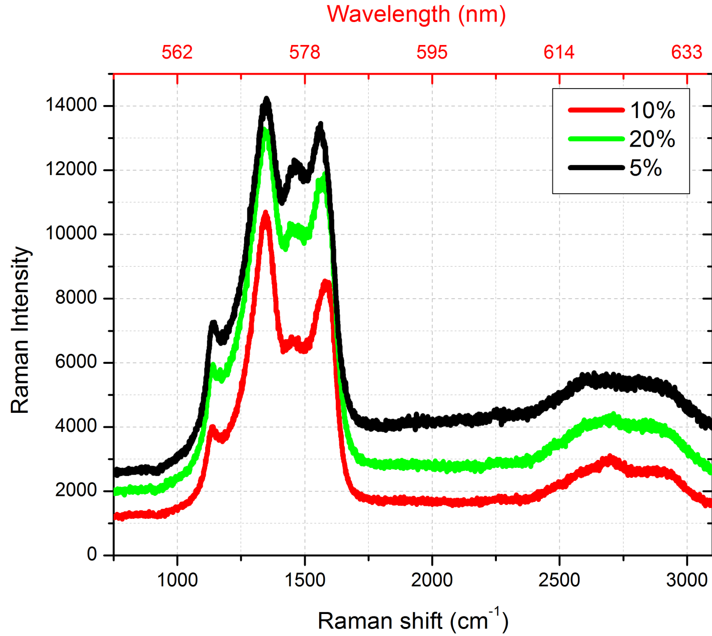

Figure 5.11: Raman spectra of the 20% (green), 10% (red), and 5% (black) nitrogen enhanced grown N-UNCD.

a Raman intensity is not dependent on the amount of nitrogen added to the gas feed stock during CVD growth.

Two broad features at about 1347 cm^{-1} and 1567 cm^{-1} are obvious. These are characteristic for these films and have been observed in [57] [58]. The first is the peak of the diamond-band (D-band) originating in the sp^3 bonds in the carbon, and the latter of the graphite-band (G-band) originating in the sp^2 bonds. The higher energy in the sp^2 bonds results in the higher frequency in the Raman shift [62]. The ratio of their intensities I(D)/I(G) relates to the level of disorder in the grain boundaries. As the ratio is related to the size of the crystalline graphite grains, a higher value indicates a higher level of disorder (see Concado et al. [62]). With higher nitrogen concentration, the grain size increases. The increased grain size leads to a more ordered graphite and is visible in a sharper and more intense D peak. According to Vlasov et al. [58] the ratio of I(D)/I(G) increases with increasing

nitrogen content. On the other hand, Chimowa et al. [63] have previously observed that the ratio rises with increasing nitrogen doping, followed by a rapid decrease in the high nitrogen percentage regime. In our data we can see an increase of I(D)/I(G) from 1.13 at 5% to 1.25 at 10% doping, then dropping back down to 1.13 with the 20% nitrogen enhanced grown film. So there is no obvious trend to be seen. The position of the G-band has been observed to shift to higher numbers with more incorporated nitrogen [58]. Our data shows a shift of the peak position from 1559.3 cm^{-1} at 5% to 1583.5 cm^{-1} at 10% and back to back to 1566.7 cm^{-1} with the 20% material. The broad 2D-band at around 2700 cm^{-2} indicates we have parts of stacked layers of graphene-like carbon in the N-UNCD films [61]. The Raman band at about 1140 cm^{-1} originates from trans-poly-acetylene (TPA-band) and can be reduced by annealing [60] or plasma etching [61]. These samples were not heat-treated; therefore they all show the TPA-band.

5.4 XPS

The RBS as well as Raman data show hardly any traces of nitrogen in the N-UNCD films. Next, we used XPS to determine the amount of nitrogen incorporated into the N-UNCD samples analogue to the work published by Garrett et al. [56]. Since XPS is very sensitive and shows even tiny contaminations on the sample surface, we hoped that XPS would enable us to compare the amount of nitrogen incorporated into the 5%, 10%, and 20% nitrogen enhanced grown samples. Garrett et al. reported no visible nitrogen in XPS spectra even for 20% N in the gas feed stock, but instead a change in the type of carbon bonds [56]. For the XPS measurements we used a Thermo k-alpha x-ray photo-electron spectrometer, located at RMIT university. The samples were under a vacuum of $p = 5 \cdot 10^{-9}$ mbar during measurements.

Fig. 5.12 top shows the survey scan in counts per 1000 seconds versus the electron binding energy of the 20% N-UNCD sample. We used a dwell

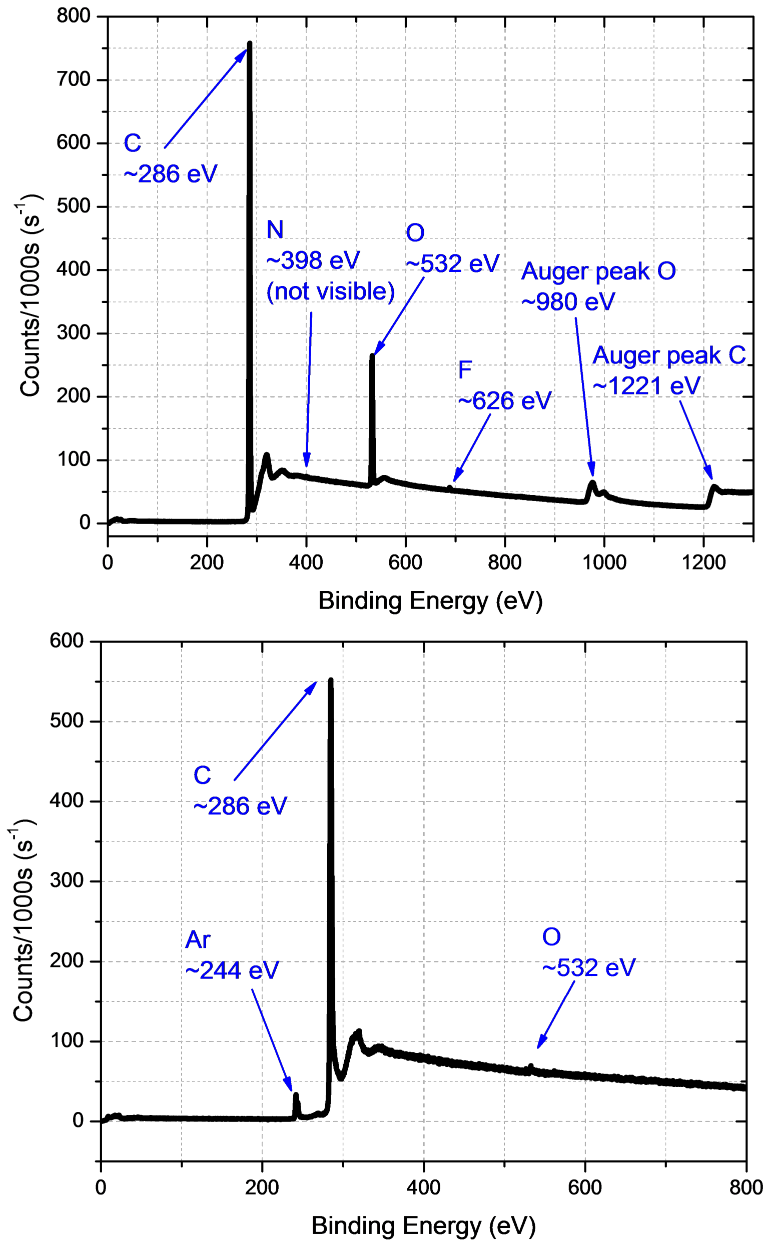

Figure 5.12: XPS spectrum of 20% N-UNCD, showing the counts per 1000 s versus the binding energy. Highlighted are the characteristic peaks for carbon, nitrogen, oxygen, as well as fluorine and the Auger peaks of oxygen and carbon. Top: Before Ar sputtering. Bottom: after the top layer was removed via Ar sputtering.

time of 10 seconds and did 20 scans per spectrum. The characteristic peaks of carbon (~285.5 eV), and oxygen (~532.4 eV) are clearly visible in the spectrum as expected (binding energies from [165]). The oxygen peak is hardly surprising, as XPS is a very sensitive technique and picks up on any element on the examined surface. With the sample having been to atmosphere, where oxygen is available in abundance, some of the oxygen will have formed bonds to the carbon on the surface. We expect to see nitrogen at around 398 eV (according to [166]), but this peak is not visible in the spectrum. On the other hand, we see fluorine at 686 eV, which may be due to possible contamination by the tweezers used to handle the sample during HF and BHF etching. We also observe the Auger peak of oxygen at ~979.7 eV and of carbon at ~1221.4 eV. The XPS spectra of the 10% and 5% sample looked very similar, with the same peaks visible in the same locations, so they are not shown here. We expected to see a nitrogen peak in the energy range 398 eV. Despite doing 50 scans in this energy area to obtain higher resolution data, no peaks corresponding to nitrogen were observed in any of the spectra. Figure 5.13 d) shows the XPS spectrum of the 20% nitrogen enhanced grown N-UNCD in counts per second versus binding energy in the area of around 400 eV. An FFT filter (red) is used to smooth the raw data (black). Even when using the FFT filter, no nitrogen peak can be seen.

Since XPS analyses only the first few nm of the surface, the results are not representative for the bulk material. In order to acquire information about the material further in, we used Ar to sputter away ca. 20 nm of the top material. A survey scan of the 20% thin film after Ar sputtering is shown in Fig. 5.12 bottom. In addition to the previous visible peaks of carbon and fluorine, we can now also see an argon peak at around 244 eV. This is due to residual argon from the sputtering process. The oxygen peak disappeared, proving our suspicion of oxygen having formed surface bonds with the top carbon layer, and proving that oxygen has indeed not penetrated the bulk material. However a nitrogen peak is still not to be seen.

According to Al-Riyami et al. [167] the presence of nitrogen in the gas feed stock changes the chemical bonds in the carbon. The ratio of sp^2 to sp^3 bonds of carbon atoms changes from mainly sp^3 bonds in the undoped diamond structure to more and more sp^2 bonds with increased nitrogen, resulting in a more graphitic structure [167]. There are reports in the literature stating that nitrogen is incorporated into the grain boundaries of UNCD when it is added to the gas feedstock [167, 56]. However our results show no evidence, within the sensitivity of the XPS measurements, of nitrogen incorporation. It is clear that the addition of nitrogen changes the properties of the films, particularly the electrical properties. But these changes must be due to subtle differences in the structure of the films induced by the presence of nitrogen in the plasma, rather than incorporation of nitrogen into the films.

	sp^2	sp^3	sp^2/sp^3
20%	(57.5±0.8)%	(67.8±0.8)%	84.8%
10%	(55.6±0.8)%	(70.3±0.8)%	79.1%
5%	(55.0±0.8)%	(71.9±0.8)%	76.5%

Table 5.1: Ratio of sp^2 and sp^3 bonds of carbon found from XPS. Errors estimated from the accuracy of the peak fitting.

Figure 5.13 shows the carbon peak of the XPS spectra of the 20%, 10%, and 5% nitrogen enhanced grown N-UNCD. The carbon peak is at a binding energy of 285.58 eV and split up into the sp^2 (green) and sp^3 (blue) bonds, with their peak positions at 285.28 eV and 285.78 eV, respectively. The fits were made according to [167] with a Voigt curve. Their superposition is presented by the red curve. The ratio of sp^2 to sp^3 bonds is given in Table 5.1. The errors of the percentages were estimated by the accuracy of fitting the peaks. There is hardly any difference visible in sp^2/sp^3 within the errors.

At this point secondary ion mass spectrometry (SIMS) would have been a plausible technique to utilize in order to determine confidently the absolute

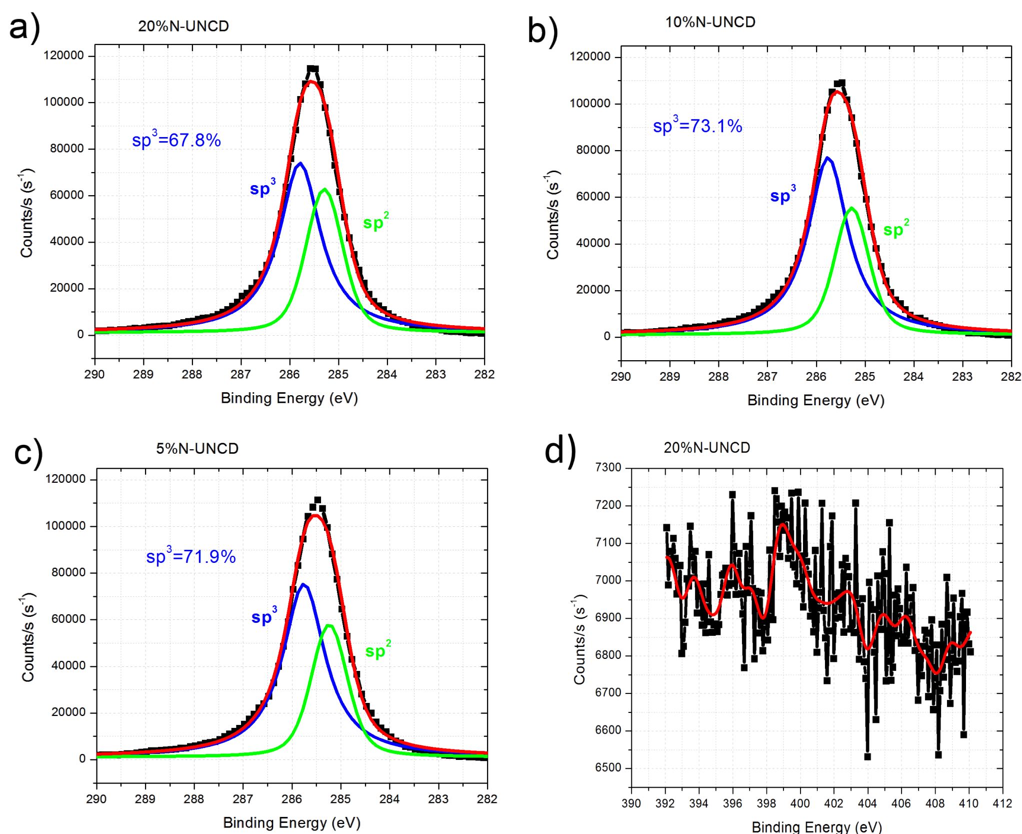

Figure 5.13: a)-c): XPS spectra of 20%, 10%, and 5% N-UNCD, showing the counts per s versus the binding energy. Black is the raw data, blue is the fit for the sp^2 carbon, green is the fit for the sp^3 carbon, and red the superposition of the two fitted curves. d) XPS spectrum of 20% N-UNCD in the area of around 400 eV, designed to search for evidence of the presence of nitrogen. An FFT filter (red) is used to smooth the raw data (black). The image consists of 50 scans, but no evidence of a nitrogen peak is visible.

amount of nitrogen in the films. SIMS is a very sensitive method to analyse the elementary composition of the surface of a solid. Unfortunately a SIMS facility was not available. Elastic recoil detection analysis (ERDA) was used by Achatz et al. [65] to determine the amount of incorporated nitrogen in relation to the amount of nitrogen in the gas phase. They reported that an increase of nitrogen in the gas phase above a certain value between 5% and 10% does not lead to an increase of nitrogen incorporation in the films. The with ERDA measured maximum nitrogen concentration normalized to the bulk volume was 5×10^{20} cm^{-3}, which was almost ten times higher than the Hall carrier concentration [65]. ERDA was not a technique available to us, so we could not use this technique to compare the materials examined.

5.4.1 Analysis of Raman and XPS

The images of the Raman spectra (see [168] for information on Raman spectroscopy) do not show a fixed tendency with increased nitrogen content. This together with the results of the XPS spectra show that there is essentially no change in nitrogen concentration between the films of varying nitrogen concentration during CVD growth. We draw the conclusion that the enhanced conductivity (presented in chapter 5.5) originates within the increased sp^2 carbon bonds. While the localized sp^3 carbon atoms present a fixed barrier, the sp^2 carbon bonds allow diffusive charge carrier transport. The Raman spectra leave the possibility that the nitrogen is in the grain boundaries of the UNCD crystals. However, the XPS measurements do not show measurable nitrogen content in any of the films of either of the doping concentrations (see section 5.4). We might as a result not speak of doping, but rather nitrogen enhanced UNCD growth as it is not incorporated into the diamond film. What the XPS scans show is a slight change in the ratio of sp^2 to sp^3 bonds in the carbon. With higher nitrogen concentration in the CVD gas there is a subtle increase in the number of sp^2 bonds. Also with higher

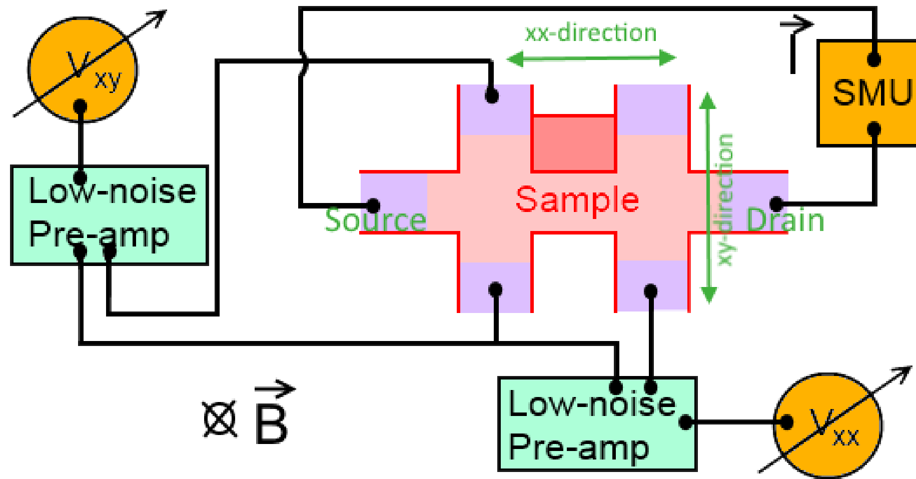

Figure 5.14: The electrical setup of the hardware for Hall bar measurements.

nitrogen concentration in the CVD gas the electrical conductivity of the film increases.

5.5 Electrical measurements

The electrical measurements were carried out in the dry dilution refrigerator described in chapter 3. Using the electrical setup of Fig. 5.14 the Hall bar configuration of the samples was used to determine resistivity, conductivity, and other parameters of the samples using the equations of section 3.4. The source-drain current I_{SD} across the length of the Hall bar was applied by a source-measure unit (SMU) by Keithley which simultaneously measured the resulting source-drain voltage V_{SD}. The voltage along the sample length V_{xx} as well as across the source drain current V_{xy} were measured with low-noise pre-amplifiers of Stanford Research Systems Model SR570 connected with 6 1/2 digit multimeters by Agilent 34410A.

The current versus voltage (IV) graph, as shown in Fig. 5.15, is used to calculate the resistivity of the films. At room temperature all N-UNCD films

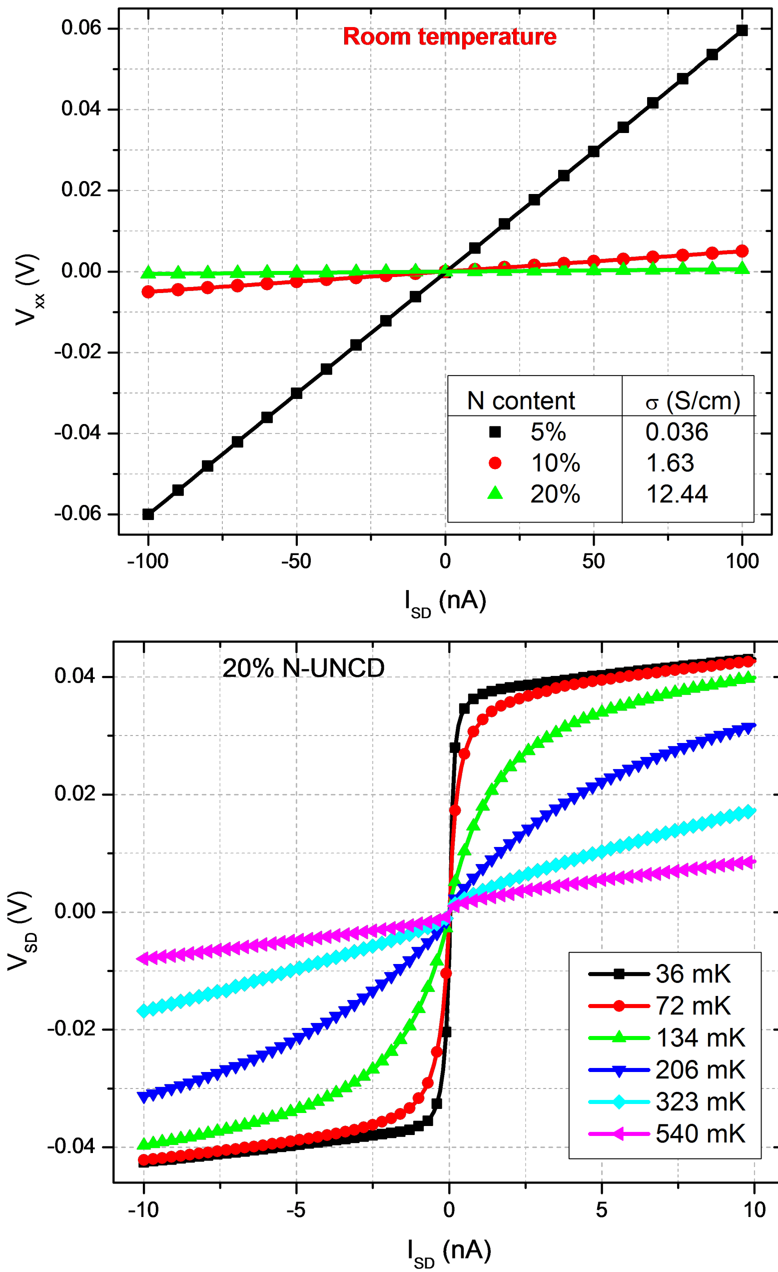

Figure 5.15: 4-terminal IV curves. Top: at RT of the 5%, 10%, and 20% N-UNCD films. Bottom: at varying low temperatures of the 20%N-UNCD film showing the non-linear feature.

are expected to show a linear response and indeed we observe it (Fig. 5.15 top). From these we calculated the conductivities of 12.44 S/cm, 1.63 S/cm, and 0.036 S/cm for the 20%, 10%, and 5% N-UNCD films respectively. Below a critical temperature, however, the IV curve shows a non-linear feature. This non-linearity becomes more prominent with decreasing temperature, as pictured in Fig. 5.15 bottom. The critical temperature depends on the amount of nitrogen in the gas feed stock. The 20% N-UNCD film starts to show the non-linearity below ∼1 K, and the 10% N-UNCD films below ∼1.5 K. We do not observe this phenomenon for the 5% N-UNCD samples, as it becomes too resistive to measure at around 14 K, at which temperature there is no non-linear feature in the IV visible yet. The non-linear behaviour is observed in both the two point voltage V_{SD} and the four-point voltage V_{xx}, as well as the V_{xy} voltage. This indicates that the origin of this feature is not found in the interface of the metal to the N-UNCD film (ohmic connection), but rather within the N-UNCD itself. Instead, a barrier is present within the bulk material itself, which can be overcome as long as the temperature (or kT) is high enough. This is in agreement with the SEM results (section 5.1) that led to the conclusion that the material is a granular thin film. Evidently a tunnelling barrier exists at some point in the interconnected network of conducting grain boundaries and at sufficiently low temperature we see Coulomb blockaded transport through the barrier. Thus it is possible that we may be observing the Coulomb blockade effect in the non-linear IVs [169, 186]. The charging energy controls the transport property of the films and is influenced by the temperature and grain size [169]. The result is an IV characteristic showing the Coulomb blockade from which we can read the threshold voltage required for linear transport [186].

Temperature dependence The temperature dependence of the conductivity was measured with a constant source-drain current of around $I_{SD} = 100$ nA. This value was chosen to ensure the IV curve was in the linear regime

throughout the whole temperature range, keeping in mind that the non-linear feature extends to higher voltage/current values at low temperatures. The voltages V_{xx} and V_{xy} were constantly monitored while the sample temperature was varied. The result of conductivity versus temperature of all three nitrogen concentrations are shown in Fig. 5.16 with the 20% N-UNCD in black, 10% N-UNCD in red and 5% N-UNCD in green. Throughout the whole temperature range the conductivity increases with increasing nitrogen content. All three films show decreasing conductivity with decreasing temperature values, and the 5% sample even experiences charge carrier freeze out at a temperature of about 14 Kelvin. Consequently no electrical measurements can be undertaken below this observed freeze-out temperature on this sample. Note that the method of using a constant source drain voltage as opposed to taking an IV measurement at each temperature point will alter the calculated sample resistivity. Accordingly, in Fig. 5.15 we can see that when the IV is in the non-linear temperature range, the calculated resistivity will always be higher than the actual value gathered from fitting the linear part in the IV curve. Unfortunately the fridge provides us with no means of holding the temperature constant for long enough to acquire a whole IV scan at every point between 4 K and room temperature. If we consider the graph of $\ln(\sigma)$ versus 1/T in the bottom of Fig. 5.16, we notice that the conductivity almost levels out below a temperature of about 200 mK for the 20% as well as 10% N-UNCD films. Since the 5% nitrogen enhanced grown sample froze out well before that, we cannot observe a flattening of the curve.

Magnetic field dependence Magneto resistance data was taken with the superconducting three dimensional vector magnet incorporated in the dilution refrigerator, as described in chapter 3. At a constant temperature, we swept the magnetic field perpendicular to the sample plane, while applying a constant source-drain current and recording the source-drain voltage, as well as V_{xx} and V_{xy}. The magnetic field dependence was only measured for the

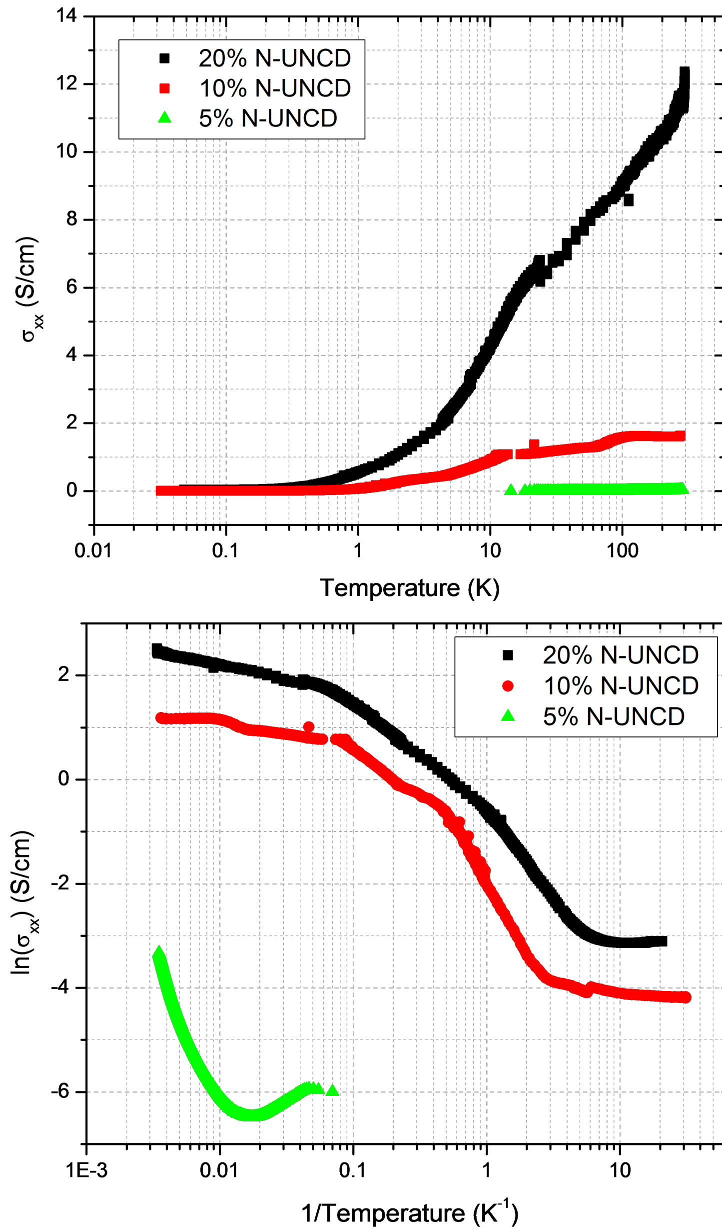

Figure 5.16: Top: Conductivity versus temperature of the 20% (black), 10% (red), and 5% (green) N-UNCD films on a half logarithmic scale. Bottom: Logarithm of conductivity versus 1/temperature on logarithmic scale of the 20% (black), 10% (red), and 5% (green) N-UNCD films.

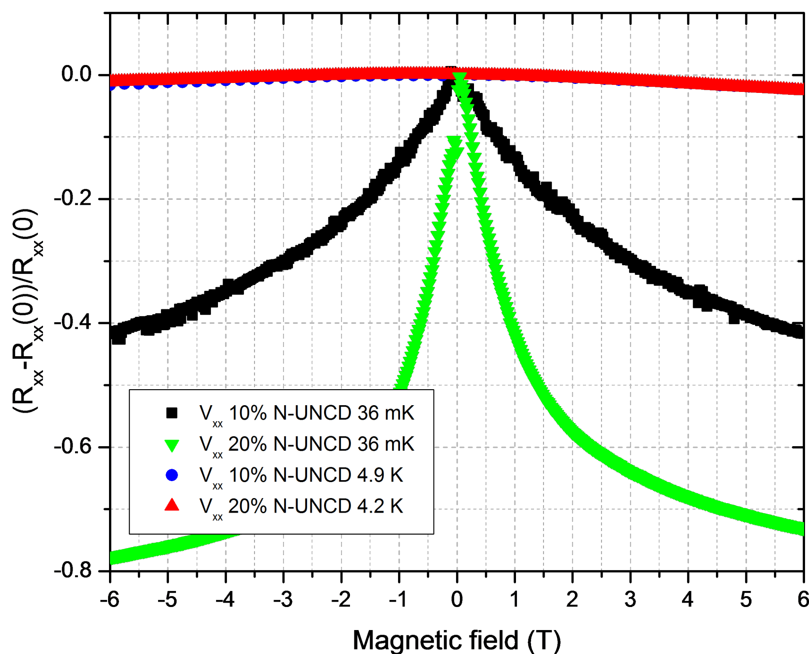

Figure 5.17: Normalized resistance as a function of magnetic field of the 20% and 10% N-UNCD films at 36 mK (green and black) and 4.2/4.9 K (red and blue - overlapped by the red).

20% and 10% N-UNCD films. It was not possible to measure the 5% films as they did not conduct below 5 K, which is the maximum temperature at which the superconducting magnet operates. The source-drain current I_{SD} was chosen to be 50 nA for all measurements on the the 10% N-UNCD, and 20 nA/1 nA was chosen for the 20% N-UNCD films at 36 mK/4.2 K. These current values are within the linear regime of the IV graph, while still being as low as possible to prevent resistive heating.

The normalized magnetoresistance $(R_{\mathrm{xx}}(B) - R_{\mathrm{xx}}(B = 0\,T))/R_{\mathrm{xx}}(B = 0\,T)$ (with the resistance at zero magnetic field $R_{\mathrm{xx}}(B = 0\,T)$) is graphed as a function of magnetic field B in Fig. 5.17. Both films show a negative magneto-resistance. This is typical for weak localization (WL) in disordered materials at low temperatures [57]. The WL peak around 0 T is much stronger for lower temperatures, in agreement with [57]. Furthermore,

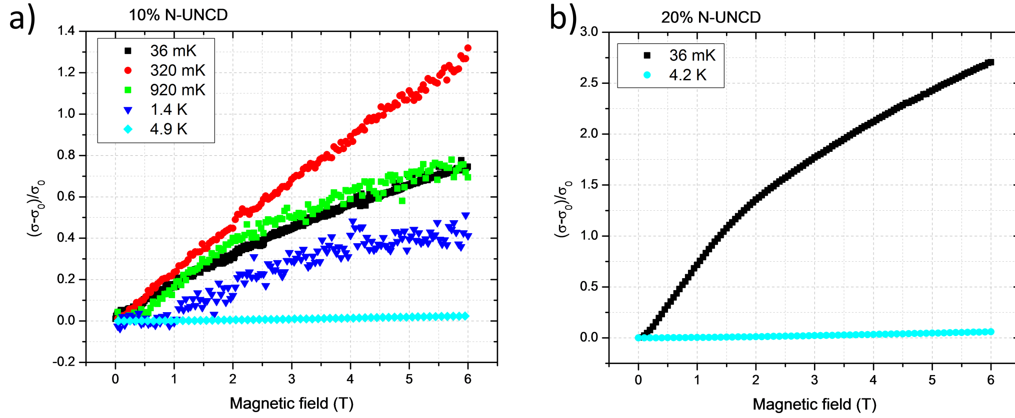

Figure 5.18: Normalized conductivity as a function of magnetic field of the a) 10% and b) 20% N-UNCD films at varying temperatures.

the WL peak is more prominent for samples with higher nitrogen doping, as has been previously observed [63].

Unlike previous published experiments, in which the minimum temperature used in tests was 4 K, we were able to do experiments at as low as 36 mK. Fig. 5.18 shows the normalized conductivity (σ-σ_0/σ_0), with σ_0 the conductivity at zero Tesla, of the 10% N-UNCD a) and 20% UNCD b) at various temperatures of 36 mK (black), 320 mK (red), 920 mK (green), 1.4 K (blue), and 4.0 K (cyan). We can observe again how the change towards lower temperatures causes the MR peak at zero Tesla to be more prominent. At zero magnetic field the reduced conductivity observed at lower temperatures as compared to higher temperatures, could possibly be caused by a larger amount of weakly localized charge carriers (see chapter 1.1.2). However, the WL is broken with the application of an external magnetic field. Thus the magnetic field has a higher impact on the conductivity at lower temperatures, than at higher temperatures. We do not know why in Fig. 5.18 a) the curve at 36 mK for the 10% nitrogen enhanced grown sample almost matches the data taken at 920 mK instead of showing a higher normalized conductivity as would be expected. We attribute this to the fact that the 36 mK data was taken in a separate cool down to the other low temperature

data. We were not able to remeasure the device at 36 mK due to the base temperature of the dilution refrigerator not allowing us to reach 36 mK again during our following attempts. Thus we cannot say how reliable the data set taken at 36 mK is. The increased noise in the data sets in a) with increasing temperature from 36 mK to 1.4 K is due to the current flow used to heat the sample to the set temperature values. We used a 100 Ω resistive heater and applied up to 30 mA to reach temperature values of 320 mK, 920 mK, and 1.4 K. This caused the noise level to increase at those temperatures. On the other hand, at 36 mK as well as 4.9 K no heating was required as the dilution refrigerator was operating at its base temperature/at the base temperature of the pulse tube with the mixture not circulating and thus the noise level was at a minimum.

We were not able to extract charge carrier mobility and density from these measurements. The films are of polycrystalline nature with insulating diamond crystals surrounded by conducting grain boundaries, causing the material to have a low mobility. Thus it is very sensitive to temperature induced voltage drifts, which are caused during magnetic field sweeps. As a result we used a different setup to approximate the charge carrier mobility and density of the 20% N-UNCD film. In this setup, the sample sat in an evacuated chamber, situated between the two coils of an electromagnet at room temperature. The electromagnet reached up to ±0.7 T. We sent a constant current of $I_{\mathrm{SD}} = 100\ \mu\mathrm{A}$ and measured the voltages V_{xx} and V_{xy} for varying B values. From this we extracted values for mobility and density as follows:

$$\mu = (8.2 \pm 0.2)\,\mathrm{cm}^2/\mathrm{Vs}$$

$$n = (9.3 \pm 0.3) \times 10^{18}\,\mathrm{cm}^{-3}.$$

These values on 20% N-UNCD films are slightly lower than those measured by Bhattacharyya et al. [55] of $\mu = 10\ \mathrm{cm}^2/\mathrm{Vs}$ and $n = 1.5 \times 10^{20}\ \mathrm{cm}^{-3}$.

LED dependency Next, we aimed to investigate the behaviour of the thin films with illumination. We know that diamond has a band gap of 5.5 eV, and that UNCD has a reduced band gap due to disorder [171]. Also, N-UNCD has additional states within the band gap due to the sp^2 bonds [171]. A blue LED was available for this experiment, allowing us to excite with an energy of ~2.64 eV. Even though UV is the preferred wavelength, 470 nm may be sufficient to excite carriers from trap states in the gap to the conduction band. We expected the added photons to be able to influence the free charge carriers by increasing the electron energy, thus helping them bridge the barrier and add to the electrical transport. Consequently, the electrical resistivity should decrease at a constant temperature if the sample was bombarded with photons. The non-linear IV behaviour observed in Fig. 5.15 was expected to appear at lower temperatures if the sample was illuminated. The observed freeze-out of the 5% N-UNCD sample was expected to happen at lower temperatures if the material was subjected to photons.

We illuminated the sample surface at low temperatures while applying a constant source-drain current and recording the voltage through the sample. The LED was connected to a voltage source via two independent lines that didn't share the same path through the probe with the electrical wires for the sample. This was as a precaution to reduce a coupling effect between the sample and the LED, since the LED required a high voltage of 10 V when turned on. In Fig. 5.19 the voltage (black) through a 10% N-UNCD sample was measured at 300 mK (temperature in blue) and plotted versus time. The LED was turned on repeatedly (LED voltage in red) and immediately switched off again. Each time the LED was turned on, a jump in the voltage through the sample towards lower values, and back up to the original value, was observed. This jump equates to a resistivity decrease of less than 0.5%. The sample temperature was monitored at the same time. Note that the temperature starts to rise slowly once the LED is turned on the first time, resulting in a slow decrease of V_{xx} over the graphed time frame due to this

heating. After a certain time the temperature settles back to its original value, and so does the voltage.

We assumed that the introduced photons would result in an increased conductivity, however, the rise in temperature also results in an increased conductivity as previously described. Since both the light and the heating have the same effect on the sample, it is difficult to separate these components as they are invariably coupled to one another. This could be prevented by repeating the measurement and substituting a light source outside the fridge for the LED, and using the optical windows in the dilution refrigerator for the photons to reach the sample. Unfortunately the dilution refrigerator is currently not fully equipped with optical windows. Another alternative to the LED would be to introduce optical fibres via the top of the fridge. These, too, would not cause the temperature to heat up and thus would allow the illumination experiment to be temperature independent.

5.5.1 Analysis of electrical measurements

In order to analyse the data of electrical measurements on the N-UNCD films, we need to understand where the electrical conductivity in these films originates. As discussed in a previous chapter 1.1.2, the Drude Model gives a classical explanation of electron transport. While this model works well for metals near room temperature, it does not fit our low-temperature experimental data. Percolation theory [172] does not fit all our low temperature data either [173], as in our case we have insulating grains with conducting grain boundaries, not vice versa. Below about 4 K these films have been found to show weak localization [2, 7, 174]. So first we attempted to use the model for 3D WL, as described in section 1.1.2, to explain the electrical data.

Temperature dependent conductivity We were able to fit the temperature dependent conductivity of the samples without the presence of a magnetic field in the range of about 3 K to 15 K with the 3D WL model in

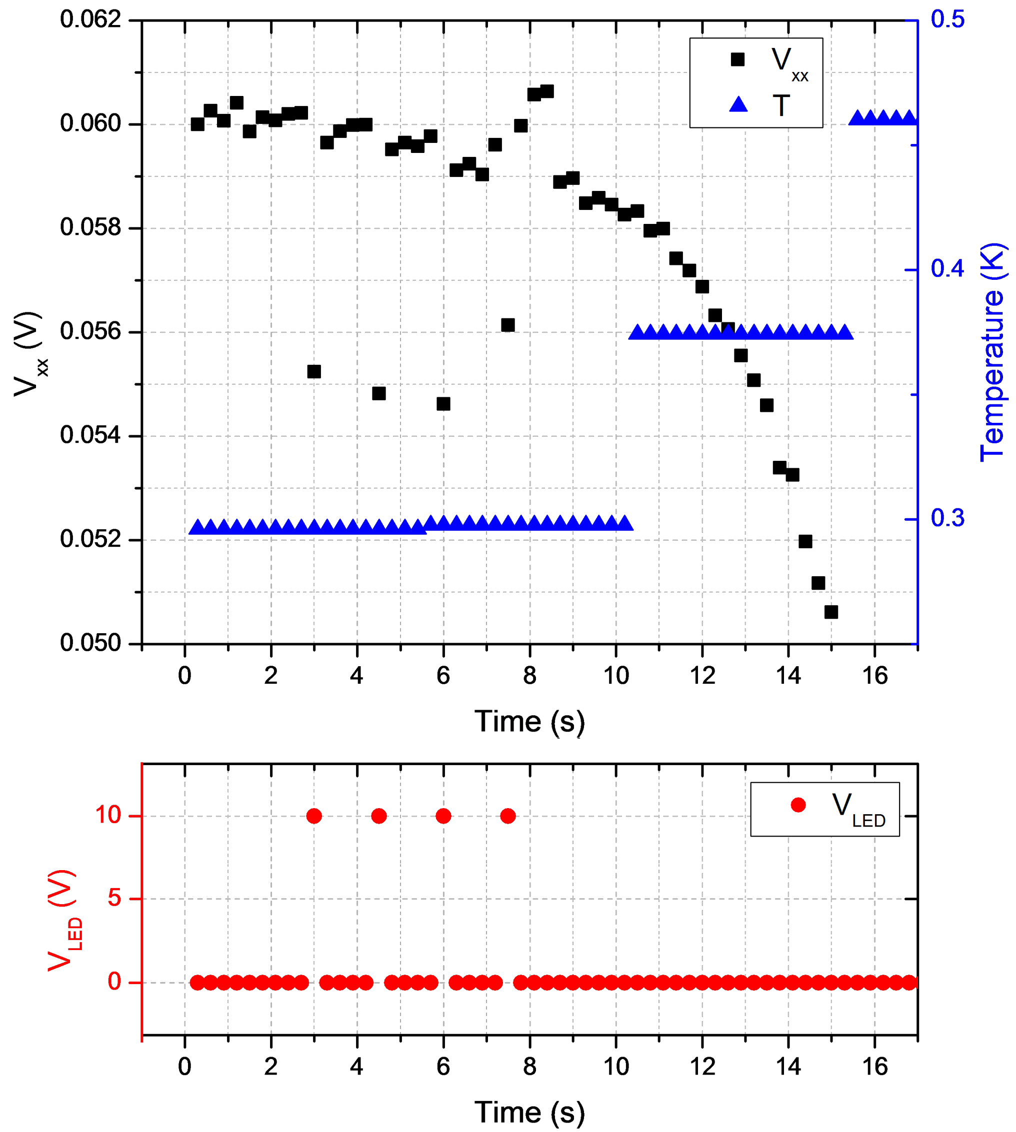

Figure 5.19: Top: Voltage (black) versus time of a 10% N-UNCD film. The sample temperature is shown in blue. Bottom: An LED directed at the sample surface is on when the LED voltage (red) is at 10 V, and off at 0 V.

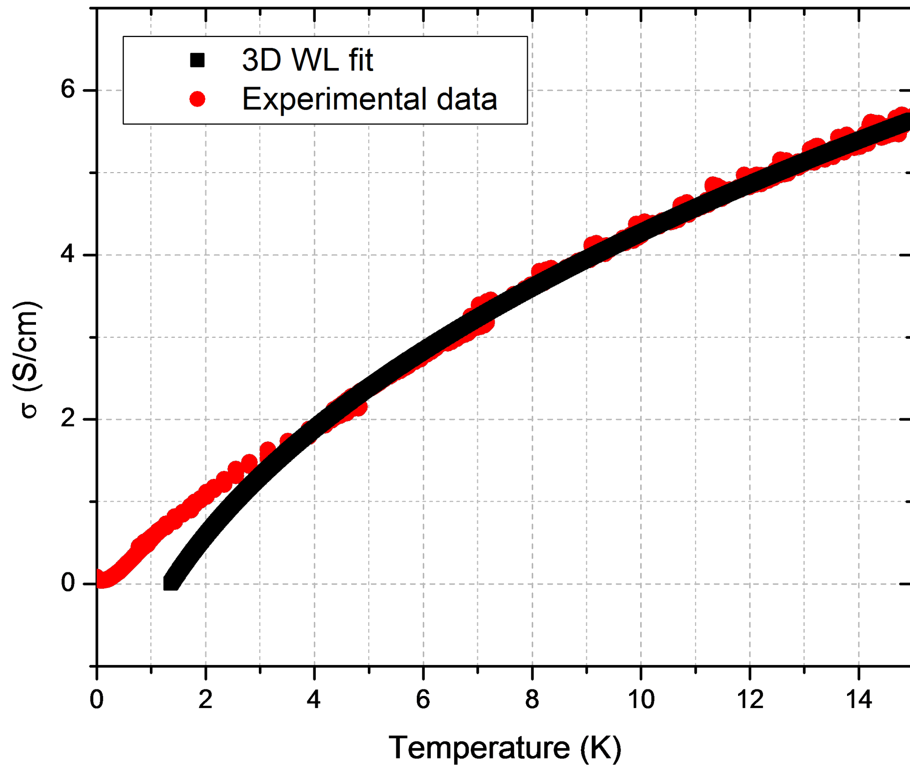

Figure 5.20: Conductivity versus temperature of the 20% N-UNCD sample between 17 mK and 15 K at zero magnetic field. The experimental data is in red and the 3D WL model fit in black.

Temperature (K)	4.9	1.4	0.920	0.320
alpha	0.016	0.15	0.52	0.5

Table 5.2: Fitting parameter alpha for the 10% N-UNCD sample.

equation 1.4. Figure 5.20 shows the experimental data of the 20% nitrogen enhanced grown N-UNCD film in red and the corresponding fit in black. Below about 3 K there is a discrepancy between the theory and the fit. The model cannot be made to fit the whole data range - while it has the same curvature at higher temperature, it has a very different trend at low temperature. Obviously the experimental data has to change its tendency at some point, as negative conductivities are not physical - which is what the model suggests. As such we conclude that the 3D WL model for zero field needs to be altered in order to be able to fit the whole temperature range of our data with this model.

Magnetic field dependent conductivity In order to verify that the N-UNCD films do indeed show 3D WL, we considered the magnetic field dependent data. Figure 5.21 shows the change in normalized conductivity $(\sigma - \sigma_0)/\sigma_0$, with the conductivity at zero field σ_0, versus the magnetic field at a temperature of 4.2 K of the 20% N-UNCD film. The experimental data is shown in red, and the theoretical fit based on equation 1.7 is in black. Both curves match really well, confirming the previous observation that at 4.2 K 3D WL is present in these samples.

Magnetic field dependence of the normalized conductivity of the 10% N-UNCD at a range of temperature values is shown in Fig. 5.22. The displayed temperatures are 4.9 K (cyan), 1.4 K (blue), 920 mK (green), and 320 mK (red). We have excluded the data set at 36 mK, shown in Fig. 5.18, as it is an anomaly and we were not able to reproduce this data due to problems with reaching 36 mK again. The experimental data (scatter) is shown together with the corresponding fit (continuous line) at each temperature value. For

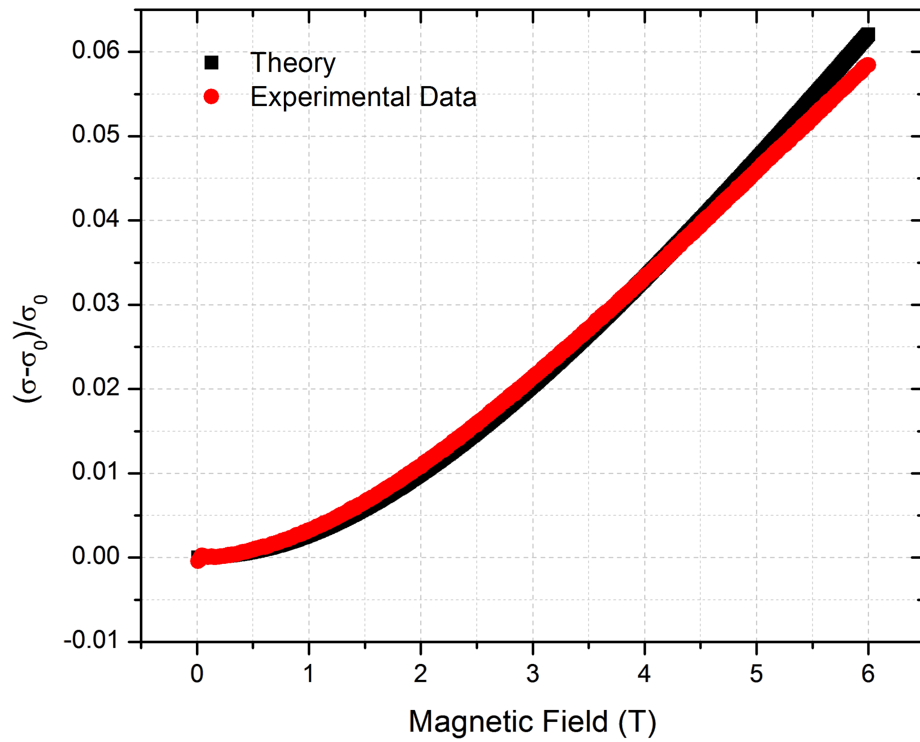

Figure 5.21: Relative conductivity versus magnetic field of a 20% N-UNCD sample at 4.2 Kelvin. The experimental data in red, the 3D WL model fit in black.

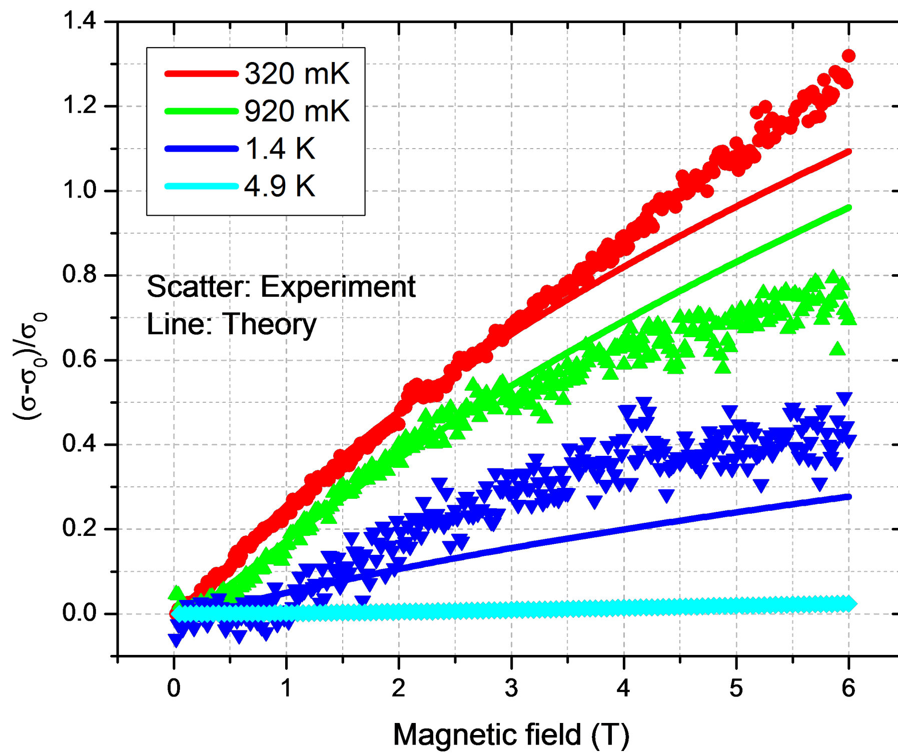

Figure 5.22: Normalized conductivity versus magnetic field of the 10% N-UNCD sample at various temperatures. The experimental data sets are the scatter, while the continuous lines are the fit at each temperature value.

the model in equation 1.7 we introduced the factor α as the correction factor, or fitting parameter, leaving the formula

$$\Delta\sigma = \alpha \frac{e^2}{2\pi^2\hbar}\sqrt{\frac{eB}{c\hbar}}F(\delta). \tag{5.1}$$

The parameter α is given in Table 5.2 for the four temperatures. The graph shows that the model fits the data perfectly at 4.9 K. At lower temperatures there is a discrepancy between experimental data and model, especially towards high magnetic field values. Here, we need to consider the limitations of the Kawabata derived model for 3D WL at low temperature and high magnetic fields [8]. As it is a perturbation model, the most reliable fit is expected in the low magnetic field area. Thus, we made the fit to match the area of lower field values. The graph also shows that with lower temperature, the normalized conductivity reaches higher values in strong magnetic fields. This is explained by the effect of WL being more pronounced at lower temperatures, so the magnetic field has more weak localized charge carriers to break up, resulting in a higher effect on the conductivity. This is shown in a higher increase of conductivity at high field values with lower sample temperatures. The fitting parameter α shows the tendency to increase with lower temperatures.

We are currently working together with the theorists Somnath Bhattacharyya and Dmitry Churochkin of the School of Physics at the University of the Witwatersrand in Johannesburg, South Africa to apply the Bruenskin-Kleinert (B-K) model - which is derived from the Kawabata model - to fit the data. So far we have not been able to apply either of the two models for the whole temperature range of data. However, work has commenced on applying the B-K theory to the low temperature data.

LED illumination The data showing the LED illumination of the N-UNCD films at low temperatures remains inconclusive. With the voltage applied to

the LED, the temperature of the probe immediately heats up. This temperature increase leads to a reduction of the resistivity in the sample. We expect the photons to be able to create more charge carriers by exciting electrons. Thus we believe the increase in photons has the same observable effect as a rise in temperature, a reduced sample resistivity. This makes it hard to distinguish the originating cause behind the change of resistivity in the measurements. Both increased photons and rising temperature are invariably coupled together and cannot be separated. A higher applied LED voltage leads to a faster increase in temperature with also a higher end temperature at equilibrium. Even though the LED already begins to emit light at 3-4 V at room temperature, we do not observe a reduction in the voltage through the Hall bar. Higher LED voltages are required in order to see a change in sample resistivity. Even with a high LED voltage of 10 V, the sample resistivity is only reduced by less than 0.5%.

The seemingly instantaneous reaction of the sample resistivity to the turning on and switching off of the LED, if we assume that the temperature does not heat up instantaneously with turning the LED on, but rather rises gradually with a slight delay, leads towards the assumption that we are observing an effect due to the photons. If these assumptions are correct, we may conclude that there is in fact a visible reduction of resistivity due to introduced photons. However, since the effect of the photons on the sample is very small and only visible with high LED voltages, we may indeed be observing just a temperature effect.

Chapter 6

Silicon devices: Experimental Results and Analysis

The following chapter shows the experimental results as well as their interpretation for the erbium doped silicon semiconductor devices. We examined various devices to characterize the behaviour of erbium dopants contained within them. The following sections describe the examination of the quality of the fabricated devices, using DLTS and PL techniques, as well as their electrical characterization at low temperatures and high magnetic fields in the dilution refrigerator.

6.1 DLTS

As previously mentioned in chapter 1.2, the implantation of erbium into silicon introduces defects in the substrate. These depend on the doping of the silicon substrate, the ion implant properties, as well as post-implant anneals. The discussed defects include VO, V_2^{2-}, VOH, VP, and V_2^{-} [102, 101, 104].

DLTS measurements were undertaken on erbium doped silicon samples to determine defects that were introduced during implantation. This DLTS study was performed on several implanted samples processed at various an-

Sample number	Anneal temperature (°C)	Anneal time (min)
1	No Anneal	-
2	200	15
3	300	15
4	400	15
5	700	10

Table 6.1: Anneal temperatures and times of the DLTS samples.

nealing temperatures, in order to study the influence of thermal anneals on the evolution of the defects in order to find the optimum annealing parameters. The DLTS measurements were undertaken as explained in chapter 1.2. All examined samples were silicon substrates (n-type, P doped with a resistivity of 0.8 - 0.9 Ωcm), implanted with erbium ions of an energy of 2 MeV and a fluence of $1\text{x}10^9$ cm^{-2}. The implant energy was considerably greater than that required for the MOS devices but is here needed to put the projected range of the Er beyond the zero-bias depletion depth in the Schottky-diode structures used in this study. Despite the energy used, the bulk defect types produced were expected to be similar to those for lower implant energies. These samples were annealed in a quartz tube furnace in a nitrogen ambient. The annealing temperatures and times are given in Table 6.1.

Measurement setup Prior to the DLTS measurements, we performed CV measurements as described in 2.1.1 in the range of -6 V to 0 V in steps of 0.1 V at 295 K and 80 K. From these we extracted the active dopant concentration n and the built-in voltage V_{bi}. Two sets of DLTS measurements were performed on each sample in the temperature range of 80 K to 295 K with a voltage offset of -3 V, and a voltage pulse height of 0 V (3 V amplitude). The bias voltage pulse settings were chosen such that we were able to probe deep enough into the sample to reach all defects. The pulse width was long enough

Pulse period: 1000 ms Pulse width: 40 ms		Pulse period: 100 ms Pulse width: 10 μs	
Delay time (ms)	Time constant	Delay time (ms)	Time constant
50	10	2	10
20	10	0.5	3
10	3	0.1	10
5	1	0.05	10

Table 6.2: Correlator initial delays and time constants for the shorter time settings.

to ensure complete filling, saturation, of the traps. Using a correlator, we then measured the difference of capacitance between two time points delayed after the pulse. The setup allowed us to use 4 correlators during one scan, so instead of only one two-point correlation, we were able to gain data from four different correlator delay times in just one measurement scan. This allowed us to obtain information of the filling of the traps on a slow as well as a fast time scale. For one DLTS scan longer delay time settings were used. Here a pulse period of 1000 ms and pulse width of 40 ms was used. The second scan used shorter correlator delay times with a shorter pulse period of 100 ms and pulse width of 10 μs. The correlator settings are given in Table 6.2. The CV curve of the as-implanted sample (sample 1) at 295 K is shown in Fig. 2.3. The CV curve at 80 K was very similar and thus is not shown here.

Defect types There are two main types of defects observed in the DLTS spectra: vacancies and substitutional defects [22]. Comparing our data with previous studies on n-type silicon reveals the most common defects [102, 175]. The vacancy oxygen, VO, consists of a vacancy in the silicon lattice accompanied by a substitutional oxygen atom. It has an energy level of 0.17 eV [175, 176] and is visible in the DLTS spectrum as a peak at around 90 K [102]. The V_2^{2-} defect is the double negatively charged di-vacancy, has an

Peak	Defect type	$E_c - E_T$ (eV) literature	$E_c - E_T$ (eV) measured
E1	V_2	0.52 ±0.02 [175]	0.60
E2	V_2^-/VP	0.42 ±0.06 [175]	0.44-0.49
E3	VOH	0.31 [103]	0.37
E4	?		0.31
E5	V_2^{2-}	0.23 [177]	0.22
E6	VO	0.17 ±0.02 [175]	0.16

Table 6.3: Observed DLTS peaks and their defect type as well as energy - calculated and literature values.

energy of 0.22 eV [177, 175] and shows on the DLTS spectrum at around 120 K [102]. The peaks of VP (vacancy phosphorus) and V_2^- (single negatively charged di-vacancy) are very close together at around 190 K and 210 K respectively. The last two may be combined as together they constitute the DLTS peak at around 200 K corresponding to a defect energy of 0.42 eV [177, 178]. Vacancy oxygen hydrogen, VOH, with an activation energy of 0.31 eV shows at around 175 K [103].

The defects observed in the DLTS spectra are marked as E1-E6 in purple in Fig. 6.1 top. This graph shows the DLTS spectra of all anneal temperatures together. The identification of the peaks is given in table 6.3. The From the DLTS graphs we can extract the defect concentration of each defect type as a function of the anneal temperature, as shown in Fig. 6.1 bottom. Unfortunately we were unable to find information in the literature on the defect observed by us in trap E4.

Results The DLTS spectra of the first sample with all measured correlator delay times is given in in Fig. 6.2. All 8 correlator settings follow the same trend. The longer delay times result in a slight shift towards higher temperatures of the peaks, causing the curves of the various delay times to

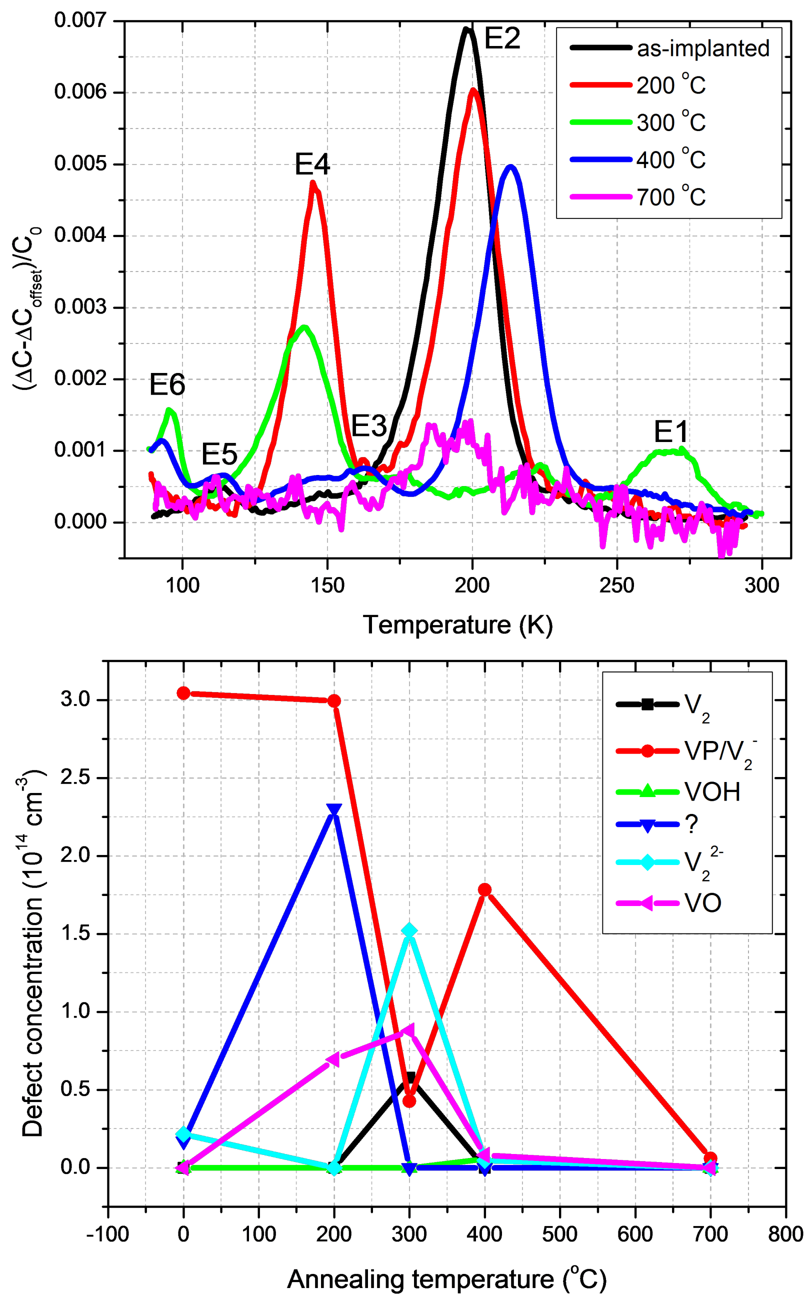

Figure 6.1: Top: DLTS spectrum of all samples together. Bottom: Defect concentration versus anneal temperature.

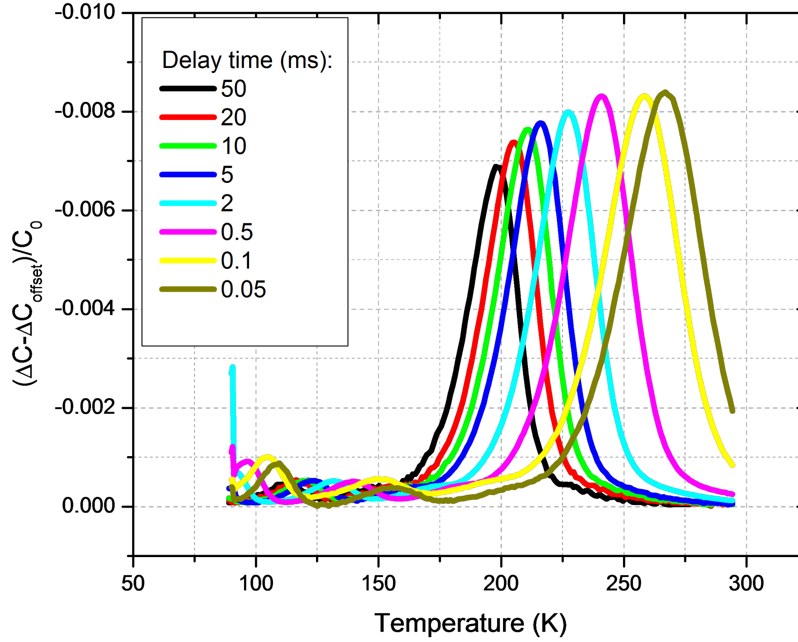

Figure 6.2: DLTS spectra of the as-implanted sample at all correlator delay times.

be 'following' each other. This is the case for all measured samples. Thus it doesn't particularly matter which particular delay time we display here to illustrate the influence of anneal temperature and time on the traps. Since showing the plots of all correlators of every sample would render comparisons between different samples difficult, an arbitrary decision was made to show in the following graphs only the 50 ms delay time of all samples, which drastically improves the transparency of the data. To determine the extraction of the energy levels of the defect, data from all correlator settings were used. Details regarding the DLTS analysis are given in chapter 2.1. The top graph in Fig. 6.3 displays the DLTS spectrum of the as-implanted sample (black) as well as the sample annealed at 200 °C (red). The defect energy level is given as the conduction band energy E_c minus the trap energy E_T and is marked in the graph in eV. The most prominent peak of the as-implanted sample is at ∼200 K at a defect energy level of ∼0.49 eV. This defect, marked as E2 in the

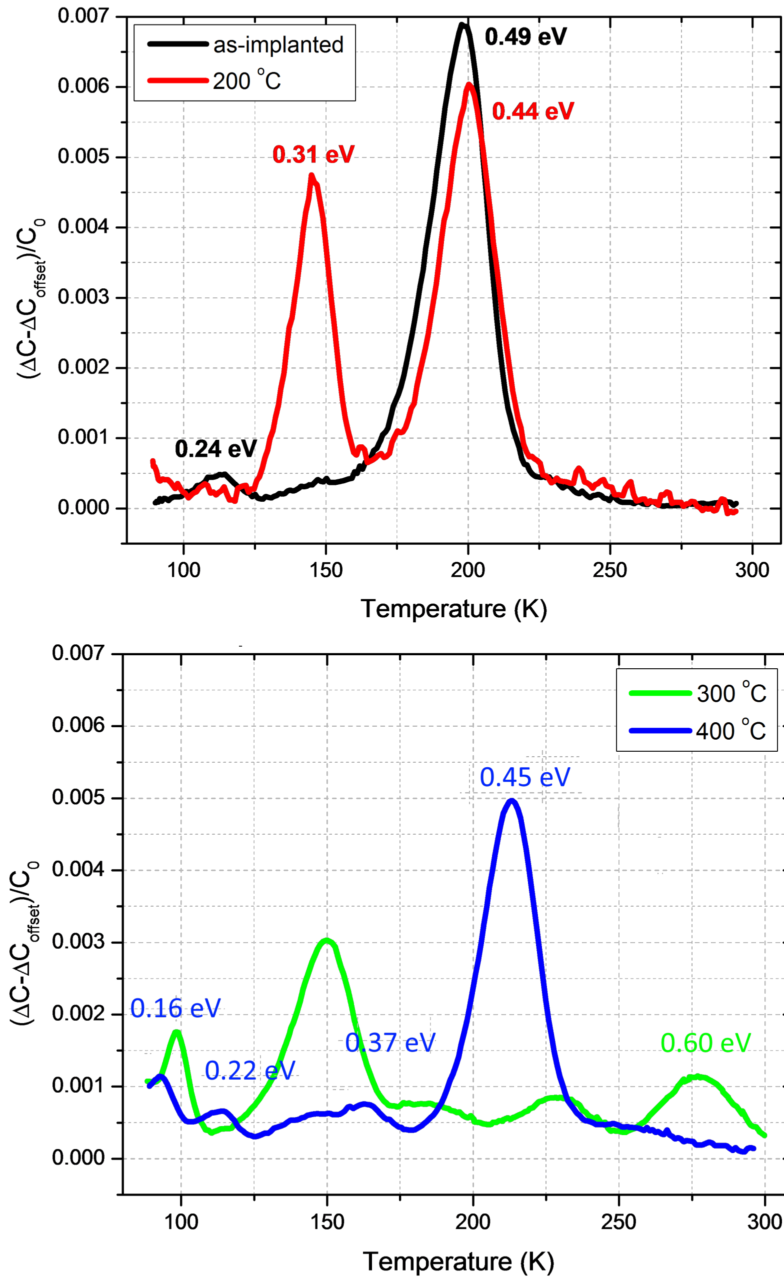

Figure 6.3: Top: DLTS spectrum of the as-implanted sample (black) and the sample annealed at 200 °C (red). Bottom: DLTS spectrum of the samples annealed at 300 °C (green) and 400 °C (blue).

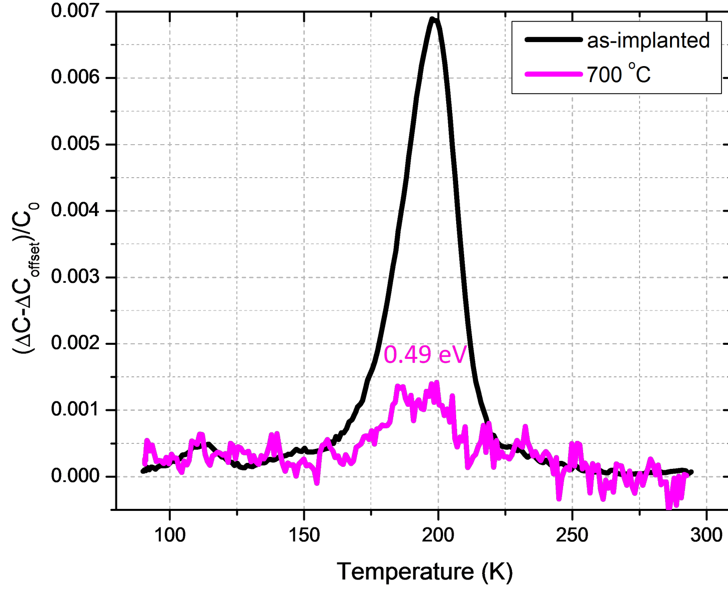

Figure 6.4: DLTS spectrum of the as-implanted sample (black) and sample annealed at 700 °C (magenta).

top graph in Fig. 6.1, is due to the superposition of the defects V_2^-/VP. It is the most prominent defect we observed in erbium doped silicon. Annealing at 200 °C causes this defect to drop slightly in concentration. On the other hand, a high peak (E4) shows up at ∼150 K with a defect energy level of ∼0.31 eV, which was visible as only a very small peak in the as-implanted sample. This shows that annealing can reduce some defect concentrations, while others can increase. The as-implanted sample also shows a small defect peak at ∼120 K, ∼0.24 eV, marked as E5 in the top graph of Fig. 6.1. This is the V_2^{2-} defect [177, 102].

The spectra of the samples annealed at 300 °C and 400 °C are given in Fig. 6.3 bottom in green and blue, respectively. There is a peak at ∼300 K for the sample annealed at 300 °C denoted E1 in Fig. 6.1 top. It has a defect energy level of ∼0.60 eV. This peak disappears again for higher anneal temperatures and is thus only visible in this one spectrum. We believe it

to be related to V_2 [175]. The as E2 marked peak shifts in the 400 °C annealed sample to a slightly higher temperature of ∼220 K from ∼200 K at all other anneal temperatures. The E4 peak decreases from the 200 °C annealed sample to the 300 °C annealed sample and is hardly distinguishable in the sample annealed at 400 °C. E5, a small peak at around 125 K, shows up in the sample annealed at 400 °C again, even though it is not visible in the 300 °C or 400 °C spectra, but only in the as-annealed spectrum. A new peak (E6) shows up at around 95 K in both the 300 °C and 400 °C samples with an energy level of ∼ 0.16 eV. This defect could be due to a VO center [175].

The sample annealed at 700 °C shows only one defect (see Fig. 6.4 in magenta), at a similar trap energy to that of the V_2^-/VP defect. The peak has a significantly reduced height as opposed to the previous spectra. Due to a low signal height (as a result of a very low amount of traps), the spectrum of the 700 °C annealed sample is noisy as compared to the spectra of the other samples. Out of this set of anneal temperatures, the 700 °C sample proved to have the fewest defects. However, it would be highly unusual for the V_2^-/VP defect to still be visible at this annealing temperature [101, 179]. Hence, it is likely that we are observing a different defect that as yet has not been positively identified [103]. All observed peaks are noted in Table 6.3 with their calculated energies as well as the defect type and energy level as given in literature.

Conclusion It is clear from the DLTS characterization that erbium introduces various defects, such as vacancies and substitutional defects in the silicon lattice, during the implantation process. The observed defects are V_2, V_2^-/VP, VOH, V_2^{2-}, VO, and an additional defect that we are not able to identify with current literature. These defects can be reduced to a minimum by high temperature annealing of the samples. We discovered that the

concentration of some defects does increase with increasing anneal temperature, whereas most defects show the tendency to decrease, or even disappear. The highest anneal temperature that was used for this experiment, 700 °C, showed by far the fewest remaining defects (see Fig. 6.1), with only a small concentration of V_2^-/VP remaining. Thus we can conclude that the samples should be treated with a high temperature anneal of more than 700 °C for optimum recovery of defects introduced during erbium implantation.

6.2 Photoluminescence

Sample number	Treatment
1	RTA
2	RTA + 10 min O_2
3	10 min O_2
4	55 min O_2

Table 6.4: Hot temperature treatment of the samples characterized with photoluminescence.

Erbium has a photoluminescence (PL) peak at around 1537 nm [10]. The as-implanted silicon samples need to be thermally annealed in order to activate the erbium, so that one can observe the luminescence [84]. The 'activation' of the erbium is important, as the Er ions in the as-implanted samples are generally inert, as in either optically or electrically inactive. Annealing at too high a temperature or for too long (i.e. above 1000 °C and for longer than 15 seconds [180]) also leads to reduction in the luminescence intensity. According to the process flow for the Hall bar devices, the samples will be subjected twice to silicon dioxide growths in the furnace after erbium implantation during fabrication. In the following paragraphs we look at the effect that the oxide growth process has on the luminescence of the erbium.

The PL spectra were collected with a Renishaw inVia Reflex micro-Raman spectroscopy system, the same system as was used for the Raman

spectroscopy on N-UNCD in chapter 5.3. The detector used was an InGaAs CCD, the excitation wavelength was 532 nm with a Nd:YAG laser. The samples were placed on a temperature controlled Linkam Stage [181] and examined at -195 °C. For this study, we implanted a silicon substrate with erbium at an energy of 400 keV and a fluence of 4×10^{12} cm^{-2}. We used a higher implant energy as well as fluence (110 keV and 6.6×10^{10} cm^{-2} for the MU devices, see chapter 4.2.1) to make the effects of high temperature treatment more prominent on this test. For comparison, we examined four different samples as outlined in Table 6.4. An anneal temperature of 900 °C was chosen for the PL measurements, based on literature [17] as well as the previous DLTS studies. The first sample was subject to an RTA at 900 °C for 30 seconds in a pure argon atmosphere. The second sample was exposed to an RTA of the same conditions, followed by an oxidation of 10 minutes at 1000 °C in O_2 atmosphere. The third sample was only exposed to the O_2 for 10 minutes, and the fourth sample was given 55 minutes in the furnace at 1000 °C in O_2. The samples going through the process of creating Hall bars would be subjected twice to the 10 minutes oxygen growth time, which falls in between the chosen oxidation times of 10 and 55 minutes in this experiment.

Fig. 6.5 shows the PL intensity versus wavelength of these four samples taken at - 195 °C. Sample 1 (in black) displays the highest intensity PL peak at 1537 nm, indicating that the used RTA parameters were a good choice for activating the erbium in the samples [17] (in addition to reducing defect concentrations as previously learned). In red is sample 2, with the second highest intensity PL peak. The peak in sample 3 (green) is not very prominent, whereas sample 4 (blue) shows a sharper and higher intensity PL peak than sample 3. A list of the observed peaks of the sample annealed at 900 °C for 30 seconds is shown in Table 6.5. These PL lines were compared with the PL lines observed by [30] on Er:Si with an implant energy of 320 keV and an anneal of 30 minutes at 900 °C.

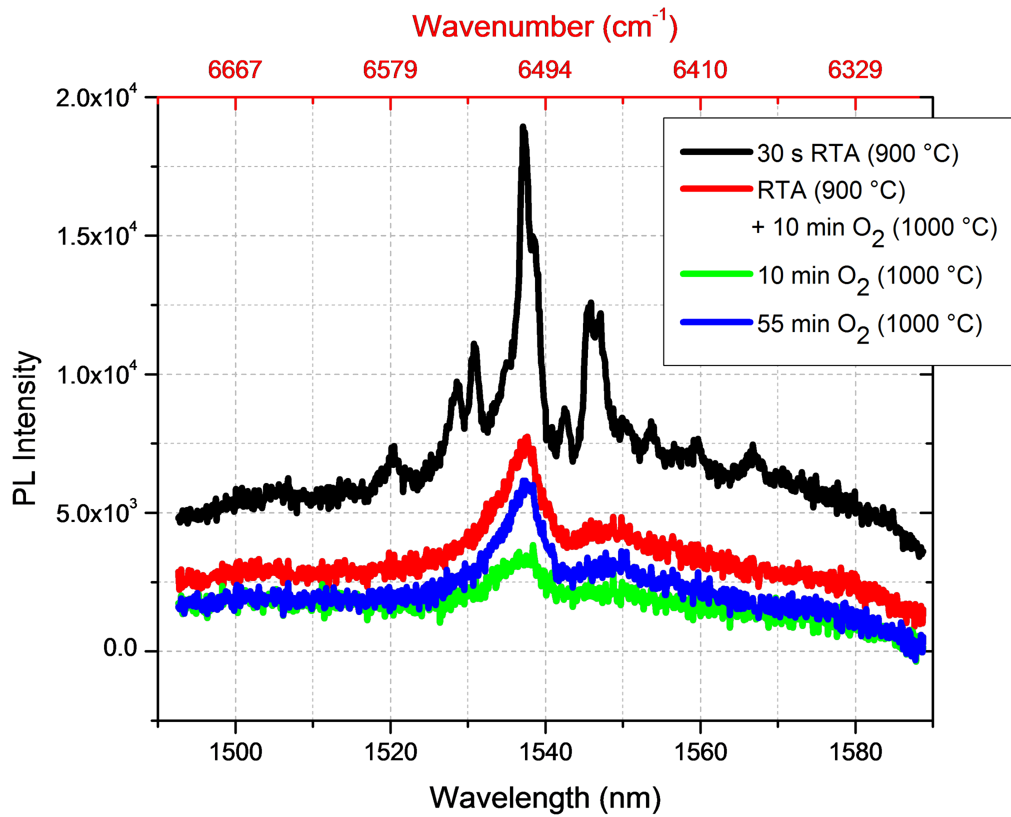

Figure 6.5: Photoluminescence of silicon doped with erbium (4x10^{12} cm^{-2}) at - 195 °C for varying anneals.

Only the dominant emitting colours of the Table of [30] are used for the comparison. The wave numbers that match up within ± 2 cm^{-1} are highlighted in grey. Our data reaches higher wave numbers than Przybylinska's does [30]. Table 6.5 shows that we are able to match 6 of 10 observed peaks. In the sample annealed for 30 seconds at 900 °C, only the development of the main peak at 6506.2 cm^{-1} is comparable to the other three test samples. The RTA shows positive results for the PL line, whereas the oxidation is deleterious for the optical properties of erbium. Nevertheless, some residual PL is still visible. The RTA clearly activates the erbium optically and thus helps to create a sharp and intense PL peak. It also seems to stabilize the erbium, and results in the exposure to the hot furnace during the following oxide growth having less effect on the PL peak. With oxidation, the peak broadens and loses its intensity, possibly due to a change in the chemical state of the Er during the oxidation process.

Wave numbers in cm^{-1} of the PL lines observed in Er:Si.	
Implant energy:	
400 keV	320 keV
Anneal temperature and time:	
900 °C, 30 sec	900 °C, 30 min
Exp. value	Lit. value [30]
6382.5	6384.3
	6438.0
6436.7	6437.3
	6438.2
6464.1	
6470.4	6471
	6472.8
6485.1	
6498.6	6498.5
6506.2	6507.5
6508.3	6508.6
6531.7	
6576.8	

Table 6.5: Comparison of experimentally found photoluminescence peaks and peaks found in the literature [30].

Conclusion The PL results show us that an RTA treatment of the samples prior to any other exposure to high temperatures ensures a high intensity PL peak due to the implanted erbium.

An anneal at 1000 °C has been found to be ideal for optically activating the erbium [17]. We chose to undertake the RTA at 900 °C for the MU devices instead, as these devices were subsequently annealed at high temperatures during oxidation. The UNSW devices on the other hand were annealed at 1000 °C, as they would not need oxidation processes after ion implantation. The RTA treatment seems to not only activate the erbium optically, but also to cause the Er to diffuse into a stable lattice location in the silicon [182, 183]. The latter could be the reason why subsequent exposures to high temperatures have less influence on the PL intensity, as the Er is less likely to diffuse further after it already occupies a lattice site.

6.3 Oxide quality and thickness

The oxide thickness and quality of MU grown SiO_2 was determined via CV measurements (see section 2.1.1). For this experiment the samples were prepared according to Chapter 2.1 as pictured in Fig. 2.2: An approximately 150 nm thick gold top contact of known area A (forming a MOS contact) was deposited directly onto the silicon dioxide layer that was formed on top of the p-type boron doped silicon substrate with a resistivity of 1 - 10 Ωcm. The back contact, consisting of InGa eutectic, formed an ohmic connection with the silicon substrate. As a result we produced the configuration of a metal-oxide-semiconductor (MOS) capacitor as sketched in Fig. 6.6 a). The green metal represents the deposited gold, blue the silicon dioxide we intended to examine, yellow the doped silicon, and the purple back contact represents the InGa. Applying a voltage to the top gate will change the capacitance through the sample (see Fig. 6.6 b)). The graph is divided into three regimes of operation [29]. In the *Accumulation* regime the charge carriers of the same type as the semiconductor majority carriers accumulate at the surface. In the *Depletion* regime the surface is void of majority carriers, leaving behind a depletion layer. In the *Inversion* regime minority carriers accumulate at

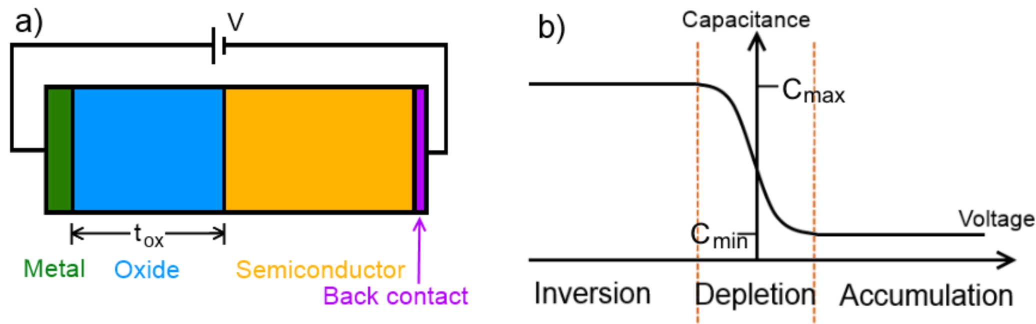

Figure 6.6: a) Sketch of a metal-oxide-semiconductor (MOS). b) Capacitance versus voltage through a MOS capacitor [29].

the surface. This inverts the conductivity type. The flatband voltage V_{FB} separates the accumulation regime from the depletion regime. Using the analogy of a parallel plate capacitor, there is no charge on the capacitor plates when the flatband voltage is applied. Consequently there is no electric field across the oxide at this point. The threshold voltage V_T separates the depletion regime and the inversion regime. In the accumulation regime the maximum capacitance C_{max} is equal to the capacitance of the oxide C_{ox} and is given by [29]

$$C_{\mathrm{ox}} = \frac{A \cdot \epsilon_{\mathrm{ox}}}{t_{\mathrm{ox}}}, \tag{6.1}$$

with the oxide thickness t_{ox}, the permittivity of the silicon dioxide $\epsilon_{\mathrm{ox}} = \epsilon_r \epsilon_0$ including the relative permittivity for silicon dioxide $\epsilon_r = 3.9$, and the area of the diode A. The gold contacts of the samples used were circular with a diameter of $\sim$800 μm.

In order to test the quality of the silicon dioxide grown with the furnace used in this project, we grew an oxide on a silicon wafer under the same conditions that are used for the gate oxide growth: i.e. 1000 °C, in O_2 ambient, for 10 minutes. On top of the oxide layer 100 nm Au contacts were evaporated. The CV measurement of this sample at room temperature is shown in Fig. 6.7 during which the voltage was swept from +3 V to -5 V. The three regimes can be clearly seen, with a measured oxide capacitance of

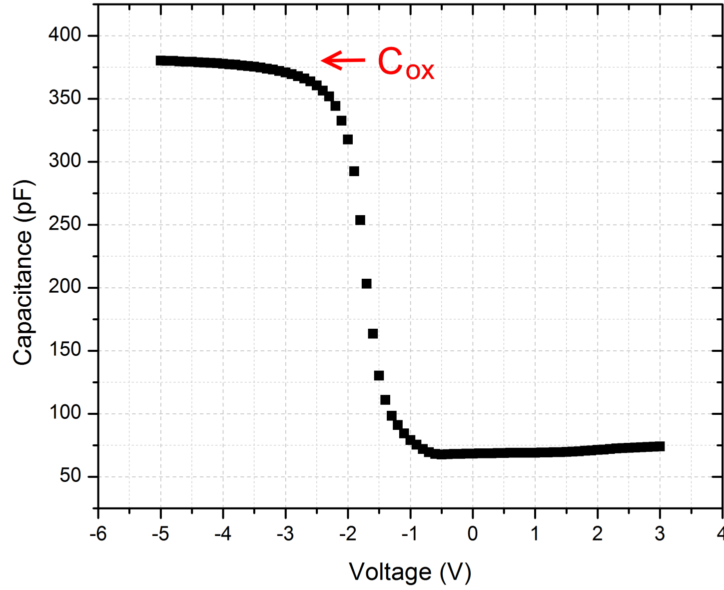

Figure 6.7: CV measurement of a silicon dioxide on a p-type silicon sample at room temperature.

C_{ox} = 375 pF. With equation 6.1, $\epsilon_r = 3.9$ for silicon dioxide, and A = (400 μm)$^2\pi$, we calculate the oxide thickness to $t_{\text{ox}} = 46$ nm. The threshold voltage (the voltage at which the MOS capacitor in the inversion region enters the depletion region [130]) exhibits a shift from the ideal MOS capacitor value of ~0.1 V to a value of ~-1.7 V, indicating the presence of a fixed charge in the oxide. This level of fixed oxide charge is not unusual for oxide growth under the conditions used. The shift of the depletion and accumulation region towards a negative gate voltage is due to the oxide layer, which causes the threshold voltage to shift. In the measured voltage regime we did not observe a current leaking through the oxide layer. Nor did we observe a break-down of the oxide, which would be visible as a rapid drop of the capacitance. The CV graph shows a regular capacitance behaviour with a stable maximum voltage, indicating a good quality of oxide suitable for use as a gate oxide in the hall bars. It is important that gate leakage current is negligible, because leakage

would cause the current to be no longer proportional to the capacitance, resulting in an erroneous oxide capacitance [121].

6.4 Electrical measurements

The electrical measurements of the Er:Si devices were undertaken in the dilution refrigerator with the electronic equipment as sketched in Fig. 5.14. To start, two-point measurements were done to test the samples, using the SMU by applying a current/voltage while reading out the voltage/current between two contacts. We also tested gate continuity this way by connecting both gate contacts together. We began by examining the first fabricated samples, the MU devices. See Fig. 6.8 top for the mask design.

MU devices: Two-point measurement tests The bottom graph in Fig. 6.8 was taken at a temperature of 5.0 K of one of the first set of fabricated devices. The other tested devices showed similar behaviour. The graph shows the two point measurement between two ohmic contacts of the Hall bar (black scatter) including its linear fit (red) as well as the two point measurement between the top gate and an ohmic contact (green scatter) including its linear fit (blue). The fit is created to determine the resistivity between the two points. We calculated a resistivity between two ohmic contacts of 5.85 kΩ and between the gate and an ohmic contact of 5.24 kΩ. The similarity between the two measurements is obvious. There was clearly a problem with the oxide integrity in the fully fabricated devices that may not show up in the oxide test capacitors. Without a usable gate, the devices were not suitable for further measurement. This was unexpected and was an indicator that something had gone wrong during the oxide growth. Unfortunately it posed a problem for the following experiments. It demonstrated that charge carriers would leak through the oxide layer, instead of following the channel in the

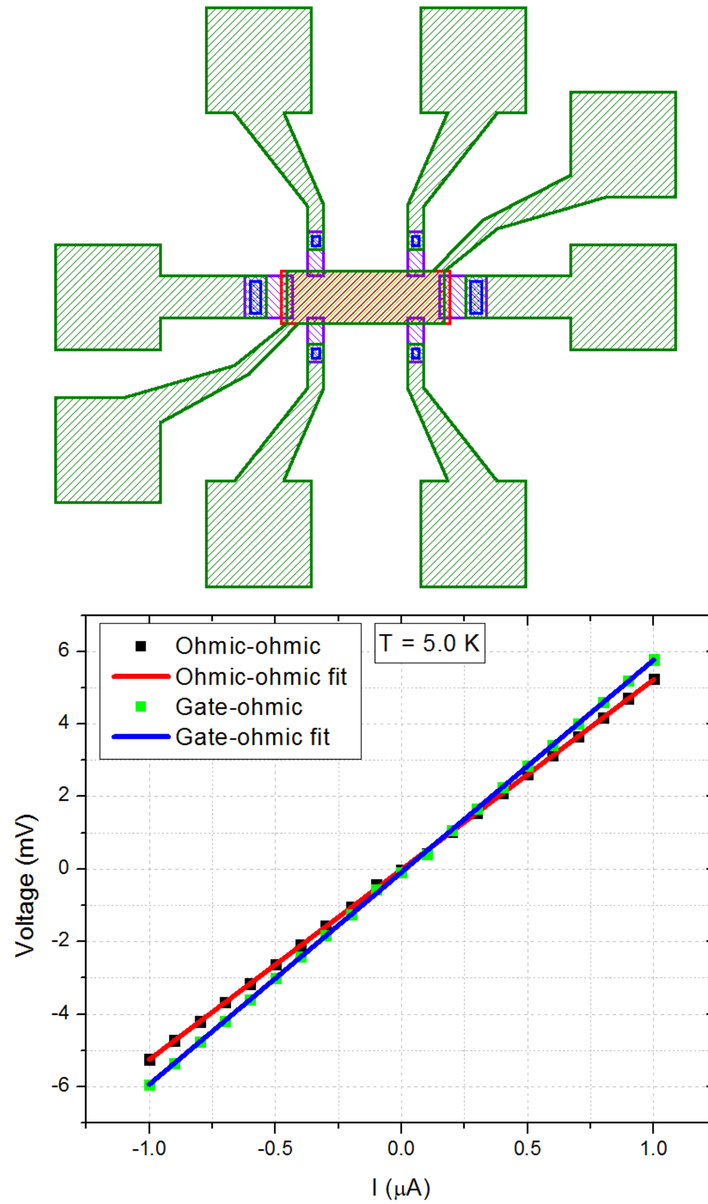

Figure 6.8: Top: MU device layout with all mask levels superimposed. The metal is shown in green, oxide windows in blue, gate oxide in orange, Er implanted area in red, and the As implanted area in purple. Bottom: Voltage versus current 2-point measurement of an Er doped Si Hall bar, between two ohmic contacts (black) and the gate and an ohmic contact (green) including their linear fits (red and blue).

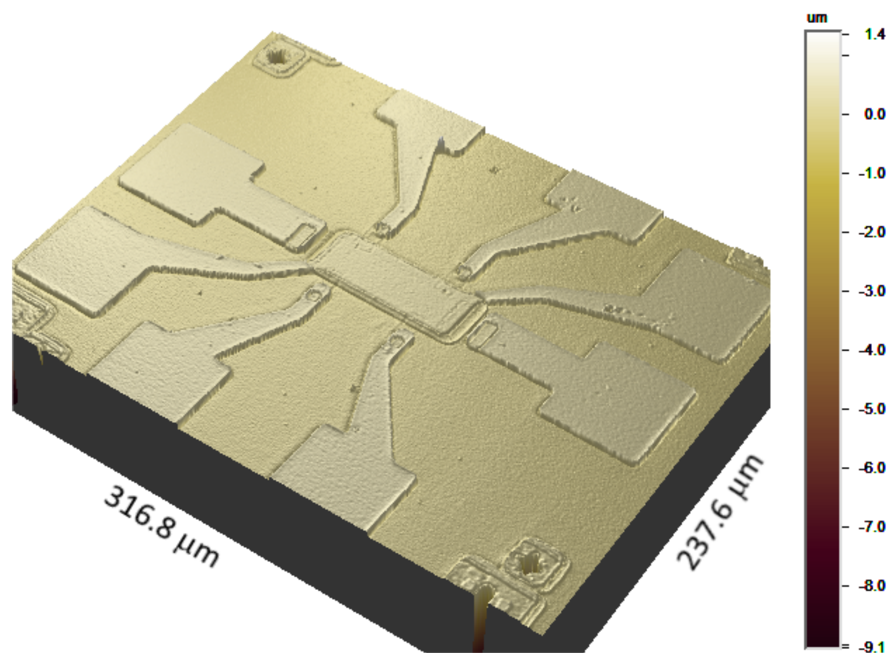

Figure 6.9: Image taken using the optical profilometer of a finished Er doped Si Hall bar device.

silicon substrate. Consequently, the gate was rendered useless, as applying a voltage to it would substantially change the current flow within the device.

A second set of devices were fabricated. Unlike the first batch, we did not experience gate leakage this time, but discovered another problem: this time all ohmic contacts exhibited very high resistance. Optical pictures taken with the profilometer showed that the problem lay within the fabrication process. Fig. 6.9 is a false colour image of one device. Depth measurements reveal that the overlapping area of the aluminium and arsenic leads still has some SiO_2 remaining. We concluded that the etch with BHF was not sufficient to remove all the oxide in that area, which is necessary for the ohmic connection to the device channel. The etch process consisted of soaking the chip in BHF for several minutes without disturbing the solution, to prevent anisotropic etching. As described in chapter 4.2.15, this method must have

prevented a complete SiO_2 etch within the etch time. For etching on the next batch of samples, we decided to risk a slight anisotropy in the etch and to stir the HF solution every 30 seconds until the completion of the etch, as well as increase the etch time. Because of the lack of connection from the device channel to the metal contacts, we were not able to test whether the gate oxide still posed a problem in these devices.

Given these processing issues, and the misalignment that occurred during fabrication (see Fig. 4.26), we redesigned the photo-lithography masks for the devices, with more tolerance to allow for misalignment of the multiple layers. We also shifted the fabrication of the samples to UNSW where a triple-wall oxide furnace was available and where structures similar to those on the redesigned masks had been successfully fabricated and measured in the past.

Batch	Implant ions	Implant energy and fluence
1	Sb	70 keV, 2x10^{11} cm^{-2}
2	Er	85 keV, 2x10^{11} cm^{-2}
3	none	–
4	Er	85 keV, 2x10^{11} cm^{-2}
	O	15.5 keV, 1.2x10^{12} cm^{-2}

Table 6.6: Er:Si batches and their additional implant ions (also see table 4.8 from chapter 4.2).

UNSW device: Gate dependency We next set out to examine the gate dependency of a Hall bar device of the design δ (see Fig. 6.10, channel length/width = 36 μm/33 μm) with Er and O dopants, batch 4 (see Table 6.6 for implant energy and fluence). Fig. 6.11 shows on the left the IV curve between the gate and the drain contact and on the right the source and the drain contact of the device. These measurements were undertaken with the SMU by applying the voltage and reading out the current with a compliance

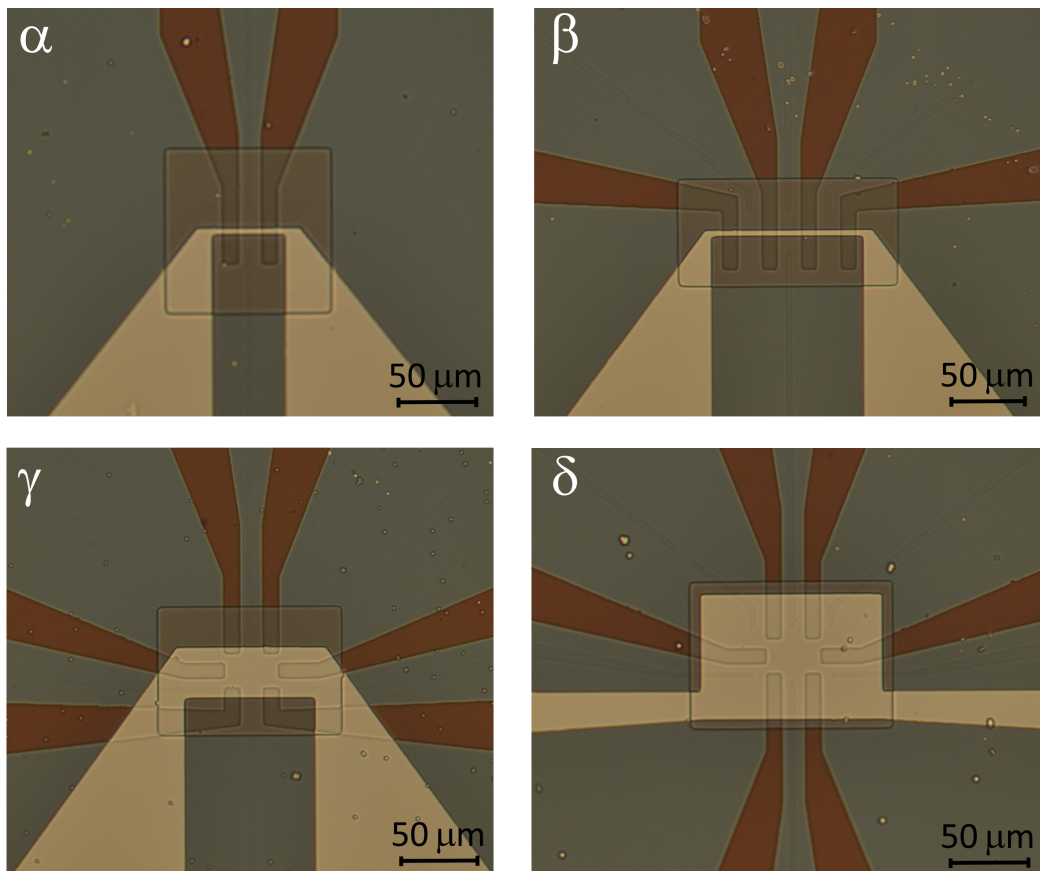

Figure 6.10: Fig. 4.13 from chapter 4.2. Optical image taken with a microscope of 20× magnification of the 4 finished designs in the channel area. The squares in the centre are the thinner gate oxides, the aluminium gates are in yellow, the phosphorus diffused leads in brown, and the surrounding thick field oxide in grey.

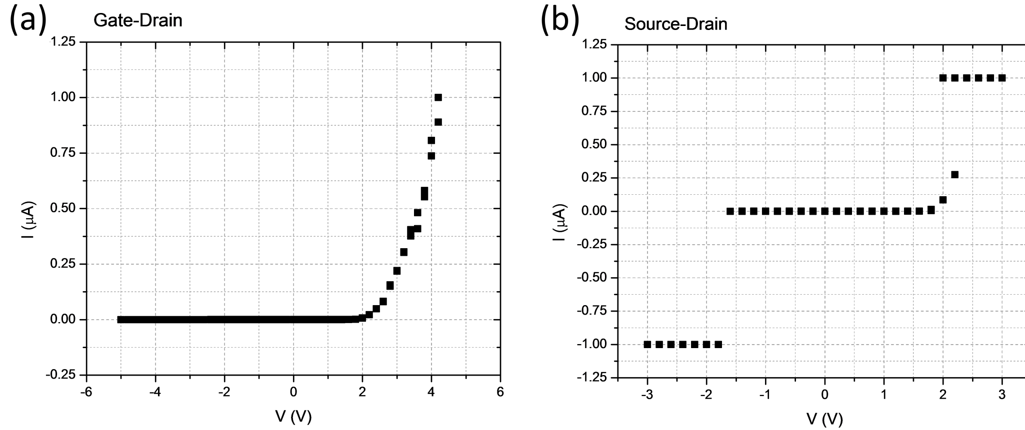

Figure 6.11: IV curves of UNSW fabricated device from batch 4, design δ. (a) gate and drain contact. (b) source and drain contact.

of 1 μA, hence the plateaus at +/- 1 μA. We limited the voltage by setting the compliance level at 1 μA in order to avoid destroying the device by allowing too high a current to flow through it. The sample temperature was at 4.1 K, no external magnetic field was applied, nor an additional gate voltage. The right graph shows a very rapid jump from 0 A to the compliance value at ca. +2.2 V and - 1.8 V. The left graph shows an exponential increase in current flow above ~2.0 V. We concluded that there is a small area in which the device allowed current transport (above 2.2 V), but gate leakage was not too high (below at least 4.0 V) in which we can drive the device. As a result, we limited the gate voltage to a maximum of 3.0 V to avoid falsifying our results by including current flowing through the gate oxide.

Fig. 6.12 (a) is a 3D graph of the two-point measurement of applied source-drain voltage (z-axis) between -1 V and +1 V, and the source-drain current (y-axis), while stepping the gate voltage (x-axis) from 0 to 3 V. The data was taken at ~4.5 K without an external magnetic field. We observed a very rapid turn on of the device with increasing gate voltage. The IV curves are not symmetric around zero. Instead, they show only a dip at negative source-drain voltage of a negative current, similar to a p-n junction.

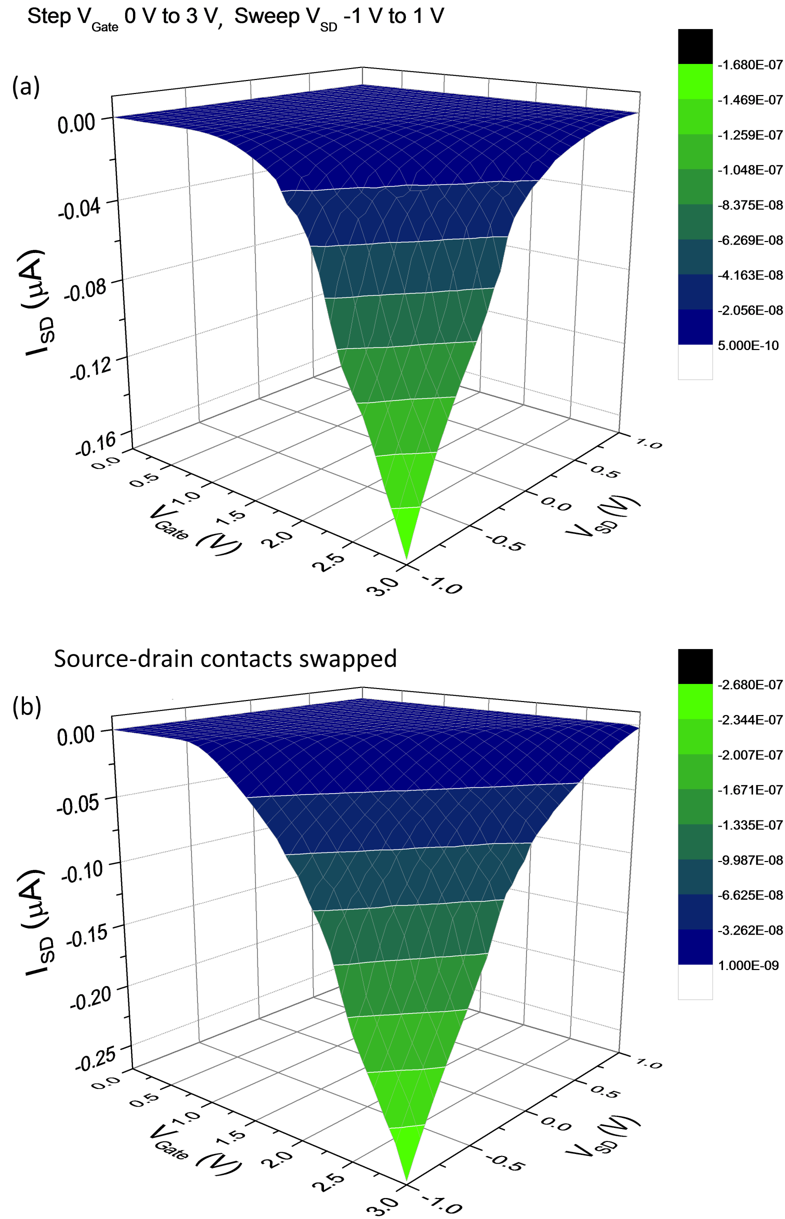

Figure 6.12: 3D graphs showing the gate dependency of a device of batch 4 at ∼4.5 K, design δ. The x-axis shows the gate voltage, y-axis the source-drain current, and z-axis the source-drain voltage. (a) and (b) have the source and drain contacts swapped in respect to each other.

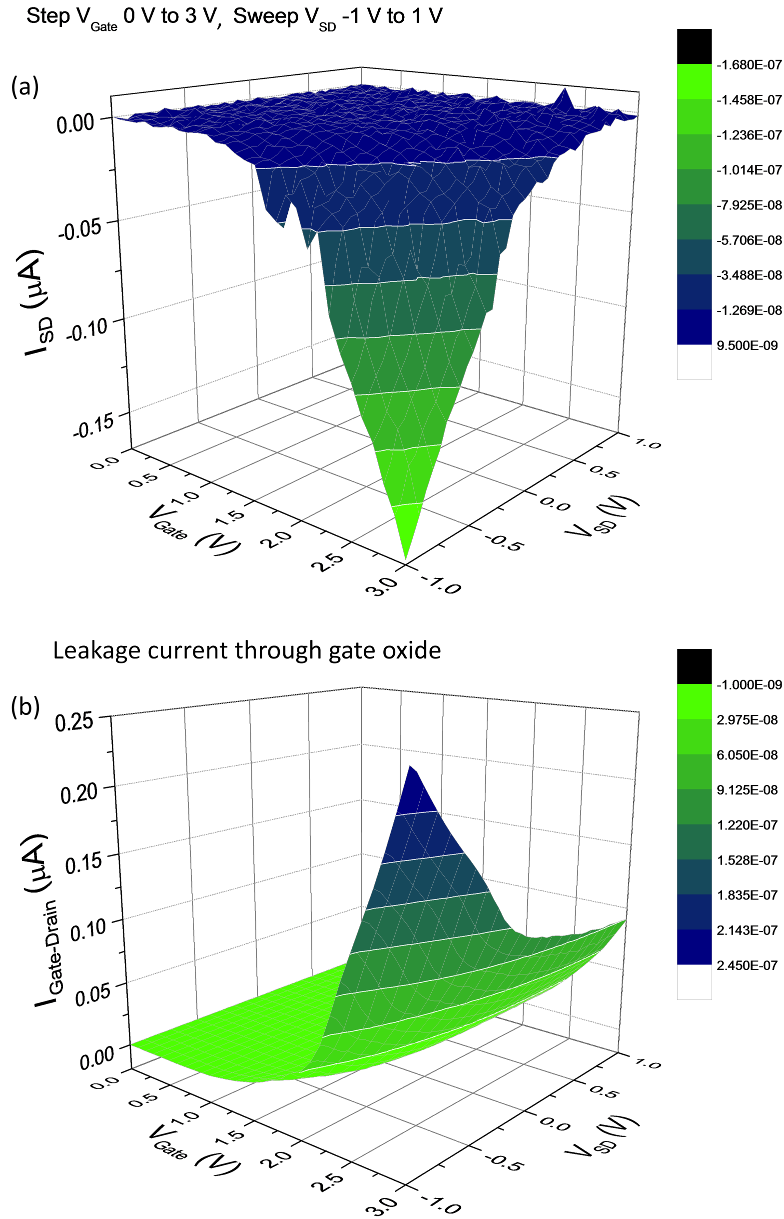

Figure 6.13: 3D graphs showing the gate dependency of a device of batch 4 at ∼4.5 K, design δ. The x-axis shows the gate voltage and the z-axis is the source-drain voltage. In (a) the y-axis is the source-drain current, while in (b) the gate-drain leakage current through the gate oxide is shown on the y-axis.

At positive source-drain voltages, they show no change in current. At 3.0 V gate voltage, we still measured only -0.16 μA at a source-drain voltage of -1.0 V. The previous gate leakage tests had shown that 2.0 V was approximately the voltage at which the current started to leak through the oxide, which is why we did not apply more than 3.0 V. Having said that, the effective gate voltage is actually greater. We were also applying negative 1 V at the source, leading to a potential difference between gate and source of 4 V. According to our findings in Fig. 6.11, we expected to see a current leaking through the gate oxide at that potential difference. This led to our assumption that the device was indeed not being turned on by the gate voltage, but that we were simply observing a current leaking through the gate oxide. We could not tell from this measurement whether the leak was globally across the whole gate oxide or confined to a local area. If the leak was confined, it might prove to be possible to measure the device avoiding this area.

In order to test this, the device was measured a second time with the source and drain contacts swapped (see Fig. 6.12 (b)). In this plot the gate voltage is on the x-axis, the source-drain current on the y-axis, and the source-drain voltage on the z-axis. Just as in Fig. 6.12 (a), we only see a source-drain current for high gate voltages and negative source-drain voltages. The absolute value of the source-drain currents is slightly higher, with I_{SD} = -0.25 μA at V_{Gate} = 3 V and V_{SD} = -1 V. This result proved that the leak was not locally confined, but occurred over a broader area across the gate oxide. With the larger source-drain current in the second configuration, it seemed that the leakage current must be higher nearer the source contact of the measurement configuration in Fig. 6.12 (b).

For absolute confirmation of the detected source-drain current originating mainly from a current leakage through the gate oxide, the experiment was repeated while simultaneously measuring the current between the source and drain contacts (see Fig. 6.13 (a) and (b)). While the y-axis on the top plot displays the source-drain current as in the previous graphs, the bottom

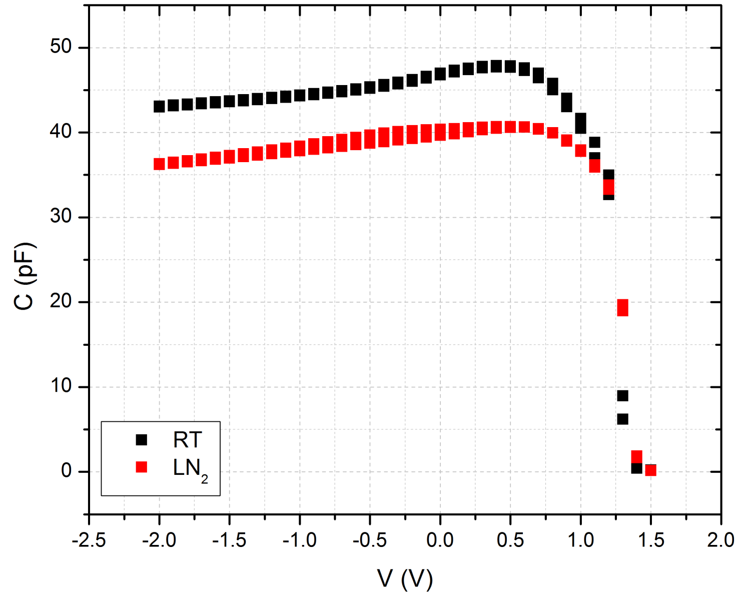

Figure 6.14: Capacitance versus voltage graph of the gate oxide of a fully fabricated device at room temperature (black) and at liquid nitrogen temperature (red).

plot displays the gate-drain current on the y-axis. We only detected a current flow through the gate oxide for high gate voltages. It was at its highest of 0.24 μA at V_{SD} = -1 V. With this measurement we clearly showed that the detected source-drain current was in fact due to a leak in the gate oxide. Unfortunately this meant that we were not able through the use of the gate to influence the charge carriers in the channel enough without also introducing new charge carriers through the applied gate voltage through the gate oxide.

CV measurements for gate oxide testing For the purpose of testing the gate oxide directly, we used the same setup as described in chapter 6.3 to apply a voltage on the gate of the device, while measuring the capacitance through the gate oxide via an ohmic contact. All remaining contacts were kept floating. As opposed to previous CV experiments, we were now doing this test on a fully fabricated device, as during the fabrication process

impurities may have been introduced. The leakage current was monitored manually, but not recorded by the software. Fig. 6.14 shows the capacitance versus voltage measurement of the same device (batch 4, design δ), at 295 K (black) as well as 80 K (red). Both data sets show the same trends, with the higher temperature curve having slightly larger capacitance values. The graph shows a shift of ca. +1.4 V in the depletion region, before the capacitance breaks down completely to 0 V as the threshold voltage is reached. This drop in capacitance occurs at the same gate voltage at which the observed leakage current begins to climb. The voltage at which the capacitance breaks down does not change with the temperature. Cooling down the sample while applying a bias of -2.0 V does not influence the CV curve. We concluded that the gate oxide must be the cause for our problems in measuring the gate dependency, as Fig. 6.14 shows that the oxide breaks down and starts to leak current at about 0.8 V. This means that we could not use a higher gate voltage than $\sim$1 V, as above this value the leakage current overwhelmed the channel current.

Conclusion We encountered fabrication problems with the production of a working gate oxide. As a consequence, there was a shift in the depletion region of the silicon dioxide by about 1.4 V. Also, we experienced gate leakage above 1.5 V - 2.0 V which rendered gate dependent measurements above that value useless. Below 1.5 V however, the applied gate voltage was too small to show an influence on the charge carriers in the underlying channel. Note that this applies only for positive gate voltages. Since the leads were phosphorus doped and thus n+ type, we assumed that a negative gate voltage caused the holes to recombine with the electrons in n+ regions. Consequently much higher negative gate voltages were necessary to observe gate leakage in the negative direction. As a consequence, we had to avoid using the top gate for further experiments and were thus not able to perform

standard MOS measurements. Instead, we next tried to activate the charge carriers by illuminating the devices.

Illumination dependency Another method of tuning the device, other than using the gate potential, is to use optical stimulation. We focused a low-temperature compatible red LED, directed at the examined device's surface, into the fridge. The LED was controlled by applying a voltage to it. Its IV at low temperature showed that it started to emit light from ca. 4.5 V onwards. In order to avoid the heating effect connected to the LED that we experienced in chapter 5.5, we did not use the coldfinger this time, but rather attached the sample and LED directly onto the MC plate of the fridge. This position gave us more cooling power due to its direct attachment to the fridge, and should consequently have led to less heating with the usage of the LED. Fig. 6.15 a) shows a measurement taken over 5 minutes during which the LED (red) was slowly turned on in 1 V steps from 0 V to 10 V, kept at 10 V for 1 minute's time, and then rapidly turned off to 0 V again. During this time the temperature (blue) was monitored. A constant source-drain voltage of 1.0 V was applied throughout the experiment. We were able to take a new temperature measurement only every ca. 3 seconds. Unfortunately this time couldn't be shortened, as otherwise the read out value became nonsensical. The AVS resistance bridge we used for the temperature readings required a stabilization time of several seconds. The exact value of the required stabilization time depended on the applied excitation voltage, as well as the resistance value of the readings. We decreased the stabilization time as well as the number of times the systems averaged the readings, and reduced the number of channels read out to the sensor at the sample only in order to achieve a maximum speed in temperature read out time. At the beginning of the measurement the sample temperature was 5.39 K. With a slow delay after turning on the LED, we could see that the temperature rose to about 5.44 K. At the same time we also recorded the resistivity through the device

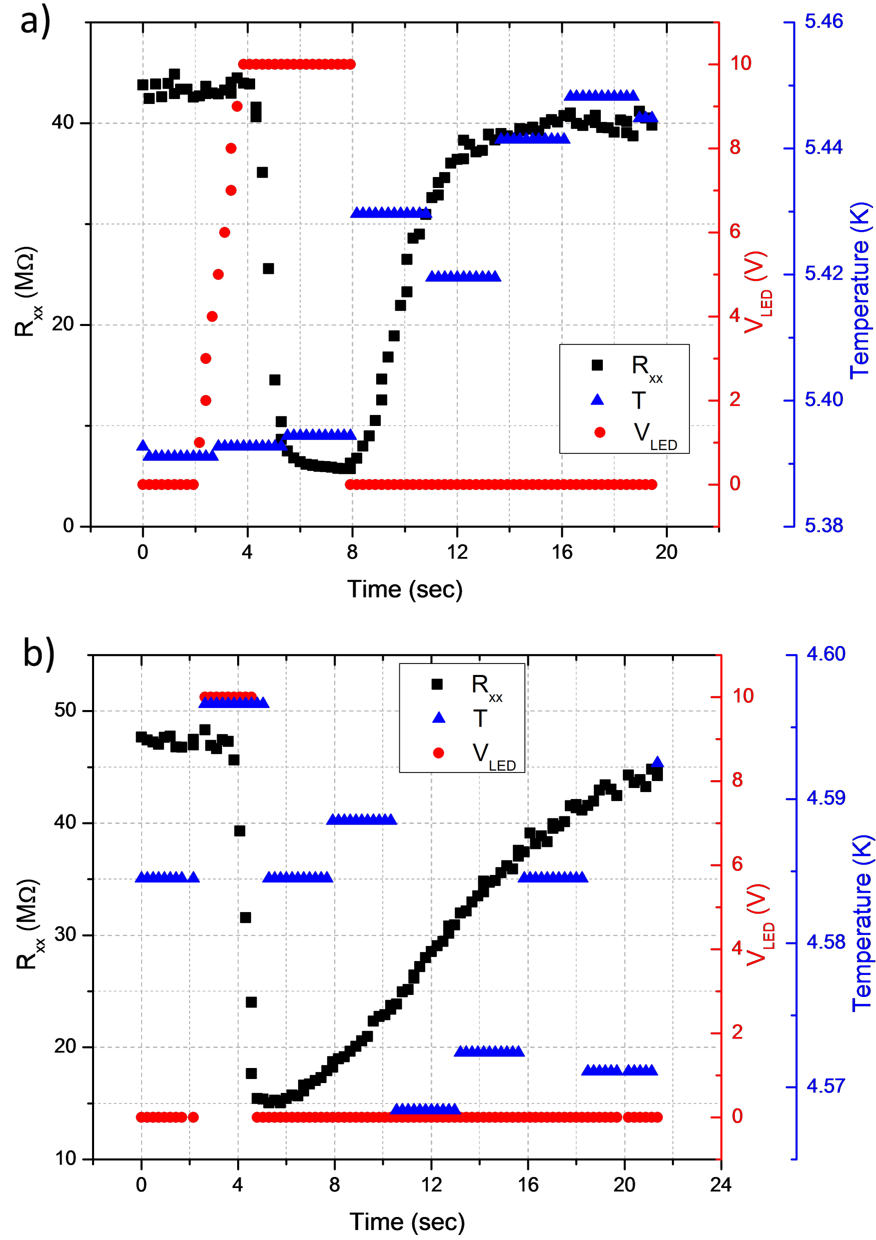

Figure 6.15: a) and b): Illumination dependency of a batch 4, design δ sample. Sample resistivity (black), LED voltage (red), and temperature (blue) versus time while applying a constant source-drain voltage of 1.0 V.

channel R_{xx}. The sample resistivity dropped from 43 MΩ to 8 MΩ within 2 seconds of the LED being turned fully on. Seemingly simultaneously with the switching off of the LED, the resistivity quickly rose again until it levelled out at 40 MΩ.

The graph below, Fig. 6.15 b), shows the behaviour of the same sample over time, with the LED this time being turned on rapidly from 0 V to 10 V (red). The source-drain voltage was still held at a constant value of 1.0 V. The temperature (blue) was constant during the experiment at 4.585 K ± 0.02 K. The sample resistivity (red) however dropped from 48 MΩ to 15 MΩ after a delay of ca. 2 seconds after the LED was turned on. Almost immediately after switching the LED off again, the resistivity began to slowly climb back up to its original value.

Conclusion The LED dependent measurements show a drastic change in the device resistivity of 18.6% (Fig. 6.15 a)) and 31.3% (Fig. 6.15 b)) with the switching on of an LED directed at the sample's surface. This did not happen immediately, but after a slight delay. Even though in graph 6.15 b) no temperature increase is recorded, the sample resistivity did not jump straight back to its original value with the turning off of the LED. Instead, it increased gradually. This, and the ca. 2 second delay time in reaction when the LED is switched on, made us suspect that we were not observing an effect due to photons, but rather a temperature related effect. This could be due to the fact that erbium doped silicon has an indirect band gap that is not bridged by the photons. The temperature sensor providing us the reading was not located directly next to the sample. The LED could possibly have been heating up a small, localized area around its tip. This would lead to the temperature sensor not recording a change, but the sample still experiencing an increase in temperature. Both the delay in reaction time when the LED was turned on, as well as the slow increase in resistivity once the LED was turned off again, would be explained by this theory. Overall, we could not

exclude an effect of the photons on the charge carriers. It may just be that we could not see the effect in this experimental setup. Thus, we now attempted to use the effect of impact ionization (recall section 1.2.1) to multiply the charge carriers in the channel area and perform electrical measurements.

Impact Ionization and magnetic field dependency As we had decided not to apply a voltage to the gate from now on, we left it fixed at 0 V for the following measurements. We intended to make use of the effect of impact ionization to create free charge carriers in the channel area (see chapter 1.2.1). This means that the source-drain current was used to tune the device.

We now inspected an Er and O implanted device (batch 4) of the design δ at ~5.0 K in dependency of an external magnetic field perpendicular to the sample plane. Fig. 6.16 shows the Hall voltage V_{xy} in dependency of an applied source-drain current I_{SD} for various magnetic fields up to 6.0 T. For positive source-drain current values we observed a hysteresis within all applied fields; the Hall voltage seems chaotic and not conclusive in that area. For negative source-drain currents on the other hand, we observed a smooth Hall voltage that turns into a curve inclined steeply towards 0 A source-drain current. For lower I_{SD} we observed a fanning out of V_{xy} for varying magnetic fields. Thus in Fig. 6.16 we show V_{xy} only for current values between -100 nA and -30 nA. The plot shows that higher field values result in higher Hall voltages, whereas smaller field values lead to lower Hall voltages.

We do not observe a change in sign of the Hall voltage with the change in sign of the external magnetic field. With a traditional Hall bar device, we expect the charge carriers to be diverted into opposite directions when the magnetic field changes its direction. This is measurable in the change of sign of the Hall voltage. In our device on the other hand, we only had a flow of charge carriers due to impact ionization. This leads to an inhomogeneous distribution of the charge carriers (see Fig. 6.17), which is not expected in traditional Hall bar devices. Unfortunately, reports about the Hall voltage in

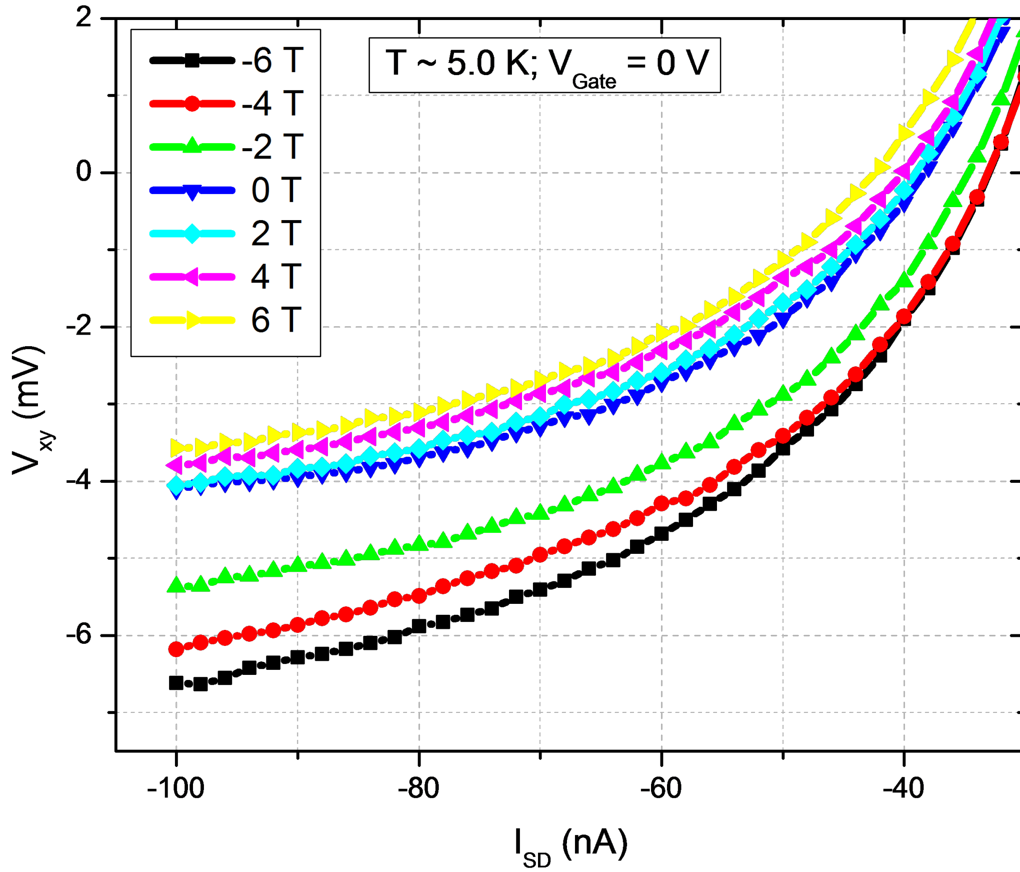

Figure 6.16: Magnetic field dependency of a batch 4, design γ device at $\sim$5.0 K. Hall voltage V_{xy} versus source-drain current I_{SD} from -100 nA to -30 nA for varying magnetic fields B.

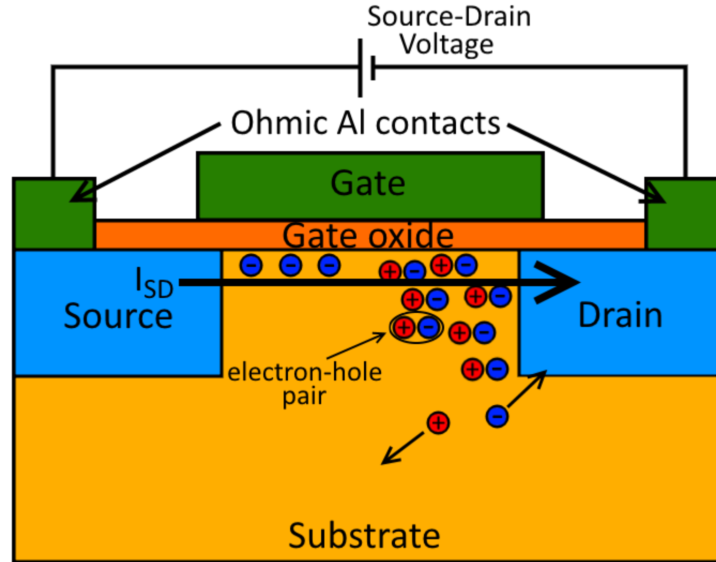

Figure 6.17: Schematic of freed electron-hole pairs according to impact ionization under the accelerating field of an applied source-drain voltage.

devices in the impact ionization regime are hard to find. It has been found that the polarity of an external magnetic field changes the recombination rate [184], which will consequently influence the Hall voltage. A stronger magnetic field reduces the charge carrier generation rate and increases the needed threshold voltage [184]. We do not have a model that completely explains the observed behaviour.

The graph a) in Fig. 6.18 displays the magnetic field dependency of the Hall resistivity R_{xy} (black) and longitudinal resistivity R_{xx} (red) at ∼5.0 K with a constant source-drain current of -50 nA. The bottom graph b) shows the FFT smooth of the sample temperature T in blue versus the magnetic field. The I_{SD} value was arbitrarily chosen in the area where Fig. 6.16 displays the fanning out of V_{xy} with varying B. Both, R_{xx} and R_{xy} are not only influenced by B, but also by the sample temperature. The Hall resistivity shows a decreasing trend with increasing magnetic field. It is almost linear, apart from jumps at -6 T and 0 T. These are due to stark

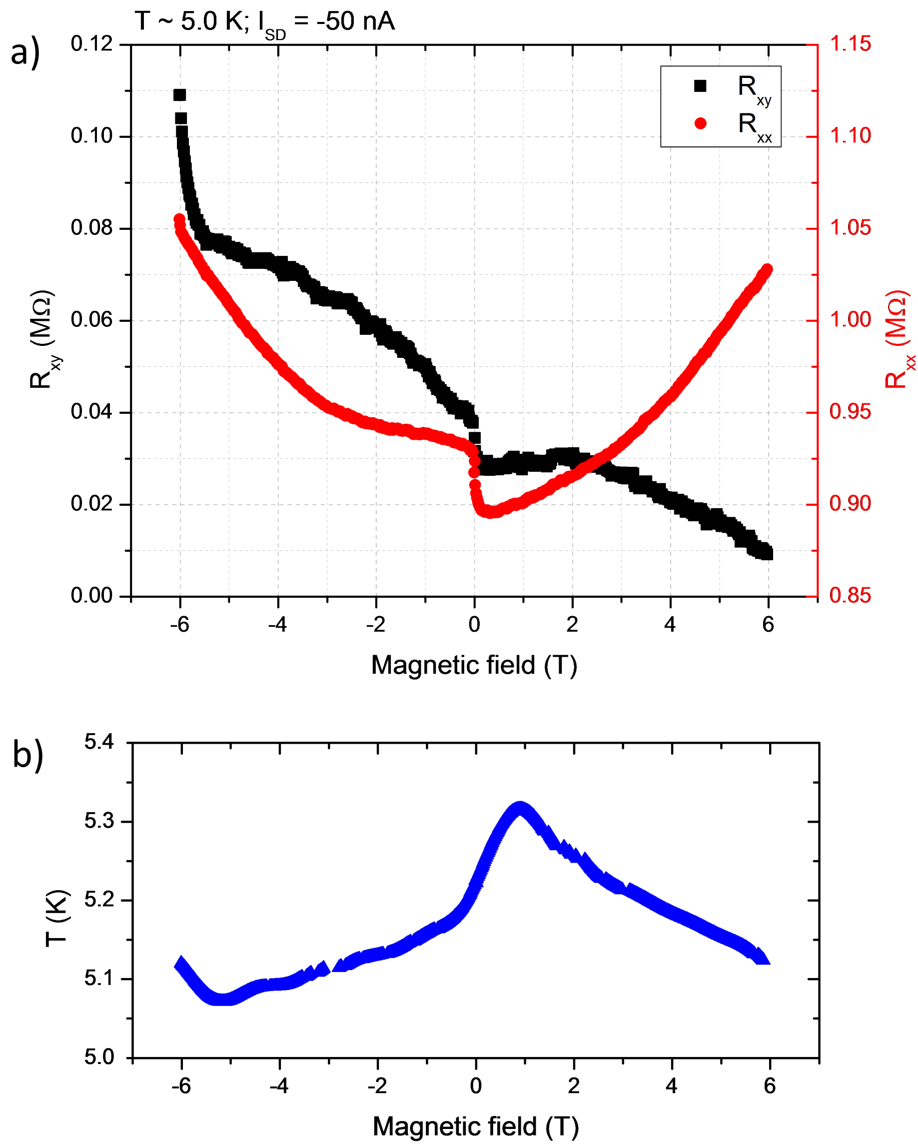

Figure 6.18: a) Hall resistivity (black) and source-drain resistivity (red) versus magnetic field at ∼5.0 K with a constant source-drain current of -50 nA. b) Sample temperature versus magnetic field.

temperature de-/increases. The longitudinal resistivity shows a decreasing trend for negative magnetic fields towards 0 T, which changes to a positive slope for positive field values. Here, also, an anomaly is observed at 0 T, due to the rapid temperature increase.

According to chapter 2.3.1, we expect the Hall voltage to change its sign with the change of polarity of B. We also expect R_{xy} to show linear behaviour. Even though our observations do show a linear behaviour of R_{xy}, this is only within the region where the temperature does not change rapidly. We believe the lack of sign change in R_{xy} is due to the device being in the regime of impact ionization, which causes it to act differently from a traditional Hall bar, as explained previously. We expected R_{xx} to be symmetric around zero Tesla, according to chapter 2.3.1. Within the experienced temperature fluctuations, this seems to be the case.

Conclusion Using the effect of impact ionization, the Hall resistivity as well as longitudinal resistivity were recorded. Unlike the case in a normal Hall probe, here the charge carrier distribution was not homogeneous in the device channel due to impact ionization. Thus we should not expect to achieve the same Hall resistivity that a normal Hall sample would show. Interestingly, we do see the expected trend in the resistivity across, as well as along the channel length. We expect that future experiments, in which the devices have functioning top gates and we are not within the regime of impact ionization, show a different magnetic field dependency. As this is not possible with the current devices, we are not able to present a satisfying model that explains the observed behaviour.

Chapter 7

Summary and outlook

Two different projects were undertaken within this thesis, after the successful installation and calibration of a dry dilution refrigerator. They are the characterization of nitrogen enhanced CVD grown ultra-nano-crystalline diamond and the examination of its conduction mechanism at ultra-low temperatures, as well as the fabrication and characterization of erbium doped silicon semiconductor devices. The conclusions and summaries to each of the two projects are given below.

7.1 Installation of a dry dilution refrigerator

We were able to successfully install a dry dilution refrigerator at Melbourne University.The mixing chamber plate recorded stable temperatures of ∼15 mK while the probe recorded a minimum of ∼36 mK. A coldfinger was designed and fabricated. It is able to hold two samples, one perpendicular to the main field direction and directly in the homogeneous area of the magnetic field lines of the integrated vector magnet, and a second sample parallel to the main field direction but slightly offset to the middle of the magnet. The 3D vector magnet was calibrated with well known samples. An offset of ∼5 mT of the main field direction was found. We suspect this offset to be due

to flux trapping, thus the value is not fixed, but will change with every cool down. Optical access through the vacuum cans was not granted for the work in this thesis, as a low temperature was higher regarded than direct optical access. Instead, the quartz windows were replaced with metal blanks. Unlike the quartz, the metal has far better radiation shielding properties and thus allows the refrigerator to reach lower temperatures due to a lower heat load, which was a main concern for the use of the dilution refrigerator during this work.

7.2 Nitrogen enhanced grown diamond

Several CVD grown UNCD Hall bars of three different nitrogen concentrations added to the gas feed stock (5%, 10%, 20%) were successfully fabricated. AFM and SEM imaging show a homogeneous structure that goes throughout the whole N-UNCD layer. There are flake-like structures of a size of an estimated 200 nm, that seem to be more edgy and spiky - as opposed to rounded - with higher nitrogen addition. Raman, RBS and XPS characterizations of the material have shown that the nitrogen enhanced growth did not cause measurable amounts of nitrogen to be incorporated into the thin films, in agreement with [56]. Instead, the nitrogen addition to the stock gas feed caused the chemical bonding structure of the carbon to change to some extent. With more nitrogen addition, there are slightly more sp^2 bondings as opposed to sp^3 bondings present. There is a clear change in room temperature conductivity within the varying nitrogen concentrations visible. We report conductivities of 12.44 S/cm, 1.63 S/cm, and 0.036 S/cm at room temperature for the 20%, 10%, and 5% N-UNCD films, respectively. The samples were examined between room temperature and as low as 40 mK - lower than ever reported previously. In the range of 3 K to 15 K we are able to fit the graph of conductivity versus temperature with the 3D WL model in accordance to [78]. Below 3 K however, the model shows a significant

discrepancy from the experimental data. It is possible to fit the magnetic field dependent data with the 3D WL model derived by Kawabata [8]. At 4 K the theory fits the data very well, but at lower temperatures and higher fields, the experimental data does not follow the theoretical fit any more. We assume that this is due to assumptions in Kawabata's model leading to inaccuracy at high fields. The data set at the lowest temperature, 36 mK, does not fit well into the overall picture of the magnetic field dependent measurements. While all other data sets show an increase in normalized conductivity at high magnetic fields, the 36 mK measurement shows too low a conductivity value to fit into this picture. Currently, we are working in collaboration with G. Chimowa and S. Bhattacharrya of the University of the Witwatersrand, Johannesburg, South Africa, to fit the experimental data with either the Bruenskin-Kleinert theory (B-K model) or the Kawabata model.

The influence of photons on the conductivity of the devices was measured at 300 mK using an LED directed at the sample surface. An immediate response of the device was noted when switching the LED on/off. This could be due to either a temperature effect induced by the 10 V applied to the LED, or due to the sudden presence of photons. Since the sample's response was immediate and jumped between two set values when the LED is on/off, we assume that what we observed is indeed an influence due to photons. Overall we confirm that at low temperatures 3D WL plays an important role in the conductivity of the N-UNCD films.

7.3 Erbium doped silicon

The fabrication of erbium doped silicon Hall bars faced problems in regards to the creation of the gate oxides. In an attempt to fix the issues, the fabrication process was overhauled and new work was undertaken at the University of NSW, following closely process flows that had previously proven to be successful. Unfortunately it was not possible to solve all fabrication

issues that occurred with this project. As a result the gate oxide leaked current from the gate into the underlying channel and is as such was not usable for device tuning purposes. The last batch of devices were subject to an unlucky mishap, the future prevention of which will certainly lead to the production of better, cleaner, and more usable gate oxides.

Despite the problems encountered, the fabrication process was optimized in regards to implantation parameters and device designs. The annealing process was optimized by commencing DLTS and photo-luminescence characterizations, leading to the result that a rapid thermal anneal at 900 °C for 30 seconds in argon ambient was best for our purposes of recovering the damaged substrate and also activating the implanted erbium. Electrical measurements revealed the effect of impact ionization which was visible without using the top gate. The magneto resistance was recorded while using the current through the device created via impact ionization. Unfortunately, unlike conventional Hall probes, our devices were not homogeneous in the impact ionization regime. As such we were not able to interpret the Hall resistivity of these devices. However, we did clearly observe an increased Hall resistivity with increasing applied source-drain current, as expected due to impact ionization. Tuning the device with photons, by placing an LED such that its light was directed at the sample's surface, again left us with the issue that the voltage applied to the LED (10.0 V when LED is turned on) led to the heating up of the sample. Even though we observed a drastic drop in resistivity by 18%-31%, we believe this change might be due to an increase in temperature. The delayed time that it took for the sample to react to the LED being switched on/off supports this opinion.

7.4 Further work

N-UNCD devices In future, it would be good to be able to measure the whole set of magnetic field dependent measurements at different tem-

peratures in one session, without warming up the sample in between. During this project's experiment, the sample was subject to various cool-downs between measurements, which may have slightly changed the device's behaviour at very low temperatures and thus altered some results (i.e. the 36 mK magneto-resistance measurement). In addition, having more than three different nitrogen concentrations in the gas feed stock would be ideal for a detailed study on the impact of nitrogen on the UNCD films. Characterizing the illumination dependency of the device with either optical fibres or via the optical windows in the dilution refrigerator would allow us to distinguish whether the device's resistivity is reacting to a change in temperature or to the presence of photons. With the completion of such further measurements, a theoretical model for the conduction mechanism in N-UNCD could be satisfactorily achieved.

Er:Si devices In order to fabricate fully functioning devices, more time needs to be spent on further refinement of the already developed fabrication process. With no unexpected issues such as we experienced while the silicon dioxide is being grown in the furnace, there should be no problems with creating a clean and robust gate oxide. This will enable the possibility of tuning the device by applying a voltage to the gate. By comparing devices of different implantation ions, it will then be possible to characterize the erbium electrically at varying temperatures, and the magneto resistance can then be measured at 4 K and below. With the help of optical fibres or optical stimulation through the windows in the dilution refrigerator, it would be possible to eliminate the heating effect we experienced with the LED, despite the fact that we placed the sample and LED directly onto the MC to give us more cooling power than the placement of the sample and LED on the probe would have. Since much foundation work has now been completed in this thesis, it should soon be possible to achieve a complete characterization

of erbium doped Hall bars. This will enable us to understand the electrical behaviour of erbium at low temperatures.

References

[1] L. Tang, C. Tsai, W.W. Gerberich, L. Kruckeberg, and D.R. Kania. *Biomaterials*, **16** (6), p. 483–488, (1995).

[2] J. J. Mares, P. Hubik, J. Kristofik, D. Kindl, M. Fanta, M. Nesladek, O. Williams, and D. M. Gruen. *Appl. Phys. Lett.*, **88**, p. 092107 1–3, (2006).

[3] J.J. Gracio, Q.H. Fan, and J.C. Mandaleno. *J. Phys. D: Appl. Phys.*, **43** (37), p. 374017 1–22, (2010).

[4] E. A. Ekimov, V. A. Sidorov, E. D. Bauer, N. N. Mel'nik, N. J. Curro, J. D. Thompson, and S. M. Smith. *Letters to Nature*, **428** (542–545), (2004).

[5] S. Mandal, C. Naud, O. A. Williams, E. Bustarret, F. Omnes, P. Rodiere, T. Meunier, L. Saminadayar, and C. Baeuerle. *Nanotechnology*, **21** (195303), (2010).

[6] Bionics Institute. Bionic Eye. `http://www.bionicsinstitute.org/research/bionicvision`, (April 2015).

[7] M. Nesladek, J. J. Mares, and P. Hubik. *New Diam. and Frontier Carbon Techn.*, **16** (6), p. 323–336, (2006).

[8] A. Kawabata. *J. Phys. Soc. Japan*, **49** (2), p. 628–637, (1980).

[9] E. Desurvire. *Sci. Am.*, **266** (1), p. 114–121, (1992).

[10] P.. Favennec, H. L'Haridoon, D. Moutonnet, M. Salvi, and M. Gauneau. *Jpn. J. Appl. Phys.*, **29** (4), p. L524–526, (1990).

[11] Y-G.F. Ren. *Erbium doped Silicon as an optoelectronic semiconductor material.* Doctor of Philosophy in Electronic Materials, Massachussetts Institute of Technology, (1994).

[12] C. Yin, M. Rancic, G. G. de Boo, N. Stavrias, J. C. McCallum, M. J. Sellars, and S. Rogge. *Nature*, **497**, p. 91–94, (May 2013).

[13] A. Krueger. *J. Mater. Chem.*, **18**, p. 1485–1492, (2008).

[14] Y. Takano, M. Nagao, I. Sakaguchi, M. Tachiki, T. Hatano, K. Kobayashi, H. Umezawa, and H. Kawarada. *Appl. Phys. Lett.*, **85** (14), p. 2851, (2004).

[15] G. Bergmann. *Weak localization in thin films, a time-of-flight experiment with conduction electrons.* North-Holland physics phyblishing-Amsterdam, (1984).

[16] Y. Takano, M. Nagao, T. Takenouchi, H. Umezawa, I. Sakaguchi, M. Tachiki, and H. Kawarada. *Diam. Relat. Mater.*, **14**, p. 1936–1938, (2005).

[17] A. Polman. *Appl. Phys. Reviews*, **82** (1), p. 1–39, (1997).

[18] J. D. Carey, R. C. Barklie, J. F. Donegan, F. Priolo, G. Franzò, and S. Coffa. *Phys. Rev. B*, **59** (4), p. 2773–2782, (1999).

[19] J.L. Benton, J. Michel, L.C. Kimerling, D.C. Jacobson, Y.-H. Xie, D.J. Eaglesham, E.A. Fitzgerald, and J.M. Poate. *J. Appl. Phys.*, **70** (5), p. 2667–2671, (1991).

[20] E.A. Gutierrez-D., M. J. Deen, and C. Claeys. *Low temperature electronics: Physics, devices, circuits, and applications.* Academic press, (2001).

[21] J. L. Cordeiro. Technological Evolution. `http://lifeboat.com/ex/technological.evolution`, (2012-2013).

[22] T. Okumura. *Encyclopedia of Electrical and Electronics Engineering*, **5**, p. 107–114, (1999).

[23] T.A. Alvesalo, P.M. Berglund, S.T. Islander, G.R. Pickett, and W. Zimmermann Jr. *Phys. Rev. A*, **4** (6), p. 2354–2368, (1971).

[24] C. Enss and S. Hunklinger. *Low-temperature physics.* Springer-Verlag, (2005).

[25] W.G. Fastowski, J.W. Petrowski, and A.E. Rowinski. *Kryotechnik.* Akademie-Verlag Berlin, (1970).

[26] L. H. Willems van Beveren, K. Y. Tan, N. S. Lai, A. S Dzurak, and A. R. Hamilton. *Appl. Phys. Lett.*, 97 (15), p. 152102, (2010).

[27] California Eastern Laboratories. NE3210S01 Datasheet. `http://www.CEL.com`, (2006).

[28] P.K. Bachmann, D. Leers, and Lydtin H. *Diam. and Rel. Mat.*, **1** (1), p. 1–12, (1991).

[29] B.J. Van Zeghbroeck. Principles of electronic devices. `http://ecee.colorado.edu/~bart/book/book/contents.htm`, (1996).

[30] H. Przybylinska, W. Jantsch, Yu. Suprun-Belevitch, M. Stepikhova, L. Palmetshofer, G. Hendorfer, A. Kozanecki, R.J.. Wilson, and B.J. Sealy. *Phys. Rev. B*, **54** (4), p. 1532–2547, (1996).

[31] H. Liander and E. Lundblad. *ASEA journal*, **28** (97), (1955).

[32] US Synthetic. High-pressure high-temperature technology. `http://www.ussynthetic.com/site/rd-sub/273/`, (April 2015).

[33] O.A. Shenderova and D.M. Gruen. *Ultrananocrystalline Diamond; Synthesis, Properties, and Applications.* William Andrew Publishing, (2006).

[34] W. von Bolton. *Z. Elektrochem.*, **17** (22), p. 971–972, (1911).

[35] J.C. Angus, H.A. Will, and W.S. Stanko. *J. of Appl. Phys.*, **39** (6), p. 2915 – 2922, (1968).

[36] B.V. Derjaguin and D.B. Fedoseev. *Sci. Am.*, **233** (5), p. 102–109, (1975).

[37] M. Kamo, Y. Sato, S. Matsumoto, and N. Setaka. *J. of Cryst. Growth*, **62**, p. 642–644, (1983).

[38] S. Matsumoto, Y. Sato, M. Tsutsumi, and N. Setaka. *J. Mater. Sci.*, **17**, p. 3106–3112, (1982).

[39] B.V. Spitsyn, L.L. Bouilov, and B.V. Derjaguin. *Prog. Cryst. Growth and Charact.*, **17**, p. 79–170, (1988).

[40] V.I. Konov, A.A. Smolin, V.G. Ralchenko, S.M. Pimenov, E.D. Obraztsova, E.N. Loublin, S. M. Metev, and G. Sepold. *Diam. and Rel. Mat.*, **4**, p. 1073–1078, (1995).

[41] L.C. Nistor, J. Van Landuyt, V.G. Ralchenko, E.D. Obraztsova, and A.A. Smolin. *Diam. and Rel. Mat.*, **6**, p. 159–168, (1997).

[42] D.M. Gruen. Conversion of Fullerenes to Diamond. US Patent 5,209,916, (November 1991).

[43] D.M. Gruen, S. Liu, A.R. Krauss, J. Luo, and X. Pan. *Appl. Phys. Lett.*, **64**, p. 1502 – 1504, (1994).

[44] C-C. Fu, H-Y. Lee, K. Chen, T-S. Lim, H-Y. Wu, P-K. Lin, P-K. Wei, P-H. Tsao, H-C. Chang, and W. Fann. *Proc. Natl. Acad. Sci. USA*, **104** (3), p. 727–732, (2007).

[45] R.M. Hazen. *The Diamond Markers.* Cambridge University Press, (1999).

[46] Y. Takano. *J. Phys.: Cond. Mat.*, **21** (253201), (2009).

[47] R. Kalish. *Diam. and Rel. Mat.*, **10**, p. 1749–1755, (2001).

[48] S. Koizumi, M. Kamo, Y. Sato, H. Ozaki, and T. Inuzuka. *Appl. Phys. Lett.*, **71**, p. 1065–1067, (1997).

[49] I. Sakaguchi, M. N.-Gamo, Y. Kikuchi, E. Yasu, H. Haneda, T. Suzuki, and T. Ando. *Phys. Rev. B*, **60** (4), p. R2139–R2141, (1999).

[50] R. Kalish, A. Reznik, C. Uzan-Saguy, and C. Cytermann. *Appl. Phys. Lett.*, **76**, p. 757–759, (2000).

[51] T.H. Borst and O. Weis. *Diam. and Rel. Mat.*, **4**, p. 948–953, (1995).

[52] M. Nesladek, M. Vancek, and L.M. Stals. *Phys. Stat. Sol. A*, **154**, p. 283–303, (1996).

[53] K. Okano, S. Koizumi, S. Ravi, P. Silva, and A.J. Amaratunga. *Letters to Nature*, **381**, p. 140–141, (1996).

[54] P. Zapol, M. Sternberg, L. A. Curtiss, T. Frauenheim, and D. M. Gruen. *Phys. Rev. B*, **65** (045403), (2001).

[55] S. Bhattacharyya, O. Auciello, J. Birrell, J. A. Carlisle, L. A. Curtiss, A. N. Goyette, D. M. Gruen, A. R. Krauss, J. Schlueter, A. Sumant, and P. Zapol. *Appl. Phys. Lett.*, **79** (10), p. 1441–1443, (2001).

[56] D. J. Garrett, K. Ganesan, A. Stacey, K. Fox, H. Meffin, and S. Prawer. *J. Neural Eng.*, **9** (1), p. 016002, (2012).

[57] M. Nesladek, D. Tromson, P. Bergonzo, P. Hubik, J. J. Mares, J. Kristofik, D. Kindl, O. A. Williams, and D. Gruen. *Diam. Relat. Mater.*, **15**, p. 607–613, (2006).

[58] I. I. Vlasov, V. G. Ralchenko, E. Goovaerts, A. V. Saveliev, and M. V. Kanzyuba. *Phys. Stat. Sol. (a)*, **203** (12), p. 3028–3035, (2006).

[59] A.C. Ferrari and J. Robertson. *Phys. Rev. B*, **61** (20), p. 14095–14097, (2000).

[60] X.J. Hu, X.H. Chen, and J.S. Ye. *AIP Advances*, **2** (032109), (2012).

[61] Y. Tzeng, S. Yeh, W.C. Fang, and Y. Chu. *Scientific Reports*, (4:4531), (2014).

[62] L.G. Cancado, K. Takai, T. Enoki, M. Endo, Y.A. Kim, H. Mizusaki, A. Jorio, L.N. Coelho, R. Magalhaes-Paniago, and M.A. Pimenta. *Appl. Phys. Lett.*, **88** (163106), p. 1–3, (2006).

[63] G. Chimowa, D. Churochkin, and S. Bhattacharyya. *EPL*, **99** (27004), p. 1–6, (2012).

[64] O. A. Williams, S. Curat, J. E. Gerbi, D. M. Gruen, and R. B. Jackman. *Appl. Phys. Lett.*, **85** (10), (2004).

[65] P. Achatz, O.A. Williams, P. Bruno, D.M. Gruen, J.A. Garrido, and M. Stutzmann. *Phys. Rev. B*, **74**, p. 155429, (2006).

[66] S. Bhattacharyya. *Phys. Rev. B*, **70** (125412), (2004).

[67] N.F. Mott. *Conduction in non-crystalline materials, Second edition.* Oxford science publications, (1992).

[68] M. C. Feliciangeli, M. C. Rossi, G. Conte, and V. Ralchenko. *Superlattices and Microstructures*, **46**, p. 188–194, (2009).

[69] C-R. Lin, W-H. Liao, D-Hua Wei, J-S. Tsai, C-K. Chang, and W-C. Fang. *Diam. and Rel. Mat.*, **20**, p. 380–384, (2011).

[70] J. Birrell, J. A. Carlisle, O. Auciello, D. M. Gruen, and J. M. Gibson. *Appl. Phys. Lett.*, **81** (12), p. 2235–2237, (2002).

[71] E. Abrahams, P.W. Anderson, D.C. Licciardello, and T.V. Ramakrishnan. *Phys. Rev. Lett.*, **42** (10), p. 673–676, (1979).

[72] E. Abrahams. *50 years of Anderson localization.* World Scientific Publishing Co. Pte. Ltd., (2010).

[73] M. Di Ventra. *Electrical transport in nanoscale systems.* Cambridge University Press, (2008).

[74] R. Kubo. *J. Phys. Soc. Japan*, **12**, p. 570–586, (1957).

[75] G. Bergmann. *Phys. Rev. B*, **28** (6), p. 2914–2920, (1983).

[76] J.S. Langer and T. Neal. *Phys. Rev. Lett.*, **16** (22), p. 984–986, (1966).

[77] P. Drude. *Annalen der Physik*, **306** (3), p. 566–613, (1900).

[78] P. A. Lee and T. V. Ramakrishnan. *Rev. Mod. Phys.*, **57** (2), p. 287–337, (1985).

[79] J. J. Mares, M. Nesladek, , D. Kindl, and J. Kristofik. *Diam. Rel. Mat.*, **15**, p. 1863–1867, (2006).

[80] N.F. Mott. *Philos. Mag. B*, **19** (160), p. 835–852, (1968).

[81] E. Bustarret, C. Marcenat, P. Achatz, J. Kacmarcik, F. Levy, A. Huxley, L. Ortega, E. Bourgeois, X. Blase, D. Debarre, and J. Boulmer. *Nature*, **444** (05340), p. 456–468, (2006).

[82] J. E. Moussa and M. L. Cohen. *Phys. Rev. B*, **77** (064518), (2008).

[83] S. Huefner. *Optical Spectra of Transparent Rare Earth Compounds.* Academic Press, (1978).

[84] A. J. Kenyon. *Semicond. Sci. technol.*, **20** (12), p. R65–R84, (2005).

[85] D.R. McCamey, G. Can Tol, G.W. Morley, and C. Boehme. *Phys. Rev. Lett.*, **102** (027601), (2009).

[86] A. Politi, M.J. Cryan, J.G. Rarity, S. Yu, and J.L. O'Brien. *Science*, **320** (5876), p. 646–649, (2008).

[87] J.P. Biersack and L.G. Haggmark. *Nucl. Instrum. Methods*, **174**, p. 257–269, (1980).

[88] G.P. Lansbergen, R. Rahman, J. Caro, S. Biesemans, G. Klimeck, L.C.L. Hollenberg, and S. Rogge. *J. Phys.: Conf. Ser.*, **109** (012003), p. 1–5, (2008).

[89] G. Granzo, S. Coffa, F. Priolo, and C. Spinella. *J. Appl. Phys.*, **81** (6), p. 2784–2793, (1997).

[90] J. Michel, J.L. Benton, R.F. Ferrante, D.C. Jacobson, D.J. Eaglesham, E.A. Fitzgerald, Y.-H. Xie, J.M. Poate, and L.C. Kimerling. *J. Appl. Phys.*, **70** (1), p. 2672–2678, (1991).

[91] S. Coffa, G. Franzo, F. Priolo, A. Polman, and R. Serna. *Phys. Rev. B*, **49** (23), p. 16313–16320, (1994).

[92] S. Coffa, F. Priolo, G. Franzo, and V. Bellani. *Phys. Rev. B*, **48** (16), p. 11782–11788, (1993).

[93] D.R. McCamey, H. Huebl, M.S. Brandt, W.D. Hutchison, J.C. McCallum, R.G. Clark, and A.R. Hamilton. *Appl. Phys. Lett.*, **89** (182115), (2006).

[94] A. Morello, J. J. Pla, F.A. Zwanenburg, K. W. Chan, K. Y. Tan, H. Huebl, M. Moettoenen, C. D. Nugroho, C. Yang, J. A. van Donkelaar, A. D. C. Alves, D. J. Jamieson, C. C. Escott, L. C. L. Hollenberg, R. G. Clark, and A. S. Dzurak. *Nature*, **467**, p. 687–691, (2010).

[95] L.H. Willems van Beveren, H. Huebl, D.R. McCamey, T.Duty, A.J. Ferguson, R.G. Clark, and ¡.S. Brandt. *Appl. Phys. Lett.*, 93 (072102), (2008).

[96] B.A. Andreev, Z.F. Krasil'nik, D.I. Krychkov, A.N. Yablonskii, V.P. Kuznetsov, T. Gregorkiewicz, and M.A.J. Klik. *Phys. Solid State*, **46** (1), p. 97–100, (2004).

[97] W. Wang, H. Isshiki, S. Yugo, R. Saito, and T. Kimura. *J. of Lumen.*, 87-89, p. 319–322, (2000).

[98] F. Priolo, S. Coffa, G. Franzo, C. Spinella, A. Carnera, and V. Bellani. *J. Appl. Phys.*, **74** (8), p. 4936–4942, (1993).

[99] P. Pellegrino, P. Leveque, J. Lalita, A. Hallen, C. Jagadish, and B.G. Svensson. *Phys. Rev. B*, **64** (195211), (2001).

[100] N.A. Sobolev, O.B. Gusev, E.I. Shek, V.I. Vdovin, T.G. Yugova, and A.M. Emel'yanov. *Appl. Phys. Lett.*, **72** (25), p. 3326–3328, (1998).

[101] S. Libertino, S. Coffa, G. Franzo, and F. Priolo. *J. of Appl. Phys.*, **78** (6), p. 3867–3873, (1995).

[102] M.D.H. Lay, J.C. McCallum, and C. Jagadish. *Phys. B*, (340-342), p. 748–751, (2003).

[103] J.H. Evans-Freeman and N. Abdulgader. *Solid State Phenomena*, **95-96**, p. 135–140, (2004).

[104] B.C. Johnson, J.C. McCallum, L.H. Willems van Beveren, and E. Gauja. *Thin Solid Films*, **518**, p. 2524–2527, (2010).

[105] S. Binetti, M. Donghi, S. Pizzini, A. Castaldini, A. Cavallini, B. Fraboni, and N.A. Sobolev. *Solid State Phenomena*, **57-58**, p. 197–206, (1997).

[106] G. E. Moore. http://www.mooreslaw.org, (2013).

[107] S. Anthony. Beyond silicon: IBM unveils world's first 7 nm chip. http://arstechnica.com/gadgets/2015/07/ibm-unveils-industrys-first-7nm-chip-moving-beyond-silicon/, (July 2015).

[108] W. Arden, M. Brillouet, P. Cogez, M. Graef, B. Huizing, and R. Mahnkopf. More-than-Moore, White Paper. http://www.itrs.net/Links/2010ITRS/IRC-ITRS-MtM-v2%203.pdf, (2001).

[109] M. Stoneham. *Physics*, **2**, p. 34, (2009).

[110] T. Shah. First commercial quantum computer by D-Wave no better than classic PC in speed test. http://www.techtimes.com/articles/8860/20140620/first-commercial-quantum-computer-by-d-wave-fails-to-impress-in-speed-test.htm, (June 2014).

[111] P.W. Shor. *SIAM Journal on Computing*, **26** (5), p. 1484–1509, (1997).

[112] S. Lloyd. *Science*, **273**, p. 1073–1078, (1996).

[113] A. J. Fisher. *Phil. Trans. R. Soc. Lond. A*, **361**, p. 1441–1450, (2003).

[114] T. Monz, P. Schindler, J. T. Barreiro, M. Chwalla, D. Nigg, W. A. Coish, M. Harlander, W. Haensel, M. Hennrich, and R. Blatt. *Phys. Rev. Lett.*, **106** (13), p. 130506, (2011).

[115] D Wave. The D-Wave Two$^{\text{TM}}$ System. http://www.dwavesys.com, (2013).

[116] E. van Oort, N. B. Manson, and M. Glasbeek. *J. Phys. C: Solid State Phys.*, **21** (23), p. 4385–4391, (1988).

[117] A. D. Greentree, P. Olivero, M. Draganski, E. Trajkov, J. R. Rabeau, P. Reichart, B. C. Gibson, S. T. Huntington S. Rubano and, D. N. Jamieson, and S. Prawer. *J. Phys. Condens. Matt.*, **18** (21), p. 825–842, (2006).

[118] R. Hanson, F. M. Mendoza, R. J. Epstein, and D. D. Awschalom. *Phys. Rev. Lett.*, **97** (087601), (2006).

[119] Gaebel, M. Domhan, I. Popa, C. Wittmann, P. Neumann, F. Jelezko, J. R. Rabeau, N. Stavrias, A. D. Greentree, S. Prawer, J. Meijer, J. Twamley, P. R. Hemmer, and J. Wrachtrup. *Nat. Phys.*, **2**, p. 408–413, (2006).

[120] D. V. Lang. *J. Appl. Phys.*, **45** (7), p. 3023–3032, (1974).

[121] D.K. Schroder. *Semiconductor Material and Device Characterization, 3rd Edition*. Wiley-IEEE Press, (2006).

[122] H. K. Nielsen. Capacitance Transient Measurements on Point defects in silicon and silicon carbide. *Doctoral thesis in solid state electronics, Stockholm, Sweden*, (2005).

[123] O. Entstrom and A. Alm. *Solid-State Electronics*, **21**, p. 1571–1576, (1978).

[124] E.W. Weiss. Boxcar Function. `http://mathworld.wolfram.com/BoxcarFunction.html`, (2014).

[125] M.B.H Breese, D.N. Jamieson, and P.J.C. King. *Materials analysis using a nuclear microprobe*. Wiley-Interscience, (1996).

[126] W-K. Chu, J. W. Mayer, and M.-A. Nicolet. *Backscattering Spectrometry*. Academic Press, Inc., (1978).

[127] Operation and Characteristics of a Semiconductor Detector. The Silicon Surface Barrier Detector. `http://livingtextbook.oregonstate.edu/chemlab/media/expt6.pdf`, (2014).

[128] Genplot. `http://www.genplot.com`, (2013).

[129] E.H. Putley. *Contemp. Phys.*, **16** (2), p. 101–126, (1975).

[130] D. Meschede. *Gerthsen Physik*, volume **24**. Springer-Verlag Berlin Heidelberg, (2010).

[131] C.L. Chien and C.R. Westgate. *The hall effect and its applications.* Springer, (1980).

[132] D. Yoshioka. *The Quantum Hall Effect.* Springer Verlag, Berlin, (2002).

[133] L. J. van der Pauw. *Philips Technical Rev.*, **20** (8), p. 220–224, (1958).

[134] L. J. van der Pauw. *Philips Research Reports*, **13** (1), p. 1–9, (1958).

[135] P. Kapitza. *Nature*, **141** (3558), p. 74, (1938).

[136] J.F. Allen and A.D. Misener. *Nature*, **142** (3597), p. 643–644, (1938).

[137] J. Emsley. *Nature's building blocks.* Oxford University Press, (2001).

[138] D.O. Edwards, D.F. Brewer, P. Seligman, M. Skertic, and M. Yaqub. *Phys. Rev. Lett.*, **15** (20), p. 773–775, (1965).

[139] C.D. Keith. Helium vapor temperature versus pressure. `https://userweb.jlab.org/~ckeith/TOOLS/HeVaporTable.html`, (2001).

[140] G.K. Walters and W.M. Fairbank. *Phys. Rev.*, 103 (a), p. 262–2632, (1956).

[141] D.G. Fink. *Electronics engineers' handbook.* Mcgraw-hill Inc, (1989).

[142] K. von Klitzing. *Rev. Mod. Phys.*, **58** (3), p. 519–531, (1986).

[143] J.W. Rohlf. *Modern physics from alpha to z.* John Wiley, (1994).

[144] S. George. *Characterizing niobium superconducting thin films.* University of Chicaco, (2011). Physics REU Program.

[145] D. Dew-hughes. *Low temperature Physics*, **27** (9-10), p. 713–722, (2011).

[146] H. Fujishiro, T. Naito, and M. Oyama. *Supercond. Sci. Technol.*, **24**, p. 075015, (2011).

[147] C. Benvenuti, S. Calatroni, I.E. Campisi, P. Darriulat, C. Durand, M.A. Peck, R. Russo, and A.-M. Valente. Workshop on RF Superconductivity, Abano Terme (Padova), Italy, (October 1997).

[148] M. H. Somerville, A. Ernst, and J. A. del Alamo. *IEEE Transactions on Electron Devices*, **47** (5), p. 922–930, (2000).

[149] International School of Physics Enrico Fermi. *The Physics of Diamond*, volume **153**. (1997).

[150] Shengkui Gao. `http://www.cse.wustl.edu/~vgruev/cse/506/slides/w4_dry_etching.pdf`, (2013).

[151] Microchemicals. `"http://www.microchemicals.eu/technical_information/chromium_etching.pdf`, (2013).

[152] S. Jeedigunta, P. Spagnol, J. Bumgarner, and A. Kumar. *Diam. and Related Mat.*, **17**, p. 2037–2040, (2008).

[153] J. F. Ziegler and J. P. Biersack. `http://www.SRIM.com`, (2013).

[154] J. F. Ziegler and J. M. Manoyan. *Nucl. Instrum. Methods B*, **35**, p. 215–228, (1988).

[155] N.F. Mott and M. Kaveh. *Philos. Mag. B*, **47** (6), p. 577–603, (1983).

[156] V.G.I. Deshmukh. *Philos. Mag. B*, **37** (5), p. 649–651, (1978).

[157] Semiconductor process simulation Wikipedia. `http://en.wikipedia.org/wiki/Semiconductor_process_simulation`, (2014).

[158] FLOOPS wiki manual. `http://www.flooxs.ece.ufl.edu/index.php/Main_Page`, (2014).

[159] F. Maloberti. *Analog design for CMOS VLSI systems*. Springer, (2001).

[160] B. E. Deal and A. S. Grove. *Journal of applied physics*, **36** (12), p. 3770–3778, (1965).

[161] M. F. Ceiler Jr., P. A. Kohl, and S. A. Bidstrup. *J. Electrochem. Soc.*, **142** (6), p. 2067–2071, (1995).

[162] Oxford Instruments Plasma Technology. The Bosch Process for Etching Micro-Mechanical Systems (MEMS) - Principles, Advances and Applications by Oxford Instruments Plasma Technology. `http://www.azonano.com/article.aspx?ArticleID=2738#3`, (June 2013).

[163] A. J. Ferguson, R. L. Clarke, and H. E. Gove. *Phys. Rev.*, **115** (6), p. 1655 – 1659, (1959).

[164] E. Rauhala. *Nucl. Instrum. Meth. B*, **12** (4), p. 447–452, (1985).

[165] A. V. Naumkin, A. Kraut-Vass, S. W. Gaarenstroom, and C. J. Powell. NIST X-ray Photoelectron Spectroscopy Database. `srdata.nist.gov/xps`, (2014).

[166] B. V. Christ. *Handbook of monochromatic XPS spectra: The elements and native oxides.* Wiley, (1999).

[167] S. Al-Riyami, S. Ohmagari, and T. Yoshitake. *Diam. Relat. Mater.*, **19**, p. 510–513, (2010).

[168] E. R. Menzel. *Laser Spectroscopy - Techniques and Applications.* Marcel Dekkar, Inc., (1995).

[169] M. Fujii, T. Kita, S. Hayashi, and K. Yamamoto. *J. Phys.: Condens. Matter*, **9**, p. 8669–8677, (1997).

[170] D.A. Zakheim, I.V. Rozhansky, and S.A. Gurevich. *Nanotechnology*, **14**, p. 366–370, (2003).

[171] O. A. Williams, M. Nesladek, M. Daenen, S. Michaelson, A. Hoffman, E. Osawa, K. Haenen, and R.B. Jackman. *Diam. and Rel. Mat.*, **17**, p. 1080–1088, (2008).

[172] D. Stauffer and A. Aharoni. *Introduction to Percolation Theory.* Taylor and Francis, (1994).

[173] D. Toker, D. Azulau, N. Shimoni, I. Balberg, and O. Millo. *Phys. Rev. B*, **68**, p. 041403 1–4, (2003).

[174] K.V. Shah, D. Churochkin, Z. Chiguvare, and S. Bhattacharyya. *Phys. Rev. B*, **82**, p. 184206–1–9, (2020).

[175] J.W. Walker and C.T. Sah. *Phys. Rev. B*, 7 (10), p. 4587–4605, (1973).

[176] G.D. Watkins and J.W. Corbett. *Phys. Rev.*, 121 (4), p. 1001–1014, (1961).

[177] A.O. Evwaraye and E. Sun. *J. of Appl. Phys.*, **47** (9), p. 3776–3780, (1976).

[178] G.D. Watkins and J.W. Corbett. *Phys. Rev.*, 134 (5A), p. A1359–A1377, (1964).

[179] G.D. Watkins. *Electrochem. Soc. Proc.*, 99-1, p. 38, (1999).

[180] A. Polman, G.N. van den Hoven, J.S. Custer, J.H. Shin, R. Serna, and P.F.A. Alkemade. *J. Appl. Phys.*, **77** (1256), (1995).

[181] Linkam Stage. `http://www.linkam.co.uk/temperature-controlled-stages/`, (March 2015).

[182] Y.S. Tang, Z. Jingping, K.C. Heasman, and B.J. Sealy. *Solid State Communications*, **72** (10), p. 991–993, (1989).

[183] X.T. Ren and M.B. Huang. *J. of Appl. Phys.*, **100** (2), p. 023525, (2006).

[184] J. Hong, T. Kim, S. Joo, J. Dong Song, S. Hee Han, K-H. Shin, and J. Chang. *Cond. Mat. Sci.*, (arXiv:1206.1094v1), (2012).

[185] P. W. Anderson. *Phys. Rev.*, **109** (5), p. 1942–1505, (1958).

[186] E. Bar-Sadeh, Y. Goldstein, C. Zhang, H. Deng, B. Abeles, and O. Millo. *Phys. Rev. B*, **50** (12), p. 8961–8965, (1994).

[187] Yinon Bentor. Chemical Element.com - Niobium. `http://www.chemicalelements.com/elements/nb.html`, (Jan 2015).

[188] Eugene P. Bertin. *Introduction to X-Ray Spectrometric Analysis.* Plenum Press, New York, (1980).

[189] E. Bourgeois, E. Bustarret, P. Achatz, F. Omnes, and X. Blas. *Phys. Rev. B*, **74** (094509), (2006).

[190] M. Calandra and F. Mauri. *Phys. Rev. Lett.*, **101** (016401), (2008).

[191] A. Kawano, H. Ishiwata, S. Iriyama, R. Okada, T. Yamaguchi, Y. Takano, and H. Kawarada. *Phys. Rev. B*, **82** (085318), (2010).

[192] A. Kawano, H. Ishiwata, S. Iriyama, R. Okada, S. Kitagoh, M. Watanabe, Y. Takano, T. Yamaguchi, and H. Kawarada. *Physica C*, **470**, p. S604–S607, (2010).

[193] Y. Ma, J. S. Tse, D. D. Klug, L. Zhang, Y. Xie, Y. Niu, and G. Zou. *Phys. Rev. B*, **72** (014306), (2005).

[194] P. W. May. *Phil. Trans. R. Soc. Lnd. A*, **358**, p. 473–495, (2000).

[195] M. D. McCluskey and E. E. Haller. *Dopants and Defects in Semiconductors.* Taylor & Francis Group, LLC, (2012).

[196] J.J.L. Morton, D.R. McCamey, M.A. Eriksson, and S.A. Lyon. *Nature*, **479**, p. 345–353, (2011).

[197] T. Muranaka, K. Kobashi, H. Kobashi, H. Okabe, T. Tachibana, Y. Yokota, K. Hayashi, N. Kawakami, and J. Akimitsu. *Diam. Relat. Mater.*, **20**, p. 1273–1291, (2011).

[198] P. F. Newman and D. F. Holcomb. *Phys. Rev. B*, **28**, p. 638, (1983).

[199] N. Oki, T. Kagayama, K. Shimizu, and H. Kawarada. *J. of Phys: Conference Series*, **215** (012143), p. 1–3, (2010).

[200] V. Solozhenko, O. Kurakevych, D. Andrault, Y. L. Godec, and M. Mezouar. *Phys. Rev. Lett.*, **102** (015506), (2009).

[201] B. Sopik. *New Journal of Phys.*, **11** (103025), (2009).

[202] K. R. Williams, K. Gupta, and M. Wasilik. *J. Microelectromech. Sys.*, **12** (6), p. 761–778, (2003).

[203] K. R. Williams and R. S. Muller. *J. Microelectrochem. Sys.*, **5** (4), p. 256–269, (1996).

[204] J. S. Williams. *Mat. Science and Eng.*, **A253**, p. 8–15, (1998).

University Library

A gateway to Melbourne's research publications

Minerva Access is the Institutional Repository of The University of Melbourne

Author/s:
Eikenberg, Nina

Title:
Characterization of silicon and diamond semiconductor devices in the low temperature regime

Date:
2015

Persistent Link:
http://hdl.handle.net/11343/57457

File Description:
Characterization of silicon and diamond semiconductor devices in the low temperature regime